Analytical Fatigue Evaluation and Test Specimen Design for Cantilevered Overhead Sign Structure Box Connections

By
© 2022
Andrea Wall
B.S., Valparaiso University, Indiana 2019

Submitted to the graduate degree program in Department of Civil, Environmental, and Architectural Engineering and the Graduate Faculty of the University of Kansas in partial fulfillment of the requirements for the degree of Master's of Science.

_____

Chair: Dr. William Collins

_____

Dr. Caroline Bennett

_____

Dr. Jian Li

Date Defended: June 9, 2022

The dissertation committee for Andrea Wall certifies that this is the approved version of the following dissertation:

Analytical Fatigue Evaluation and Test Specimen Design for Cantilevered Overhead Sign Structure Box Connections

_____

Chair: Dr. William Collins

Date Approved: June 10, 2022

Abstract

Cantilevered overhead sign structures (COSS) are susceptible to fatigue at many of their connection details, in particular the connection between the pole and mast-arm, due to stresses caused by natural wind gusts, truck-induced wind gusts, and galloping. There have been cases of structures within the Kansas Department of Transportation (KDOT) inventory, failing at the gusseted box connection, which is the connection detail utilized by KDOT to connect the pole and mast-arm. Behavior and fatigue life of these connection details are not well understood, which limits the ability to identify which structures should be considered for repair, retrofit, or replacement.

This research was focused on analyzing behavior of the box connection used in COSS. A finite element analysis investigation was conducted on 21 different COSS based on KDOT designs to investigate the effects of changing geometry of the structure and the impact of switching from a gusseted box connection to a ring-stiffened box connection.

Findings from the finite element analyses included: 1) thickening the mast-arm and pole aids in decreasing stresses experienced by the box connection, 2) as pole thickness increases, peak demands shift to the mast-arm socket connection for out-of-plane loading and to the baseplate socket connection for in-plane loading, and 3) utilization of the ring-stiffened box connection decreased stresses at the box connection for both out-of-plane and in-plane loading.

Keywords: Cantilevered Overhead Sign Structure; fatigue; box connection; hot spot stress analysis

Acknowledgements

I would like to start by expressing my gratitude to my advisor, Dr. William Collins, for picking me up for this research project as well for all of his support during the course of it. I would also like to thank Dr. Caroline Bennett and Dr. Jian Li for their guidance and aid.

I am also thankful for the aid that fellow graduate students have provided to me, in particular, Danqing Yu and Zahra Andalib for their aid in understanding Abaqus early on and Tristan Yount for all of his help in understanding the equipment for the experimental testing. Along with that lab technicians Kent Dye and David Woody were invaluable for their patience, aid, and understanding during the many ups and downs that took place in beginning the experimental testing. Fellow graduate student Afeez Badmus has also been essential in the performance of the experimental testing, as well as hourly assistant, Conrado Sacco. I would also like to thank my peers, Jordan Nutter and Mary Juno, for their support and friendship.

Furthermore, I want to thank the Kansas Department of Transportation, for without the support and funding this research would not have been possible and Steve Johnson for the fabrication of the experimental specimens.

Finally, I want to express my appreciation to my friends and family for their support and encouragement during my studies, especially Alex Bond for all of his support and patience with me.

Table of Contents

Table of Figures

Table of Tables

Notation

AASHTO	American Association of State and Highway Transportation Officials
AASHTO SLT	AASHTO LRFD Specifications for Structural Supports for Highway Signs, Luminaires, and Traffic Signals
AWS	American Welding Society
CAFT/CAFL	Constant-Amplitude Fatigue Threshold/Limit
COSS	Cantilevered Overhead Sign Structure
DIC	Digital Image Correlation
DNV	Det Norske Veritas
FEA	Finite Element Analysis
HSS (σ_{hs})	Hot Spot Stress
‴Q ةشيفشيچث	Distance from the ground to the bottom edge of the sign
‴Q جچب	Distance from the ground to the bottom of the top or bottom mast-arm
IIW	International Institute of Welding
KDOT	Kansas Department of Transportation
LRFD	Load and Resistance Factor Design
TIWG	Truck-Induced Wind Gusts
T+G	Truck-Induced Wind Gusts plus Galloping
SCF	Stress Concentration Factors
NCHRP	National Cooperative Highway Research Program
NW	Natural Wind

Chapter 1: Introduction

1.1 Background

Cantilevered overhead sign structures (COSS) are commonly employed as an important component of highway infrastructure across the United States. They are used to convey signage information to motorists in an effective manner and their cantilevered design minimizes the space they require. In recent years, the discovery of fatigue cracking within COSS connection details has become more common. These fatigue cracks limit the structures' service life. To combat the problem of fatigue cracking, design provisions focused on fatigue performance and design have been developed and implemented, first introduced by the American Association of State Highway and Transportation Officials (AASHTO) in the Load and Resistance Factor Design (LRFD) Specifications for Structural Supports for Highway Signs, Luminaires, and Traffic Signals (AASHTO SLT) in 2001. Prior to this specification fatigue considerations were not mandated for sign structures. Evolving understanding of fatigue behavior has resulted in the requirements being refined in each subsequent version of the specification since their introduction.

Three primary loading mechanisms induce fluctuations on COSS: natural wind (NW), truck-induced wind gusts (TIWG), and galloping. As the large area of typical signs allow for the accumulation of pressure from natural wind, NW load effects in the horizontal direction dominate demand on the structure. The structures are also affected by truck-induced wind gusts, which are vertical fluctuations induced by trucks driving underneath the sign at high speeds. The horizontal impact of TIWG is minimal and disregarded by AASHTO specifications as NW will always produce a larger horizontal impact, therefore controlling the demand in the horizontal direction. The third load mechanism experienced by COSS is galloping, which is caused by a coupling between structural vibrations and the forces from wind loading. Oscillations resulting from galloping only occur if the natural frequency of the structure is excited. The fluctuations caused by these loads create cyclic loading that acts upon the structure, placing fatigue demand on the components and connections.

There are four main construction types of COSS, characterized by the number of horizontal mast members: 1) monotube, 2) two mast-arms, 3) three mast-arms, and 4) four mast-arms. An example of each of these four types of COSS are shown in Figure 1.1. Each type has the same

general shape, but the assemblies differ and details of these four main types may vary significantly from state to state. The focus of this project is on the two mast-arm COSS structures widely used in the state of Kansas. COSS with two mast-arms have been shown to be more prone to fatigue failures than other COSS designs, as they experience higher fatigue stresses due to natural wind gusts (Gallow et al. 2015). There have also been occurrences of defective welds observed in two mast-arm COSS failures.

Figure 1.1. COSS Construction Types: a) monotube; b) two mast-arms; c) three mast-arms; d) four mast-arms (Senior 2018)

Often, fatigue damage is localized near connection details where the horizontal mast-arms meet the vertical poles. Two mast-arm COSS often utilize a box connection detail at this location. Two common designs for the box connection are referred to as gusseted and ring-stiffened, Figure 1.2.

a) b)

Figure 1.2. Standard Gusseted and Ring-Stiffened Box Connection Designs: a) Gusseted Box Connection and b) Ring-Stiffened Box Connection (AASHTO SLT 2015)

1.2 Problem Statement

The box connection between the pole and mast-arm of COSS is susceptible to fatigue cracking due to stresses caused by in-service loading. The Kansas Department of Transportation (KDOT) has observed fatigue failures at the top and bottom corners of the side-plate in standard gusted box connections details. Structures taken out of service by KDOT and provided to the University of Kansas contained cracks at these locations which were between 0.75 in. (1.9 cm) and 5.75 in. (14.6 cm) in length. An example of cracking at a box connection corner of a decommissioned COSS is shown in Figure 1.3.

Figure 1.3. Cracking on COSS Box Connection (KDOT)

As the behavior of these connection details is not well understood, estimating remaining fatigue life is currently inaccurate or impossible. Adequate assessment of these connections for repair, replacement, or retrofit cannot be performed. Due to this, there is a need to characterize the expected fatigue life of the box connection details, both for standard gusseted and ring-stiffened box connections, and to provide design, fabrication, or retrofit alternatives to improve fatigue performance.

1.3 Research Objectives

The purpose of the research described within this thesis is to assess the fatigue performance of the cantilevered box connection utilizing the design specifications of structures within the KDOT highway inventory. Finite element modeling was performed to establish fatigue resistance estimations on a full-sized structure, and to determine an experimental set-up that mimics results from full-sized structures. The gusseted and ring-stiffened box connections were considered in the analyses.

1.4 Thesis Organization

Chapter 2 is a literature review of related studies and findings on current problems related to the fatigue life of COSS connection details, focusing on the box connection. Results from the studies focused on the box connection are summarized and synthesized. The literature review also covers background information related to two mast-arm COSS, information on approaches related to the methodologies utilized in this study, and the documented fatigue cracking experienced by structures within the KDOT inventory.

Chapter 3 describes the methodology used in the current research, addressing analytical modeling techniques as well as preparations for experimental testing. Chapter 4 presents the results of the analytical analyses, while Chapter 5 summarizes the results and presents conclusions. Recommendations for future work are also included. The appendix provides construction documentation, both provided by KDOT and created for this research, as well as calculations and additional results from the analyses.

Chapter 2: Literature Review

2.1 Introduction to Fatigue and Evaluation Methods

2.1.1 Overview

Fatigue is the process of cumulative damage due to the repeated application of cyclic and fluctuating load or vibration. This damage appears as cracks, which form, propagate, and can lead to failure through fracture. Crack initiation and propagation are due to localized stresses, caused by cyclic loading, which exceed the yield stress of the material. As such the higher the localized stresses, the shorter the time to initiation of the fatigue crack. Fatigue life of a structure is a function of both crack initiation and propagation life and is dependent upon how well a component can resist fatigue damage.

There are many factors that affect fatigue performance of a structure, on both the resistance and demand side of analysis. Demand is controlled by applied stress range and any applicable compounding environmental effects. Fatigue resistance is generally considered to be a function of detail geometry, fabrication, and material. The primary factor that affects fatigue behavior is the fluctuation in the localized stress or strain, and one of the most effective methods for increasing the fatigue life is to decrease the severity of the stress concentration (Barsom and Rolfe 1999).

2.1.2 Nominal Stress Approach and S-N Curves

Traditional fatigue analysis of welded sections is based on the use of nominal stresses and the subsequent classification of details, as performed by AASHTO in its fatigue design recommendations and S-N curves. This approach evaluates the nominal stresses acting on a structural component against known resistance behavior for given geometric details. However, the nominal stress approach ignores the actual variations in dimensions of structural details, capturing the effects of these details only through empirical data.

Stress-life (S-N) curves plot the magnitude of the nominal stress range, S, against the number of cycles, N, until failure for a given combination of material and detail geometry. These

curves are empirically created through experimental testing. Repeated testing of similar details is performed at the same stress ratio, but with different maximum stress values (Barsom and Rolfe 1999). The results of these tests are then plotted to form the S-N curve for that detail type, allowing for an estimation of the fatigue life of the detail of interest. Standardized curves are the result of the testing of a large database of constant-amplitude loading specimens, focused on several details of interest.

AASHTO's S-N curves were first introduced in the AASHTO LRFD Bridge Design Specifications and were introduced into the AASHTO SLT in 2001. The S-N curves used for design were developed at two standard deviations below the mean exhibited fatigue resistance, providing fatigue strength with the desired level of safety (Fischer et al. 1998). The connection details used in sign structures have been assigned detail categories based upon the constant-amplitude fatigue threshold or limit (CAFT or CAFL), from AASHTO LRFD Bridge Design Specifications (2015) along with the American Welding Society (AWS) Structural Welding Code-Steel D1.1 (2004). These detail categories and their associated steel CAFT's are shown in Table 2.1, and the S-N curve is shown in Figure 2.1 (AASHTO SLT 2015). The fatigue performance of the detail category decreases as reference lines move from Category A to K_2. AASHTO SLT (2015) no longer lists details with their detail category letter, but instead with their associated CAFT value.

The probability for a detail to incur fatigue damage can be determined by looking at the stress ranges experienced by the detail, as well as its CAFT. Fatigue damage occurs when the stress ranges are above the CAFT for the detail, causing it to be in the finite life region. When stress ranges are below the CAFT, minimal to no fatigue damage is accumulated and the detail is in the infinite life region.

Table 2.1. AASHTO CAFT for all detail categories

Detail Category	CAFT, ksi (MPa)
A	24 (165)
B	16 (110)
B’	12 (83)
C	10 (69)
D	7 (48)
E	4.5 (31)
E’	2.6 (18)
ET	1.2 (8)
K_2	1.0 (7)

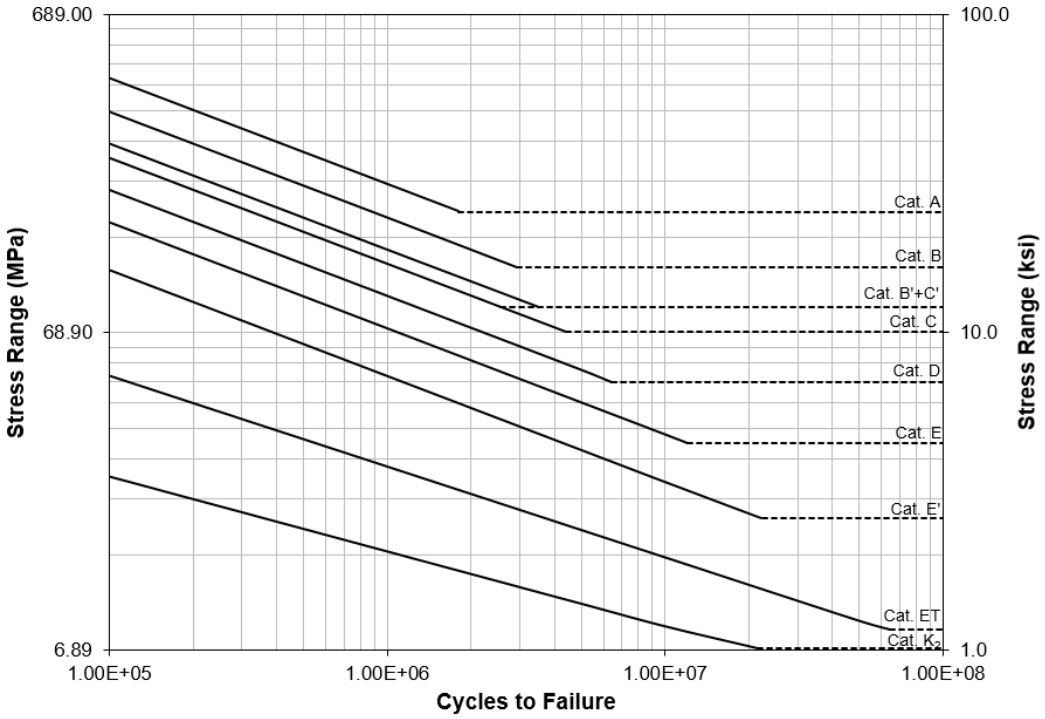

Figure 2.1. Nominal Stress S-N Curves for all Detail Categories

Determination of the nominal fatigue resistance, $(\Delta F)_n$, for finite life is calculated by:

$$\text{ÿO}_{\text{ح سي}} \frac{\text{ö}}{\text{ü}} \text{٥٧١} \qquad \text{Eq. 2.1}$$

where *N* is the number of stress cycles and *A* is the finite life constant, shown in Table 2.2, for all detail categories. Finite life constants are provided in the AASTHO LRFD Bridge Design Specifications (2012). It should be noted that this approach does not apply to details in categories

ET or K_2, as these categories were adopted directly from AWS D1.1 and were not standardized in the same fashion as the other detail categories within AASHTO. Detail categories ET and K_2 only apply to details involving fillet-welded T-, Y-, and K-tube-to-tube, angle-to-tube, or plate-to-tube connections.

Table 2.2. Detail Category Constant, A

Detail Category	Constant, A*10^8, ksi^3 (MPa^3)
A	250 (1724)
B	120 (827)
B’	61 (421)
C	44 (303)
D	22 (152)
E	11 (76)
E’	3.9 (27)

2.1.3 Hot Spot Stress Approach

The hot spot stress analysis approach explicitly considers the dimensions of the details as it includes the stress concentrating effects of the detail itself. Hot spot stress analysis is used with the AASHTO Category C S-N curve, as it reflects fatigue cracking associated with weld toe geometry.

Methods for Determining Structural Hot Spot Stress in Finite Element Analysis

Finite element analysis (FEA) is a useful tool for determining structural hot-spot stress. Analysis can occur in two stages: a coarse model to identify the hot-spot locations and then sub models or a refined model focusing on the hot-spot locations themselves. The second stage will involve a finer mesh on the model at the areas of interest.

When a relatively coarse element mesh is applied in conjunction with solid elements, linear extrapolation at distances 0.5t and 1.5t from the weld toe along with Equation 2.2 to calculate the hot-spot stress. This approach is utilized by Det Norseke Veritas (DNV RP-C203) and the International Institute of Welding (IIW) (Recommendations for Fatigue Design) in guidelines for non-tubular structures.

„ژ خ سي ρ8ϖ „ي خ ط π8ϖ „ه خ Eq. 2.2

where *t* is the thickness of the non-tubular structure.

However, a relatively fine element mesh in conjunction with solid elements utilizes stresses at distances 0.4t and 1.0t along the member. IIW guidelines recommends this approach for non-tubular structures, and it was the approach utilized for non-tubular structures in this study.

„ژ خ سي ρ8ϕ χ„ي خ ط π8ϕ χ„ه خ Eq. 2.3

Appendix D of the AASHTO SLT (2015) specifications recommends that 20-node solid hexahedron elements be utilized in modeling the connection. At least two elements should be used in the thickness direction and there should be a maximum aspect ratio of 1:4 for all elements in the model. The equations and extrapolation locations given in Equation 2.3 only apply for hot spot stresses taken from non-tubular structures. For tubular structures, to extrapolate the hot spot stress, it should be taken on the tube surface at 0.1 Ì ì z òfrom the hot spot, where *r* is the outer radius and *t* is the thickness of the tube. This resulting hot spot stress is still used with the Category C S-N curve. This approach matches DNV guidelines for tubular structures and was used in analysis for this project.

2.2 Two Mast-Arm COSS Design

2.2.1 Overview

As mentioned, there are four main construction types of COSS: monotube, two mast-arm, three mast-arm, and four mast-arm. The two mast-arm COSS assembly is the focus of this study. The two mast-arm COSS consists of five main components: the pole, the two mast-arms, the web or truss, the sign, and the baseplate. Often the structure will also have a steel walkway underneath the sign and a handhole near the bottom of the pole. The web is welded to the mast-arm typically through fillet-welds, and a mast-arm to pole connection is utilized to attach the two. A common type of mast-arm to pole connection is the box connection, which is the focus of this study. Socket

weld connections are commonly utilized to connect the mast-arm to an endplate, which in turn is bolted to the mast-arm to pole connection, as well as for the pole to the baseplate connection. An elevation view of this assembly is shown in Figure 2.2.

Figure 2.2. Two Mast-Arm COSS General Assembly (Senior 2018)

2.2.2 COSS Design

2.2.2.1 AASHTO Wind Loads

Section 11 of the AASHTO LRFD Specifications for Structural Supports for Highway Signs, Luminaires, and Traffic Signals (AASHTO SLT 2015) specifies the fatigue design criteria, including design loads in relation to natural wind (NW), truck-induced wind gusts (TIWG), and galloping loads. Vortex shedding is a fourth type of loading but has been determined to not affect COSS (Kaczinski et al. 1998) and thus will not be discussed herein. An overview of each of the other three types of loading will be discussed in detail below.

Natural Wind

Natural wind gusts are the result of the variability in the velocity and direction of air flow. The changes in the velocity and direction produce fluctuating pressures on the structure, which can cause vibrations and result in fatigue damage in the long term.

AASHTO SLT (2015) states that cantilevered and non-cantilevered overhead sign and overhead traffic signal supports are to be designed for an equivalent static natural wind gust pressure range of:

$$Q_{ز} = 0.00256 V_{ز}^2 C_d \text{ (psf)}$$
$$Q_{ز} = 0.0473 V_{ز}^2 C_d \text{ (Pa)} \qquad \text{Eq. 2.4}$$

C_d is the appropriate drag coefficient, based on the yearly mean wind velocity of 11.2 mph and is specified in Section 3 of AASHTO SLT (2015). The fatigue influence factor, I_F, is dependent on the degree of hazard to traffic in event of failure and is tabulated in Table 11.6-1 of AASHTO SLT (2015), shown in Table 2.3. The pressure range is applied in the horizontal direction to the exposed area of all support structure members, signs, traffic signals, and/or miscellaneous attachments and is often applied as out-of-plane loading.

Table 2.3. Influence Factors, I_F, for COSS (AASHTO SLT 2015)

Fatigue Importance Category	Galloping	Natural Wind Gusts	Truck-Induced Gusts
I	1.0	1.0	1.0
II	0.70	0.85	0.90
III	0.40	0.70	0.80

Truck-Induced Wind Gusts

Truck-induced wind gusts (TIWG) are produced by the passage of trucks beneath sign structures. The pressures that result act horizontally on the sign structure as well as vertically on the underside of the mast-arms and sign, resulting in an in-plane load upon the sign structure. Typically, the horizontal pressure induced by natural wind is larger than the horizontal pressure from TIWG on the front area of the sign, and thus natural wind controls in this direction and

horizontally-applied forces induced by TIWG are be neglected. As such only vertical TIWG pressures are applied to the underside of the mast-arms and sign. These pressures are more critical for sign structures that have large projected areas parallel to the ground, as may be the case for variable message signs. The equation for the TIWG pressure range is:

$$0_{\text{سي ρ}} \text{ (psf)}$$
$$0_{\text{سي ω}} \text{ (Pa)} \qquad \text{Eq. 2.5}$$

The pressure range is applied in the vertical direction to the horizontal support as well as the area of all signs, attachments, walkways, and/or lighting fixtures projected on the horizontal plane. The range is applied along any 12 ft. (3.7 m) length, excluding any portion of the structure not located directly above a traffic lane. The pressure linearly decreases above a sign height of 20 ft. (6 m), reaching zero pressure at a height of 33 ft. (10 m). This linear decrease in TIWG pressures is based on work performed by Creamer et al. (1979) and expanded on in National Cooperative Highway Research Program (NCHRP) Reports 412 (Kaczinski 1998) and 469 (Dexter et al. 2002).

Galloping

Galloping-induced oscillations are caused by forces that act on a structural element as it is subject to periodic variations in the angle of attack of the wind flow (Kaczinski 1998). If the structure is excited at its natural frequency in the mode of the in-plane vibrations, the mast-arm can twist and sway in the vertical direction. While galloping is considered for fatigue design of sign structures, it is generally accepted that galloping is only important when examining single mast-arm cantilever sign structures (Kaczinski 1998). Work performed by Li et al. (2006) determined that out-of-plane vibrations, those acting in the horizontal direction corresponding with the natural wind direction, occur at a lower frequency than those acting in-plane vibration, which is the direction coincident with by both TIWG and galloping loading. Past research has tied the occurrence of galloping more closely with TIWG than NW, in part because both loads are in the in-plane direction and because the natural frequency is achieved more often with TIWG. Based on this, it is generally accepted that galloping does not significantly contribute to critical stresses for COSS with more than one mast-arm.

AASHTO SLT (2015) dictates that overhead cantilevered sign and traffic signal support structures be designed for galloping-induced cyclic loads by applying an equivalent static shear pressure vertically to the surface area of all sign panels and/or traffic signal heads and backplates rigidly mounted to the cantilevered horizontal support. The vertical shear pressure range is:

$$0.00256 V_c^2 C_d \text{ (psf)}$$
$$0.0123 V_c^2 C_d \text{ (Pa)} \qquad \text{Eq. 2.6}$$

2.2.2.2 KDOT Design

The construction drawings for the two mast-arm COSS provided by KDOT are located within 0. These include drawings from 1981 as well as updated drawings from 2015.

The 1981 KDOT designs conformed to 1975 AASHTO SLT specifications and were minimally designed with fatigue stress in mind, as fatigue was not incorporated as a limit state until the 2001 AASHTO SLT specifications. Both the pole and mast-arm are tapered to 0.14 in./ft. (1.17 cm/m) and a gusseted box connection was utilized. Seven different designs were created, varying pole and arm diameter and thicknesses, as well as weld thickness and the components of the box connection. The 1981 designs were used as the basis for the tapered pole models created for this study, as they correspond to majority of the tapered pole structures still in service and are the designs utilized by the decommissioned structures donated to this project by KDOT, which experienced cracking in their box connections.

In 2015, KDOT redesigned their two mast-arm COSS to utilize straight tubes instead of tapered for the mast-arm and pole and eight different designs were created, with Designs #1-6 having gusseted box connections, while Designs #7-8 utilized ring-stiffened box connections. These designs became the basis of the straight pole and ring-stiffened box connection models created for this study and are discussed later. The fabrication approaches also changed, altering the design of the gusseted box connection, as the welds no longer wrap fully around the gusset and side-plates (Figure 2.3).

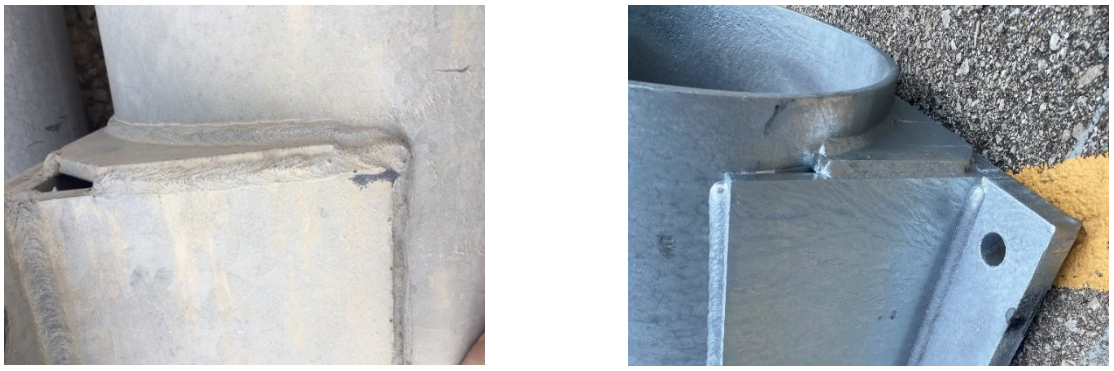

a) b)

Figure 2.3. Gusseted Box Connection Welding on: a) Donated Structure 165 and b) Test Specimen

2.2.2.3 Decommissioned Structures

Two COSS were donated to the project by KDOT. The first, Structure 165, correlates to Design #3 of the 1975 tapered designs, while the second, Structure 309, correlates to Design #7 of the 1975 tapered designs. The individual construction drawings for both structures can be found within Appendix A. Both structures exhibited cracking along the corners of the box connection, where the side-plate is welded to the pole. The geometry of these structures and cracking experienced is documented below.

Structure 165

Structure 165 was built in 1982 along I-435. It was designed according to Design #3 of the 1981 KDOT plans, and an elevation drawing is shown in Figure 2.4. The total mast-arm length is 18 ft. (5.49 m) and the total pole height is 27 ft. (88.58 m). Other dimensions that correlate to the 1981 Design #3 are shown in Table 2.4.

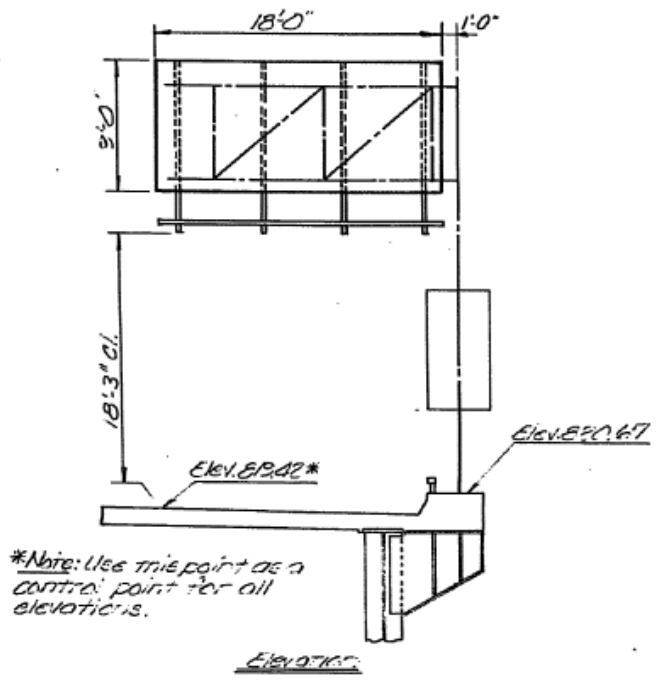

Figure 2.4. Structure 165 Elevation View (KDOT)

Table 2.4. Design #3 Dimensions

	in. (cm)
Pole Diameter	18 (45.72)
Pole Thickness	0.25 (0.64)
Arm Diameter	11 (27.94)
Arm Thickness	0.1875 (0.48)

Multiple cracks were documented on this structure. The top box connection experienced a 0.75 in. (1.9 cm) crack at the top corner of the back side-plate and a 1.5 in. (3.81 cm) crack at the top corner of the front side-plate along with a 1.5 in. (3.81 cm) crack at the bottom corner. On the bottom box, a 0.625 in. (1.59 cm) crack developed at the bottom corner of the back side-plate and a 1.0 in. (2.54 cm) crack occurred at the bottom corner. These cracks are shown in Figure 2.5.

a) b) c) d) e)

Figure 2.5. Cracking on Structure 165: a) bottom corner of back side of top box; b) top corner of front side of top box; c) bottom corner of front side of top box; d) bottom corner of back side of bottom box; e) bottom corner of front side of bottom box (KDOT)

Structure 309

Structure 309 was built in 1981 along I-435. It was designed according to Design #7 of the 1981 KDOT plans, for which the dimensions can be seen in Table 2.5 and an elevation drawing in Figure 2.6. The total arm length is 34 ft. (111.55 m) and the pole has a height of 29 ft. (95.14 m). The test specimen was developed based upon this structure's design.

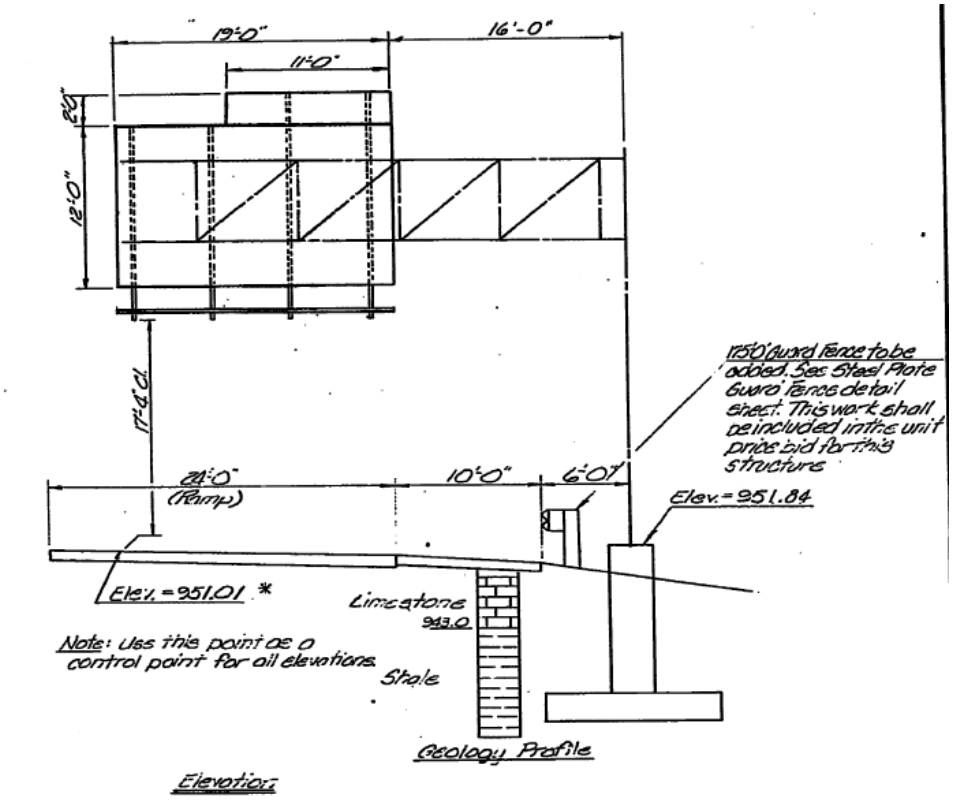

Figure 2.6. Structure 309 Elevation View (KDOT)

Table 2.5. Design #7 Dimensions

	in. (cm)
Pole Diameter	18 (45.72)
Pole Thickness	0.3125 (0.79)
Arm Diameter	13 (33.02)
Arm Thickness	0.3125 (0.79)

The structure experienced cracking at corners of the bottom box connection. The crack on the front side was 5.75 in. (14.6 cm) and the back side had a crack of 2.5 in. (6.35 cm), shown in Figure 2.7.

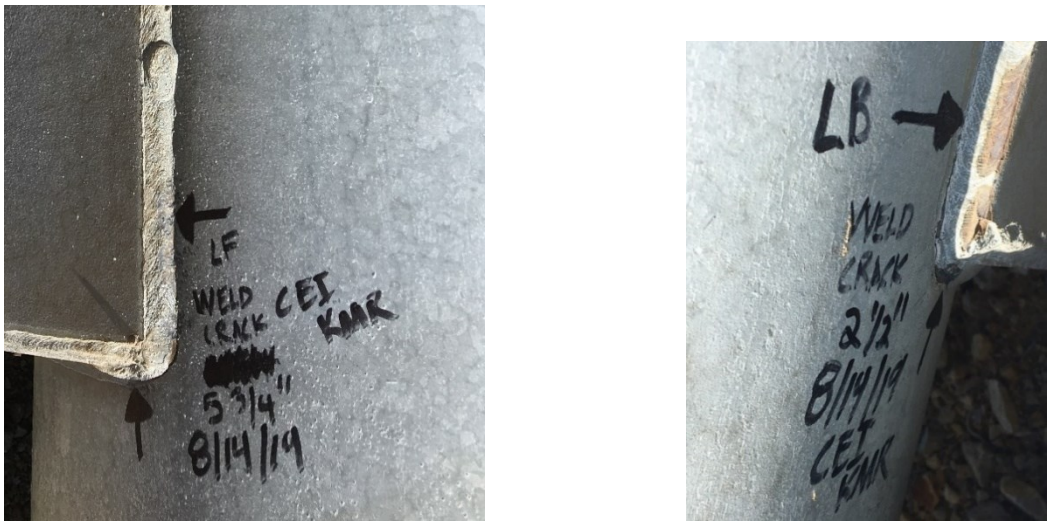

a) b)

Figure 2.7. Cracking on Structure 309: a) bottom corner of front side of bottom box and b) bottom corner of back side of bottom box (KDOT)

2.3 Box Connection Design

2.3.1 Components

It is not often practical to transport a pole with the mast-arms attached, so a bolted connection between the pole and mast-arms is typically used. This bolted connection allows for on-site erection. In the state of Kansas, this is typically accomplished through a built-up box connection. The built-up box connection is made using three plates in the shape of a box: two side-plates attached to the sides of the pole and one flange plate welded to the side-plates. An endplate is bolted to the flange plate and is welded to the mast-arm, through a socket connection. Figure 2.8 shows an elevation drawing of gusseted box connection with terminology utilized in this report. The two main versions of the box connection are the gusseted box connection and the ring-stiffened box connection (Figure 2.9).

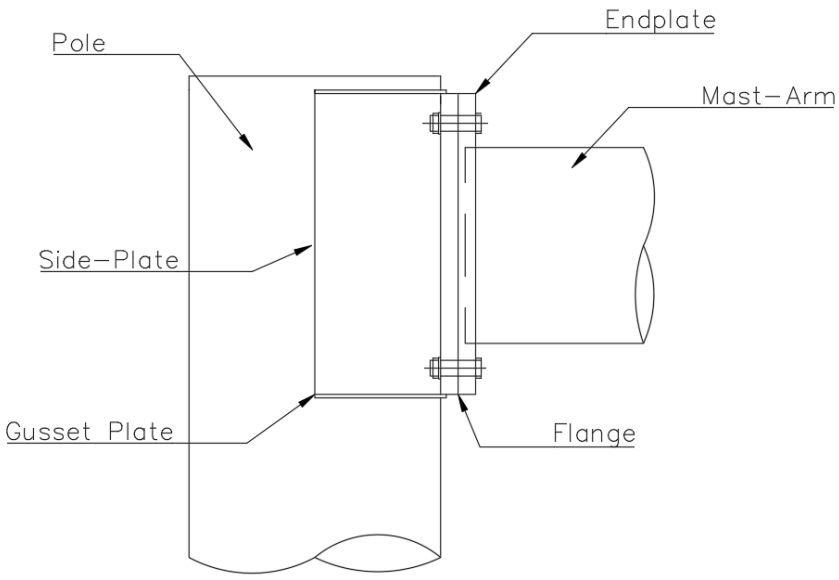

Figure 2.8. Box Connection Detail Terminology

a) b)

Figure 2.9. Standard Box Connection Designs: a) Gusseted and b) Ring-Stiffened (AASHTO SLT 2015)

While there both analytical and experimental research have been performed regarding the box connection, there is still much that is unknown regarding fatigue life and behavior of these connection details. Past research has verified that the corner of the side-plate to pole weld of the built-up box connection is one of the most fatigue-susceptible regions (Ocel et al. 2006). AASHTO SLT Section 11 (2015) provides stress ranges for components of this detail, however refinement to these classifications is still needed.

2.3.2 Design of Box Connections

AASHTO SLT (2015) includes Table 11.9.3.1-1, which classifies typical components, mechanical fasteners, and welded details. These details are broken into categories, with constant-amplitude fatigue thresholds (CAFT) assigned to each category. CAFT is the nominal stress range below which a particular fatigue detail can withstand an infinite number of repetitions without fatigue failure. When the detail experiences stress above this stress range, fatigue damage occurs. When applied stress is below the CAFT, the detail is in the infinite life region, and above it is in the finite life region. The detail categories and their CAFT levels are shown in Table 2.6.

Table 2.6. AASHTO CAFT for all detail categories

Detail Category	CAFT, ksi (MPa)
A	24 (165)
B	16 (110)
B’	12 (83)
C	10 (69)
D	7 (48)
E	4.5 (31)
E’	2.6 (18)
ET	1.2 (8)
K_2	1.0 (7)

Within the 2015 version of AASHTO SLT, both the fillet-welded gusset and ring-stiffened box connections are assumed to have infinite life, per Article 5.14.7. However, this classification is due to other critical details failing before the box connection within testing performed as part of NCHRP Report 176 (Roy et al. 2011), which is discussed in more detail in Section 2.4.3.3. Thus, to better understand the fatigue life of the box connection, the components of it have been broken into ‘sub-details’, which are shown with their associated categories in Figure 2.10. These ‘sub-details’ align with how the box connection was shown in AASHTO SLT (2009), Figure 11-1, Example 8, however the details have been updated to align with the categories given to them in AASHTO SLT (2015).

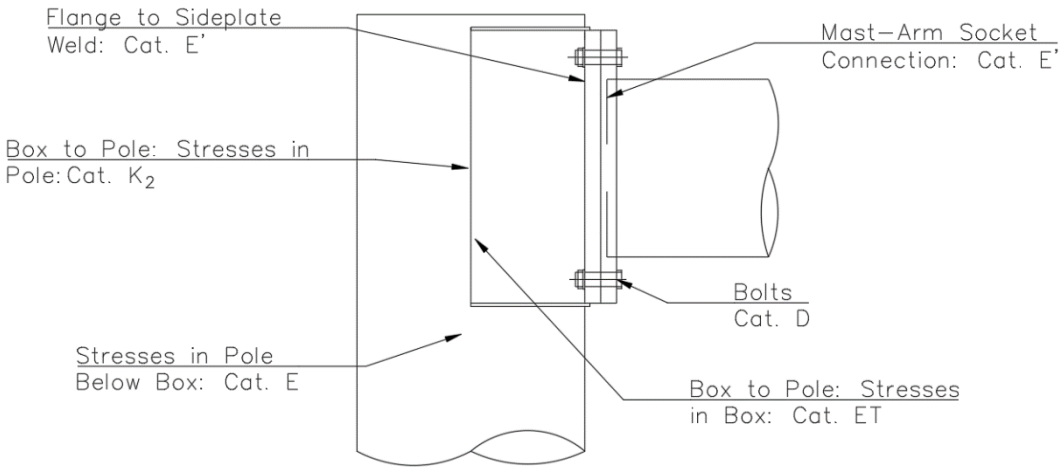

Figure 2.10. Box Connection Detail Categories

2.3.3 Nominal Stress Calculations

To calculate the stresses occurring in different connection details in COSS, bending stress equations are commonly utilized:

$$\sigma = \frac{M c}{I} \qquad \text{Eq. 2.7}$$

where *M* is the moment, *c* is the centroid, and *I* is the moment of inertia.

This approach is shown within the NCHRP Report 469 Appendix B design examples (Dexter and Ricker 2002) and is utilized by KDOT in their COSS design. A complete example of this approach is shown in Appendix B.2 of this paper, analyzing the donated KDOT Structure 309. Bending stress was also utilized in the experimental testing performed at the University of Wyoming to calculate the forces to apply to the test specimen (Peiffer 2008), expanded on in Section 2.4.3.3.

Equations 2.8 through 2.10 display the approach shown in NCHRP Report 469, focusing only on the mast-arm socket connection, pole-to-baseplate socket connection, and the stresses in the pole below the box connection, as these were the three locations of interest for this study. The stresses in the pole below the box connection was the location of the box connection examined as the cracking on the KDOT structures developed around the corners and was likely due to stresses developing at this location.

Eq. 2.8

Eq. 2.9

Eq. 2.10

where *D* is the outer diameter of the tube.

Moments are calculated based on natural wind, galloping, and truck-induced wind gusts loading. Figure 2.11 displays the standard axis utilized in design. The galloping and truck-induced moments are bending moments at the centerline of the column (M_{z_G} and M_{z_TG}), while two different natural wind moments are calculated; one at the base of the column (M_{x_NW}) and the other at the mast-arm connection (M_{y_NW}). As the galloping moment is normally larger than the truck-induced moment, truck-induced moments are commonly neglected in stress calculations.

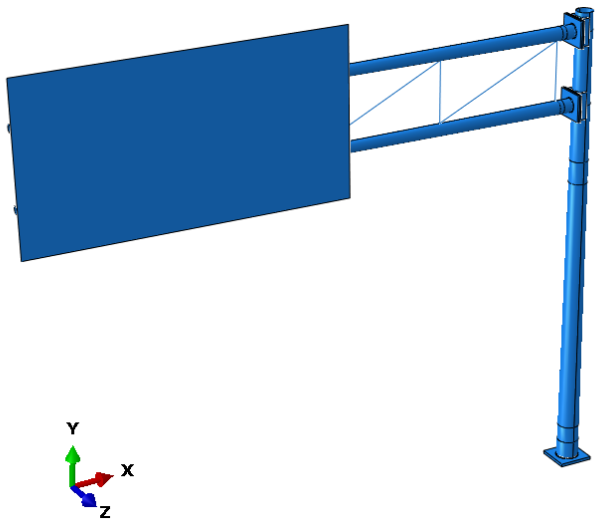

Figure 2.11. Standard Coordinates for COSS Design

In the examination of the stresses at the pole-to-baseplate socket connection, both M_{z_G} and M_{x_NW} are examined through separate calculations. This is also done for the mast-arm socket connection, although the M_{y_NW} is utilized instead of M_{x_NW}. While the KDOT design is similar to the NCHRP Report 469 examples, it does differ in the calculation for stress at the mast-arm socket

connection due to natural wind, as it divides the moment by two. It is not certain why this was done.

The stress in the pole below the box connection is calculated using M_{z_G} as well as with M_{y_NW}, as it is stress within the pole, the diameter and moment of inertia of the pole are utilized instead of utilizing the moment of inertia of the box or mast-arm.

In the development of the loads for Peiffer's (2008) research, which focused on the fatigue life of box connections, bending stresses were utilized to calculate loads. Desired stresses were chosen based on AASHTO CAFT and loads were subsequently calculated from there. Bending stress was used as the test setup had been built to resist torsional rotation at the support. This study is discussed in more detail in Section 2.4.3.3.

Utilizing bending stress equations for all calculations involving COSS and their connection details has the chance to oversimplify calculations and the stresses that result may be conservative and/or incorrect. While the whole system is experiencing bending as the primary stress for in-plane loads, bending stress is not necessarily the primary stress at every connection detail for out-of-plane loading, especially for box connection details.

2.3.4 Alternative Approaches for Multiaxial Stress Calculations

One alternative approach to calculating the stresses that develop that the box connection due to natural wind loading is through calculating the effective stress amplitude, σ_a (Dowling 2013).

$$\sigma_a = \frac{\sqrt{2}}{2}\sqrt{(\sigma_{1a}-\sigma_{2a})^2+(\sigma_{2a}-\sigma_{3a})^2+(\sigma_{3a}-\sigma_{1a})^2} \qquad \text{Eq. 2.11}$$

where σ_{1a}, σ_{2a}, and σ_{3a} are principal stresses. σ_{1a} and σ_{2a} can be calculated through the application of Mohr's Circle, while σ_{3a} is zero.

In the application of Mohr's circle, the bending and torsional stress at the pole beneath the box connection would be calculated and then principal stresses.

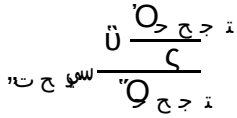

Eq. 2.12

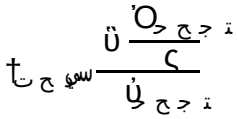

Eq. 2.13

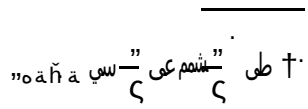

Eq. 2.14

where J is the polar moment of inertia.

2.4 Previous Research

While many cantilevered overhead sign structures perform well for the duration of their service life, there have been instances of fatigue problems in these structures, causing concern among many state Department of Transportations (DOTs) throughout the United States. Multiple research programs have focused on various issues related to fatigue and COSS performance. The literature presented herein provides an overview of the research that has significantly influenced AASHTO SLT design guidelines, examined and refined knowledge of both general and fatigue behavior of COSS and their connection details, and is relevant to the current study.

2.4.1 Development of COSS Fatigue Provisions

2.4.1.1 National Cooperative Highway Research Program Reports

The National Cooperative Highway Research Program (NCHRP) supported a series of research projects focused on analyzing and providing recommendations to the revisions of the AASHTO LRFD Specifications for Highway Bridges, from which the fatigue provisions in AASHTO SLT was later derived in 2001. Later reports also focused solely on revisions to AASHTO SLT fatigue provisions once they had been included.

The first of these projects is presented within NCHRP Report 286 (Keating and Fisher 1986). Results from this report were incorporated into the 1986 version of the AASHTO LRFD

Specifications for Highway Bridges. A database of fatigue test results from studies performed in 1970 and 1974 was enlarged to include new detail types, structure configurations, and full-scale specimens, all of which were lacking in the original database. This enlarged database of fatigue test results was then examined and the AASHTO fatigue design curves were revised. A constant slope of -3 was applied to the finite life of all curves and more detail types were added to the database, such as longitudinal groove welds in flat-plates and box members. A seventh S-N curve, Category B', was created to account for partial penetration longitudinal groove welds, which are common in box-types and built-up members.

NCHRP Report 412 (Kaczinski et al. 1998) studied the fatigue resistance of cantilevered signal, sign, and light supports, in which 80 structures were examined. The goal was to clarify and improve the fatigue design specifications included in AASHTO SLT (1994), in particular to define the wind loads to be utilized in design and analysis. Four wind loading types, vortex shedding, galloping, natural wind, and truck-induced gusts, were identified and examined. Vortex shedding was later disregarded as it was determined that, "cantilevered signal, sign, and luminaire support structures are generally not susceptible to significant vibrations due to the shedding of vortices" (Kaczinski et al. 1998).

To obtain information regarding the galloping behavior of structures, wind-tunnel tests were performed on one-eighth scale test models. The results of these tests demonstrated that cantilevered structures are susceptible to galloping when signal attachments or sign attachments are on the structure. Without the attachments, the structures alone were deemed to be not susceptible to galloping-induced oscillations. It was noted that while galloping is a possible phenomenon that has been observed on in-service structures, it is very sensitive to specific conditions and does not frequently occur. It is recommended that structures located along high-volume, high-speed roads be designed to resist galloping loads, but in other low-risk cases the risk of fatigue failure due to galloping may be acceptable.

Finite element models were also created to identify the appropriate design loadings to be used with all four loadings, with the goal of estimating the pressures that each loading type applies to the structure. For galloping, an equivalent pressure range of 21 psf (1,005.48 Pa) was determined to be appropriate, with the pressure applied vertically to the surface area of all sign and signal attachments mounted on the horizontal mast-arm. For natural wind, it was determined that an equivalent pressure range of 5.2 psf (248.98 Pa) times the drag coefficient, C_d, should be used, and

the pressure is applied horizontally to the projected area of any exposed portions of the structure and attachments. Finally, the truck-induced gust loads are represented by an equivalent static pressure of 36.6 psf (1,752.41 Pa), applied vertically to the horizontally projected area of the structural members and attachments mounted to the horizontal mast arm, along a length of the mast arm greater than the length of the sign or 12 ft. (39.37 m).

NCHRP Report 469 (Dexter et al. 2002) revised the TIWG pressure equation. The 36.6 psf (1,752.41 Pa) pressure was reduced to 18.8 psf (900 Pa), as the original equation was based on limited data and was calibrated with an incorrect drag coefficient of 1.45, instead of 1.7, as is in the 2001 AASHTO SLT Specifications. The pressure applied for the TIWG should also be reduced linearly from 19.7 ft. (64.63 m) above ground level to zero at 32.8 ft. (107.61 m) above ground level.

NCHRP Report 469 (Dexter et al. 2002) also advised revisions to the fatigue design section that had been newly incorporated into AASHTO SLT 2001 from the AASHTO LRFD Specifications for Highway Bridges. Sign structures were examined along with cost-effective ways to redesign them to reduce their susceptibility to fatigue. One structure examined was a cantilevered monotube traffic signal structure in Rock Springs, Wyoming. After investigation, it was determined that the structure had failed due to cracks that had propagated through the pole wall at the toe of the weld connecting to the built-up box connection. It is believed these structures were affected by natural winds and not by galloping, due to the constant windy conditions present in Wyoming. As the cracking was located at the pole wall and not within the built-up box itself, it was suggested to always design for some galloping load, as it is believed that through this, it will no longer be necessary to check details for punching-shear based on Category K_2. This would be helpful as it is nearly impossible to successfully design for punching-shear in box connections and it is believed that Category K_2 is too conservative (Dexter et al. 2002).

2.4.2 Behavioral Research on COSS

2.4.2.1 Frequency and Vibration Analysis

Gallow et al. (2015) explored three different COSS layouts, four mast-arm, two mast-arm, and monotube, to determine the effect of stiffness and mass distribution on fatigue damage caused by wind-induced gusts. Modifications in the members' shape, arrangement, size, and structure layout were examined to control the structural frequency and mitigate the fatigue damage.

Two-dimensional line models of the structures were created with the goal of obtaining the structure's frequency upon the application of natural wind gusts and truck-induced wind gusts. The two mast-arm COSS had the largest fatigue stresses, whereas the monotube and four mast-arm experience similar fatigue stresses. In all cases, larger stresses were caused by the natural wind gusts than the truck-induced wind gusts. It was determined that increasing the natural frequency reduced fatigue stresses caused by natural wind gusts. The recommended ways to do that included increasing the structures stiffness, mainly in the pole, and reducing its mass, mainly in the horizontal support.

Hosch et al. (2017) conducted research to identify the modes of vibration that contribute to the deformation of a cantilevered sign structure in response to truck-induced wind gusts. Experimental evaluation of an in-service structure was undertaken, and corresponding finite element models were created in SAP2000 for comparison purposes. A four mast-arm COSS was selected as the in-service structure, and strain gauges and anemometers were applied to measure ambient wind velocity. Truck-induced wind gust loading was applied by driving a test truck underneath the structure.

Before the start of experimental testing, finite element analyses were performed to characterize the modal properties of the structure. Five model shapes and associated frequencies were determined for this type of structure. Mode 1 was a horizontal movement of the truss in the y-direction, creating torsion of the post about the z-axis and horizontal flexure of the post about the x-axis. Mode 2 was a vertical rocking of the structure, which created a vertical movement of the truss in the z-direction and horizontal flexure of the post about the y-axis. Mode 3 was flexure of the post about the x-axis, while Mode 4 was about the y-axis. Finally, Mode 5 was torsion of the truss about the x-axis. Figure 2.12 displays these modes.

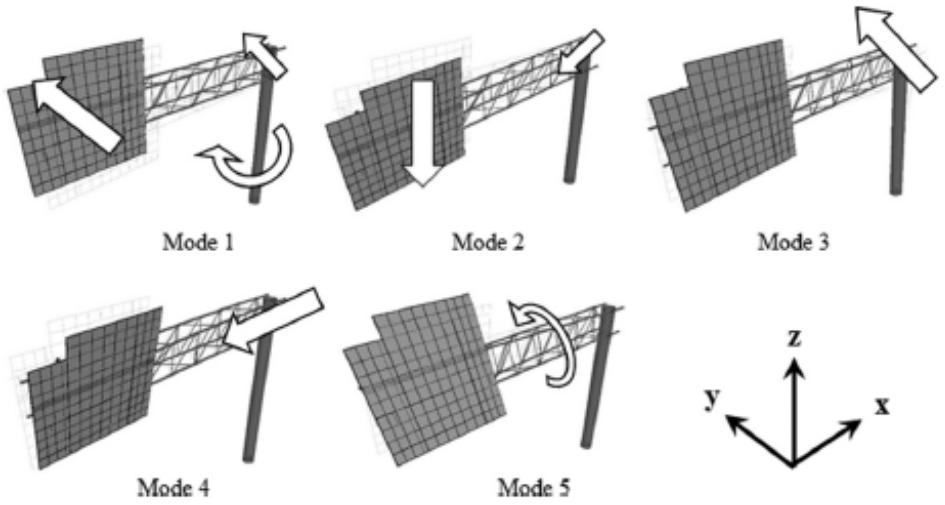

Figure 2.12. FEA Modal Shapes (Hosch et al. 2017)

Modes 1 and 2, the dominant modes, aligned closely between experimental values and FEA results and were determined to have a significant contribution to the deformation of the pole when exposed to truck-induced wind gusts. It is believed that the operational deflected shape is due to a combination of these two modes.

Strain data were compared to the strains computed in a model based on the application of the AASHTO SLT (2013) TIWG load. There was a discrepancy between the FEA results and experimental data, with a difference of 34.7% between the maximum strains. This result implies that the AASHTO equation predicts forces approximately 35% greater than the forces the structure sees when in service. The AASHTO TIWG load equation only accounts for Mode 2 loading, resulting from vertical pressures on the sign structure. However, the tested model experienced deformation due to Modes 1 and 2, leading to the conclusion that the horizontal effects of TIWG have an effect on structures in service. Due to this, AASHTO SLT specifications are likely too conservative in respect to TIWG, as a single mode, single degree of freedom, system does not represent the behavior of the pole, in-service, when TIWG loads are applied to it.

2.4.2.2 Senior (2018)

Senior (2018) performed computational fluid dynamic (CFD) analysis and wind tunnel testing to determine the impact of the steel grate walkway on the dynamic performance of two mast-arm COSS. Models were created of 27 different two mast-arm COSS configurations, focusing on the effects of vortex shedding and natural wind loading. The impact of the walkway on the natural frequency of the structure was also examined.

The COSS configurations were determined based upon three design characteristics: 1) sign size, 2) mast-arm length, and 3) pole height. Each was broken into three sizes, based upon small, medium, and large dimensions, determined by construction specifications provided by the Kansas Department of Transportation (KDOT). CFD models were created to extract member forces due to the wind across a time history. A sub-model of the sign, butterfly supports, and walkway was modeled in ABAQUS/CFD 2016 for the sake of simplicity. The time-dependent forces from this model were then applied as dynamic loads to the 27 base models. A scale model of the large size sign structure was also created and tested within a wind tunnel to verify results from the CFD models.

It was concluded that removal of the walkway results in a higher natural frequency for the structure, however, it does not have a significant effect on the dynamic properties of the structure. Instead, sign size has the greatest impact on the dynamic properties, followed by mast-arm length and finally pole height. There was a good correlation of results between the wind tunnel and CFD models in relation to the pressures resulting from a wind speed of 30 mph (13.4 m/s), proving that the data from the CFD models is reliable. It was also concluded that removing the walkway did not increase loads due to galloping, vortex shedding, or natural wind and it did not have a significant effect on the stresses in the box connection or the pole.

2.4.3 Fatigue Research on COSS

2.4.3.1 Li et al. (2006)

Li et al. (2006) utilized finite element models to evaluate the fatigue performance of two mast-arm COSS due to natural wind loading. Dynamic analysis was utilized to study the structures, through the creation of finite element models in ANSYS. Connection details analyzed included: the anchor rods, the mast-arm-to-endplate and pole-to-baseplate socket connections, the built-up box connection, and the handhole. Sub-models were created of the connections and stress time-histories were obtained for each detail in order for the estimation of their fatigue life.

Calculating the nominal stress ranges at the pole-to-baseplate socket connection, the CAFT exceedance was between 0.738% and 1.236%. A high level of exceedance will lead to a lower fatigue life. To demonstrate how large the exceedance at the baseplate was, the next highest was by the box connection where exceedance varied from 0.062% to 0.494%.

The vertical fillet weld of the built-up box was checked for stress in the side-plate where the fillet weld connects to the pole, stress in the pole wall due to the punching shear stress, and stress at the fillet weld where the side-plate connects to the flange plate. From this analysis, it was concluded that the fatigue life of the built-up box connection is controlled by the stress at the weld connecting the side-plate and flange plate.

Based upon the analysis of the two mast-arm models, it was determined that the most critical detail is the pole-to-baseplate socket welded connection, followed by the fillet welds in the built-up box connection. The mast-arm-to-endplate socket weld connection has the third shortest fatigue life, with the handhole connections performing the best of the details studied.

2.4.3.2 Development of Stress Concentration Factors (SCFs)

Koenigs et al. (2003) fatigue tested 55 full-size mast-arm specimens to determine their resistance and compare experimental values to the fatigue life dictated in AASHTO SLT 2001. Finite element models were also created to compare with the experimental data and generate stress concentration factors (SCFs) for different connection geometries.

Experimental testing was performed by attaching a singular mast-arm to a load box, which was in turn attached to an actuator. Two arms were tested at a time, one on each side of the load box and constrained, pin on one end and roller on the other, recreating a simply supported beam. When a specimen failed, it was rotated so that the crack was on the compression side of the mast-arm and testing resumed until either the second mast-arm failed or the first one experienced a second failure. Both fillet-welded and stiffened socket connections were testing along with socket connections utilizing an external collar, internal collar, and a full penetration weld.

Finite element models were created by modeling one-half of the mast-arm, socket connection, and endplate. SCFs were calculated and the effect on different connection geometry was analyzed in detail, for example the effect of mast-arm thickness on the SCF. It was determined that mast-arm thickness does not have a significant effect on the SCF at the socket weld, but if a stiffener was utilized, thickness does affect the SCF there. The experiments verified the classification of the fillet-welded socket connection detail as Category E' in AASHTO SLT 2001.

Foley and Diekfuss (2016) performed fatigue testing on COSS to develop reliability-based procedures for assessing crack initiation. The procedures require that the uncertainty present in loading demands, resistance, modeling error, and accumulated fatigue damage are quantified. Through the results of the fatigue testing, new detail subcategories, as part of AASHTO Category E', were created. These subcategories were based on the SCF of details, including fillet-welded socket connections and both gusseted and ring-stiffened build-up box fillet-welded connections. High-fidelity finite element models were created to determine the SCFs. This research concluded that classifying connections based on SCF is more reliable than classifying by appearance when reliability-based analysis is performed.

2.4.3.3 Experimental Research focused on the Box Connection

While several studies have been performed analytically on box connections, there has been limited physical testing performed. Three experimental studies were Ocel et al., NCHRP Report 176, and research performed at the University of Wyoming. Both Ocel et al. and the NCHRP Report 176 provided recommendations for improvement to AASHTO SLT 4th Edition, 2001, which were implemented in later editions. Each study is summarized below, with all results compiled and discussed.

Overview

Ocel et al. (2006) performed experimental testing on several different specimens, but only Type I specimens included the box connection. The Type I specimens utilized eight-sided polygonal tubes for both the pole and mast-arm. With an eight-sided polygonal pole, the flange bears directly onto the tube and is continuously fillet-welded everywhere the flange touches the tube, as can be seen in Figure 2.14. This creates a direct load path between the mast-arm and pole as the flange bears directly onto the pole, which is accomplished by the inclusion of gusset plates when the tube is round. The dimensions of the specimens are shown in Table 2.7.

Table 2.7. Ocel Specimen Dimensions

	in. (cm)
Pole Corner-to-Corner Distance	14 (35.56)
Pole Thickness	0.3125 (0.79)
Arm Corner-to-Corner Distance	11.6 (29.46)
Arm Thickness	0.3125 (0.79)

Two different types of socket connection were applied to the mast-arms, with four of the mast-arms having fillet-welded socket connections with four triangular gusset plates, while the other four utilized full penetration tube-to-transverse plate welds in the socket connections. The mast-arm was 5 ft. (16.4 m) long, with two different pole lengths tested, a short version at 7 ft. (23 m) and a long version at 10 ft. (32.8 m).

Load was applied to the tip of a single mast arm, with the pole restrained to the strong floor. The structure was loaded in-plane, out-of-plane, and at a 45-degree angle to simulate all possible loading cases the structure would experience, i.e. TIWG, NW, and galloping. Cracking occurred in the box connection for the out-of-plane loading (NW) and 45-degree loading, however the baseplate socket connection cracked first during the in-plane loading (TIWG), which was initially loaded from the floor up towards the mast-arm. When in-plane loading was switched so that it was loaded from the ceiling down onto the mast-arm, which avoided extra stress on the baseplate socket connection, the box cracked.

Four out-of-plane fatigue tests were performed. The first two experienced cracking at the top corner of the side-plate while the last two tests cracked at the bottom corner, as shown in Figure 2.13. It was concluded that there is no bias between the top and bottom corners of the side-plate for out-of-plane cracking in the box connection. The location of this cracking corresponds to that experienced by the structures donated to this project by KDOT. Cracking also occurred at the top corner of the side-plate in one of the 45-degree loading tests.

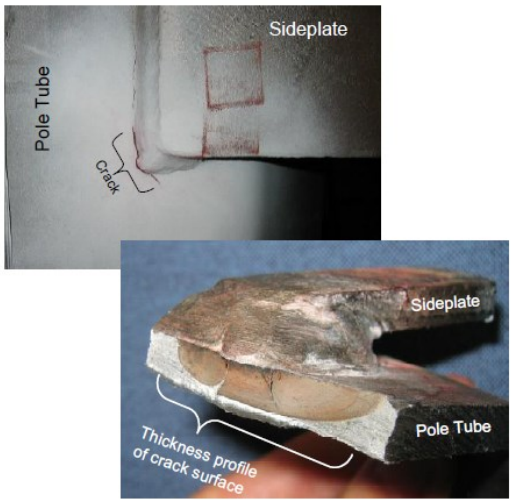

Figure 2.13. Out-of-plane cracking in box connection (Ocel et al. 2006)

For in-plane loading, in Specimen 3 cracks formed at the bottom intersection between the side-plate and flange which originated at the weld root and grew outwards, as shown in Figure 2.14.

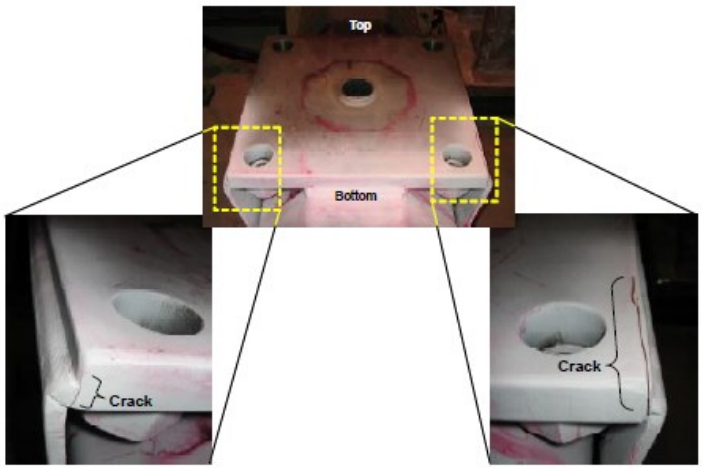

Figure 2.14. In-plane loading induced cracking on Specimen 1 (T1P2) (Ocel et al. 2006)

However, on the second specimen tested using in-plane loading, the side-plates buckled out-of-plane at the bottom, where they transferred compression. The side-plates buckled away from the pole and the weld root opened between the side-plate and flange; the cracking that occurred can be seen in Figure 2.15.

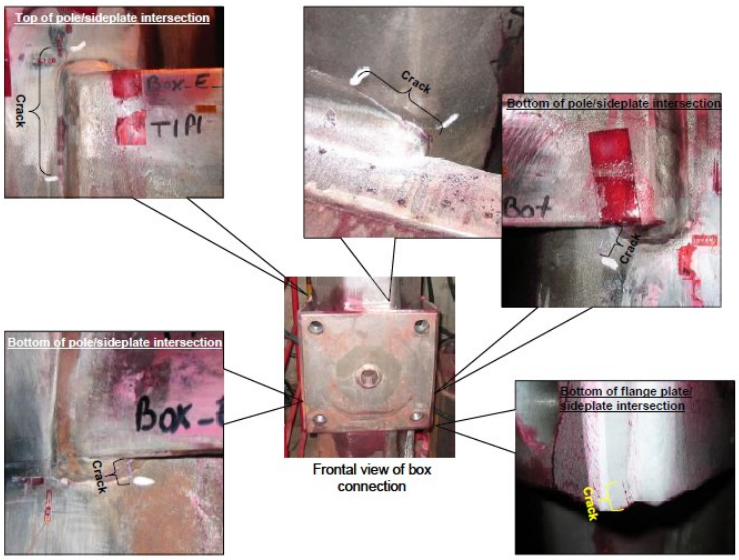

Figure 2.15. In-plane loading induced cracking on Specimen 2 (T1P1) (Ocel et al. 2006)

The third specimen also experienced cracking at the bottom corner of the side-plate to flange weld, however it only reached failure criterion once two cracks formed in the top corners of the flange to pole weld (Figure 2.16).

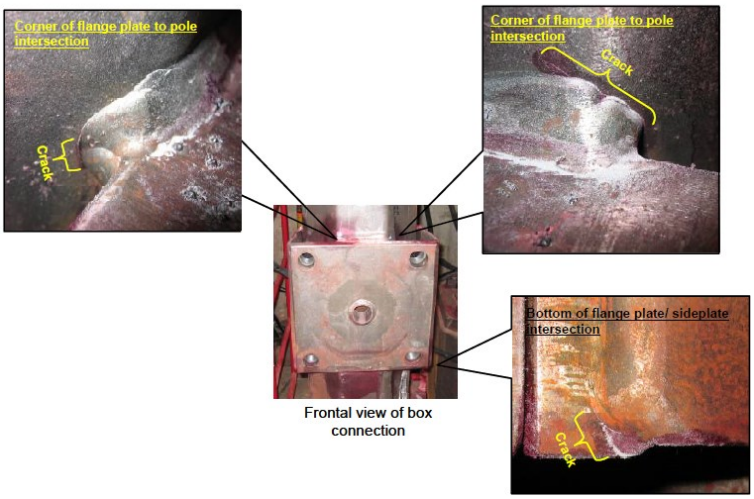

Figure 2.16. In-plane loading induced cracking on Specimen 3 (T1P3) (Ocel et al. 2006)

The conclusion from this report was that AASHTO specifications for fatigue were correct for the box connection for all except the weld between the flange and side-plate, which should be changed from Category E' (2.6 ksi, 18 MPa) to Category ET (1.2 ksi, 8 MPa). The specifications were revised to include this.

The initial research performed by Gray (1999) and Deschamp (2002) at the University of Wyoming focused on three different types of box connections: the open connection, the closed connection, and the ring-stiffened connection. The open connection is the gusset box connection type used by KDOT.

a)

b)

c)

Figure 2.17. Box Connection Designs: a) Open Box Connection; b) Closed Box Connection; c) Ring-Stiffened Box Connection (Hamilton et al. 2002)

As occurred in the Ocel testing, the loading was focused on in-plane, out-of-plane, and a diagonal loading, which was 30-degrees instead of 45-degrees. Since the primary focus of the research was on non-destructive evaluation (NDE), with determination of fatigue resistance secondary, the loading was not within a particular stress range, but rather increased as testing on each singular specimen progressed. Fatigue testing was interrupted every 250,000 cycles so that dye penetrant and acoustic emission testing could be performed. Also due to the focus on NDE methods, a rotational restraint was applied to the pole, through a variety of methods but for most tests using a clamping block. The rotational restraint was necessary for acoustic emission testing, however it resulted in many tests ending early due to cracks forming on the pole underneath the clamping block.

For the Gray and Deschamp research, a total of 19 poles were tested: 16 previously in-service and 3 newly-fabricated. Run-out was set at 3 million cycles for the new poles. As stated

above, for the previously in-service poles, the goal was the initiation and propagation of cracks for NDE while the focus on the new poles was the categorize the fatigue resistance. The cracking that occurred on the out-of-plane specimens was similar to that of KDOT's donated structures; occurring in the welded corners of the side-plate where it connected to the pole. Only the results from the 3 new specimens has been included in the analysis of these studys.

Peiffer's (2008) research continued from Gray and Deschamp's, though it focused solely on quantifying the fatigue resistance of the ring-stiffened box connection. Testing was still halted daily for either visual or dye penetrant inspection and a run-out limit of 13 million cycles was used to ensure that the beginning of the CAFT for Category E was exceed by at least 10%. The limit for Category E is about 11.5 million cycles.

The loading was still in-plane, out-of-plane, and diagonal; however load was now applied as cyclic loading in order to produce stress ranges up to 16 ksi (110 MPa) in the pole. To compute testing loads, a nominal bending stress calculation was performed at a point in the pole located one foot below the intersection of the pole and mast-arm (referred to as the design point). This is shown in the drawing for the out-of-plane (NW) set-up (Figure 2.18).

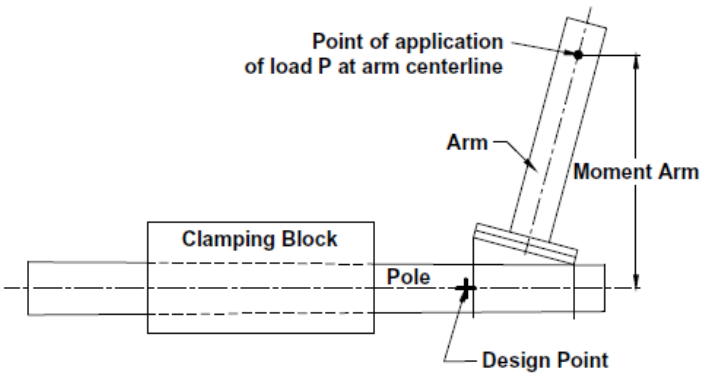

Figure 2.18. Moment arm for out-of-plane test set-up (Peiffer 2008)

Bending stress was used as the test set-up had been built to resist torsional rotation at the support. AASHTO specifications were utilized to determining the loading process, with the "nominal stresses in the main member, for an untested connection, just below the connection of the branching member, not exceeding Category E (4.5 ksi, 31 MPa)" (Puckett et al. 2010).

A total of 16 full-scale newly-fabricated specimens were tested. The clamping block was used again for this study and five of the specimens failed on the pole at or around this clamping

block. There were two different poles tested, a small pole which was round and a large pole which was 16-sided. The mast-arms were 12-sided and were at a 15-degree angle from the horizontal, see Figure 2.19. The dimensions for the poles and mast-arm are shown in Table 2.8.

Table 2.8. Peffier Specimen Dimensions

	in. (cm)
Small Pole Diameter	10.1 (25.65)
Small Pole Thickness	0.239 (0.61)
Large Pole Diameter	12 (30.48)
Large Pole Thickness	0.3125 (0.79)
Arm Corner-to-Corner Distance	12 (30.48)
Arm Thickness	0.3125 (0.79)

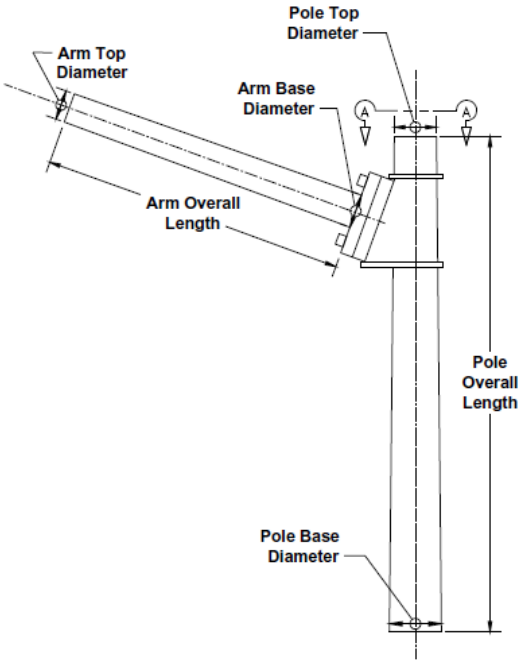

Figure 2.19. Test Set-ups (Peffier 2008)

For the in-plane results, it was determined that the limiting factor may not be due to the box connection, but rather due to bolt fatigue, internal thread fatigue in the baseplate, or mast-arm complete joint penetration weld fatigue. It was suggested that more research be conducted into the bolted connection of the box connection. Conclusions in the report suggested that bolted

connection failures may be due to a prying action from deformation of the arm flange plate under in-plane loads or an improper pretensioning of the connection bolts, causing an unexpected distribution of the load.

NCHRP Report 176 (Roy et al. 2011) covers fatigue testing of approximately 80 full sized galvanized specimens of sign, signal, and high-level luminaire support structures. Some of the fatigue tests were performed in past research and results incorporated in the report. Seventy-eight new and two retrofitted (previously fatigue cracked) specimens were examined and classified into 12 groups, the first six of which were round while the rest were multi-sided. Only types I-IV incorporated box connections, both gusseted and ring-stiffened, for a total of about 22 specimens.

All four specimen groups use the same arm and pole designs. The pole was 7 ft. (23 m) tall, and the mast-arm was 8 ft. (26.25 m) long. Both were tapered. Other dimensions are shown in Table 2.9.

Table 2.9. Roy et al. Specimen Dimensions

	in. (cm)
Pole Diameter	13 (33.02)
Pole Thickness	0.239 (0.61)
Arm Diameter	10 (25.4)
Arm Thickness	0.179 (0.45)

Table 2.10 shows the different connection details applied to each specimen group. The backing ring utilized in the full penetration groove weld socket connection was 0.25 in. (0.64 cm) thick and 2 in. (5.08 cm) high.

Table 2.10. Roy et al. Specimen Connection Types

Specimen	**Type of Box**	**Socket Connection Type**
1	Ring-Stiffened	Fillet-Welded
2	Gusseted	Full Penetration
3	Ring-Stiffened	Full Penetration
4A and 4B	Gusseted	Full Penetration

All specimens were loaded in-plane, except for 4B which was loaded diagonally at 45-degrees to determine the effects of out-of-plane loading.

Fatigue cracking at the box connection only occurred for one of the tests, on Specimen 4B.1, however a crack arrest hole was drilled, and the crack did not propagate further as testing continued, later ending due to cracking at the handhole. For all other tests, cracking occurred at other details in the structure first. Due to this, current design specifications allow for the assumption of infinite life for design purposes for both the gusseted and ring-stiffened box connection. Further testing on these details is suggested.

Summary of Findings from Prior Work

The results from all the studies discussed are compiled and discussed in the following; only results utilizing new specimens was included. While the focus will be on the box connection, cracking which occurred at other connection details will be discussed as well. Table 2.11 and Table 2.12 summarize the cracking that occurred at the box and mast-arm. Results for cracking at the handhole and baseplate are in Appendix C. N refers to the number of cycles the specimen experienced, while σ_R is the stress range applied.

Table 2.11. Box Cracking

Source	Specimen	N	σ_R, ksi (MPa)	Type of Tube	Socket Connection Type	Box Type	Notes
In-Plane (IP) Loading							
Ocel	T1P1	4.01E+06	4.56 (31.44)	Multi-Sided	Fillet-Welded Socket Connection	Gusseted	
	T1P2	1.46E+07	2.62 (18.06)				
	T1P3	6.56E+06	3.04 (20.96)				
Peiffer	1L-IP-7.5	1.31E+07	7.5 (51.71)	Multi-Sided	Full Penetration Socket Weld	Ring-Stiffened	Run-out
	5L-IP-16	1.30E+07	16 (110.32)				
	3L-IP-7.5	1.30E+07	7.5 (51.71)	Round Pole and Multi-Sided Arm			
	5S-IP-16	1.30E+07	16 (110.32)				
	1S-IP-7.5	1.31E+07	7.5 (51.71)				
	3S-IP-7.5	1.30E+07	7.5 (51.71)				
Out-of-Plane (OOP) Loading							
Ocel	T1P4	4.00E+06	2.17 (14.96)	Multi-Sided	Fillet-Welded Socket Connection	Gusseted	
	T1P5	8.00E+05	2.89 (19.93)				
	T1P6	1.29E+06	2.89 (19.93)				
	T1P7	2.29E+06	2.89 (19.93)				
Peiffer	6S-OP-7.5	1.30E+07	3.1 (21.37)	Round Pole and Multi-Sided Arm	Full Penetration Socket Weld	Ring-Stiffened	Run-out
	10L-OP-16	4.63E+06	6.5 (44.82)	Multi-Sided			
Diagonal (Dia.) Loading							
Ocel	T1P8	4.18E+06	2.3 (15.86)	Multi-Sided	Fillet-Welded Socket Connection	Gusseted	
Roy	4B.1	1.40E+07	1 (6.89)	Round	Full Penetration Socket Weld		
Peiffer	11L-DIAG-16	3.06E+06	16 (110.32)	Multi-Sided	Full Penetration Socket Weld	Ring-Stiffened	
	P1	1.00E+05	4.61 (31.78)				
Deschamp	P2	3.06E+05	5.65 (38.96)	Round			
	P3	2.30E+07	4.5 (31.03)				Run-out

Table 2.12. Mast-Arm Cracking

Source	Specimen	N	σ_R, ksi (MPa)	Socket Connection Type	Box Type
In-Plane (IP) Loading					
Roy	2.1	1.68E+06	11.90 (82.05)	Full Penetration Socket Weld	Gusseted
	2.2	2.03E+06	9.90 (68.26)		
		2.03E+06	11.90 (82.05)		
	2.3	2.08E+06	9.90 (68.26)		
		2.08E+06	11.90 (82.05)		
	4A.1	2.71E+07	9.45 (65.13)		
	4A.2	4.26E+07	12.38 (85.38)		
	1.1	1.80E+05	12.00 (82.74)	Fillet-Welded Socket Connection	Ring-Stiffened
	1.2	4.10E+05	12.00 (82.74)		
	1.3	1.77E+06	12.00 (82.74)		
	1.4	2.73E+06	12.00 (82.74)		
	1.5	5.98E+06	7.00 (48.26)		
	1.6	2.21E+07	4.87 (33.56)		
	1.7	2.29E+07	4.97 (34.26)		
	3.1	1.43E+06	12.00 (82.74)	Full Penetration Socket Weld	Ring-Stiffened
	3.2	5.09E+06	12.00 (82.74)		
	3.3	2.20E+06	12.00 (82.74)		
	3.4	3.01E+07	9.57 (65.97)		
	3.5	7.43E+06	10.00 (68.95)		
	3.6	9.64E+06	10.00 (68.95)		
	3.7	8.42E+06	10.28 (70.90)		
	3.8	6.75E+06	16.00 (110.32)		
	3.9	4.70E+05	16.00 (110.32)		
	3.10	5.20E+06	16.00 (110.32)		

The data in these tables have also been plotted in a series of S-N curves in Figure 2.20 and Figure 2.21, which are based on the loading direction and crack location. S-N curves have been created for the baseplate and handhole as well and are in Appendix C. Run-out tests are designated with a horizontal arrow pointing right. The box connection crack S-N curves contain data from all studies, while cracking at the mast-arm, handhole, and baseplate was only reported by Roy et al.

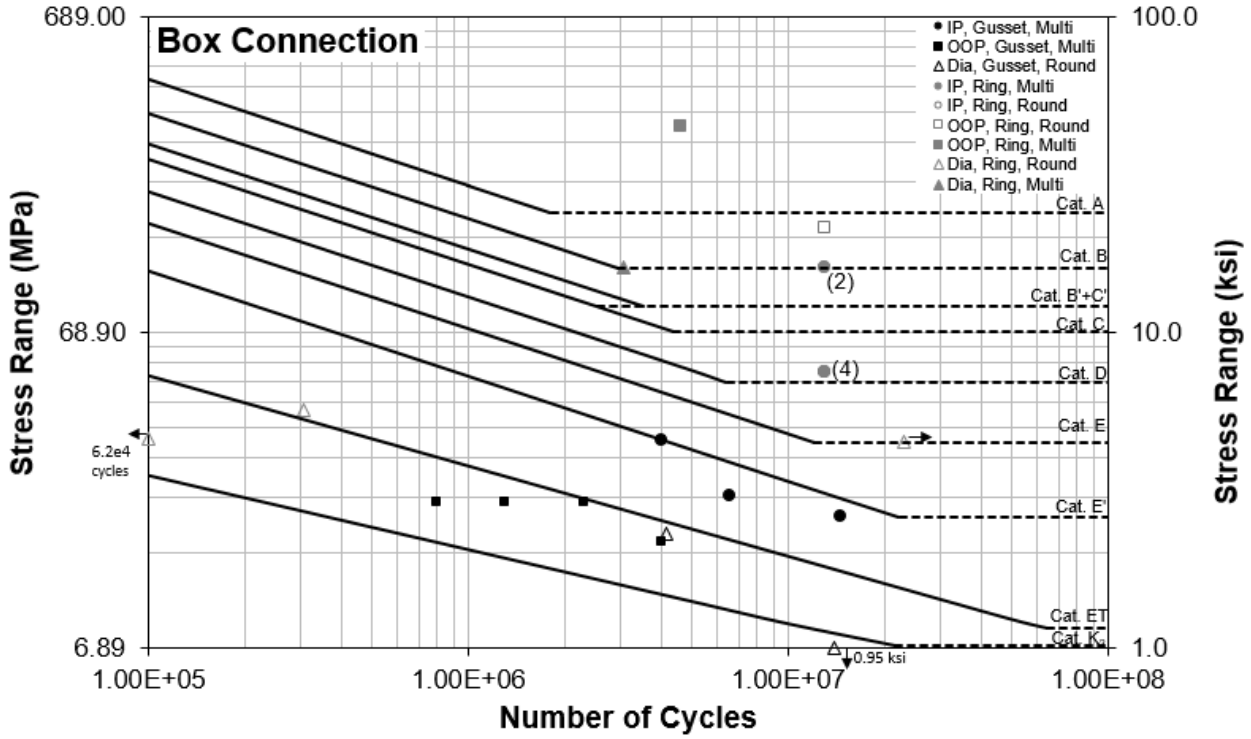

Figure 2.20. S-N Curve for Box Cracking

Ring-stiffened boxes are intended to be an improvement on the gusseted box design, and indeed, more cracking has been observed on the gusseted boxes than the ring-stiffened boxes. More tests were performed successfully on multi-sided poles/arms than on the round ones, so it is difficult to determine the effect of the pole type on the results accurately from this set of data. The box connection failed at a lower number of cycles and often lower stress ranges for the out-of-plane (NW) loading than the in-plane (TIWG) loading, which supports the conclusion other research has come to that NW is more impactful than TIWG on these structures. As the results for the diagonal (30-45 degree) loading was too variable to draw a conclusion, more research should be performed before a proper conclusion can be drawn. Finally, although more tests utilize a fillet socket weld than a full penetration weld with backing ring for the mast-arm connection, the effect of this on the cracking near the box seems minimal, though this is hard to say definitively as many of the full penetration weld structures experienced run-out as can be seen in Figure 2.20.

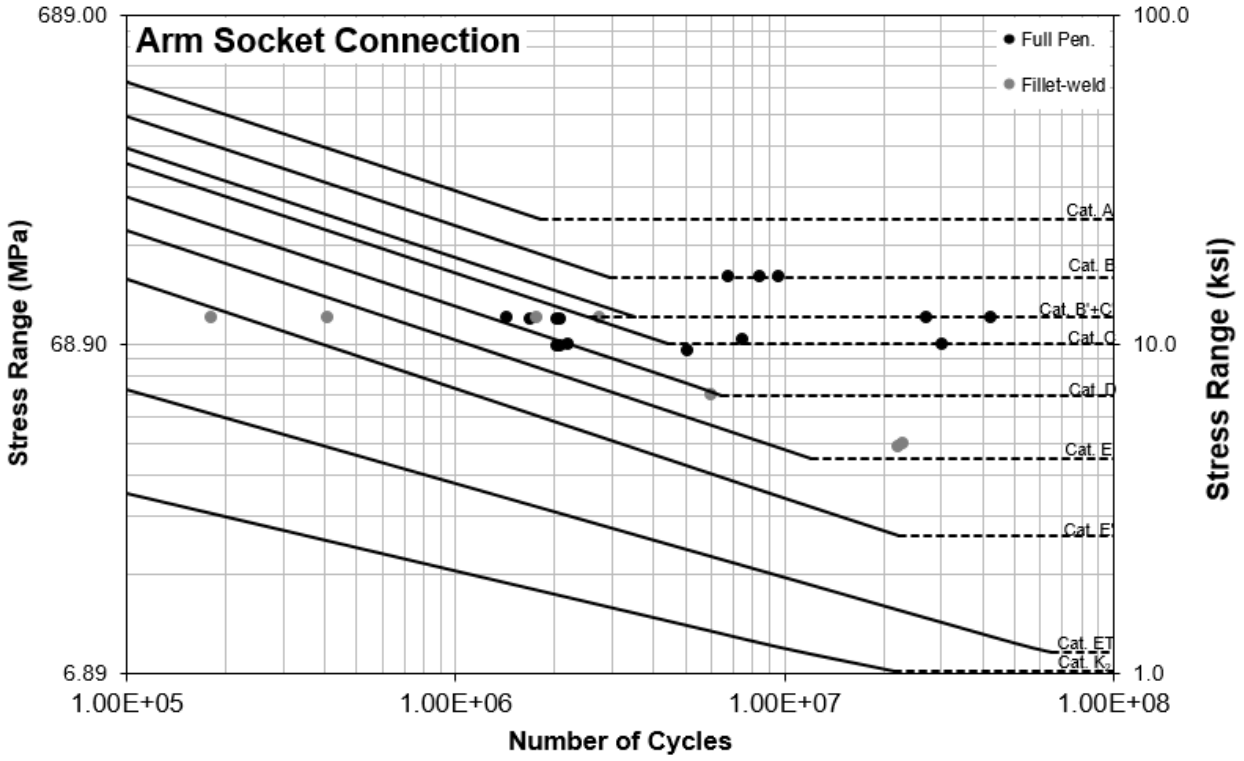

Figure 2.21. S-N Curve for Mast-Arm Cracking

Cracking that occurred at the mast-arm connection only occurred for the in-plane (TIWG) loading tests on specimens with round tubes. The cracks occurred at a higher stress range than for the box connections, however the number of cycles they failed at were not consistent. The fillet-welded socket connection tended towards lower stress ranges and number of cycles than the full penetration with backing ring connection experienced. Arm cracking often occurred first during the NCHRP 176 tests, and after this occurred, the broken arm was replaced, and testing continued until cracking occurred elsewhere. The type of box connection had minimal to no effect on the cracking experienced at the mast-arm socket connection.

Summary of Prior Work

Of the 21 specimens that experienced box connection cracking, 14 had multi-sided poles. While this could lead to the conclusion that a multi-sided pole increases the chance of cracking around the box connection, it cannot be definitively stated through this analysis as the specimens and set-ups utilized were different and most of the specimens in the studies discussed were multi-sided, thus skewing results.

On average, the ring-stiffened box connections performed better than the gusseted box connections, as they failed at higher stress ranges and higher number of cycles. This is shown best through the in-plane loading tests as all ring-stiffened specimens experienced run-out while all of the gusseted box specimens cracked. Run-out occurred at 13 million cycles for the ring-stiffened specimens. For the out-of-plane and diagonal loading tests, the ring-stiffened specimens that did not run-out still performed better than the gusseted specimens. Again, this is only in general terms as many of the gusseted and ring-stiffened specimens were from different studies and had different general geometries for the pole and mast-arm (thickness, diameter, height, length), all of which have an effect in the performance of the box connection. It is noteworthy that the only box cracking for the NCHRP 176 study occurred on a gusseted box, as both ring-stiffened and gusseted were examined on similar set-ups, however a crack arrest hole was able to prolong the fatigue life of the specimen until cracking occurred at another connection detail.

As more in-plane tests were conducted than out-of-plane, it is hard to conclude which one is overall worse for the box connections performance from this data set. In regard to cracking at the box, the Ocel results could be compared, see Table 2.11, as about the same number of tests were run for both loading types. Ocel only looked at the gusseted box connection and cracks formed at a slightly higher stress range and number of cycles for the in-plane tests than the out-of-plane tests, so it could be stated that it is more likely that in-plane loading will be worse for box connections than out-of-plane. This seems to only be true when looking at things in experimental testing, as in-field tests and finite element models performed have shown the opposite, such as work by Gallow et al. (2015), Hosch (2017), and Senior (2018).

Chapter 3: Procedure and Methods

Chapter 3 includes the methodology utilized for the performance of finite element (FE) analysis and experimental testing. The FE analysis modeling techniques, discussed in Section 3.1, were used for the examination of full-sized structures as well as the development of the test specimen, which was later constructed for the experimental testing. Abaqus (Simulia 2017) was used for all finite element modeling. Section 3.2 covers the construction and placement of the test specimens as well as all experimental testing methods.

3.1 Finite Element Modeling Procedure

The four different types of models created for the examination of the COSS are:

1) Tapered: The 1981 KDOT design incorporated a 0.14 in./ft. (1.17 cm/m) taper in both the mast-arm and pole along with a gusseted box connection
2) Straight: The 2015 KDOT design incorporated a straight mast-arm and pole along with a gusseted box connection
3) Ring-Stiffened: The 2015 KDOT design utilized a ring-stiffened box connection
4) Test Specimen: Scaled versions of the tapered structures

The construction drawings provided by KDOT as well as created for the fabrication of the test specimen are included in Appendix A.

Section 3.1.1 gives an overview of the techniques used for all models, including discussion of material properties and meshing techniques. Section 3.1.2 focuses on the full-sized tapered, straight, and ring-stiffened models. Finally, Section 3.1.3 covers the approaches that were specific to the FE models of the test specimens.

3.1.1 Finite Element Modeling Techniques

Part and Assembly Creation and Meshing

Each full-sized model consisted of 36 parts while the test specimen models consisted of 23 parts. To simplify the models, the walkway and butterfly supports were not modeled. This decision was based on prior research performed by Senior (2018), where it was determined that removing the walkway does not have a significant effect on the stresses in the box connection or the pole.

After each part was created, it was assigned a material section, placed within the assembly, and then meshed. Figure 3.1a shows the full assembly of full-sized model tD7L, while Figure 3.1b shows the assembly of the test specimen, and Figure 3.1c, the assembly of the bottom gusset box connection only.

Solid elements were used for all model components, with two exceptions in the case of the full-size models. In the full-scale models, the web was modeled as a wire element, and the sign was modeled using shell elements with a thickness of 1/16 in. (0.159 cm).

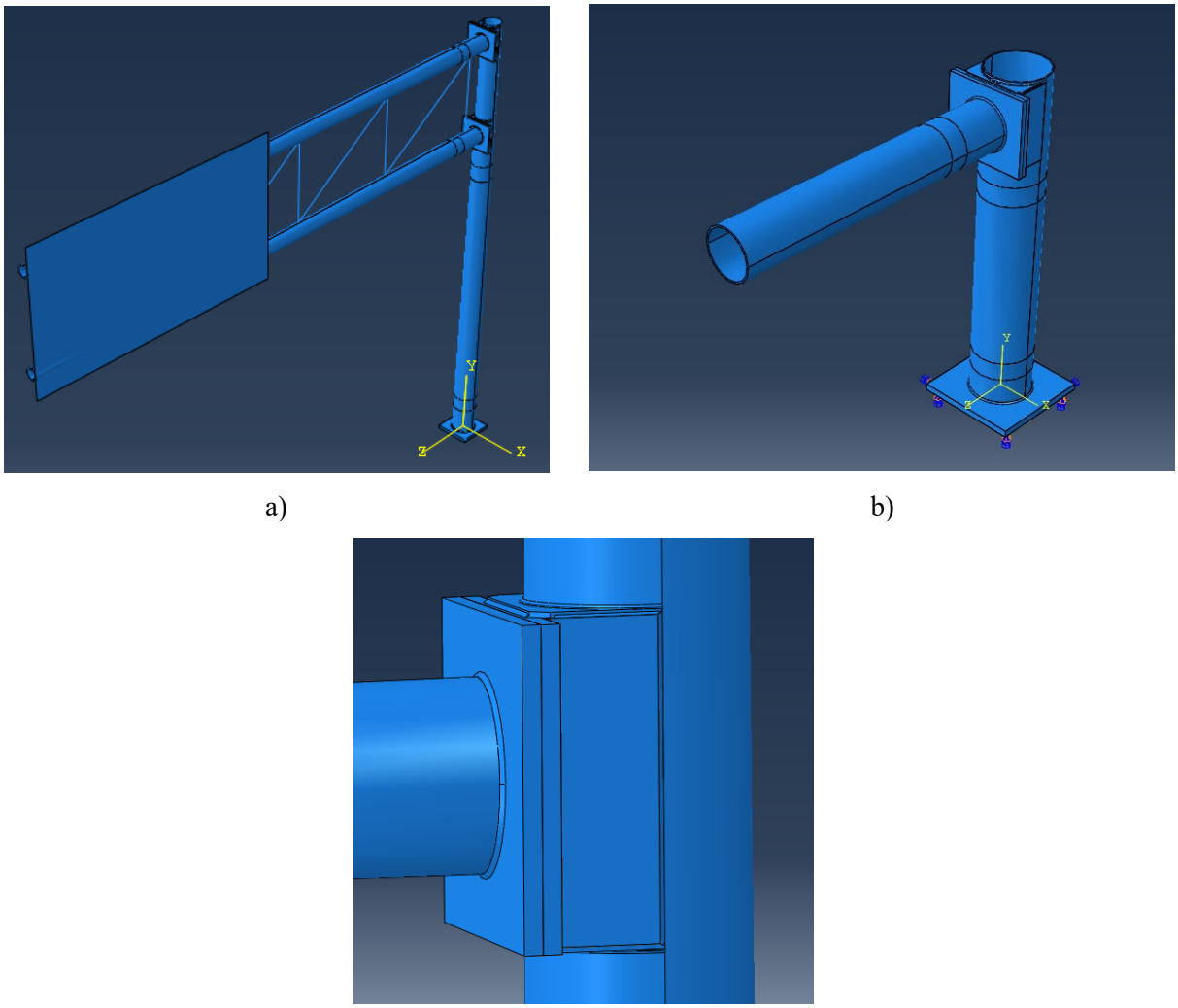

Figure 3.1. Abaqus Models: a) Full Assembly of tD7L; b) Test Specimen Assembly; c) Bottom Box Connection Assembly

Per AASHTO SLT specifications for hot spot analysis, all parts were required to be meshed with 20-node quadratic elements (C3D20R) for the hexagonal mesh and 10-nodes (C3D10) for the tetrahedral mesh. Because the web was a wire element, linear-beam meshing techniques were used for it. Areas of the pole and mast-arm removed from the mast-arm and base plate connection details were partitioned and meshed with a larger seed size to optimize model runtime (Figure 3.1a). Table 3.1 presents the type and typical seed size used to mesh each part.

Table 3.1. Mesh Type and Size

Part	Mesh Type	Seed Size, in. (cm)
Baseplate	Hex	0.3 (0.762)
Flange	Hex	0.2 (0.508)
Endplate	Hex	0.2 (0.508)
Arm (near box)	Hex	0.1 (0.254)
Arm (away from box)	Hex	1.5 (3.81)
Arm Exterior Weld	Tet	0.15 (0.381)
Arm Interior Weld	Tet	0.15 (0.381)
Side-plate	Hex	0.2 (0.508)
Front Gusset Weld	Tet	0.3 (0.762)
Gusset Weld	Hex	0.2 (0.508)
Gusset to Pole Weld	Tet	0.2 (0.508)
Pole (by box and baseplate)	Hex	0.1 (0.254)
Pole (between box and baseplate)	Hex	5 (12.7)
Pole Exterior Weld	Tet	0.15 (0.381)
Pole Interior Weld	Tet	0.15 (0.381)
Sign	Hex	14 (35.56)
Web	N/A	11 (27.94)
Box Weld	Tet	0.1 (0.254)

Material Definitions

Two materials were defined in the models in a manner consistent with KDOT construction specifications. Linear-elastic properties for aluminum were used in the sign, while all other parts were assigned linear-elastic properties for structural steel. Table 3.2 displays the materials and their properties (ASTM A709/A709M-18 2018, ASM International 1990).

Table 3.2. Model Material Properties

Material	Description	Mass Density	Young's Modulus	Poisson's Ratio
		lb/ft^3 (kg/m^3)	ksi (GPa)	
Steel	A709 Gr. 36	1.27 (20.37)	29000 (200)	0.29
Aluminum	6061-T6	0.0182 (0.291)	10150 (70)	0.33

Connections, Boundary Conditions, and Step Creation

All connections between the parts were modeled utilizing tied constraints, except for between the web and mast-arm. Table 3.3 details all the interactions and shows which part was the master surface and which the slave surface. Figure 3.2 shows the kinematic coupling connection between the nodes at the end of the web to nodes on the mast-arm, constraining all degrees of freedom. Bolt holes were modeled using a partition on the bottom of the baseplate and an encastre boundary condition was applied at each bolt hole location.

Table 3.3. Interaction Types

Master	Slave	Type
Web Node	Arm Node	Coupling
Endplate front	Arm Exterior Weld, back	Tie
Endplate, inside hole	Arm Interior Weld, sides	Tie
Flange, back	Side-plate, flange facing edge	Tie
Flange, bolt holes	Endplate, bolt holes	Tie
Pole, sides	Gusset to Pole Weld, sides	Tie
Gusset Plate, top	Gusset to Pole Weld, bottom	Tie
Baseplate, inside hole	Pole Interior Weld, sides	Tie
Pole, bottom edge	Pole Interior Weld, bottom	Tie
Arm	Arm Exterior Weld, sides	Tie
Arm	Arm Interior Weld, bottom	Tie
Side-plate, edges	Box Weld, inside edges	Tie
Flange, top/bottom edges	Front Gusset Weld, bottom	Tie
Gusset plate, front edge	Front Gusset Weld, back	Tie
Pole, bottom sides	Pole Exterior Weld, sides	Tie
Baseplate, top	Pole Exterior Weld, bottom	Tie
Sign, back	Arm, sides	Tie
Gusset, side edges	Box Weld, top/bottom side edges	Tie
Pole, sides	Box Weld, pole side edges	Tie

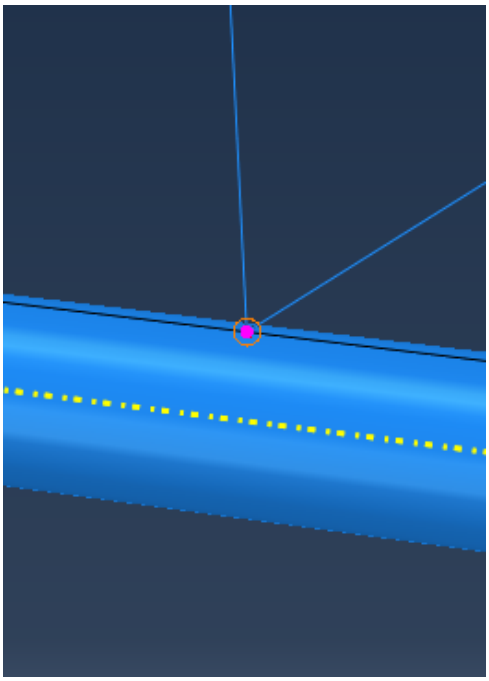

Figure 3.2. Coupling Connection between Web and Mast-Arm

Hot Spot Stress Analysis Approach

To conduct hot spot analysis, maximum principal stress values from the box connection, mast-arm socket connection, and baseplate socket connection were obtained so that results could be compared between different models. These results are discussed in Section 4.1. The approach described below was followed for all finite element analysis, i.e., all full-sized and test specimen models.

For each output file, a path was considered that originated from the visible hot spot and spanned along the mast-arm or pole, depending upon the connection detail of interest. The location of the hot spot stress along the path can be calculated using Eq. 3.1, which is only valid for tubular structures, where *r* is the outer radius and *t* is the thickness of the tube (AASHTO SLT 2015).

Eq. 3.1

These paths are shown in Figure 3.3, using the tapered pole model, tD7L.

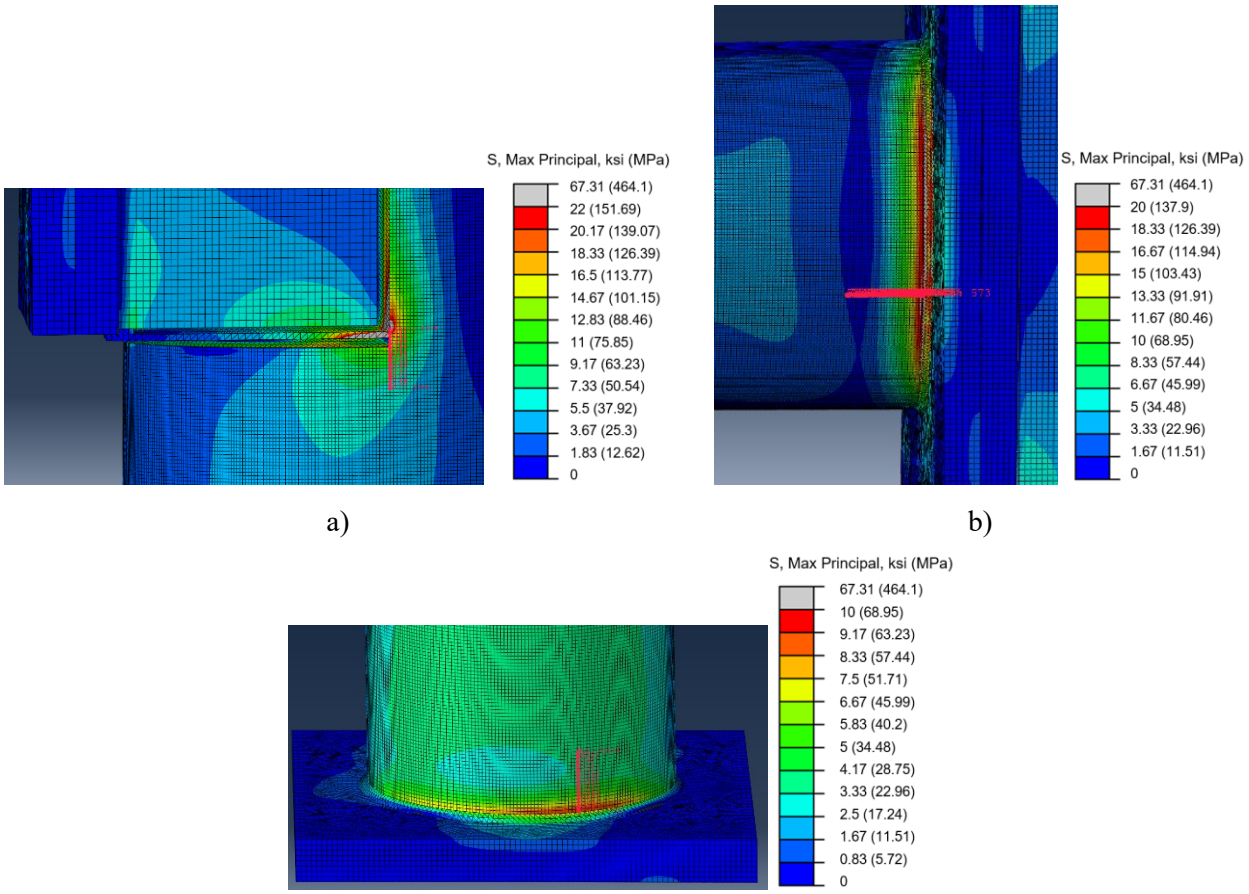

Figure 3.3. Paths for HSS on tD7L, NW: a) Box Connection; b) Mast-Arm Socket Connection; c) Baseplate Socket Connection

The data extracted from each path shows how maximum principal stress varies with distance along the path.

For models with ring-stiffened box connections, the hot spot at the box connection detail occurred in two possible locations. The first location was in the center of the front side-plate, along the weld that connects it to the flange of the box (Figure 3.4). As this hot spot is on the side-plate, a non-tubular structure, Equation 3.2 was utilized.

Eq. 3.2

where $\sigma_{0.4t}$ and $\sigma_{1.0t}$ are the stresses at the distances of 0.4t and 1.0t from the hot spot, respectively, and *t* is the thickness of the plate.

The second location was below the ring, in line with the edge of the side-plate (Figure 4.2). Since the hot spot on the sideplate was consistently larger than the hot spot below the ring, it was utilized as the hot spot stress for the box connection of the ring-stiffened box connection structures in later analyses. Hot spot locations for the mast-arm socket connection and baseplate socket connections were consistent with the tapered and straight pole models and thus were based on tubular equation (Equation 3.1).

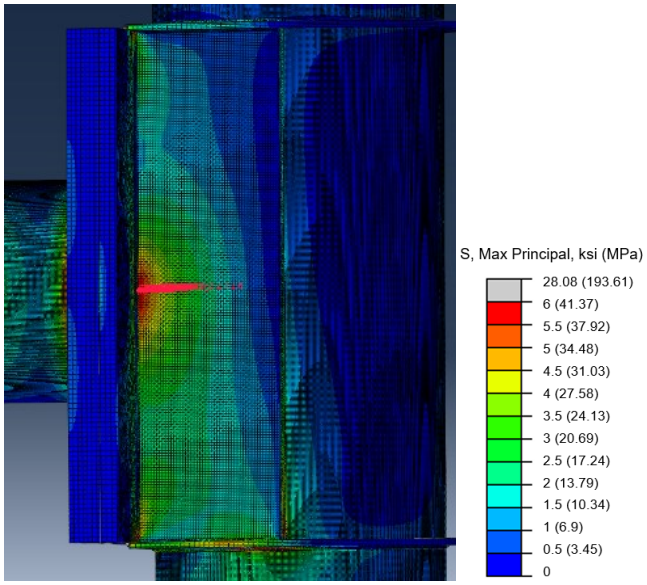

Figure 3.4. Path for HSS by Box Connection, rD7L, NW

Utilizing the paths generated from Abaqus and Equations 3.1 and 3.2, it is possible to determine the hot spot stress, which can be graphed on the AASHTO Category C S-N curve. In some cases, interpolation was necessary to determine the hot spot stress at the location, as it sometimes fell within an element rather than at a node line. The results from this analysis are discussed in Section 4.1 and tabulated in Appendix D.

3.1.2 Full Sized Models

Model Matrix

The primary intention of the finite element analysis was to inform the experimental testing plan and aid in the determination of a test specimen that accurately represented behavior of full-sized structures. To this end, full-sized model configurations were based on KDOT COSS standard designs. While not a fully-parameterized analysis, this approach was chosen to allow for comparison between the primary KDOT structures.

An analytical model matrix was created to examine how changing structural geometry affects stresses at the box connection within the context of KDOT structures. This included an evaluation of performance differences between the KDOT 1981 tapered structures, the KDOT 2015 straight structures, and the KDOT 2015 ring-stiffened structures. The construction plans for all three structure types are in Appendix A.

To capture differences in member sizes and shapes, models were broken into groups based on KDOT design groups. They were further classified based on site-specific geometry or structure layout, which defines the sign size, pole height, and mast-arm length. KDOT provided 110 examples of design drawings for constructed COSS, fabricated based on the 1981 tapered designs. These examples allowed for a database to be created, from which a range of site-specific geometries for the KDOT design groups were identified, leading to the development of a model matrix representing the scope of designs in service.

Designs #1, #3, and #7 were chosen from the 1981 tapered KDOT structures in order to represent the range of design groups. Design #1 and #7 were chosen to represent the full scope of potential member sizes, with #1 being the smallest possible option and #7 the largest. Design #3 as an intermediate-sized structure, and matched one of the structures donated by KDOT, discussed in Section 2.2.2.3.

The 2015 KDOT redesign merged the 1981 Design #1 and #2 into Design #1, lowering the total number of design numbers to six. Thus, for a direct comparison between the tapered tube and straight tube structures, 2015 Designs #1, #3, and #6 were utilized. The 2015 redesign also incorporated the inclusion of two designs which utilize a ring-stiffened box connection instead of a gusseted box connection. Design #7 from these plans was chosen, as it incorporated similar mast-

arm and pole diameters to tapered Design #7 and straight Design #6, allowing for better comparison between structure types. Design #8 was excluded because the mast-arm and pole diameters were much larger than any utilized on the other KDOT standard designs.

Table 3.4 shows the mast-arm diameter and thickness as well as the pole diameter and thickness for each chosen structure type and design number.

Table 3.4. Design Geometry Parameters

	Arm Dia., in. (cm)	Arm Thickness, in. (cm)	Pole Dia. at Base, in. (cm)	Pole Dia. at bottom box, in. (cm)	Pole Thickness, in. (cm)
Tapered Tube Structures					
Designs 1 and 2	9.2 (23.4)	0.25 (0.64)	15 (38.1)	Varies (pole is tapered at 0.14 in./ft. (1.17 cm/m))	0.25 (0.64)
Design 3	11 (27.9)	0.1875 (0.48)	18 (45.7)		0.25 (0.64)
Design 7	13 (33)	0.3125 (0.79)	18 (45.7)		0.3125 (0.79)
Straight Tube Structures					
Design 1	8.625 (21.9)	0.5 (1.27)		16 (40.6)	0.375 (0.95)
Design 3	12.75 (32.4)	0.25 (0.64)		18 (45.7)	0.375 (0.95)
Design 6	12.75 (32.4)	0.5 (1.27)		18 (45.7)	0.5 (1.27)
Ring-Stiffened Box Structures					
Design 7	14 (35.56)	0.625 (1.59)		18 (45.7)	0.75 (1.9)

The diameter of the pole at the bottom box varied for all tapered structures, due to the 0.14 in./ft. taper. On average, the diameter of the pole at the bottom box is between 12.16-12.3 in. (30.89-31.24 cm) for Design #1 and #2, and 14.63-15.33 in. (37.16-38.94 cm) for Designs #3 and #7. The mast-arm diameters shown in the table are the diameters at the socket connection. The weld thickness also varied between structure type and design number and can be seen in Table 3.5 and Table 3.6 for the socket connections at the mast-arm and baseplate as well as at the box connection.

Table 3.5. Socket Connection Weld Geometry

	Arm Exterior Socket Weld, in. (cm)	Arm Interior Socket Weld, in. (cm)	Pole Exterior Socket Weld, in. (cm)	Pole Interior Socket Weld, in. (cm)
Tapered Tube Structures				
Designs 1 and 2	0.375 (0.95)	0.25 (0.64)	0.375 (0.95)	0.25 (0.64)
Design 3	0.3125 (0.79)	0.1875 (0.48)		
Design 7	0.4375 (1.11)	0.3125 (0.79)	0.4375 (1.11)	0.3125 (0.79)
Straight Tube Structures				
Design 1	0.375 (0.95)	0.5 (1.27)	0.375 (0.95)	0.3125 (0.79)
Design 3	0.25 (0.64)	0.25 (0.64)		
Design 6	0.375 (0.95)	0.5 (1.27)	0.5 (1.27)	0.4375 (1.11)
Ring-Stiffened Box Connection Structures				
Design 7	0.4375 (1.11)	0.3125 (0.79)	0.5 (1.27)	0.4375 (1.11)

Table 3.6. Box Connection Weld Geometry

	Gusset to Flange Weld, in. (cm)	Gusset to Pole Weld, in. (cm)	Side-plate to Flange Weld, in. (cm)	Side-plate to Gusset Welds, in. (cm)	Side-plate to Pole Weld, in. (cm)
Tapered Tube Structures					
Designs 1 and 2	0.25 (0.64)	0.25 (0.64)	0.25 (0.64)	0.1875 (0.48)	0.25 (0.64)
Design 3					
Design 7			0.3125 (0.79)		0.375 (0.95)
Straight Tube Structures					
Design 1	0.25 (0.64)	0.375 (0.95)	0.3125 (0.79)	0.25 (0.64)	0.3125 (0.79)
Design 3					
Design 6					
Ring-Stiffened Box Connection Structures					
Design 7	0.3125 (0.79)	0.25 (0.64)	0.3125 (0.79)	0.1875 (0.48)	0.3125 (0.79)

Within the database generated from the 110 KDOT design cases, the COSS were catalogued by design number and then a small, medium, and large site-specific geometry for each design was determined. The primary parameter considered was sign size, with arm length and pole height secondary conditions when choosing the geometry for each group (small, medium, large). The chosen parameters are presented in Table 3.7.

Table 3.7. Site-Specific Parameters

	Sign Height, ft. (m)	Sign Length, ft. (m)	Arm Length, ft. (m)	Pole Height, ft. (m)
		Design #1		
Small	4 (13.12)	12 (39.4)	29 (95.1)	25 (82)
Medium	7.5 (24.6)	14.5 (47.6)	29 (95.1)	26 (85.3)
Large	9 (29.5)	17.5 (57.4)	31 (101.7)	26 (85.3)
		Design #3		
Small	8 (26.2)	18 (59)	18 (59)	27 (88.6)
Medium	8.5 (27.9)	19.5 (64)	31 (101.7)	27 (88.6)
Large	9.5 (31.2)	18.5 (60.7)	30 (98.4)	30 (98.4)
		Design #6/7		
Small	6 (19.7)	11.5 (37.7)	30 (98.4)	27 (88.6)
Medium	10 (32.8)	15 (49.2)	31 (101.7)	32 (105)
Large	12 (39.4)	19 (62.3)	34 (111.5)	29 (95.1)

The general site-specific parameters in Table 3.7 were than modeled as each of the tapered, straight, and ring-stiffened, based on design number. The ring-stiffened box connection models were only created based upon the Design #6/7 site-specific geometry groups.

Notation for the models is based on structure type, design number, and then geometry group. For example, the tapered, Design #7, large geometry structure would be notated as tD7L. A total of 21 full sized structure models were created with nomenclature in Table 3.8.

Table 3.8. Model Nomenclature

Nomenclature	Structure Type	Design #	Site-Specific Geometry Group
tD1S	Tapered Tube	1	Small
tD1M			Medium
tD1L			Large
tD3S		3	Small
tD3M			Medium
tD3L			Large
tD7S		7	Small
tD7M			Medium
tD7L			Large
sD1S	Straight Tube	1	Small
sD1M			Medium
sD1L			Large
sD3S		3	Small
sD3M			Medium
sD3L			Large
sD6S		6	Small
sD6M			Medium
sD6L			Large
rD7S	Ring-Stiffened Box	7	Small
rD7M			Medium
rD7L			Large

Loading Methodology

AASHTO SLT (2015) provides the wind loads that COSS must be designed to resist. The loading types considered in this research were natural wind (NW), truck-induced wind loading (TIWG), and galloping. Based on prior research, these were divided into two loads: natural wind, which was applied out-of-plane, and TIWG plus galloping (T+G), which was applied in-plane. An example of the loading calculations can be found in Appendix B.

Natural wind loading was determined using Equation 3.3. An influence factor, I_F, of 1 was selected from Table 11.6-1 of AASHTO SLT (2015), aligning with the worst case possible, Category I structures. Coefficient of drag, C_d, values of 1.1 and 1.12 were used for the mast-

arm/pole/web and sign respectively. These were chosen based on values utilized by KDOT in their design.

$$\begin{aligned} &\text{(psf)} \\ &\text{(Pa)} \end{aligned} \qquad \text{Eq. 3.3}$$

Natural wind loading was applied as a line load along each node of the mast-arm, web, and pole. To do this, the pressure from Equation 3.3 was multiplied by the mesh size of that section of mast-arm, web, or pole. For the sign, the load was applied directly to the face of the sign as a pressure.

The TIWG load was determined using Equation 3.4 and applied as a line load to the mast-arms in the same manner as the NW load. However, the TIWG load was only applied along the last 12 ft. length of the mast-arm, following what is dictated in the AASHTO SLT (2015) specifications and performed in NCHRP Report 469 (Dexter et al. 2002) design examples. The load was applied as a line load to the bottom of the sign.

$$\begin{aligned} &\text{(psf)} \\ &\text{(Pa)} \end{aligned} \qquad \text{Eq. 3.4}$$

The TIWG load decreases linearly above a height of 20 ft. (6 m) to zero at a height of 33 ft. (10 m). The pressure obtained from Equation 3.5 was corrected to account for this for all mast-arms and sign edges that fell within this range, using calculated linear equations. *H* is the distance from the ground to the bottom edge of the sign ( ) or to the bottom side of the top/bottom mast-arm ( ).

$$\begin{aligned} &\text{(psf)} \\ &\text{(Pa)} \\ &\text{(psf)} \\ &\text{(Pa)} \end{aligned} \qquad \text{Eq. 3.5}$$

Galloping was determined using Equation 3.6 and was multiplied by the sign height to apply the load as a line load to the bottom edge of the sign.

$$0_{\text{ي سي}}\ \varsigma\ \rho_{\text{ي}}\ \text{(psf)}$$
$$0_{\text{ي سي}}\ \rho\ \pi\ \pi\rho_{\text{ي}}\pi\text{(Pa)} \qquad \text{Eq. 3.6}$$

Figure 3.5 shows the placement of the loads upon the model for all three loading cases. TIWG and galloping loads were applied simultaneously.

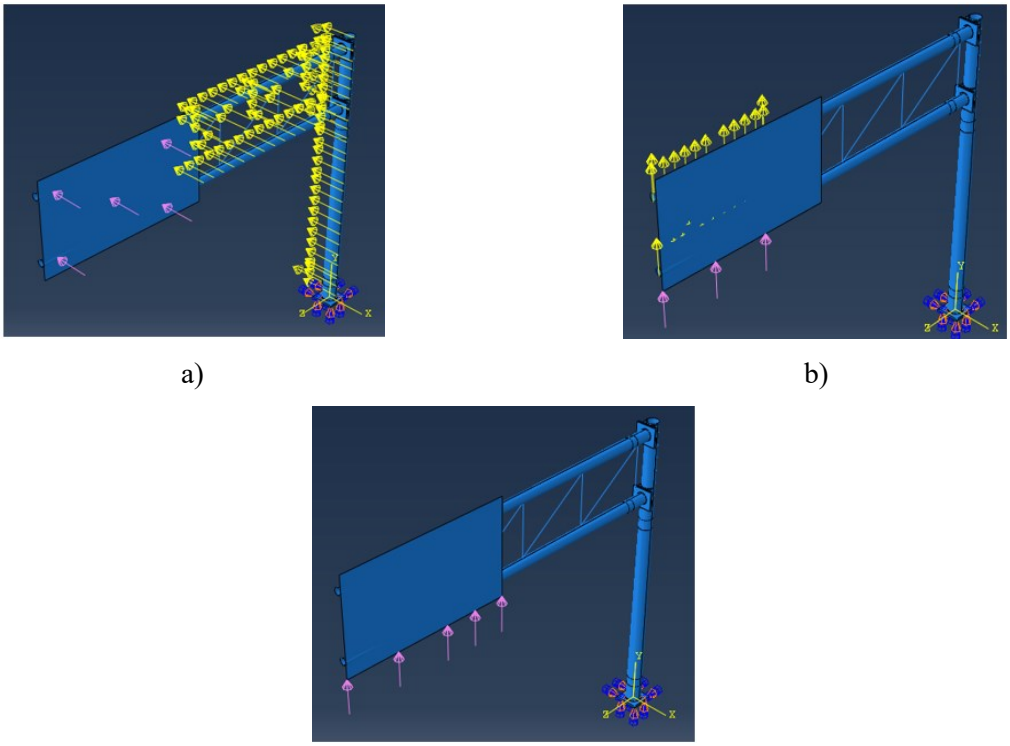

a) b)

c)

Figure 3.5. Load Placements: a) Natural wind; b) Truck-induced gust; c) Galloping

3.1.3 Test Specimen Models

The goal of the test specimen modeling effort was to ensure the best specimen design accurately captured stress distributions in the real KDOT COSS, using the donated Structure 309, full sign model tD7L, as a baseline. It will be referred as the "real structure" for the remainder of this section.

Both a two mast-arm, matching the design of the real structure, and a single mast-arm design were considered. After FEA analysis of both possible specimen designs, the single mast-arm was selected for ease of testing, as it was possible to replicate the stress distribution of Structure 309 utilizing a single arm specimen. As such, only the exploration of single mast-arm test specimens is discussed here.

Load Calculations

Scaled point loads were calculated based upon the moment obtained from hand calculations of stress analysis of the real structure, see Appendix B for an example. To calculate the NW scaled point load, F_{NW}:

$$F_{NW} = \frac{M_{NW}}{L_{arm}} \qquad \text{Eq. 3.7}$$

where L_{arm} is the moment arm, i.e. length from design point to load point, and M_{NW} is the moment at the bottom box resulting from the natural wind loading on the real structure.

The design point was located 12 in. (30.5 cm) below the midpoint of the side-plate, as illustrated in Figure 3.6.

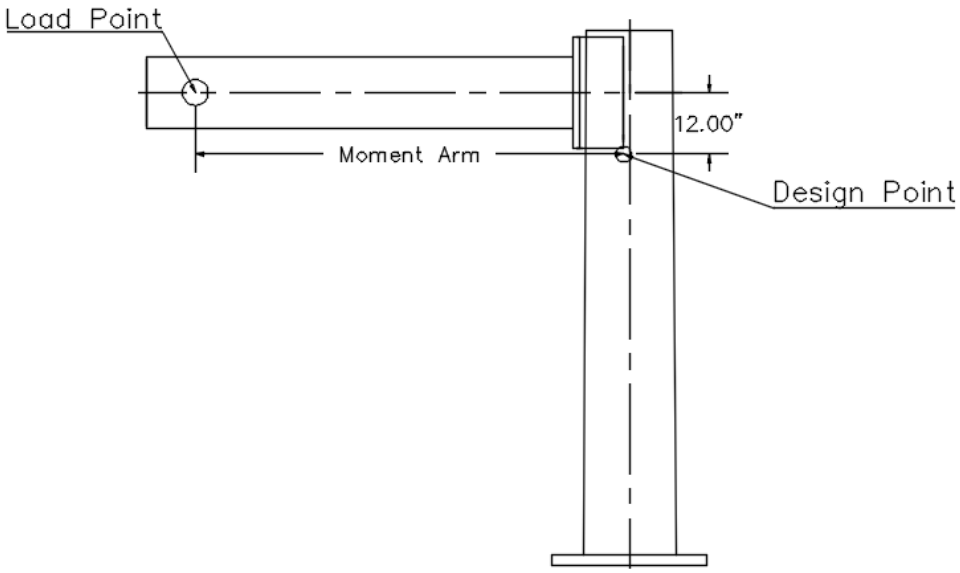

Figure 3.6. Test Specimen Moment Arm and Design Point

The scaled point load utilized to check T+G was calculated the same way. However, further investigation regarding T+G was not performed for the test specimen, as it was determined that T+G was not the driving force behind the cracking experienced in KDOT structures, based on stress distributions generated on the full-sized models. This is discussed in detail in Section 4.1.3.

Test Specimen Alternatives

Eleven possible specimen alternatives were examined, shown in Table 3.9. The order of notation is mast-arm length (SA) and pole length (P), based on this the 3 ft. (9.8 m) arm and 6.5 ft. (21.3 m) pole is noted as SA3P6.5.

Table 3.9. Test Specimen Alternatives

Arm Length (SA), ft. (m)	Pole Height (P), ft. (m)
3 (9.8)	6.5 (21.3)
	8.5 (27.9)
5 (16.4)	6.5 (21.3)
	8.5 (27.9)
	10.5 (34.4)
7 (23)	6.5 (21.3)
	8.5 (27.9)
	10.5 (34.4)
	15 (49.2)
9 (29.5)	6.5 (21.3)
	8.5 (27.9)
	10.5 (34.4)

To determine the optimal specimen, the von Mises stress distribution generated around box for the specimen and real structure were compared. To ensure that the behavior of the test specimen mimicked the real structure, hot spot stress ratios of the between the box connection and mast-arm socket connection and between the box connection and baseplate socket connection were created. Ensuring that the stresses at the box connection, baseplate socket connection, and mast-arm socket connection were equivalent between the two models.

Chosen Set-up

The SA7P8.5 specimen configuration was chosen as its stress distributions and ratios matched the real structure well. However, the forces at the mast-arm were too large compared to those generated on the real structure, and as such, alternatives to stiffen it were examined.

The 1981 KDOT design specifications called for a 0-gauge tube to be used for the Design #7 mast-arms. The following alternatives to this were tested: 000-gauge, 00000-gauge, 0000000-gauge, HSS12.75x0.5, HSS14x0.375, HSS14x0.5, and HSS14x0.625. The diameters of 12.75 in. (32.4 cm) and 14 in. (35.6 cm) were used for the HSS sections, so that the diameter of the real structure was maintained, which was 12 in. (30.5 cm).

The HSS14x0.5 section was selected for the mast-arm. Utilizing Equation 3.7 and a L_{arm} of 6.94 ft. (22.8 m), the equivalent NW force applied to the structure was 2,776.25 lb (12.35 kN). Table 3.10 displays the hot spot stress ratios for both the test specimen, SA7P8.5, and the real

structure, while Figure 3.7 displays the von Mises stress distributions for both the real structure, on the left, and test specimen, on the right.

Table 3.10. Hot Spot Stress Ratios for Chosen Test Specimen and Real Structure Models

Real: Box/Arm	0.89
SA7P8.5: Box/Arm	0.89
Real: Box/Baseplate	1.39
SA7P8.5: Box/Baseplate	1.36

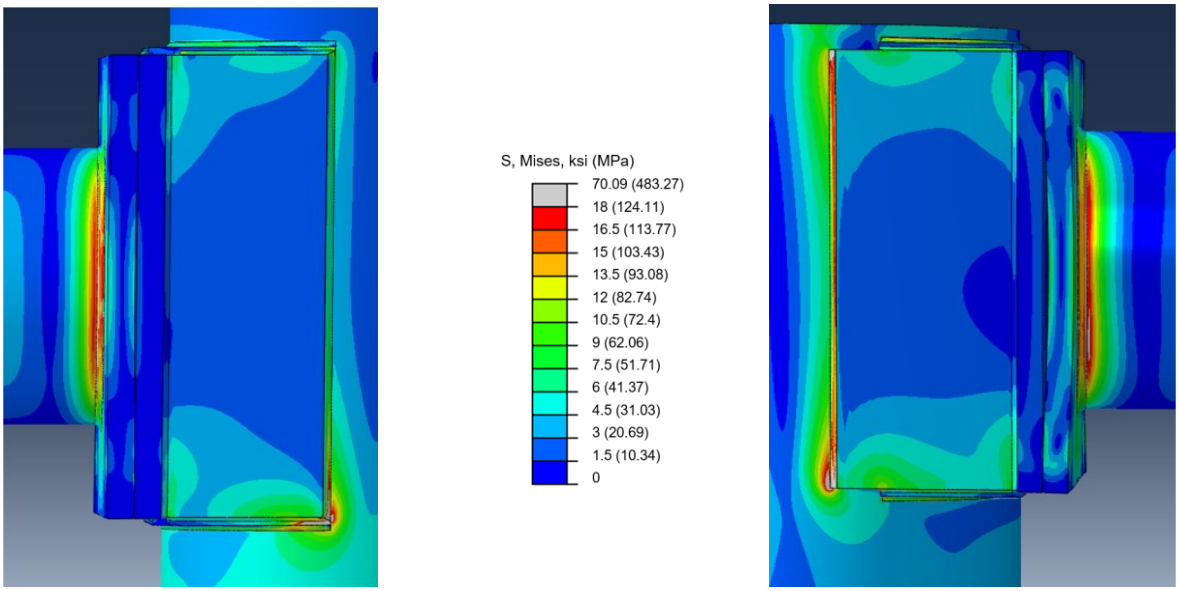

a) b)

Figure 3.7. von Mises Stress Distributions by Box Connection: a) Real Structure and b) Chosen Test Specimen

The construction drawings for the test specimen can be found in Appendix A. A total of six specimens were fabricated. The general dimensions of the specimens corresponded to the 1981 tapered Design #7 structure, with changes noted in Table 3.11. The test specimens also have a straight mast-arm and pole instead of a tapered one.

Table 3.11. Changes from Full Sized Structure to Test Specimen

	Full Sized Structure	Test Specimen
Pole Height, ft. (m)	26 (85.3)	8.5 (21.59)
Pole Thickness, in. (cm)	0.3125 (0.79)	0.375 (0.95)
Arm Length, ft. (m)	31 (101.7)	7 (17.78)
Arm Diameter, in. (cm)	13 (33.02)	14 (35.56)
Arm Thickness, in. (cm)	0.3125 (0.79)	0.465 (1.18)
Baseplate Length/Width, in. (cm)	26.5 (67.31)	30 (76.2)
Baseplate Thickness, in. (cm)	2.5 (6.35)	2 (5.08)

3.2 Experimental Testing Procedure

Work done to develop the experimental testing procedure and begin experimental testing is discussed below. Results from the experimental testing will not be discussed as the testing is still on-going.

3.2.1 Test Specimen Construction

Fabrication Geometry

The plans provided by KDOT did not display an alteration to the fabrication of the structures, however for the past decade, the top and bottom gusset have been cut shorter so that they do not span the whole length of the side-plate. Due to this, the welding no longer wraps around the whole box, and instead the top, bottom, and side welds are all separate, which is shown in Figure 3.8. The donated structures were constructed before this alteration was common practice and thus have the gusset plate span the whole length of the side-plate and all welds around the side-plate connecting.

a) b)

Figure 3.8. Gusseted Box Connection Welding: a) Donated Structure 165 and b) Test Specimen

Further analytical research into the possible impacts of this welding redesign is recommended, as the stresses along the side of the side-plate-to-pole weld do increase.

Laboratory Set-up

Drawings for laboratory placement are in Figure 3.9. The baseplate of the specimens was bolted down to the strong floor with a torque of 55 lb*ft (74.57 N*m) utilizing Superbolts to pretension the rods. An actuator connector was fabricated to ensure that the load was applied as a point load at the distance utilized for calculations, described in Section 3.2.2. The specimens were loaded out-of-plane in tension through a sinusoidal cyclic loading.

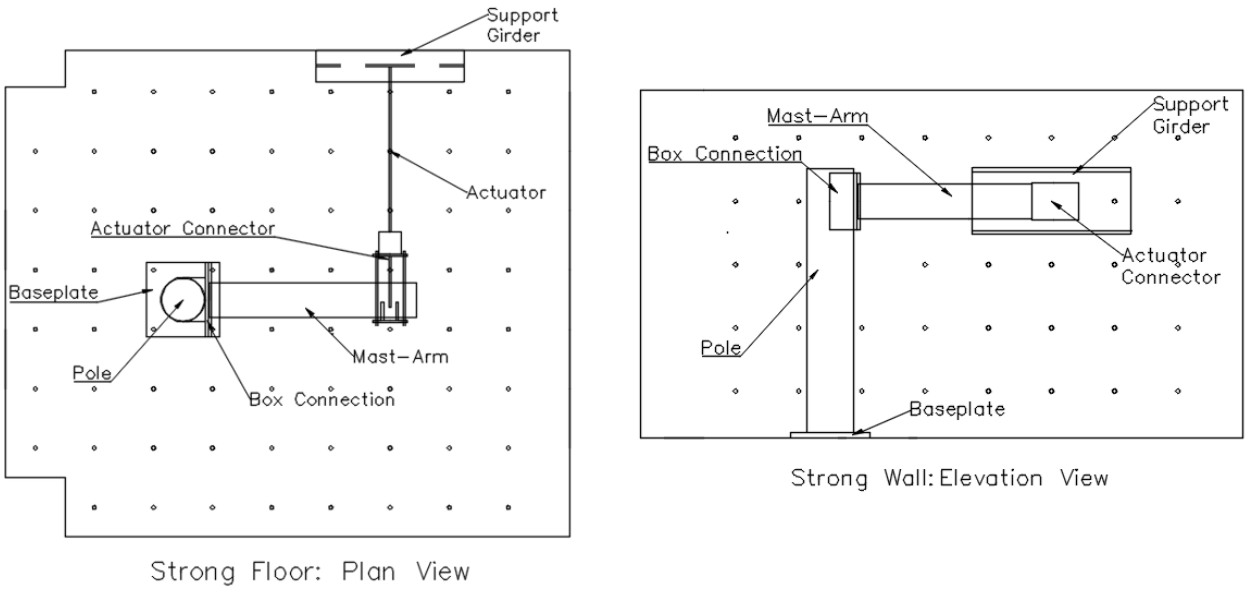

Figure 3.9. Laboratory Placement of Experimental Specimen

Figure 3.10 shows the set-up in the lab. The chain seen was attached loosely to the mast-arm with the yellow strap and only served as a fail-safe in case of failure in the mast-arm.

Figure 3.10. Test Specimen

3.2.2 Loading Methodology

The calculation for loads for experimental testing was performed in a similar fashion to the process performed within the University of Wyoming research, see Section 2.4.3.3. Equation 3.8 gives the equation for bending stress, while Equation 3.9 is reworked to solve for force instead of the bending stress.

$$\sigma = \frac{Mc}{I} \quad \text{Eq. 3.8}$$

$$F = \frac{\sigma I}{L_{arm} c} \quad \text{Eq. 3.9}$$

where, c equals r_o, the outer radius of the mast-arm, and L_{arm} is the moment arm. For the SA7P8.5 test specimen, $r_o = 9$ in. (22.86 cm), and $L_{arm} = 83.24$ in. (211.43 cm).

The $\sigma_{desired}$ is the desired stress, which aligned with the CAFT of the AASTHO detail categories. These stresses and the calculated forces are shown in Table 3.12, while the testing plan is shown in Table 3.13.

Table 3.12. Experimental Testing Forces

AASHTO Detail Category	CAFT, ksi (MPa)	Bending Force, k (kN)
A	24 (165.47)	21.57 (95.95)
B	16 (110.32)	14.38 (63.97)
B'/C'	12 (82.74)	10.79 (48)
C	10 (68.95)	8.99 (39.99)
D	7 (48.26)	6.29 (27.98)
E	4.5 (31.03)	4.04 (17.97)
E'	2.6 (17.93)	2.34 (10.41)
ET	1.2 (8.27)	1.08 (4.80)
K_2	1 (6.89)	0.90 (4)

Table 3.13. Fatigue Testing Plan

Specimen Number	Desired Stress Range, ksi (MPa)
1	10 (68.95)
2	To Be Determined
3	To Be Determined
4	To Be Determined
5	To Be Determined
6	To Be Determined

While the desired stress ranges for the other five specimens are yet to be determined, 10 ksi (68.95 MPa) was chosen to be the highest stress range tested. The tests for Specimen 1 were performed at a rate of 0.5 Hz and the fatigue loads were applied via a sinusoidal forcing function. It is possible that future specimens will have a higher rate applied to them, but that will be determined based on the response of Specimen 1.

3.2.3 Data Acquisition

To collect data from the test specimens, three approaches were utilized. The first was to obtain data from the actuator itself, through a load cell that collected force and deflection data, which could be translated to stress/strain through hand-calculations. The second method was through the application of strain gauges near each connection detail: box connection, arm socket connection, and baseplate socket connection. The data from each of the first two methods could be compared to finite element model output. The final data acquisition method was through the utilization of the Digital Image Correlation (DIC) software, VIC-3D-V7. This method will not be discussed in detail in this paper as it is the focus of another research.

Hand-Calculations from the Load Cell

The bending stress equation, Equation 3.10, was utilized to convert the force data obtained from the load cell of the actuator to stresses at the location of each strain gauge/rosette on the specimen.

$$\sigma = \frac{My}{I} \qquad \text{Eq. 3.10}$$

where F is the applied force over the course of testing, L is the moment arm to each strain gauge, y is the centroid, and I is the moment of inertia of either the arm or the pole depending on the gauge examined.

To determine the stress for the box and the arm, the horizonal moment arm from the load point to the strain gauge/rosette was utilized, while the vertical moment arm from the floor to the strain gauge was used for the baseplate.

Strain Gauge Implementation

Strain gauges were applied to verify the outputs from the actuator and DIC and compare to the finite element models. Labview was utilized to collect the data from the strain gauges. A strain gauge rosette was applied near the box connection in an 0-45-90 configuration to obtain the most accurate reading near the detail of interest of the project. Near the baseplate and arm socket connections only a singular strain gauge was utilized as they were secondary connection details of interest. Figure 3.11 through Figure 3.13 display the location of each strain gauge/rosette.

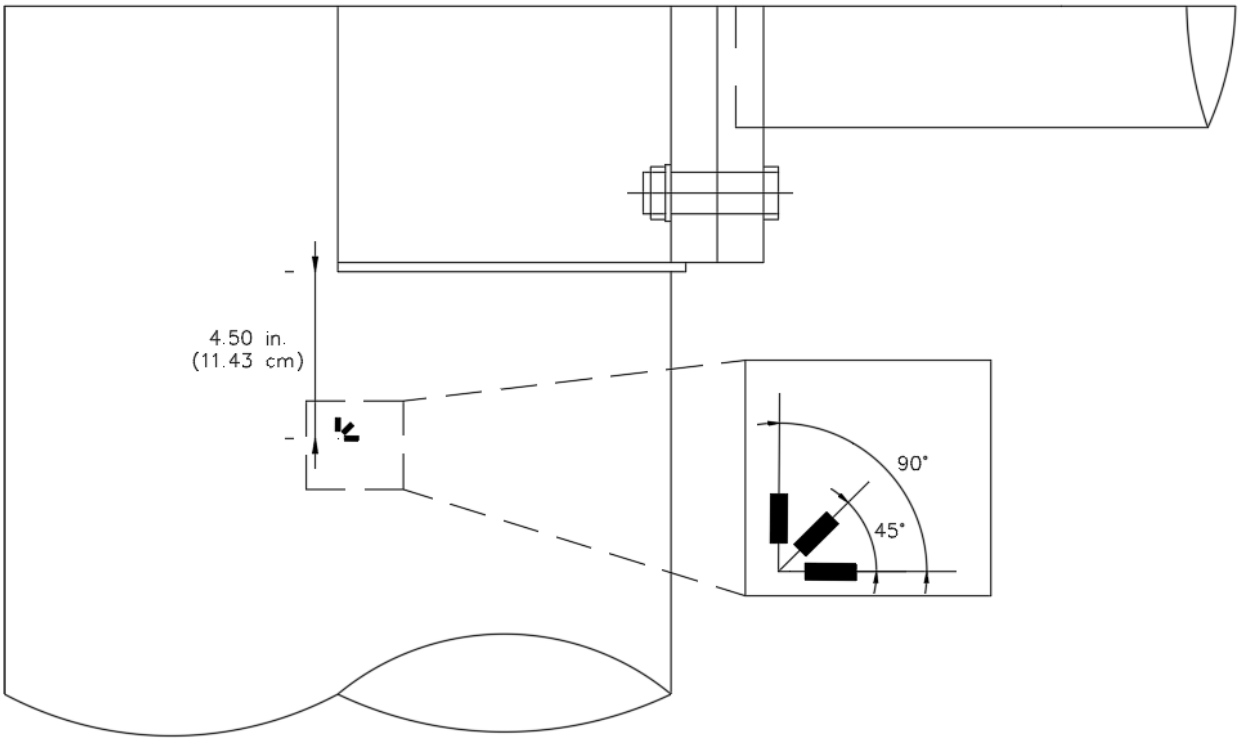

Figure 3.11. Box Connection Strain Gauge Rosette

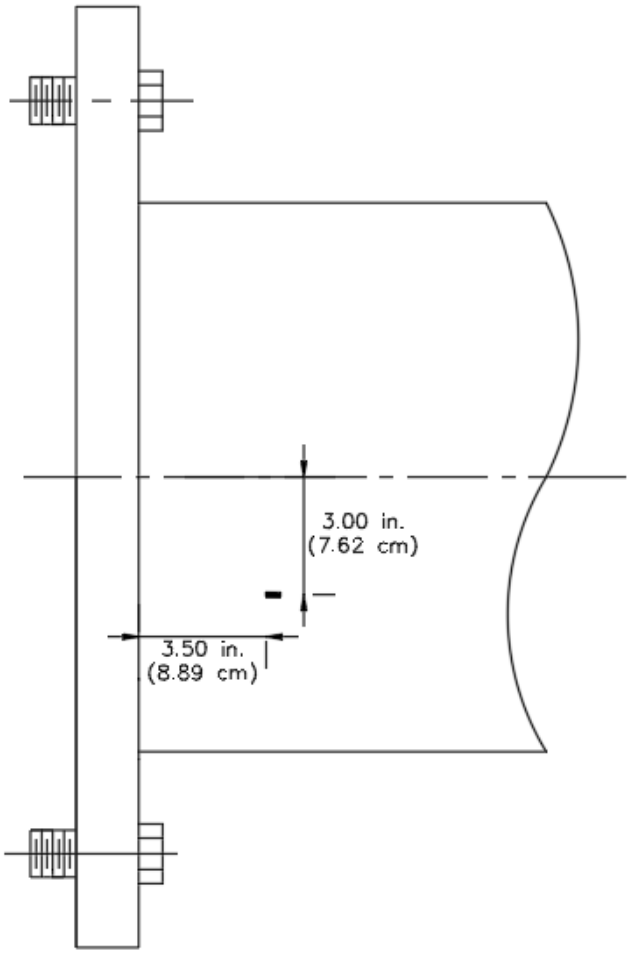

Figure 3.12. Arm Strain Gauge

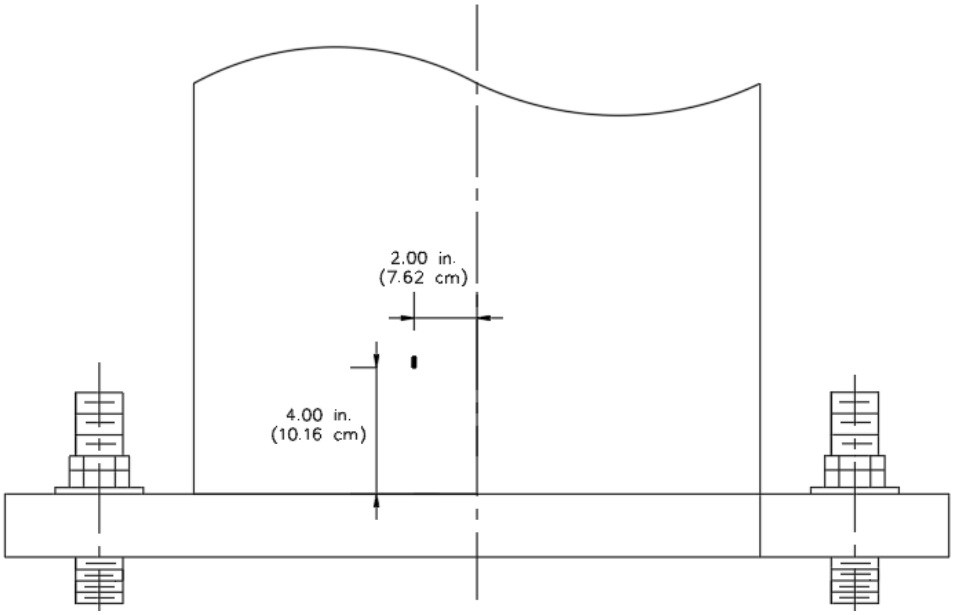

Figure 3.13. Baseplate Strain Gauge

Equations 3.11 through 3.14 were utilized to convert the strain output from the rosette by the box connection into a single principal strain and later principal stress value.

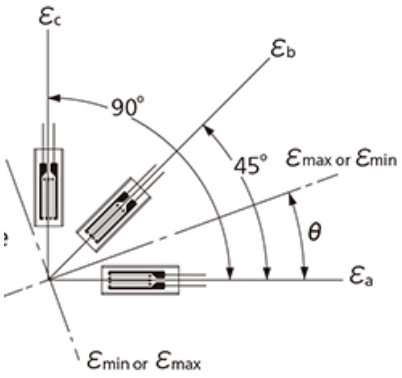

Figure 3.14. 0-45-90 Strain Gauge Rosette

-ة سي -ز Eq. 3.11

-ت سي -ز Eq. 3.12

-ج ة ز سي° -ة ط ط -ت ط ط شي ج -ة ط ي -ت ٠ ط -ت ط ي -ت ٠) Eq. 3.13

where ε_{max} is the max principal strain. To calculate max principal stress instead of strain, Equation 3.14 is used instead.

$$\sigma_{max} = \frac{E}{1-\nu^2}\left(\varepsilon_{max} + \nu\varepsilon_{min}\right) \quad \text{Eq. 3.14}$$

For all specimens, elastic modulus, E = 29,000 ksi for steel (200 GPa) and [illegible] To convert the strains obtained from the arm and baseplate strain gauges, the results were multiplied by the elastic modulus.

Digital Image Correlation (DIC)

VIC-3D-V7 was utilized to obtain digital images showing the strain profile around the expected hot spot locations of the box, mast-arm socket, and baseplate socket connections. Two cameras were utilized to obtain a 3D picture of each location, 2D pictures were also obtained using one camera. Each 3D set-up for Specimen #1 is shown in Figure 3.15.

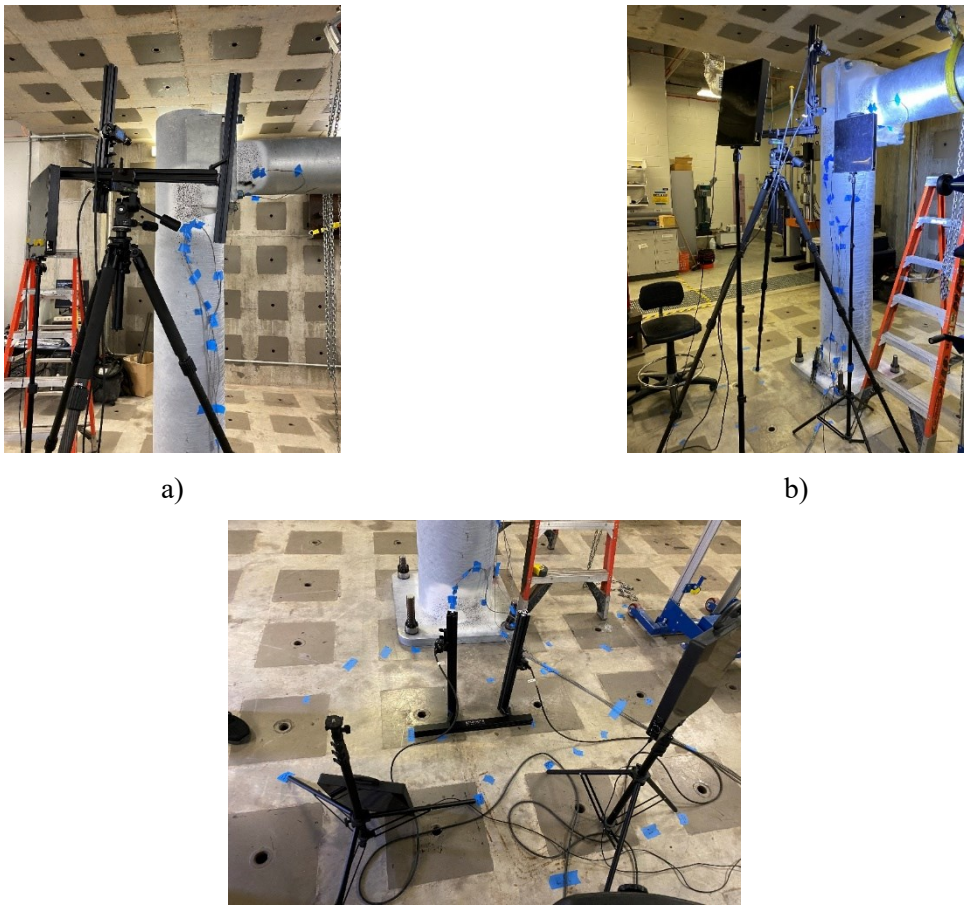

a) b)

c)

Figure 3.15. 3D DIC Set-up for Specimen #1: a) Box; b) Mast-Arm; c) Baseplate

To ensure repeatability of each set-up, as cameras were taken down between tests, marks were made on the ground dictating where the legs of the tripod would go, camera location was measured, and angles were measured for both the cameras and the bars supporting the cameras.

Once the system was set up, it was calibrated on the unloaded specimen. After the cameras had been calibrated, pictures were taken by applying the cyclic load at 0.1 Hz for 5 cycles. This was performed after each 10,000 cycles were applied to the specimen. Strain data could then be obtained from these pictures.

Chapter 4: Results

4.1 Finite Element Modeling Results

Twenty-one full-sized COSS finite element models were created and analyzed to determine trends based on their geometry and other design parameters. Of these, nine models consisted of the 1981 tapered pole and mast-arm design, nine were the 2015 straight pole and mast-arm design, and three had the modern ring-stiffened box connection instead of the standard gusseted box connection. The three with the ring-stiffened box also had a straight pole and mast-arms.

The 1981 tapered pole and mast-arm design experienced the highest stresses for both natural wind (NW) and truck-induced wind gusts plus galloping (T+G) loadings. Stresses decreased when the structure is detailed according to the 2015 straight pole and mast-arm design and decreased even more when a ring-stiffened box connection is utilized instead of a gusseted box connection. The cause for this stress decrease is discussed in greater detail later, however the largest contributors were increasing the thickness of the pole and mast-arm and the utilization of the ring-stiffened box connection.

Section 4.1.1 overviews the effects of structure type, i.e., tapered versus straight poles and gusseted versus ring-stiffened box connection. Section 4.1.2 discusses the effect of changing both the design specific geometry, i.e., member sizes and dimensions, as well as the site-specific geometry of the structure, i.e. sign size, pole height, and mast-arm length. Appendix D comprises of all results from the finite element analysis, including tables of the hot spot analysis results, S-N curves, paths utilized to determine hot spot stresses, and pictures of von Mises stress distributions for each model.

4.1.1 Effect of the Type of Structure

Natural Wind Loading

The locations of the hot spots were consistent for both the tapered and straight pole models. These hot spots were located on the load facing side of the bottom mast-arm, the front of the pole by the baseplate, and the bottom corner of the front of the bottom box connection. The front side

of the model is designated as the load facing side of the structure, for natural wind loading. Figure 4.1 shows the hot spot locations for tD7S and sD6S, respectively.

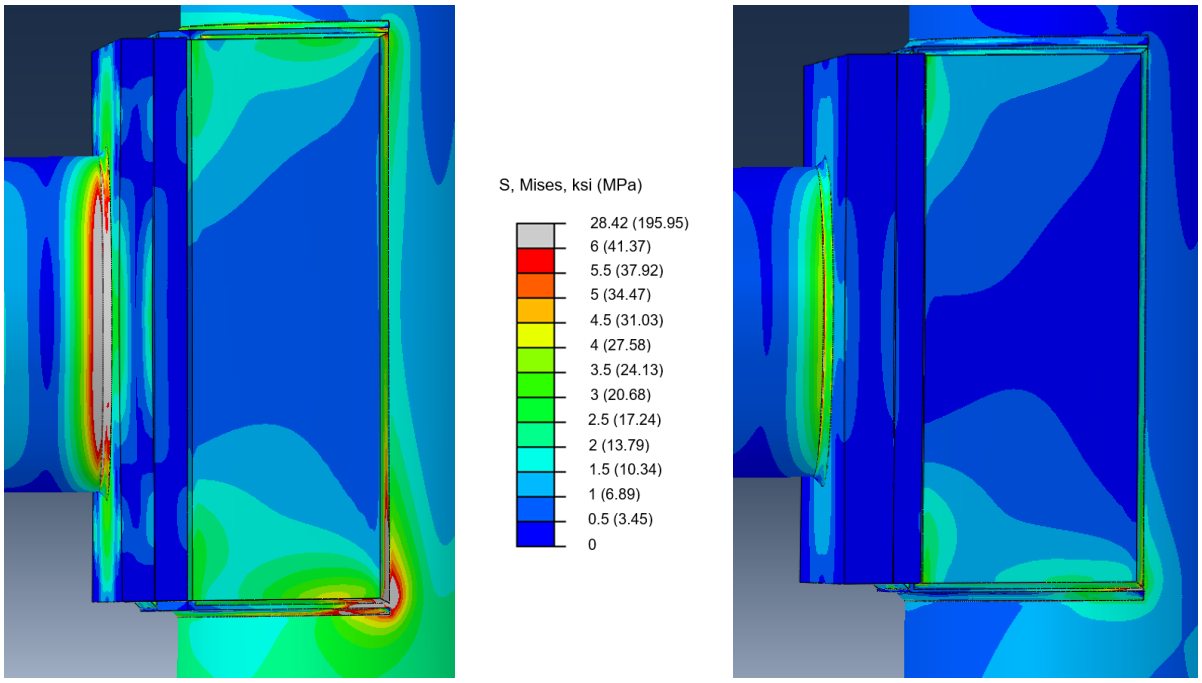

a) b)

Figure 4.1. Box and Arm Hot Spot Locations for NW: a) tD7S and b) sD6S

While hot spot locations for the mast-arm and baseplate were the same for the ring-stiffened box connection models, the location of the hot spot by the box changed. There are two locations that are possible points for the box hot spot for the ring-stiffened box connection models; the first is in the center of the front side-plate, along the weld that connects it to the flange of the box, and the second is below the ring and in line with the edge of the side-plate. Figure 4.2 shows the locations of these hot spots for the small sign model, rD7S. As the hot spot occurring by the side-plate to flange weld was larger than that below the ring, it was utilized as the hot spot stress for the box connection of the ring-stiffened structures.

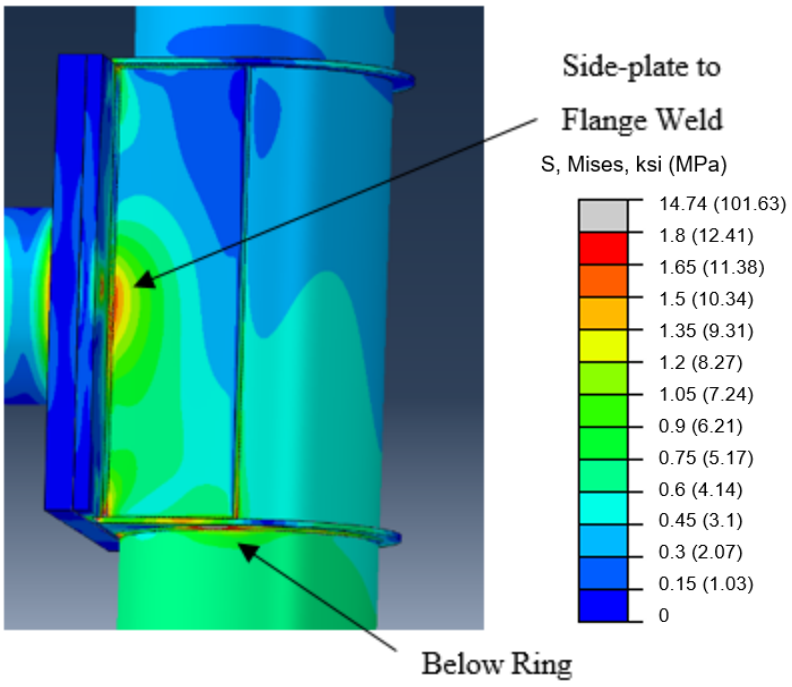

Figure 4.2. Box Hot Spot Locations on rD7S, NW

It is difficult to determine which of the two locations is the more important one based solely on hot spot stress analysis, as all measured hot spot stresses are compared to a Category C S-N curve, where the CAFT is 10 ksi (69 MPa). However, when looking at nominal stress to compare the locations, each has a different stress category and CAFT. The side-plate-to-flange weld is categorized as Category E', CAFT =2.6 ksi (18 MPa), while underneath the ring is Category E, CAFT = 4.5 ksi (31 MPa). While the difference in hot spot stress values does point to the side-plate-to-flange weld as the more critical of the two details, more focused research should be performed in the future if failure in ring-stiffened box connections at either location becomes a problem.

The utilization of a straight pole and baseplate as well as a ring-stiffened box connection aided in decreasing hot spot stresses near the box connection, as well as near the mast-arm and baseplate socket connections. There was an average stress decrease at the box connection of 74% from tapered to ring-stiffened models and 35% from straight to ring-stiffened models, for the Design #6/7 models. At the mast-arm socket connection, there was an average stress decrease of 55% between the tapered and ring-stiffened models and 20% between the straight and ring-stiffened models. The average decreases were 52% and 34% respectively at the baseplate socket

connection. The percentage of stress decrease between models was computed using Equation 4.1. These values are shown tabulated in Appendix D.

$$\text{Eq. 4.1}$$

where $\sigma_{tapered\ or\ straight}$ is the stress at the location desired on the tapered or straight model, depending on which is being examined, and $\sigma_{ring\text{-}stiffened}$ is the stress at the location desired on the ring-stiffened model.

The peak hot spot stress was at the box connection for majority of the tapered pole models and moved to be primarily at the mast-arm socket connection for the straight pole and ring-stiffened box connection models. Most of the measured stresses for the ring-stiffened box connection and many of the straight pole structures also fell within infinite life for Category C, decreasing the probability of failure by those connection details.

Table 4.1 has been organized based on site-specific geometry (sign size, mast-arm length, and pole height) to highlight how changing from the tapered tube design to the straight tube or ring-stiffened box connection designs aid in decreasing the stresses experienced at all three connection details examined. This is also shown in Figures 4.3 through 4.5, which display S-N Curves for all Design #6/7 models, organized by site-specific geometry group. When the stresses are below the CAFT of 10 ksi (69 MPa), for Category C, the detail is likely to have better performance and a decreased chance for crack formation and failure.

Table 4.1. NW Hot Spot Stress Results

	Hot Spot Stress, ksi (MPa)		
Model	Box	Arm	Baseplate
tD1S	10.44 (71.96)	9.19 (63.34)	3.64 (25.10)
sD1S	3.26 (22.48)	5.55 (38.26)	3.39 (23.39)
tD1M	24.53 (169.12)	18.86 (130.06)	10.33 (71.22)
sD1M	8.17 (56.30)	11.71 (80.73)	7.56 (52.13)
tD1L	36.17 (249.38)	28.38 (195.66)	14.86 (102.42)
sD1L	12.00 (82.71)	17.14 (118.16)	9.30 (64.14)
tD3S	12.50 (86.17)	12.21 (84.22)	10.64 (73.35)
sD3S	4.29 (29.60)	6.93 (47.78)	8.38 (57.80)
tD3M	27.65 (190.65)	25.40 (175.15)	12.68 (87.46)
sD3M	9.73 (67.09)	17.64 (121.59)	9.97 (68.73)
tD3L	28.37 (195.63)	27.33 (188.44)	15.45 (106.53)
sD3L	10.69 (73.68)	18.10 (124.80)	12.19 (84.07)
tD7S	8.11 (55.89)	8.55 (58.93)	4.64 (31.97)
sD6S	2.91 (20.07)	4.21 (29.00)	2.84 (19.57)
rD7S	1.73 (11.93)	3.16 (21.78)	2.09 (14.43)
tD7M	17.19 (118.50)	18.37 (126.63)	11.29 (77.82)
sD6M	5.53 (38.13)	8.69 (59.95)	9.23 (63.66)
rD7M	4.06 (28.01)	7.25 (50.01)	5.23 (36.04)
tD7L	17.85 (123.09)	18.80 (129.60)	13.39 (92.34)
sD6L	9.61 (66.23)	13.79 (95.05)	10.21 (70.43)
rD7L	6.06 (41.76)	11.15 (76.87)	7.00 (48.26)

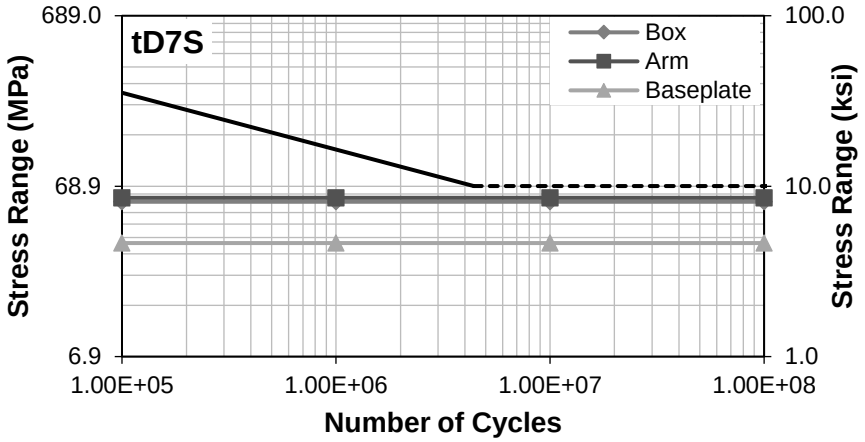

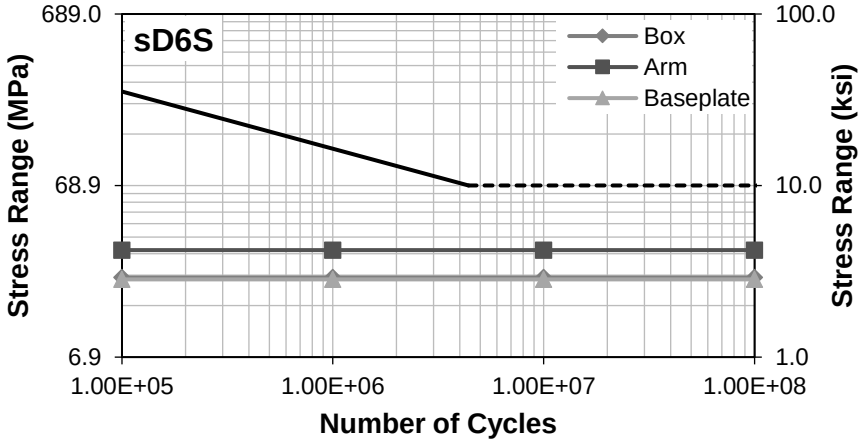

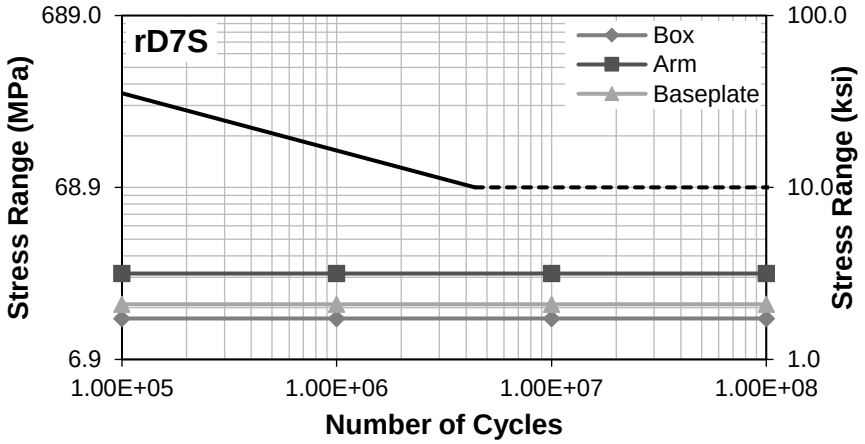

Figure 4.3. S-N Curves for Small Geometry Design #6/7 Models, NW

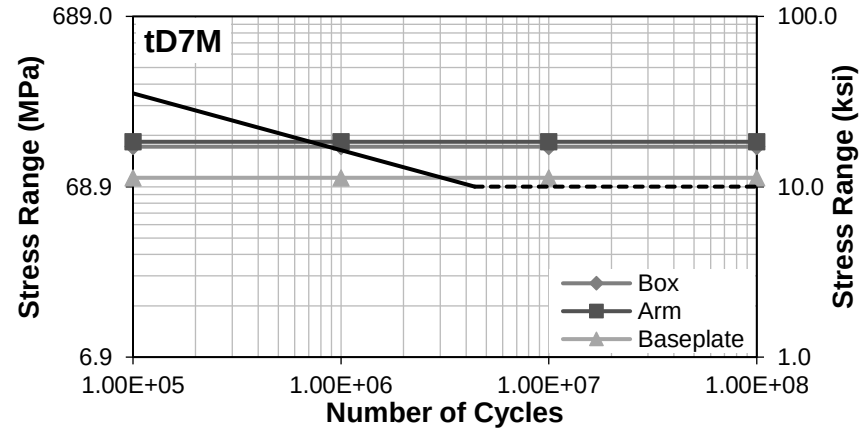

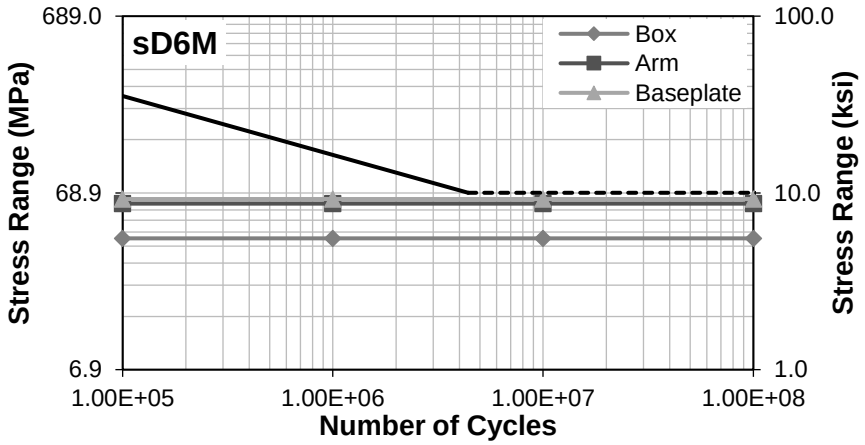

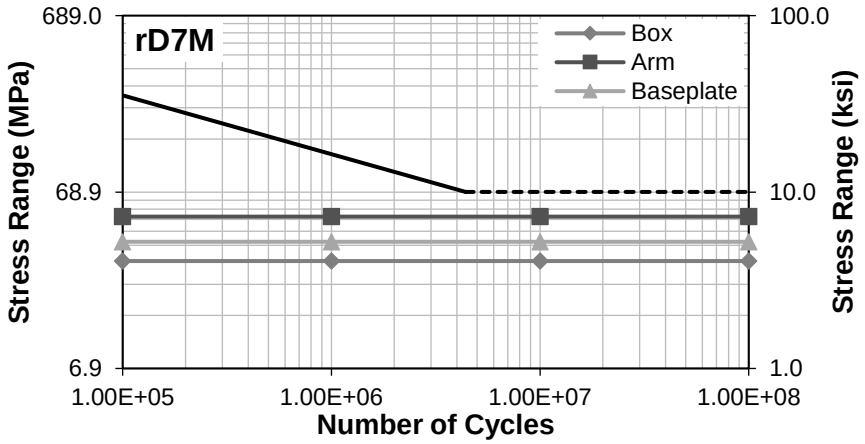

Figure 4.4. S-N Curves for Medium Geometry Design #6/7 Models, NW

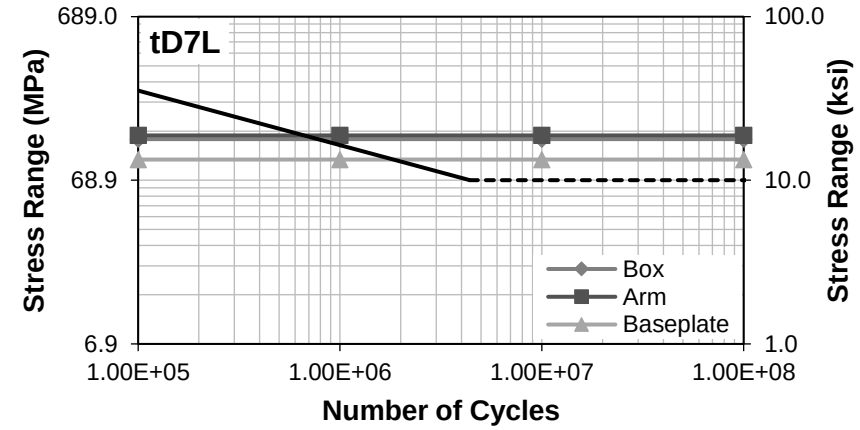

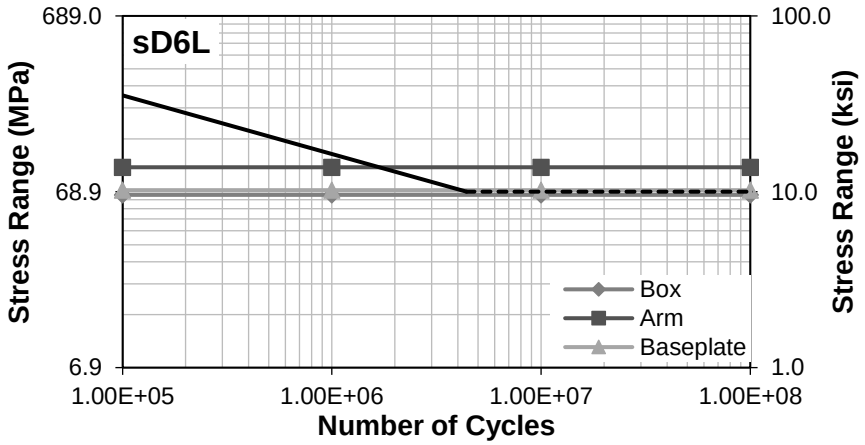

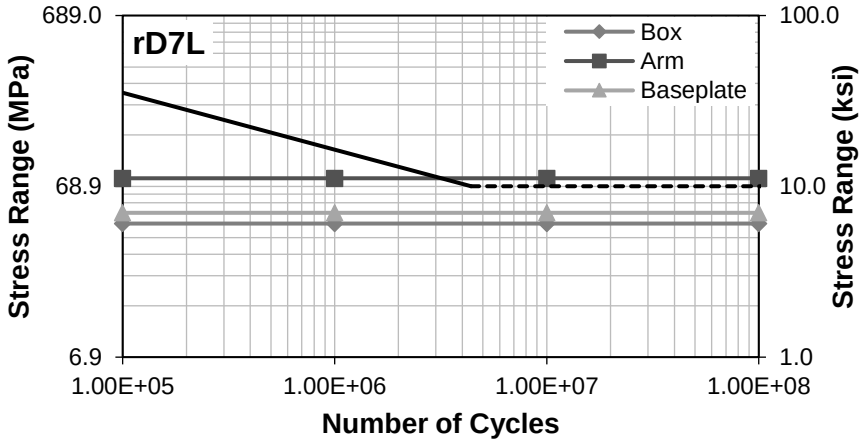

Figure 4.5. S-N Curves for Large Geometry Design #6/7 Models, NW

An in-depth examination of the effect of different variables is performed in Section 4.1.2 for both site-specific geometry and design specific geometry.

Truck-Induced plus Galloping Loading

Unlike natural wind loading, the hot spot locations for all three types of structures were not the same for truck-induced wind gusts plus galloping (T+G) loading. The hot spot location for the mast-arm is located on the underside of the bottom mast-arm, while the location for the box is underneath the bottom gusset plate/ring on the bottom box. The hot spot for the baseplate socket connection is located on the side of the pole underneath the mast-arms. Figure 4.6 display the hot spot location for the box connection for tD7S, sD6S, and rD7S.

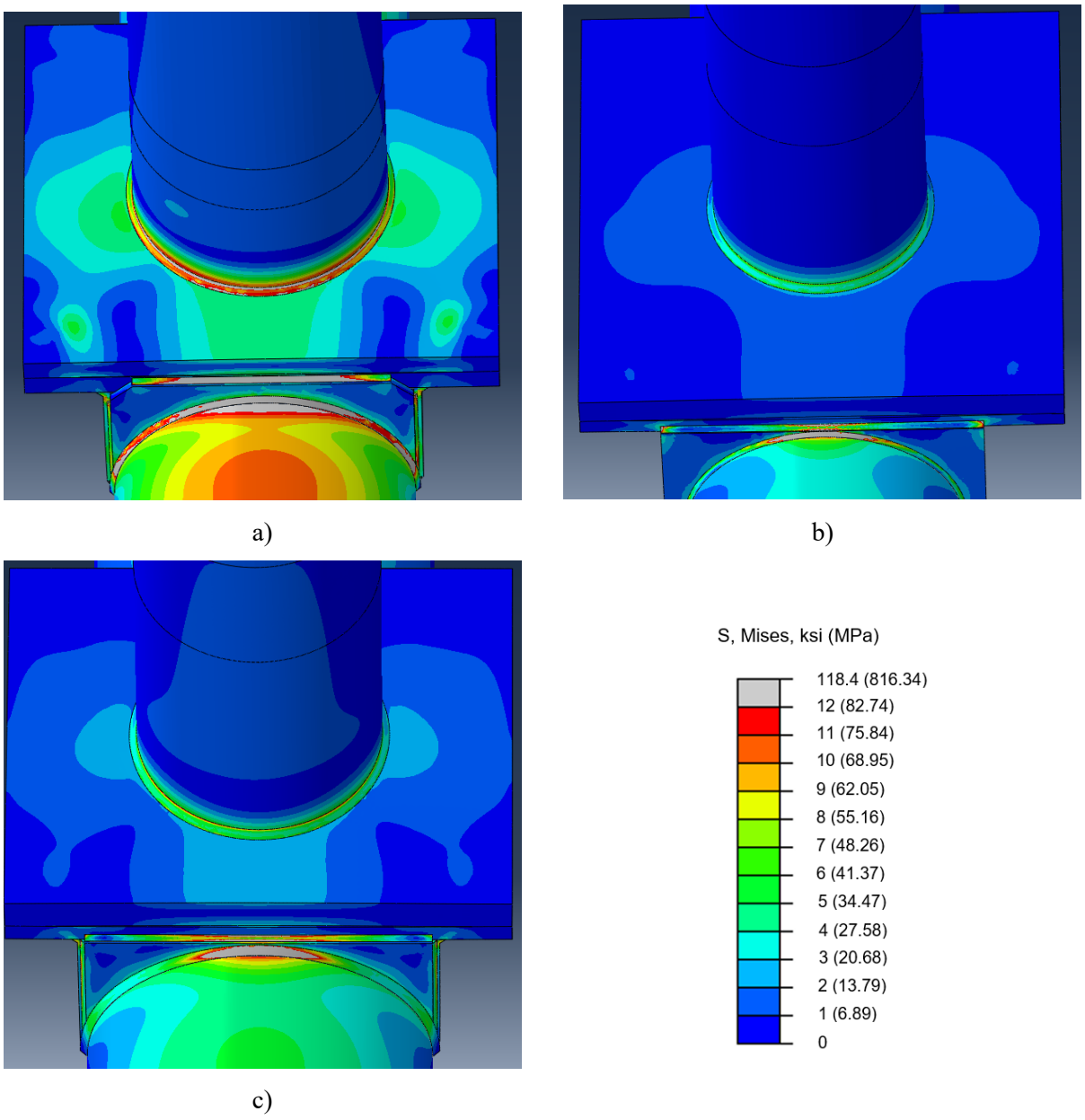

Figure 4.6. Box Hot Spot Locations for T+G: a) tD7S; b) sD6S; c) rD7S

As was the case with NW loading, the box connection experienced the highest hot spot stresses for majority of the tapered pole models. For the straight pole and ring-stiffened box connection models, it was more likely that the baseplate socket connection would experience the highest hot spot stresses instead of the box connection. These results can be seen in Table 4.2, with Figures 4.7 through 4.9, showing the S-N Curves for all Design #6/7 models, organized by site-specific geometry group.

Table 4.2. T+G Hot Spot Stress Results

	Hot Spot Stress, ksi (MPa)		
Model	Box	Arm	Baseplate
tD1S	28.25 (194.77)	16.06 (110.73)	14.84 (102.32)
sD1S	13.53 (93.29)	8.09 (55.78)	13.48 (92.95)
tD1M	51.49 (354.99)	32.03 (220.83)	33.97 (234.24)
sD1M	25.01 (172.41)	11.94 (82.32)	25.39 (175.05)
tD1L	73.29 (505.30)	39.43 (271.85)	48.30 (333.01)
sD1L	35.34 (243.63)	21.65 (149.28)	30.56 (210.67)
tD3S	20.88 (143.93)	13.29 (91.60)	18.50 (127.53)
sD3S	13.71 (94.52)	10.93 (75.39)	16.03 (110.50)
tD3M	41.02 (282.85)	27.69 (190.91)	41.48 (285.97)
sD3M	29.42 (202.87)	20.46 (141.08)	34.96 (241.07)
tD3L	50.52 (348.35)	29.90 (206.17)	40.94 (282.27)
sD3L	29.34 (202.32)	20.49 (141.28)	35.39 (244.03)
tD7S	17.97 (123.90)	12.98 (89.50)	19.44 (134.01)
sD6S	12.02 (82.88)	6.60 (45.47)	11.37 (78.43)
rD7S	8.83 (60.88)	5.06 (34.87)	9.42 (64.97)
tD7M	35.98 (248.10)	24.26 (167.23)	33.80 (233.02)
sD6M	20.97 (144.58)	11.52 (79.45)	22.12 (152.51)
rD7M	7.83 (54.01)	5.72 (39.40)	11.02 (75.99)
tD7L	45.03 (310.50)	26.72 (184.21)	32.86 (226.53)
sD6L	32.95 (227.18)	18.99 (130.91)	35.12 (242.16)
rD7L	13.21 (91.06)	7.29 (50.30)	14.25 (98.27)

The utilization of the ring-stiffened box also aided in decreasing the stresses experienced at the box with a 67% average stress decrease between the tapered and ring-stiffened Design #6/7 models and a 50% average stress decrease between the straight and ring-stiffened models.

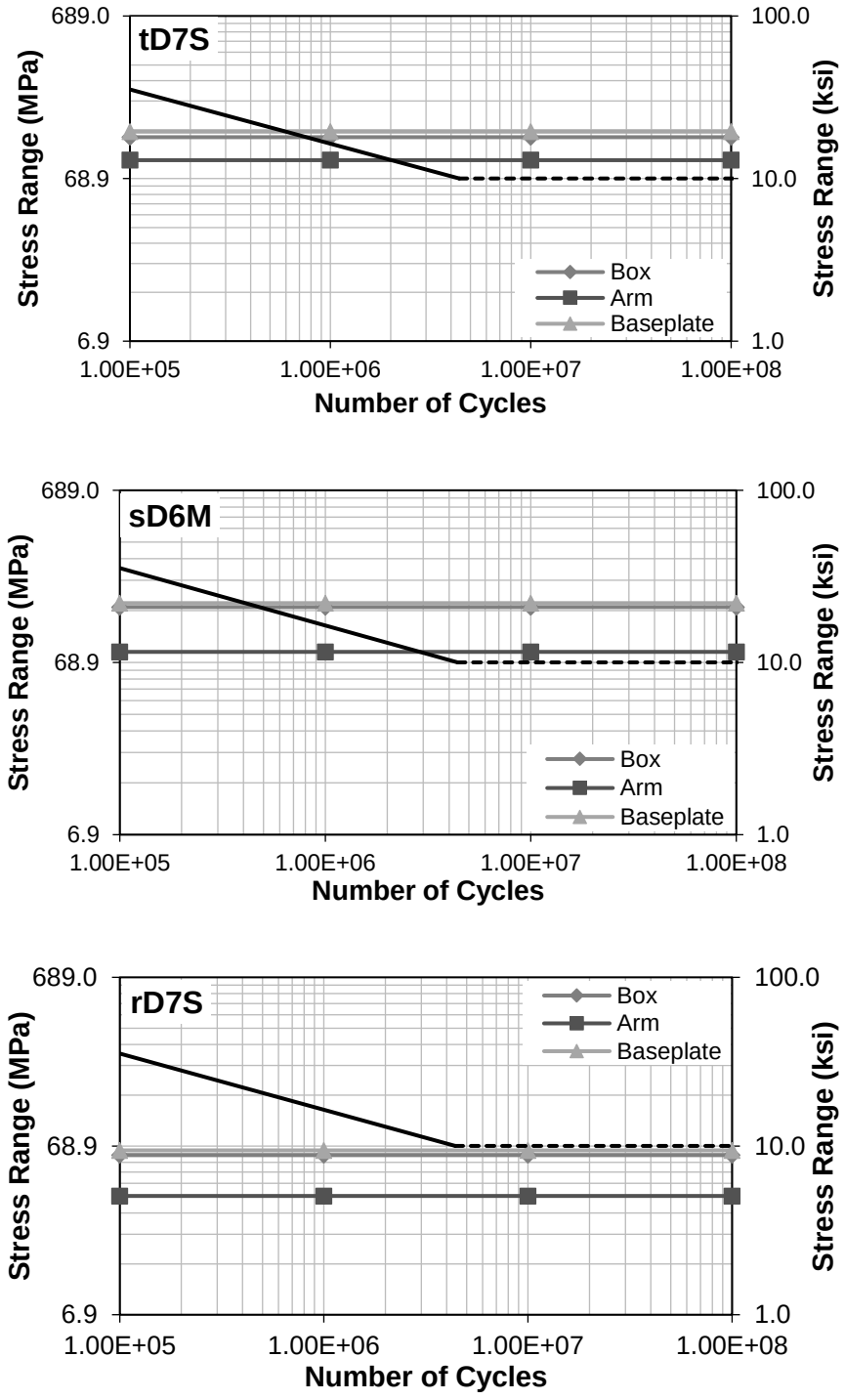

Figure 4.7. S-N Curves for Small Geometry Design #6/7 Models, T+G

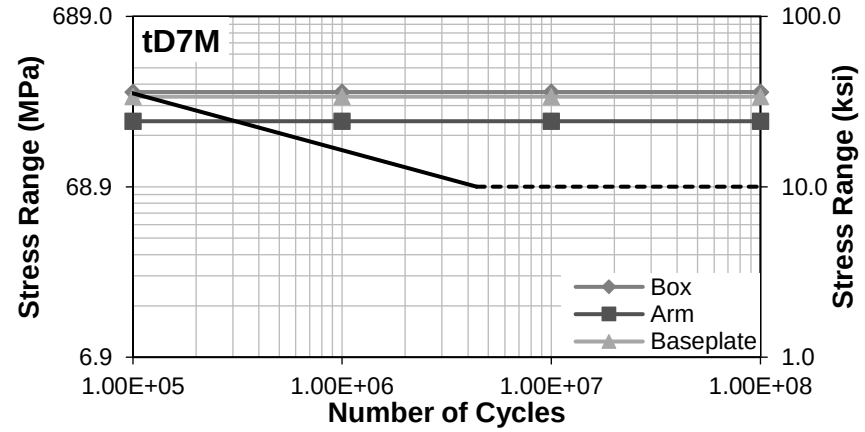

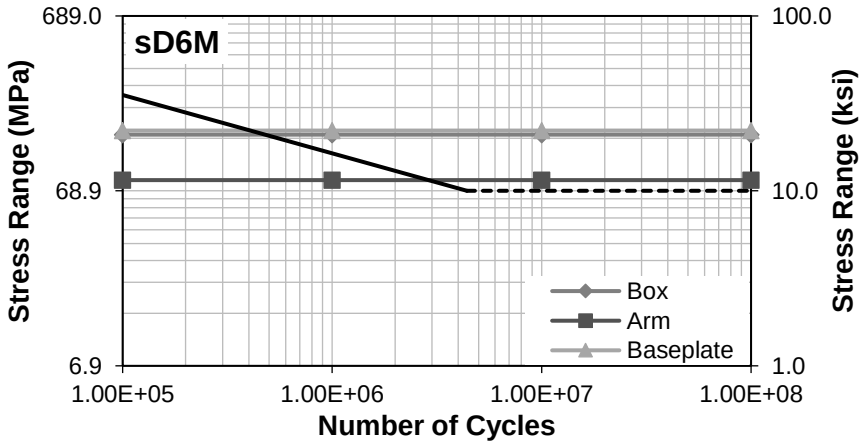

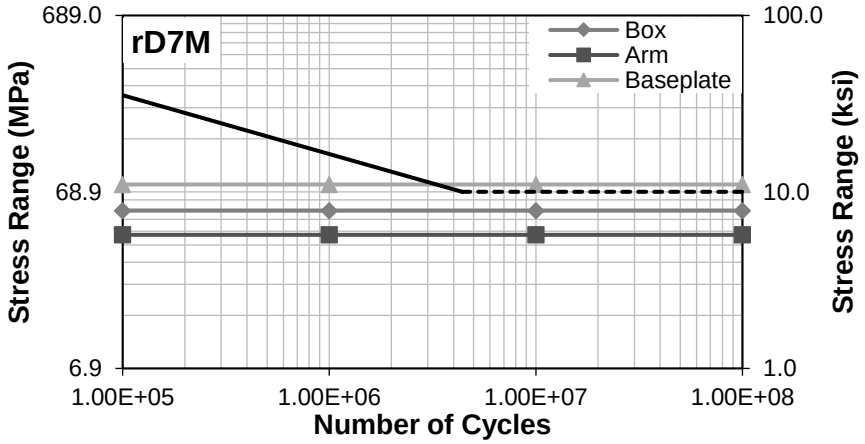

Figure 4.8. S-N Curves for Medium Geometry Design #6/7 Models, T+G

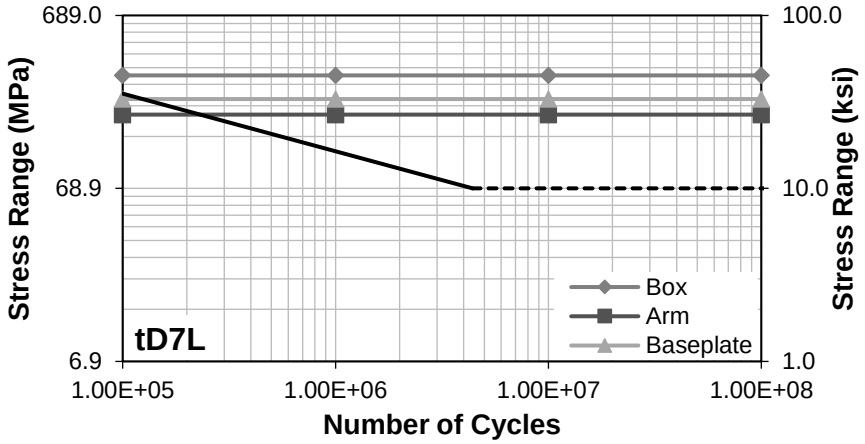

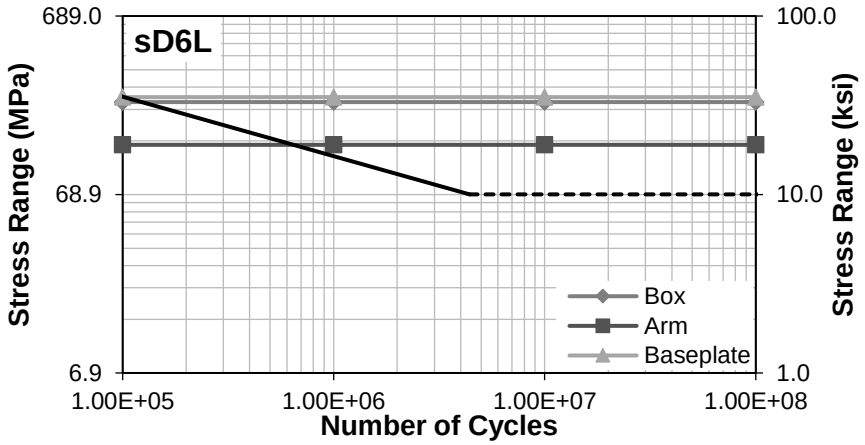

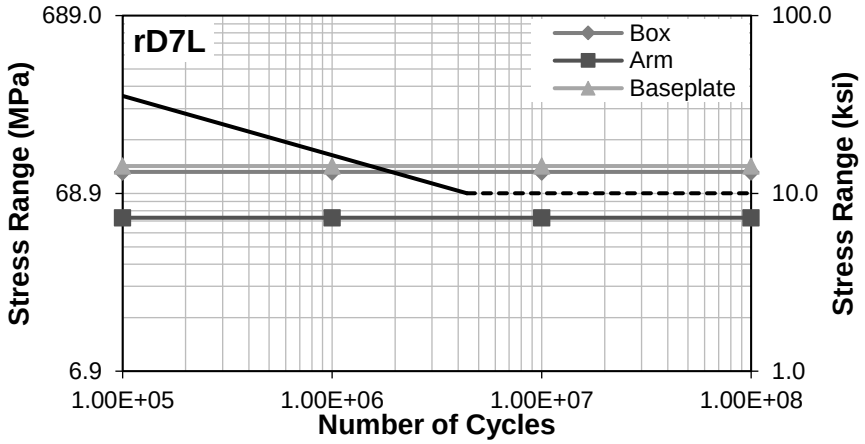

Figure 4.9. S-N Curves for Large Geometry Design #6/7 Models, T+G

An in-depth examination of the effect of different variables is performed in Section 4.1.2 for both site-specific geometry and design specific geometry.

4.1.2 Geometry Trends

The other aspect analyzed within the finite element models, was the effect of both the site-specific geometry parameters (sign size, arm length, and pole height), along with the effect of design specific parameters (member geometry). To examine the effects of changing the general parameters the models were analyzed within their respective design groups, to minimize the effect that different thicknesses and other design specific variables had on the analysis. When looking at the design specific parameters, models were analyzed within sign size groups, thus minimizing the effect of the general parameters on the analysis of those variables. The design groups will be noted as Design #1, #3, and #7, with the straight Design #6 models falling within the Design #7 group, as they are the largest of the straight pole designs. When values are the same, the order will be based on first the type of structure (tapered pole, straight pole, and then ring-stiffened box connection) and then within the types, in increasing design number order.

Natural Wind Loading

The effect of the arm length, sign length, and sign height in relation to the stresses generated due to natural wind loading are similar, as all three parameters showed a general increase in stresses as length or height increases within the design groups. However, for the Design #3 models, there is a slight decrease in stresses when examining the impact of arm length and sign length, shown in Figure 4.10b and Figure 4.11b. This decrease occurs between the last two Design #3 models and does not occur when looking at sign height, Figure 4.12b, as the order of these last two models switch, due to the short length model having a taller sign than the longer length model. This means it is likely that the sign height is the controlling variable when looking strictly at the site-specific geometry of the structure, with sign length and arm length serving to aid in increasing the stresses.

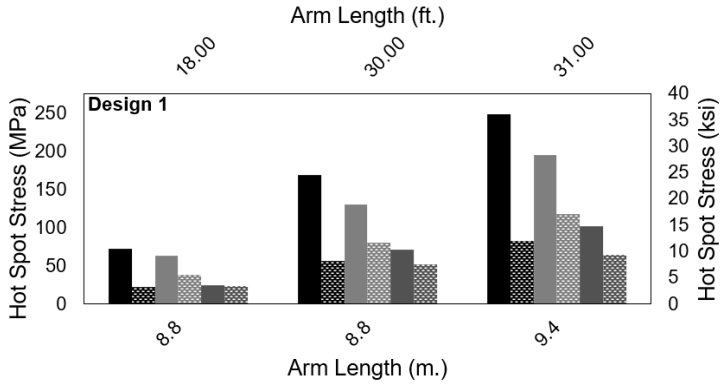

a)

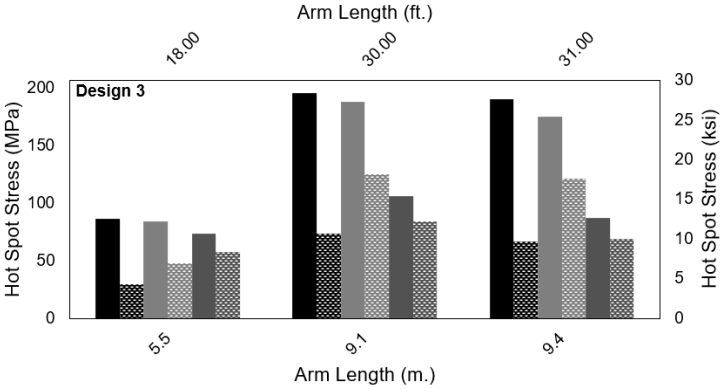

b)

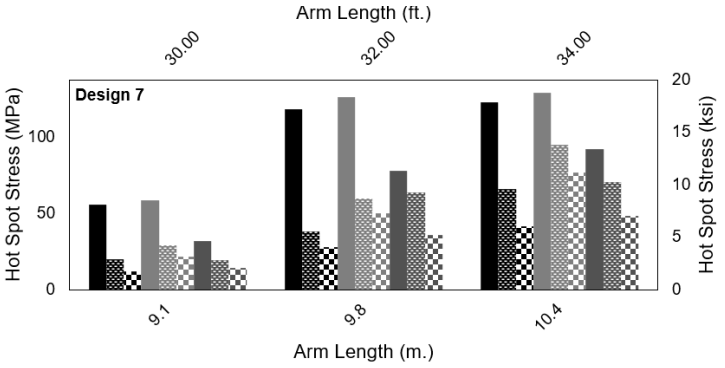

c)

d)

Figure 4.10. Arm Length Graphs, NW

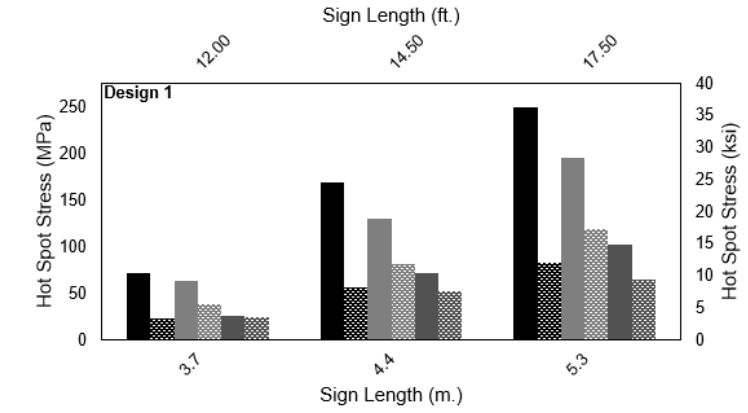

a)

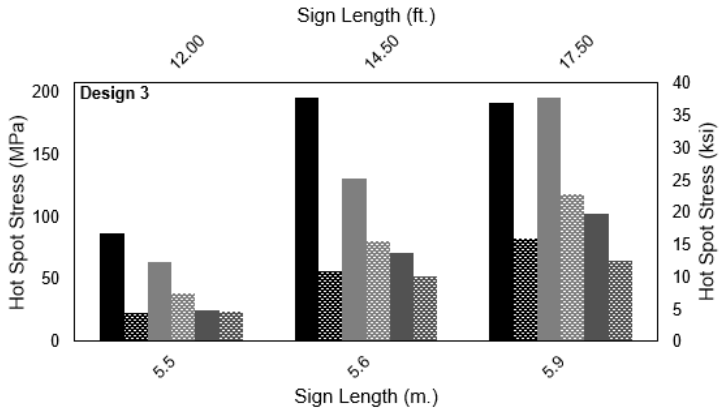

b)

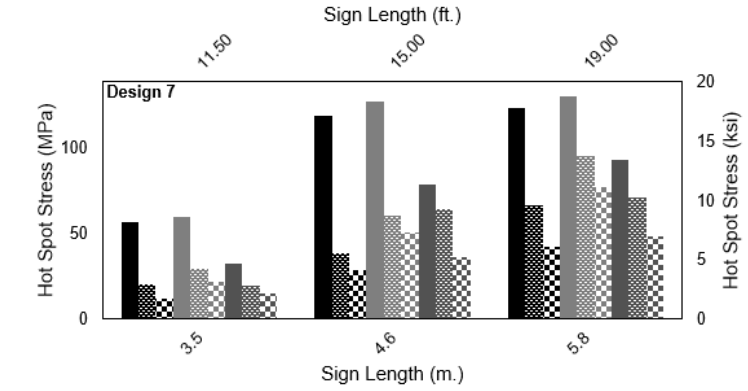

c)

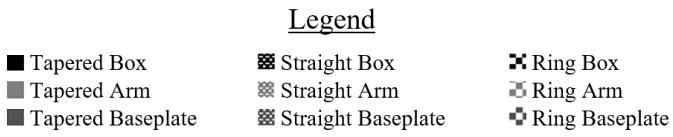

d)

Figure 4.11. Sign Length Graphs, NW

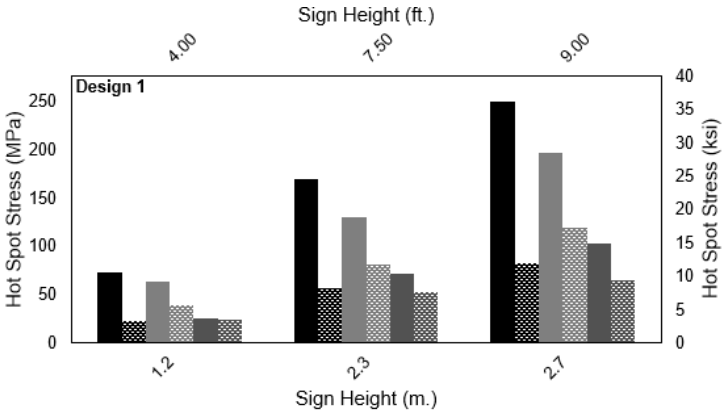

a)

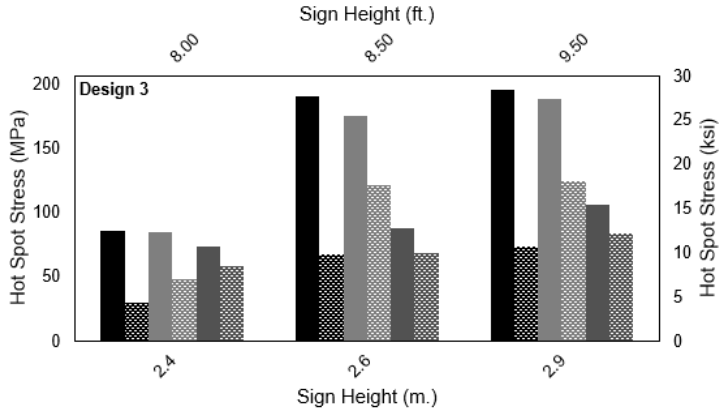

b)

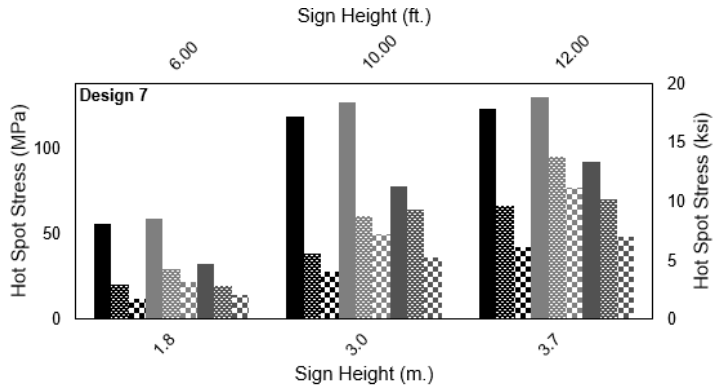

c)

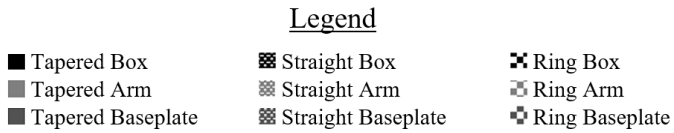

d)

Figure 4.12. Sign Height Graphs, NW

Changing pole height had minimal influence on the stresses, compared to the other three site-specific geometry parameters. There was no consistent positive or negative trend in the stresses for any of the design groups, and within both Design #1 and #3, there are two models with the same pole heights that experienced significant changes in stress. These are the last two models of Design #1 and the first two of Design #3. In both cases, while the pole height remains the same, the second model has a larger sign than the first, contributing to the discrepancy in stresses. If pole height had a more prominent effect on the stresses generated by NW loading, the difference in stresses would not be as large as it is.

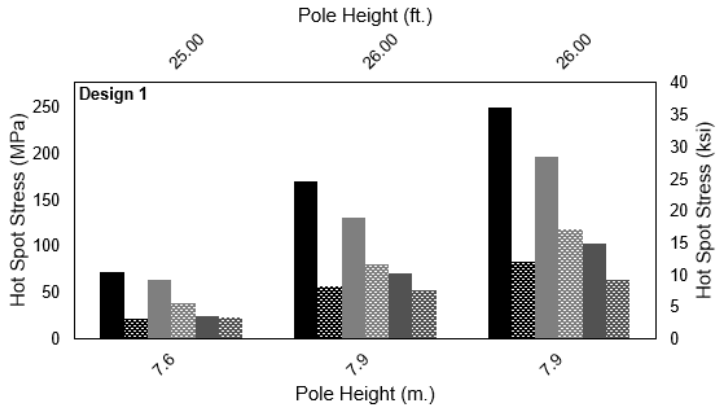

a)

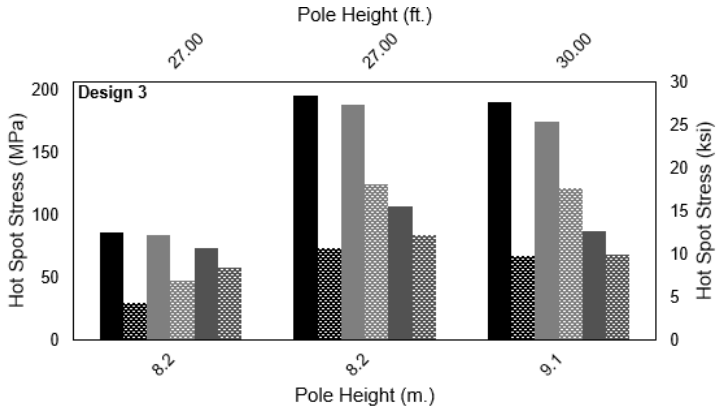

b)

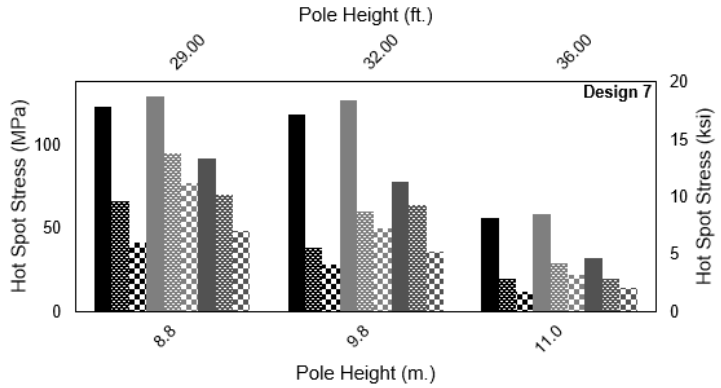

c)

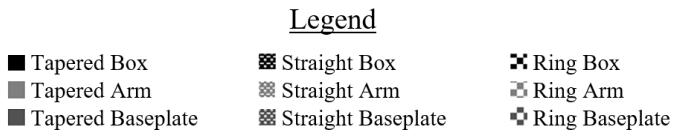

d)

Figure 4.13. Pole Height Graphs, NW

When the design specific parameters are focused on, the member thickness has the greatest effect on the stresses experienced. For the most part, as thickness of the mast-arm increased, stresses decreased (Figure 4.14). As the thickness of the mast-arm has a greater effect on the stresses experienced in the mast-arm socket connection than the box connection or the baseplate socket connection, only the stresses in the mast-arm are shown.

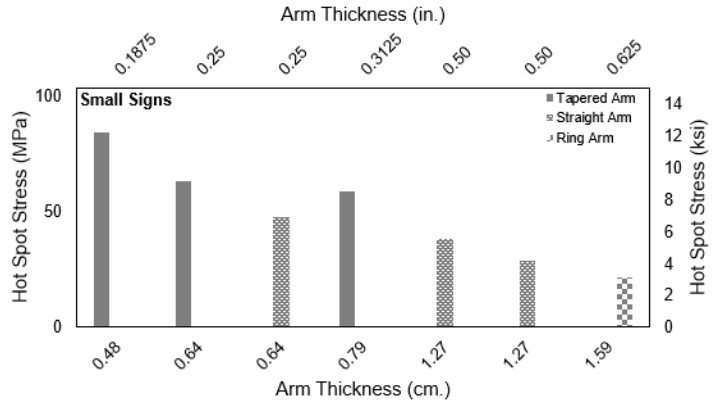

a)

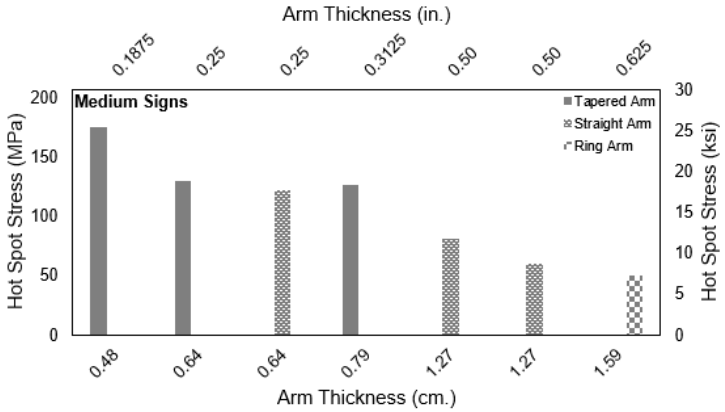

b)

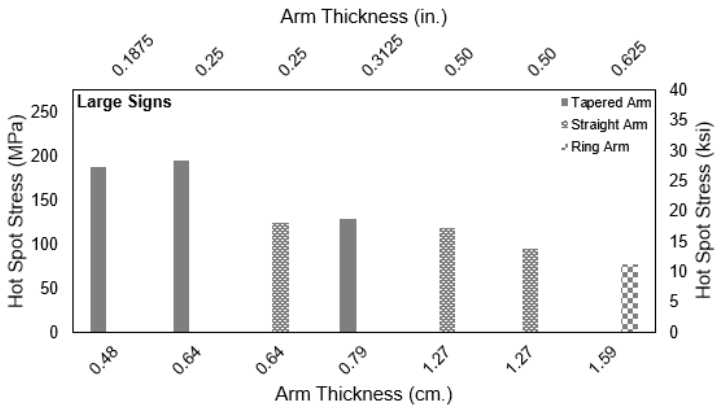

c)

Figure 4.14. Arm Thickness Graphs, NW

The thickness of the pole is also important; as the pole thickness increased, the stresses in the box connection and baseplate socket connection decreased. As was done for the mast-arm thickness, Figure 4.15 shows only the box and baseplate stresses as they are more affected by the change in the pole thickness.

The large increase in the stresses at the baseplate socket connection for both the straight and tapered of the small sign models is due to the geometry of the structure, namely the arm length and sign size, which caused the structure to experience a greater stress near the baseplate than other models. That model, D3S, has the shortest arm and largest sign of all the small models.

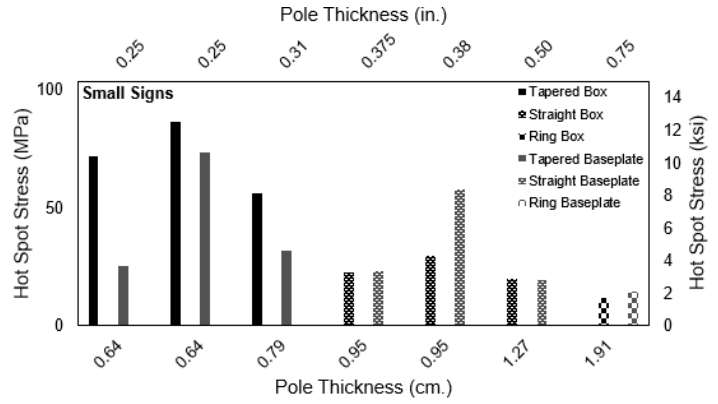

a)

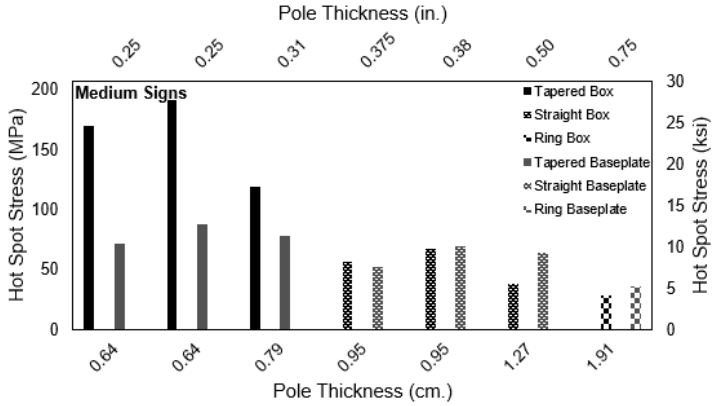

b)

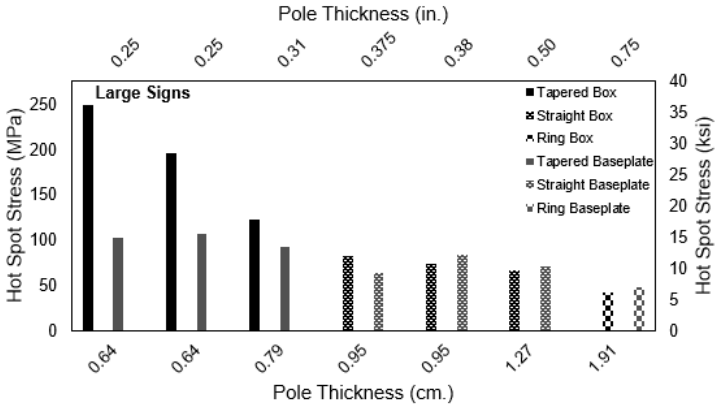

c)

Figure 4.15. Pole Thickness Graphs, NW

Increasing diameter also aided in decreasing stress, although to a lesser degree than increasing the thickness of the member. As was the case when looking at pole thickness, as the pole diameter increased, stresses decreased. Any reference to the pole diameter, refers to the pole diameter at the bottom box, Table 4.3, where the hot spot was located. Increasing the diameter was

more noteworthy for the tapered pole models, as their diameters at the bottom box varied widely and there were less differences within the straight pole and ring-stiffened box connection models. This relationship is shown in Figure 4.16.

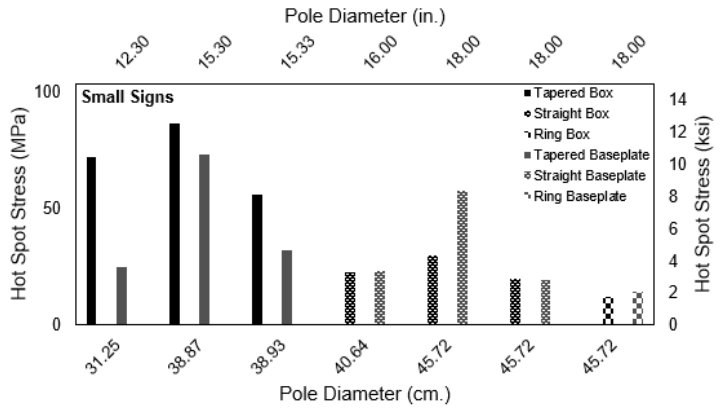

a)

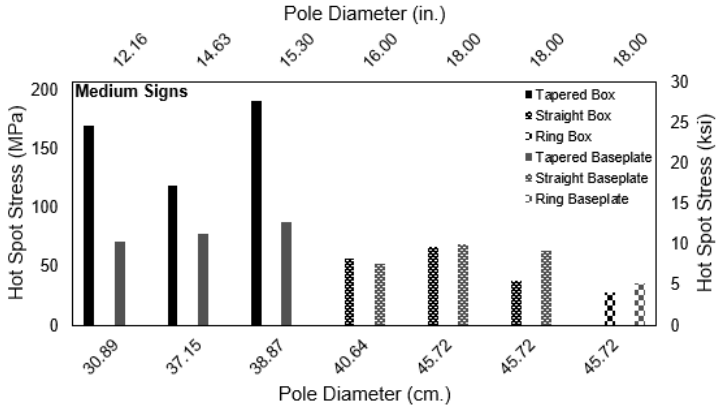

b)

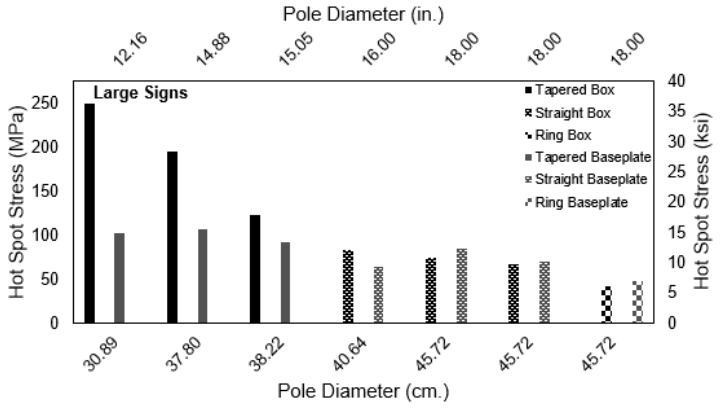

c)

Figure 4.16. Pole Diameter at Bottom Box Graphs, NW

Table 4.3. Pole Diameter at Bottom Box

Model	Pole Diameter at Bottom Box, in. (cm)
tD1S	12.30 (31.25)
tD3S	15.30 (38.87)
tD7S	15.33 (38.93)
tD1M	12.16 (30.89)
tD3M	15.30 (38.87)
tD7M	14.63 (37.15)
tD1L	12.16 (30.89)
tD3L	14.88 (37.80)
tD7L	15.05 (38.22)

To consider whether thickness or diameter was more impactful, diameter/thickness ratios were examined for both the pole and bottom mast-arm. For majority of the calculations, larger ratios correlated to smaller thicknesses and often smaller diameters.

The graphs related to the diameter/thickness ratios for the pole are shown in Figure 4.17, with Table 4.4 showing the diameter and thickness of each ratio value. Generally, the stresses for both the box and baseplate increased as the ratio increased. Arm stresses have been removed, as the diameter and thickness of the pole do not significantly affect stresses there.

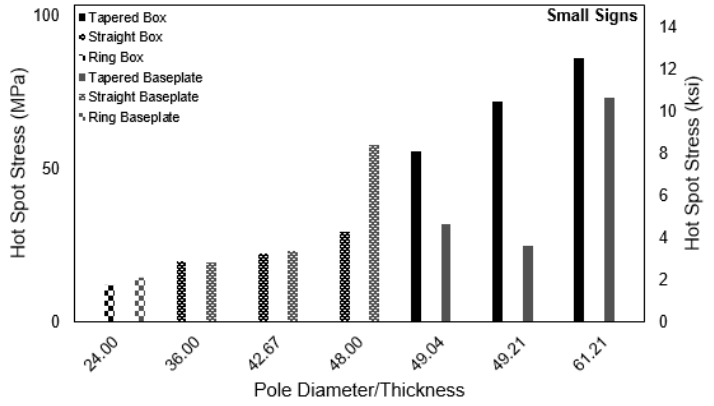

a)

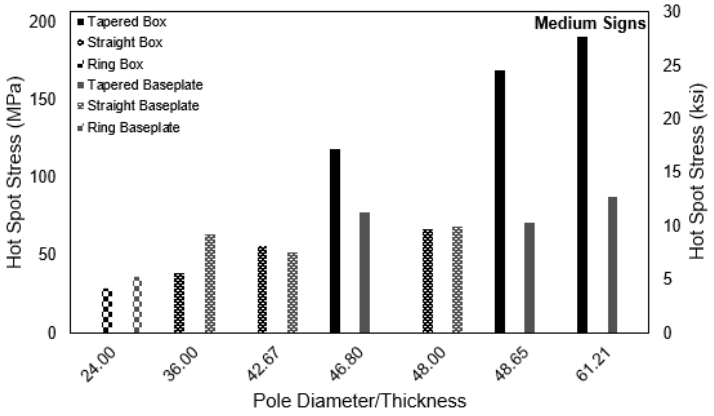

b)

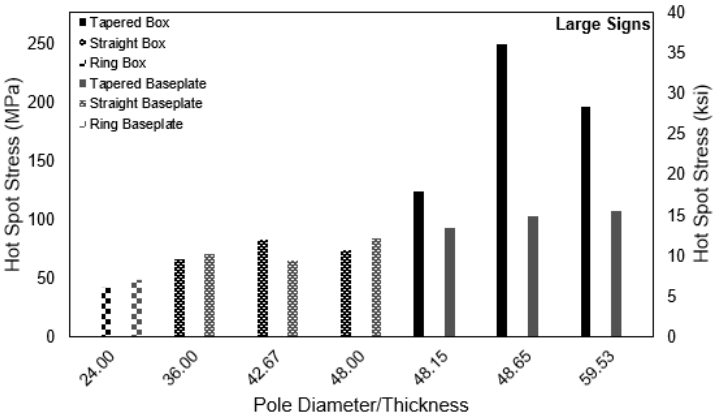

c)

Figure 4.17. Pole Diameter/Thickness Graphs, NW

Table 4.4. Pole Diameter/Thickness Ratios

Model	Pole Diameter/Thickness	Pole Diameter at Bottom Box, in. (cm)	Pole Thickness, in. (cm)
rD7S	24.00	18.00 (45.72)	0.75 (1.91)
sD6S	36.00	18.00 (45.72)	0.50 (1.27)
sD1S	42.67	16.00 (40.64)	0.375 (0.95)
sD3S	48.00	18.00 (45.72)	0.375 (0.95)
tD7S	49.04	15.33 (38.94)	0.3125 (0.79)
tD1,2S	49.21	12.30 (31.24)	0.25 (0.64)
tD3S	61.21	15.30 (38.86)	0.25 (0.64)
rD7M	24.00	18.00 (45.72)	0.75 (1.91)
sD6M	36.00	18.00 (45.72)	0.50 (1.27)
sD1M	42.67	16.00 (40.64)	0.375 (0.95)
tD7M	46.80	14.63 (37.16)	0.3125 (0.79)
sD3M	48.00	18.00 (45.72)	0.375 (0.95)
tD1,2M	48.65	12.16 (30.89)	0.25 (0.64)
tD3M	61.21	15.30 (38.86)	0.25 (0.64)
rD7L	24.00	18.00 (45.72)	0.75 (1.91)
sD6L	36.00	18.00 (45.72)	0.50 (1.27)
sD1L	42.67	16.00 (40.64)	0.375 (0.95)
sD3L	48.00	18.00 (45.72)	0.375 (0.95)
tD7L	48.15	15.05 (38.23)	0.3125 (0.79)
tD1,2L	48.65	12.16 (30.89)	0.25 (0.64)
tD3L	59.53	14.88 (37.80)	0.25 (0.64)

Repeating this analysis for the mast-arm did not reveal as clear lessons as it did for the pole (Figure 4.18). While both the tapered and straight pole models experience a decrease in stresses within the second model of all three sign groups, the overall trend was that stresses increased as the ratios increased.

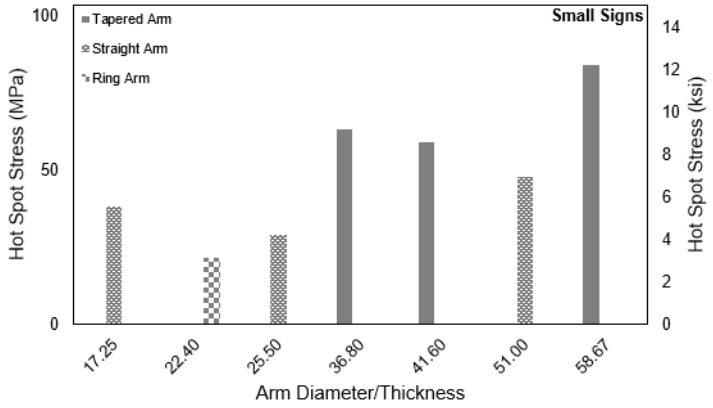

a)

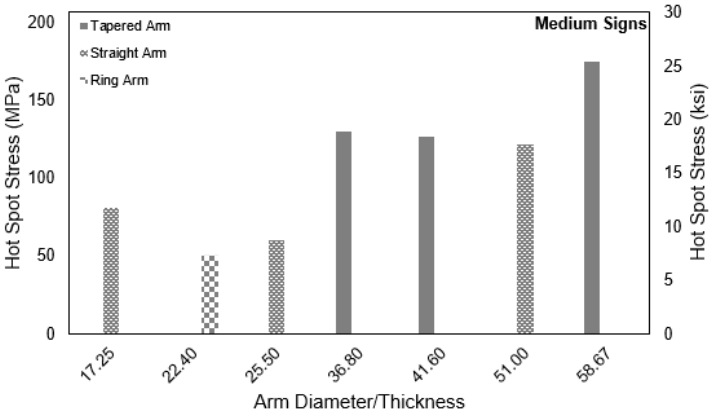

b)

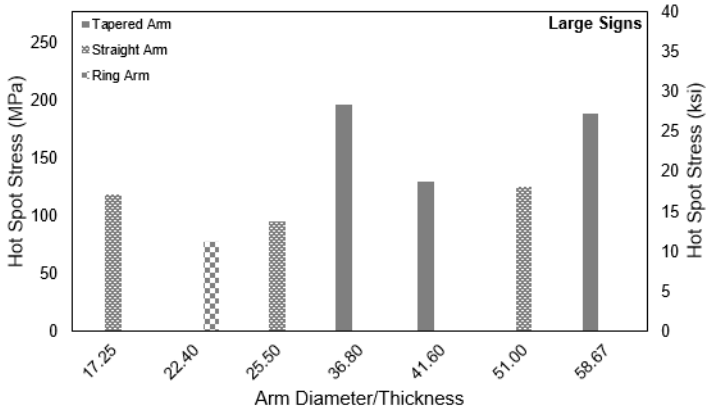

c)

Figure 4.18. Arm Diameter/Thickness Graphs, NW

Table 4.5. Arm Diameter/Thickness Ratios

Model	Arm Diameter/Thickness	Arm Diameter, in. (cm)	Arm Thickness, in. (cm)
sD1S	17.25	8.625 (21.91)	0.50 (1.27)
rD7	22.40	14.00 (35.56)	0.625 (1.59)
sD6	25.50	12.75 (32.39)	0.50 (1.27)
tD1,2	36.80	9.20 (23.37)	0.25 (0.64)
tD7	41.60	13.00 (33.02)	0.3125 (0.79)
sD3	51.00	12.75 (32.39)	0.25 (0.64)
tD3	58.67	11.00 (27.94)	0.1875 (0.48)

To determine if the diameter or thickness of the mast-arm is a more impactful design variable, a more in-depth analysis is required. Figure 4.19 shows only the stresses of the straight pole structure models. A case study can be performed analyzing results from the sD1 and sD6 models. Shown in Table 4.5, these models have the same thickness but sD6 has a larger diameter. Due to this larger diameter, a slight decrease in stresses when the design number changes within the same site-specific geometry, going from sD1S to sD6S for example. On the other hand, sD3 and sD6 models have the same diameters but sD3 has a smaller thickness. In performing similar analysis, going from sD3S to sD6S for example, an increase in stresses results. Due to there being a larger peak stress difference between models with different thickness than in the models with different diameters, it can be concluded that as was the case with the pole, thickening the mast-arm will do more to aid in reducing stresses than increasing the diameter.

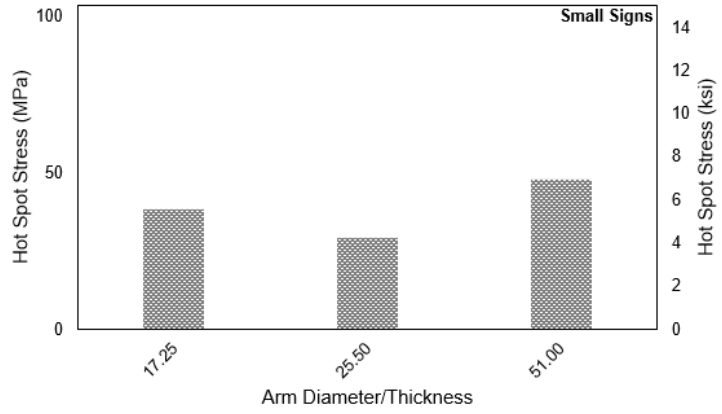

a)

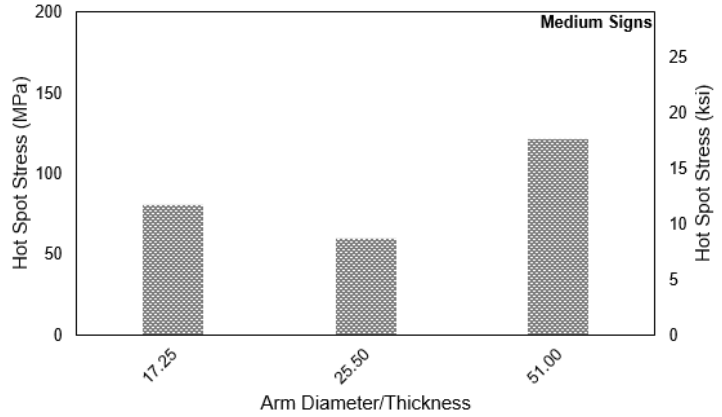

b)

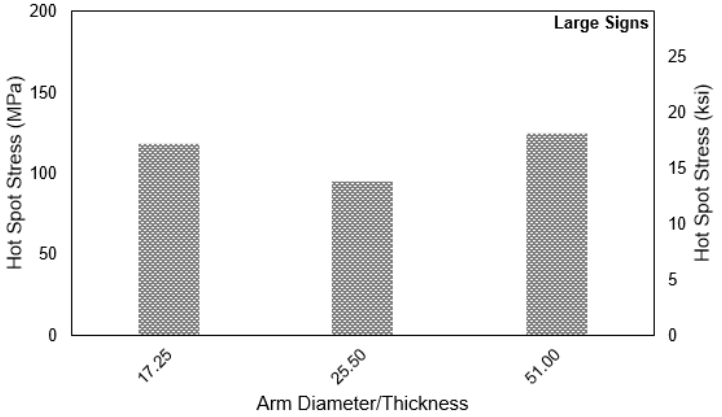

c)

Figure 4.19. Arm Diameter/Thickness Graphs (Straight Pole Design Only), NW

Truck-Induced plus Galloping Loading

As was the case for the NW loading, sign height is one of the most influential site-specific geometry parameters for T+G loading. As the sign height increased across the models, so did the stresses, as shown in Figure 4.20. The driving force of the stress increase is more likely due to the effects of galloping than of TIWG, as a larger sign area leads to larger galloping forces, per AASHTO equations, whereas the amount of TIWG load will change depending on the distance from the ground to the bottom edge of the sign, making a combination of sign height and pole height important. This is due to the TIWG loads linearly decreasing from P_{TG} at 20 ft. (6 m) to zero at 30 ft. (9.14 m), as discussed in Sections 2.2.2.1 and 3.1.2.2.

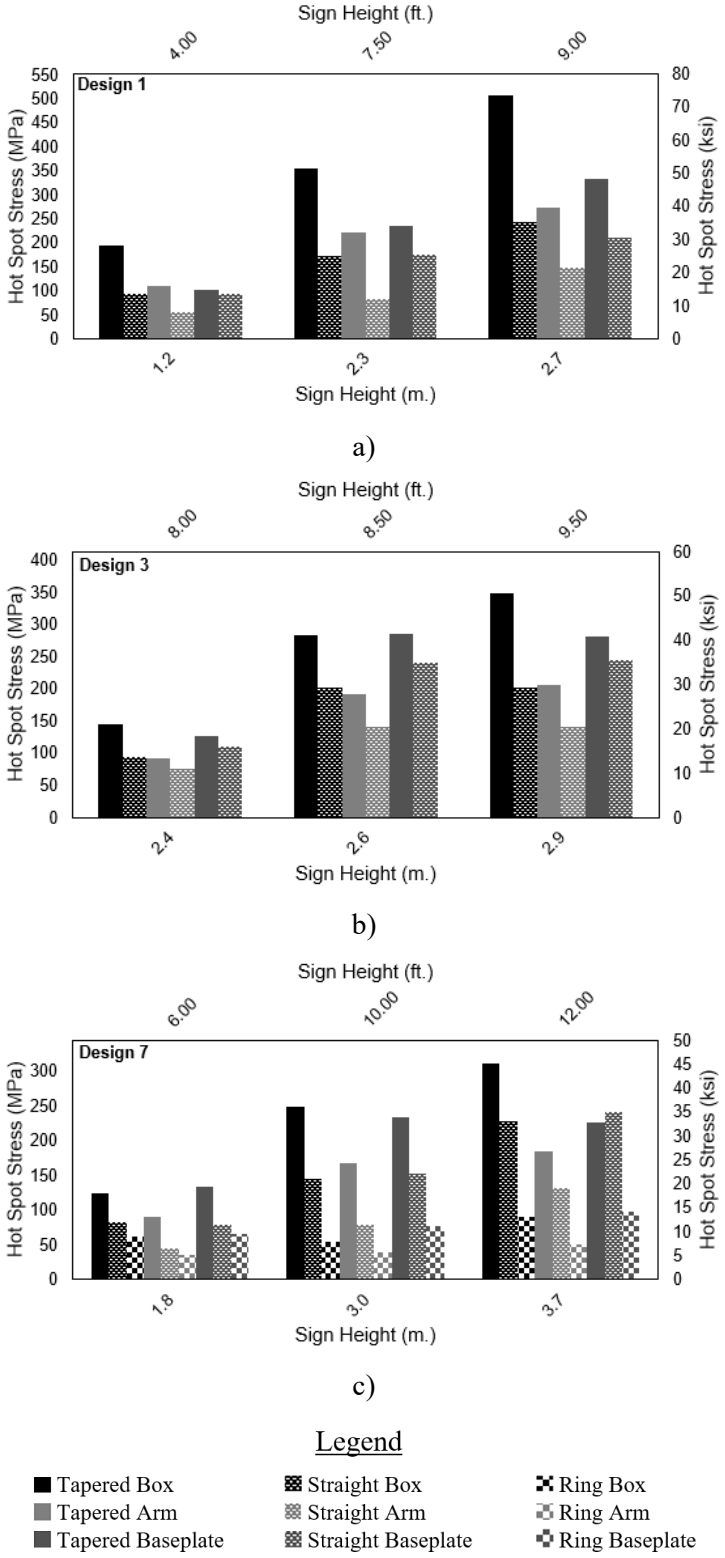

Figure 4.20. Sign Height Graphs, T+G

Sign length is also an influential site-specific geometry parameter, as a larger sign length led to higher stresses for most of the models, as shown in Figure 4.21. This is due to a larger sign length often relating to larger sign areas, subsequently increasing the galloping force. An outlier of this trend occurs within the last two Design #3 models, where the longest sign has lower stresses than the second longest. These two models have sign areas close to each other, with the second longest sign having an area of 175.75 ft^2 (3,684 m^2), while the longest sign was smaller at 165.75 ft^2 (4,092 m^2). This highlights the effect that a larger overall sign area has on the stresses generated by T+G loading, as ultimately it is the overall sign area that generates a larger galloping load and individually sign height and length have a smaller effect.

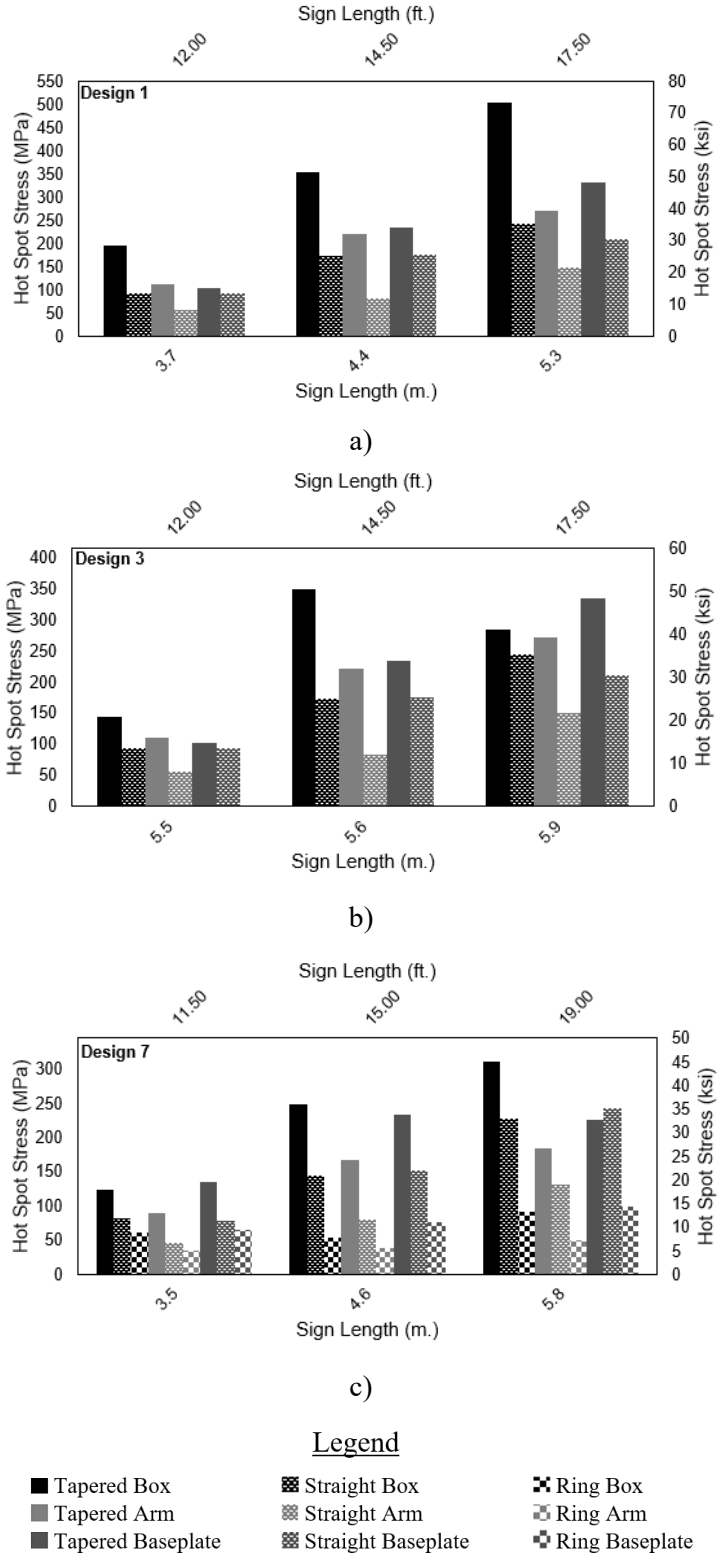

Figure 4.21. Sign Length Graphs, T+G

To aid in understanding the effect of the sign height, pole height was examined, shown in Figure 4.22. As occurred with the sign height graphs, stresses increased as pole height increased for most of the structures. While this was the trend for the Design #1 and #3 models, where both sign size and pole height increased together, the reverse occurred within the Design #7 models, where sign size decreased as pole height increased. This proves that, as was the case with NW, pole height has a minimal effect on the stresses experienced by the structure, when compared to the effect of the sign size. The minimal effect of pole height is further highlighted when comparing stresses of models with the same height, as is the case for the last two models of Design #1 and the first two models of Design #3. Despite being the same height, there is a large increase in stresses, particularly in Design #3, as the sign size increases.

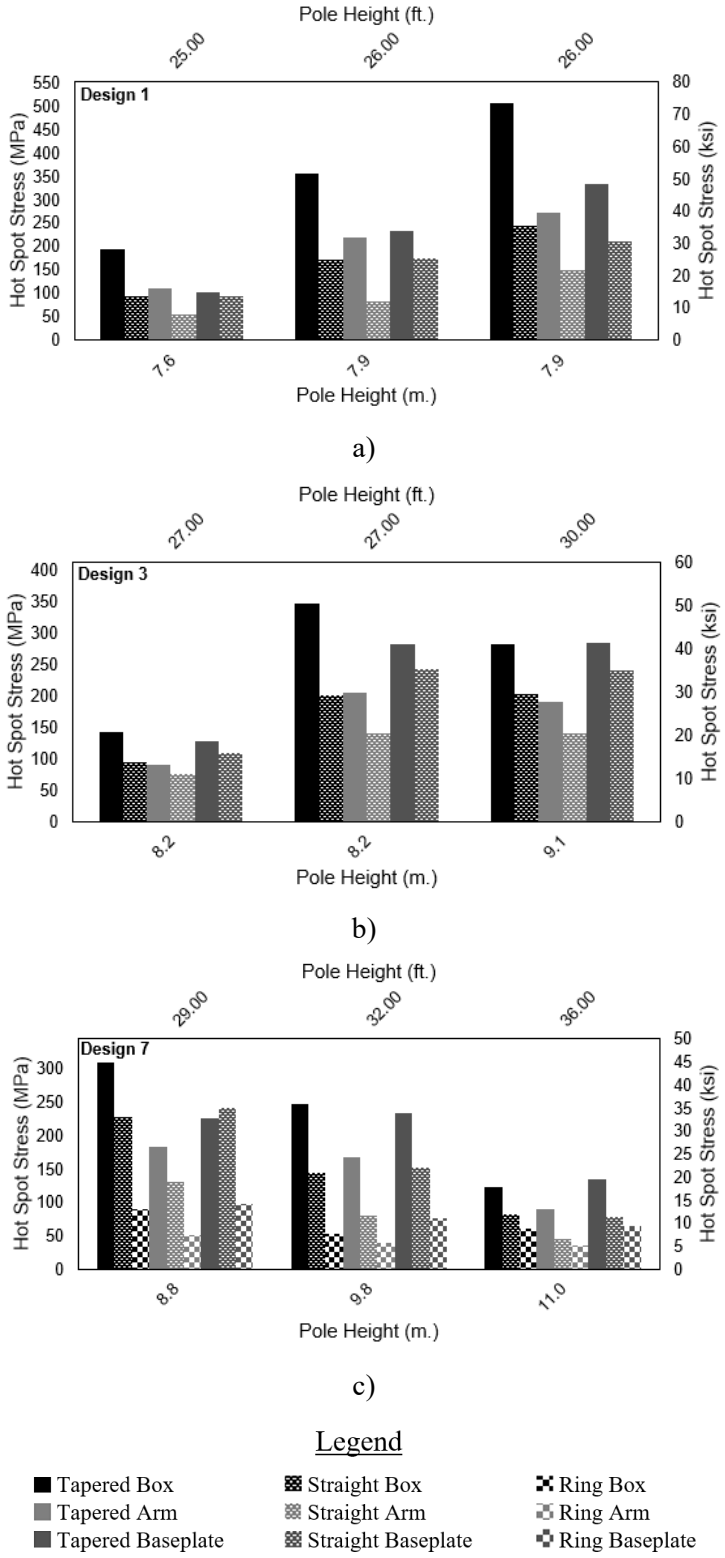

Figure 4.22. Pole Height Graphs, T+G

Looking at the pole height is important, as TIWG loading decreases from P_{TG} at a height of 20 ft. (65.6 m) linearly down to zero at a height of 30 ft. (98.4 m). As such, taller structures have a lower amount of truck-induced loading applied to them than shorter structures do. However, the fact that similar height structures do not exhibit similar stresses and there is no decrease, barring Design #7, as discussed above, as pole height increases, shows that when looking at TIWG and galloping combined, the primary driving force is going to be the galloping force as it is much larger than TIWG.

The final site-specific geometry parameter is the mast-arm length. TIWG loading is only applied along a 12 ft. (3.66 m) length onto the mast-arms and sign, to create the maximum stress range (AASHTO SLT 2015), and in many design examples and practices, this 12 ft (39.4 m) length is located at the end of the mast-arm (NCHRP Report 469, Appendix B) and for larger sign lengths, only covers the last 12 ft. (39.4 m). Galloping, on the other hand, is a larger load based on AASHTO SLT equations and considers overall sign size more than TIWG. As was the case for the sign length, for the most part, as the mast-arm length increased so did the stresses experience by the structure. Once again, there was the case in Design #3 where the second model had higher stresses than the third model, and this was because the second model had the larger sign area. Due to this, it can be concluded that like pole height, the effect of the mast-arm length falls secondary to the effect of the overall sign area.

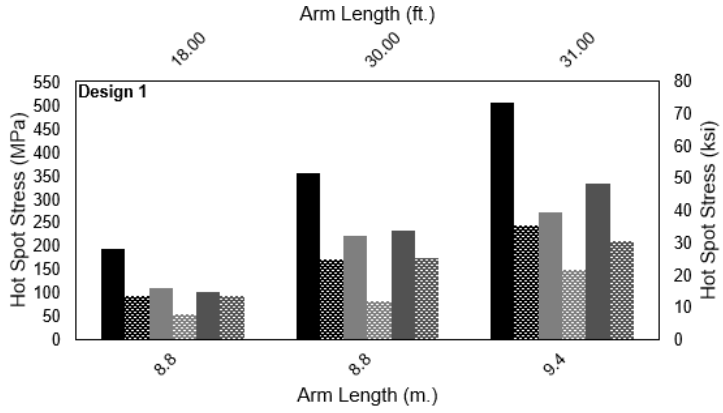

a)

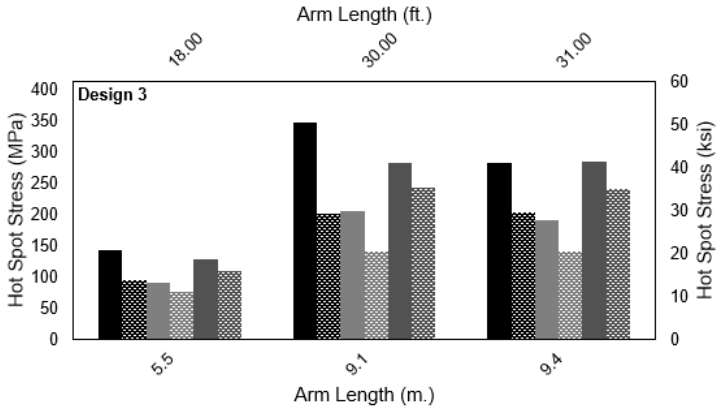

b)

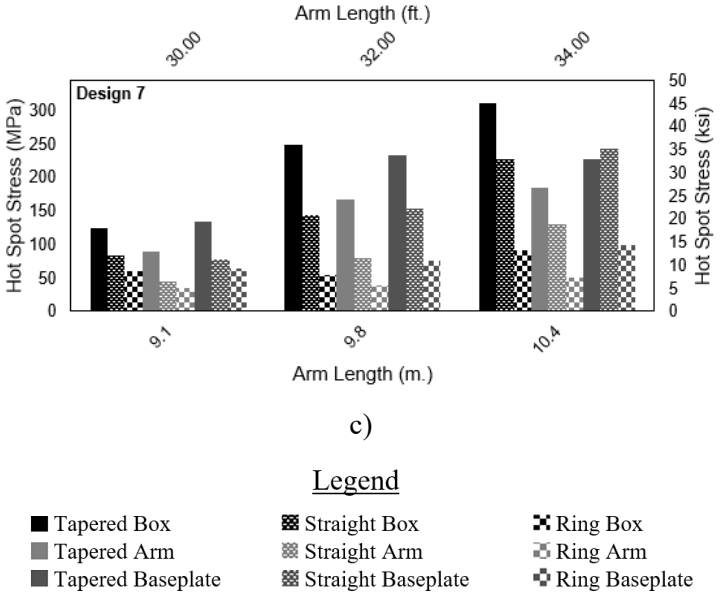

c)

d)

Figure 4.23. Arm Length Graphs, T+G

The first design parameter to focus on is mast-arm diameter, seen in Figure 4.24. As the arm diameter increased, the majority of the stresses related to both the tapered and straight pole structures decreased. As the mast-arm diameter will have minimal effect on the box and baseplate stresses, only the mast-arm stresses are shown. Looking at the Medium Signs graph makes it more evident that as occurred with NW, a larger diameter arm aids in decreasing the stresses generated at the mast-arm socket connection. It is important to note that the straight pole models for the small and medium sign groups experienced a jump in stress within their second models, which is due to the effect of thickness being greater than that of diameter, as was the case with NW. The second model for both corresponds with sD3, which has an arm thickness of 0.25 in. (0.64 cm), while the other two, sD1 and sD6, have larger thicknesses at 0.5 in. (1.27 cm). The effect of arm thickness will be discussed in greater detail later.

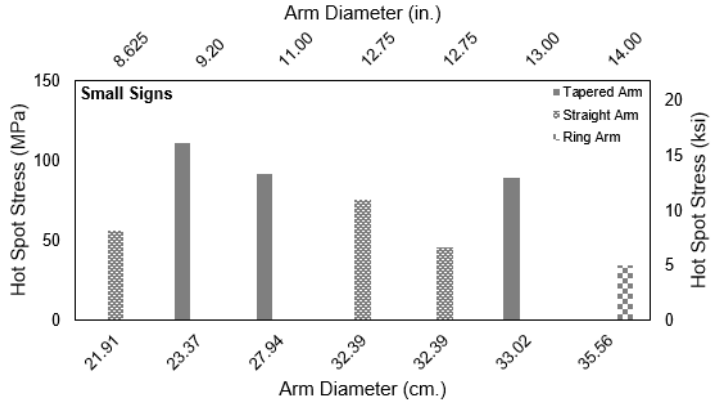

a)

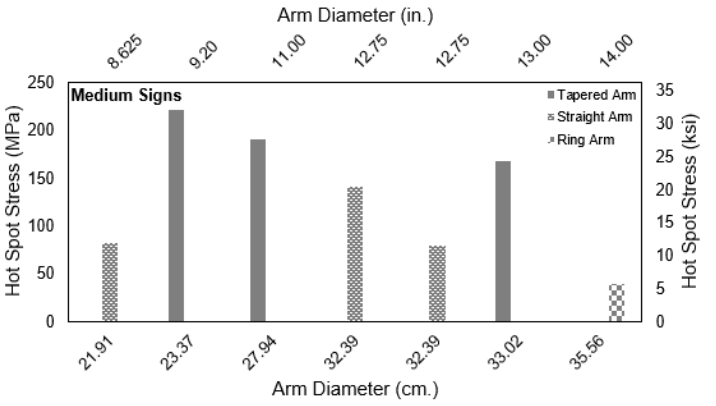

b)

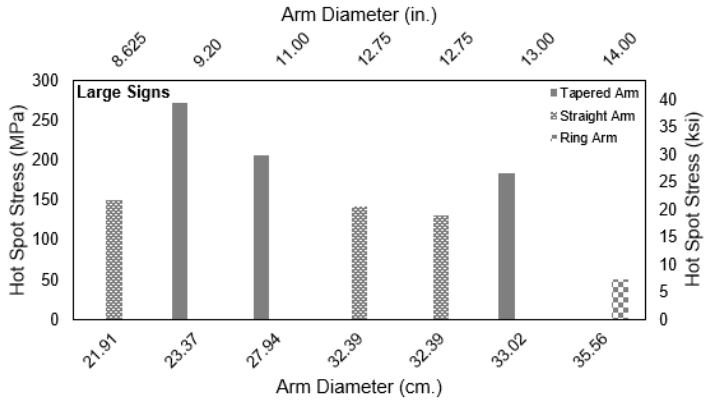

c)

Figure 4.24. Arm Diameter Graphs, T+G

As seen in Figure 4.25, which shows only the stresses generated at the mast-arm socket connection, as the mast-arm thickness increased, the stresses decreased. There is an outlier case within all sign size groups, when looking at the first two tapered pole models, as the second model experienced a larger stress than the first. This could be due to the mast-arm diameter having a

greater overall effect within tapered pole structures for T+G loading, as the second model has a smaller diameter than the first model. The third of the tapered pole models, which has the lowest stresses, has both the largest thickness and largest diameter. On the other hand, for the straight pole models, it appears that thickness controls far more than the diameter as the smallest thickness has the largest diameter, yet its stresses are much greater than the second straight pole model, which has the largest thickness and the smallest diameter.

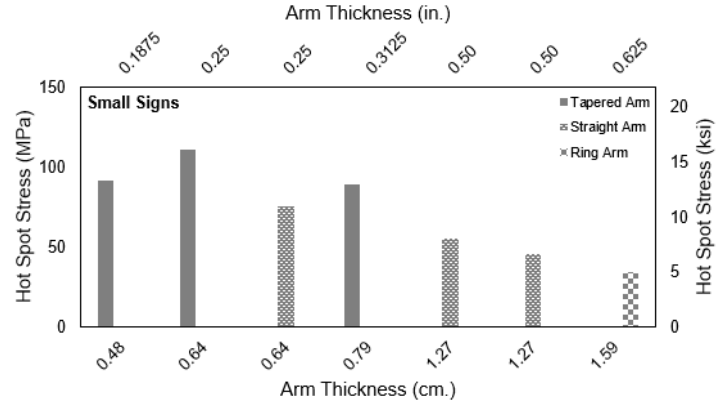

a)

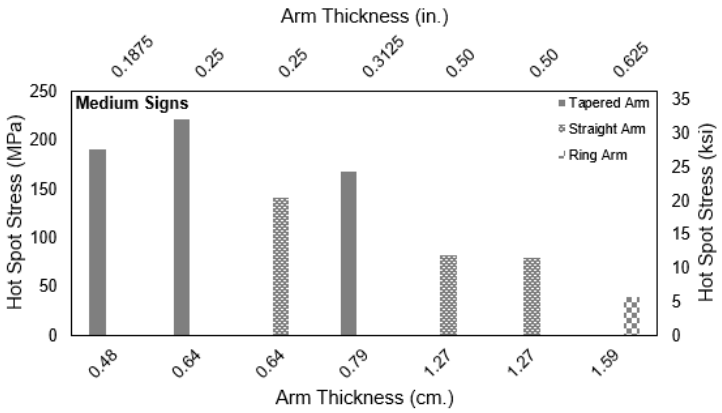

b)

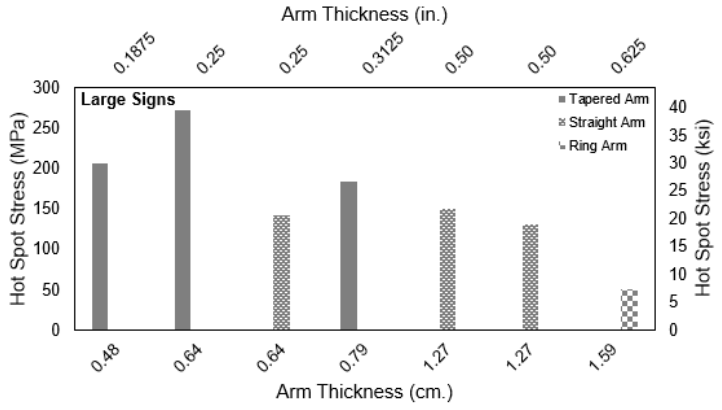

c)

Figure 4.25. Arm Thickness Graphs, T+G

As can be seen in Figure 4.26, a larger pole diameter aids in lowering the amount of stress generated at the box connection. While the stresses generally decrease for both tapered and straight pole models, there are a couple of outliers that are likely due to the effect of the pole thickness being greater than that of the diameter, as was the case for NW loading.

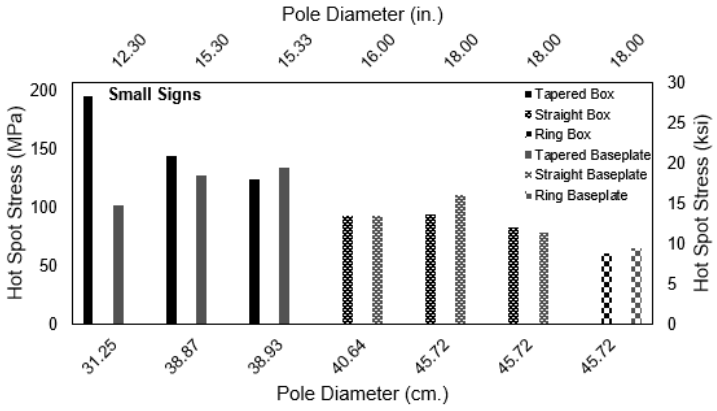

a)

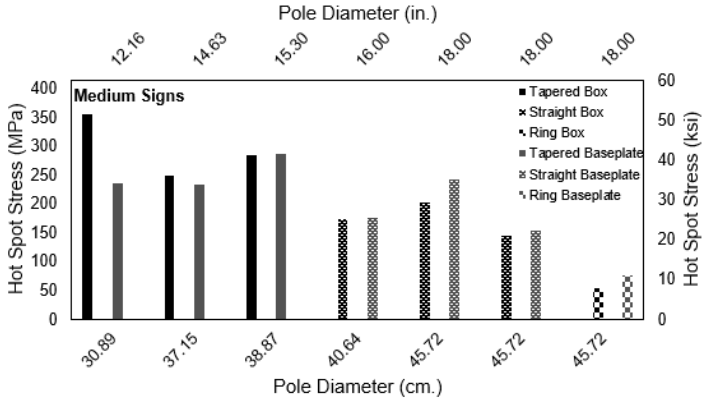

b)

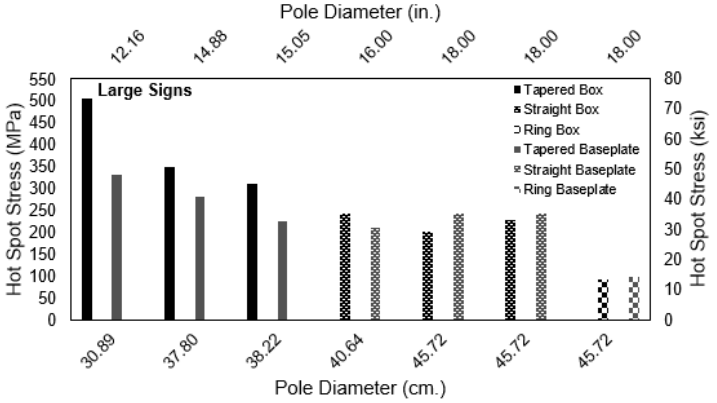

c)

Figure 4.26. Pole Diameter Graphs, T+G

Further showing the importance of the pole thickness on stresses, the graphs in Figure 4.27 show a downward trend of the stresses as the pole thickness increases which is more linear than the trend from the pole diameter graphs. The increase in stresses shown in the second straight pole

model of all three sign groups is due to that model, sD3, having the larger sign size of the two 0.375 in. (0.95 cm) thick models.

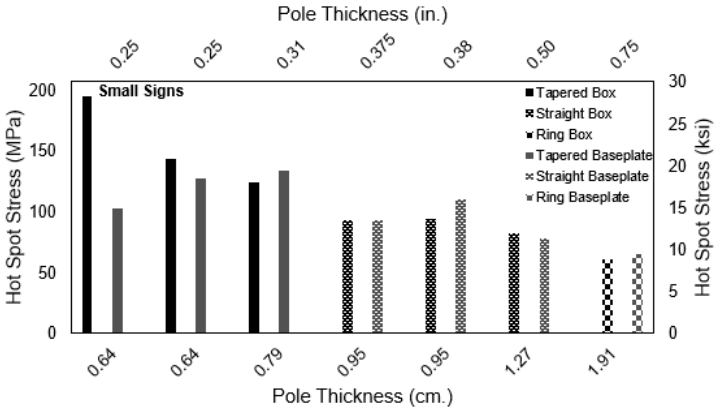

a)

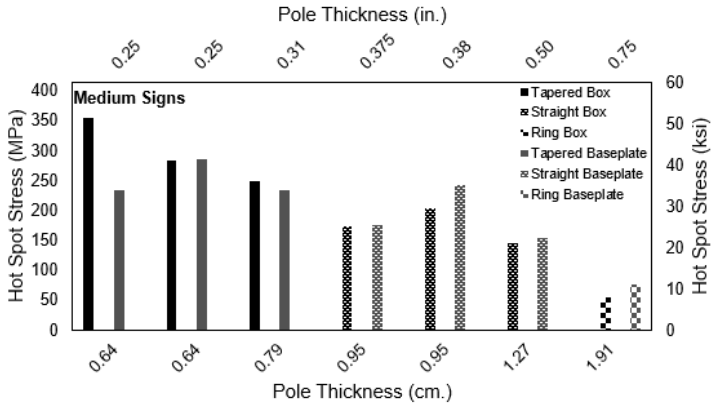

b)

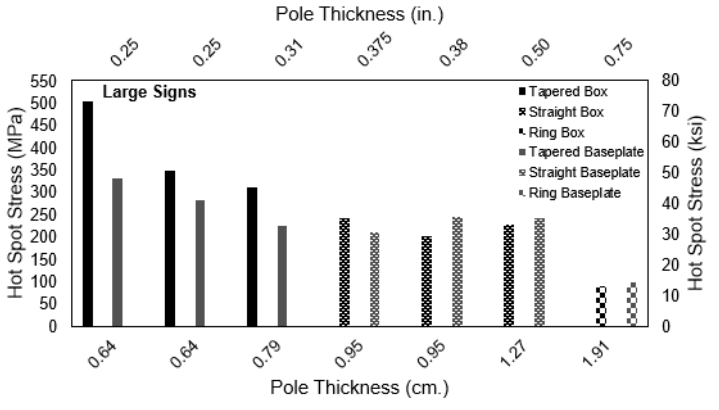

c)

Figure 4.27. Pole Thickness Graphs, T+G

4.1.3 Justification for the Exclusion of T+G from Experimental Testing

Through the course of the analytical study, it was determined that the cracking experienced by the COSS within the KDOT inventory is more likely caused by the effects of natural wind gusts rather than truck-induced wind gusts or galloping.

The cracking experienced by the two sign structures donated by KDOT to this project begins around the bottom and/or top corner of the weld that connects the side-plate to the pole and continues to grow along the vertical edge of the side-plate. This is shown in Figure 4.28 and discussed in more detail in Section 2.2.2.3.

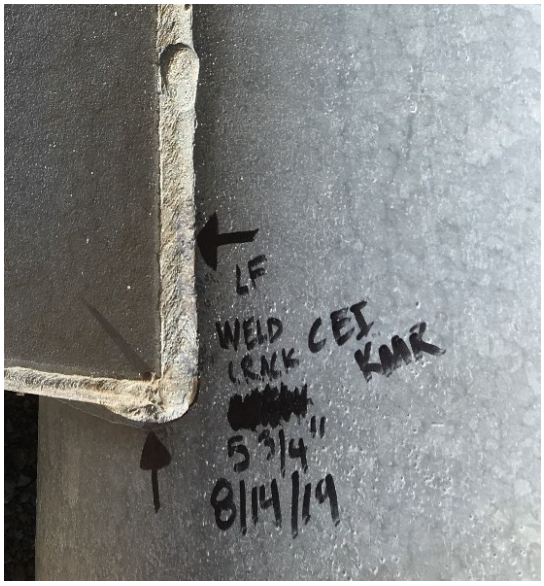

Figure 4.28. Cracking Along Bottom Corner of Bottom Box Connection, KDOT Structure 309 (KDOT)

Analysis was performed on the full-sized version of Structure 309, which is built according to 1981 tapered KDOT Design #7, utilizing loads determined by AASHTO SLT guidelines for both natural wind (NW) gusts and a combination of truck-induced wind gusts and galloping (T+G). This is model tD7L when the results from FE modeling are being discussed.

When the stress distributions were examined, in terms of von Mises stress, the “hot spot” stress location around the box was similar to the cracking patterns experienced by the donated structures, as the hot spot occurred near the bottom corner of the box. The lack of a hot spot in the top corner is likely due to the natural wind only being applied in-plane, in the direction of the sign,

whereas in the field, natural wind can come from a wide variety of directions. The Von Mises stress distributions can be seen in Figure 4.29, where the units are in ksi.

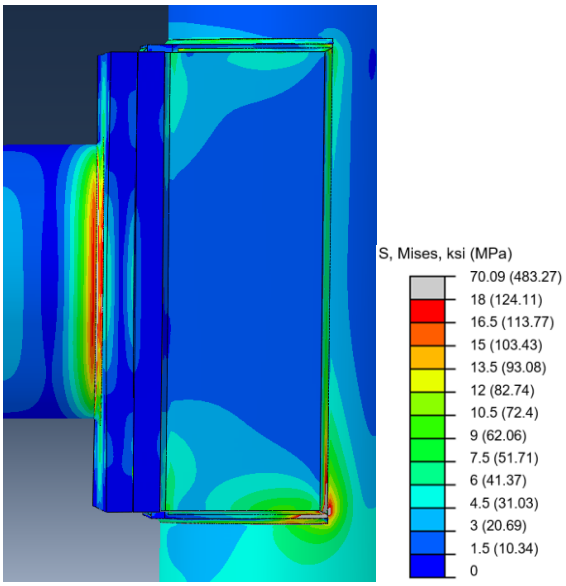

Figure 4.29. Mises Stress Distributions for Structure 309 (tD7L), NW

On the other hand, the results from the combined truck-induced and galloping (T+G) loads pushed the structure upwards, in out-of-plane loading, which resulted in the hot spot being located below the bottom mast-arm's box connection and around the weld that connects the gusset plate to the pole, see Figure 4.30.

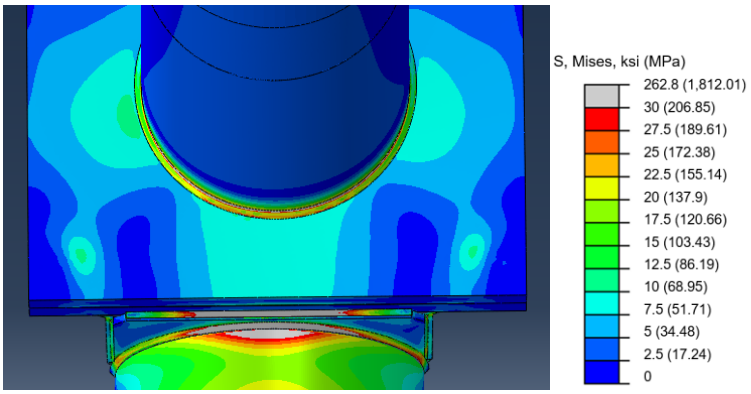

Figure 4.30. Mises Stress Distributions for Structure 309 (tD7L), T+G

As this is not where the cracking experienced by the two donated sign structures occurred, nor in any information provided by KDOT, it can be concluded that T+G is not the primary driving

force behind the cracking experienced by these structures within KDOT's inventory. All three structure types (tapered pole, straight pole, and ring-stiffened box connection) had hot spot locations around the box in the same locations for T+G loading. Due to this and in order to optimize experimental testing, only NW loading was utilized in the experimental tests.

Chapter 5: Conclusions and Recommendations

Finite element analyses was performed to assess the fatigue performance of the box connection detail on two-mast arm cantilevered overhead sign structures, utilizing design specifications of structures within the KDOT highway inventory. Twenty-one full sized COSS models, based on KDOT design specifications, were created to investigate the effects of changing geometry of the structure and the impact of utilizing the ring-stiffened box connection instead of the gusseted box connection. Geometric parameters included were examined within the context of the KDOT design groups, which denoted member sizes and shapes as well as the site-specific geometry, which defined the sign size, mast-arm length, and pole height.

Conclusions based on the results from the finite element analysis are presented in Section 5.1. Suggestions for future work are presented in Section 5.2.

5.1 Conclusions

The analysis of the three different COSS structure types, along with the effects of changes within their site-specific details and geometric parameters led to multiple conclusions.

The first is that the cracking experienced by structures in the KDOT inventory was most likely caused by natural wind loading. This was determined due to the location of maximum hot spot stresses, in the corners of the side-plate-to-pole weld, matching the location of the cracking on the donated KDOT structures when subjected to natural wind loading. The hot spot location for T+G loading was below the front of the box connection, on the gusset-plate-to-pole weld, and no cracking of in-service KDOT structures has been reported at this location.

The second main conclusion is that component thickness is inversely proportional to stress. Increasing the thickness of the mast-arm and/or pole results in decreased stresses at the box connection, mast-arm socket connection, and the baseplate socket connection. When examining all models together, increasing the mast-arm thickness decreased peak stresses on average of 60% and 39% at the box connection and at the mast-arm socket connection, respectively, when subject to NW loading Similar results were observed for T+G loading, with the same increase in thickness resulting in 48% and 47% at the box connection and mast-arm socket, respectively. Increasing the pole thickness also decreased the NW-induced peak stresses by an average by 60% and 33% at the box connection and at the baseplate socket connection, respectively. Pole thickness also influenced

stresses experienced under T+G loading, with 47% and 31% average decrease at the box connection and at the baseplate socket connection, respectively. Specifics regarding exact stress decreases in conjunction with thickness changes can be found tables in Appendix D.4. The impact of component thickness was also observed when comparing the tapered tube models and the straight tube models, as the straight tube models utilize thicker mast-arms and poles than comparable tapered structures. The straight designs also had larger diameter mast-arms and poles than the tapered structures, which also contributed to decreased stresses at the connection details examined. Component thickness appears to have more of an impact on peak stress than component diameter.

Incorporating the ring-stiffened box connection detail rather than the gusseted box connection detail also decreased stresses at the box connection for both NW and T+G loading. Comparing tapered tube and ring-stiffened designs, average peak stresses at the box decreased by 74% due to NW loading and 67% due to T+G loading. It should be noted that the ring-stiffened models are based on the 2015 redesign, meaning these models had thicker members and larger diameters than the tapered tube models, which also contributes to the reduction in stress. A more direct comparison can be made between the straight tube and ring-stiffened models, where the primary difference between models was the box connection type. Comparing these structures, utilizing the ring-stiffened box connection resulted in average stress reductions of 35% and 50% for NW and T+G loading, respectively.

These results indicate the 2015 KDOT redesign was beneficial in decreasing the stress demand at the box connection. As sign size has the greatest impact on the amount of stresses experienced by COSS components and details, KDOT designs should continue to be organized based on the required sign size as well as other site-specific requirements, and structures experiencing higher demand should utilize the ring-stiffened box connection detail.

It is possible that increasing member thickness may change the detail most susceptible to fatigue failure. For example, analyses indicated that as the pole thickness increased, peak stresses under NW loading were experienced at the mast-arm socket connection rather than the box connection. Thicker poles also move T+G load-induced peak stresses to the baseplate socket connection. Any future changes to COSS design should be performed with this possibility in mind.

5.2 Recommendations and Future Work

Recommendations for future work to expand upon knowledge regarding box connection behavior and further improve design of two-mast arm COSS are:

- A parametric study directly comparing the effects of tapered and straight tubes, utilizing the same thickness and/or base diameter in each structure type.
- Additional evaluation of ring-stiffened box connection behavior should be undertaken. In particular, the location of the peak stress when experiencing NW loading as a secondary peak stress location developed at the side-plate-to-flange weld.
- Reexamination and clarification of the appropriate calculations for determination of nominal stresses to be used in fatigue design with S-N curves. Specifically, guidance is needed regarding nominal stress determination around the box connection detail when structures are subject to loading in the NW direction.
- Further analytical research should be performed to examine the impact of the fabrication detailing around the box connection. Welding details are not specifically called for in the KDOT design specifications, and the effects of wrapping the weld around the corners of the side-plate are unknown.
- All experimental testing of sign structure specimens should be completed to validate and complement the analytical evaluations presented in this study.

References

American Association of State Highway and Transportation Officials (AASHTO) (2012). *AASHTO LRFD Bridge Design Specifications*, Washington, D. C.

American Association of State Highway and Transportation Officials (AASHTO) (2001). *Standard Specifications for Structural Supports for Highway Signs, Luminaires and Traffic Signals*, 4th Edition, Washington, D. C.

American Association of State Highway and Transportation Officials (AASHTO) (2015). *Standard Specifications for Structural Supports for Highway Signs, Luminaires and Traffic Signals*, 6th Edition, Washington, D. C.

American Society for Metals (ASM) International Handbook Committee (1990). *Metals Handbook:* Vol. 2, Properties and Selection- Nonferrous Alloys and Pure Metals. ASM International Handbook. New York, NY.

American Society for Testing Materials (ASTM) "ASTM Standard A709/A709M-18." (2018). *Standard Specification for Structural Steel for Bridge*. ASTM International. West Conshohocken, PA.

American Welding Society (2004). *Structural Welding Code-Steel D1.1*, Miami.

American Welding Society (2003). *Structural Welding Code-Aluminum D1.2*, Miami.

Barsom, J.M. and Rolfe, S.T. (1999). *Fracture and Fatigue Control in Structures: Applications of Fracture Mechanics*, 3rd Edition, ASTM, West Conshohocken, PA.

Creamer, B.M., Frank, K.H., and Klinger, R.E. (1979). "Fatigue Loading of Cantilever Sign Structures from Truck Wind Gusts." Research Report 209-IF, Project 3-5-77-209, Center for Highway Research, The University of Texas, Austin, TX.

Deschamp, B. (2002). "Fatigue Testing of Traffic Signal Structures." MS thesis, University of Wyoming, Laramie, WY.

Dexter, R.J. and Ricker, M.J. (2002). "Fatigue Resistant Design of Cantilevered Signal, Sign, and Light Supports." NCHRP Report 469, Transportation Research Board, Washington, D.C.

Det Norske Veritas. (2014). “DNV-RP-C203: Fatigue Design of Offshore Steel Structures.”.

Dowling, N.E. (2013). *Mechanical Behavior of Materials: Engineering Methods for Deformation, Fracture, and Fatigue.* 4th ed. Pearson Education

Fisher, J. W., Kulak, G. L., Smith, I. F. C. (1998). *A Fatigue Primer for Structural Engineers*, National Steel Bridge Alliance (NSBA).

Foley, C.M., and Diekfuss, J.A. (2016). “Reliability-Based Inspection Protocols for Mast-Arm Sign Support Structures.” *Journal of Structural Engineering*. 142(7). 04016043.1-04016043.10.

Gallow, M.S., Fouad, F.H., Hosch, I.E. (2015). “Mitigating Fatigue in Cantilevered Overhead Sign Structures.” *Transportation Research Record: Journal of the Transportation Research Board, No. 2522,* Transportation Research Board, Washington, D.C., pp.18-26.

Grey, B. (1999). “Fatigue Effects on Traffic Signal Structures.” MS thesis, University of Wyoming, Laramie, WY.

Hamilton, H.R., J.A. Puckett, B. Gray, P. Wang, B. Deschamp, and P. McManus, *Traffic Signal Pole Research Final Report*, A Report to the Wyoming Department of Transportation, University of Wyoming, Laramie, WY, June 2002.

Hobbacher A. (2008). “Recommendations for Fatigue Design of Welded Joints and Components.” IIW doc. IIW-1823-07 ex XIII-2151r4-07/XV-1254r4-07. Paris, France, 2008.

Hosch, I.E. (2009). “Design of Highway Overhead Cantilever-Type Sign Support Structures for Fatigue Loads.” PhD Dissertation, The University of Alabama at Birmingham, Birmingham, Alabama.

Hosch, I.E., Fouad, H.F., Gallow, M., and Traylor II, L. (2017). “Operational Post Deformation of Cantilever Sign Support Structures from Truck-Induced Wind Gusts.” *Practice Periodical Structural Design and Construction.* 23(1). 04017033.1-04017033.12.

Kacin, J., Rizzo, P., and Tajari, M. (2010). “Fatigue Analysis of Overhead Sign Support Structures”. *Engineering Structures*. 32. 1659-1670.

Kaczinski, M.R., Dexter, R.J. and Van Dien, J.P. (1998). "Fatigue Design of Cantilevered Signal, Sign, and Light Supports." NCHRP Report 412, Transportation Research Board, Washington, D.C.

Keating, P.B., and Fisher, J.W. (1986). "Evaluation of Fatigue Tests and Design Criteria on Welded Details." NCHRP Report 286, Transportation Research Board, Washington, D.C.

Koenigs, M.T., Botros, T.A., Freytag, D. and Frank, K.H. (2003). "Fatigue Strength of Signal Mast Arm Connections." Research Report 4178-2, Project 0-4178, Center for Transportation Research, The University of Texas, Austin, TX.

Li, X., Whalen, T. M., and Bowman, M. D. (2006a). "Fatigue strength and evaluation of sign structures. Volume 1—Analysis and evaluation." FHWA/IN/JTRP-2006/16, Joint Transportation Research Program, Indiana Dept. of Transportation and Purdue Univ., West Lafayette, IN.

Moses, F., Schilling C. G., and Raju, K. S. (1987). "Fatigue Evaluation Procedures for Steel Bridges," NCHRP Report 299, Transportation Research Board, Washington, DC.

Novak,, M., "Aeroelastic Galloping of Prismatic Bodies," *Journal of the Engineering Mechanics Division*, ASCE, Vol. 95, No. EM1, 1969.

Niemi, Erkki, et al. *Fatigue Analysis of Welded Components: Designer's Guide to the Structural Hot-Spot Stress Approach*, Springer, 2017. ProQuest Ebook Central, http://ebookcentral.proquest.com/lib/ku/detail.action?docID=4987727.

Ocel, J.M., Dexter, R.J., and Hajjar, J.F. (2006). "Fatigue Resistant Design for Overhead Signs, Mast-Arm Signal Poles, and Lighting Standards." MN/RC-2006-07, Minnesota Department of Transporation and University of Minnesota., St. Paul, Minnesota.

Peiffer, J.P. (2008). "Fatigue Testing of Stiffened Traffic Signal Structures." MS thesis, University of Wyoming, Laramie, WY.

Puckett, J.A., Erikson, R.G., and Peiffer, J.P. (2010). "Fatigue Testing of Stiffened Traffic Signal Structures." *Journal of Structural Engineering*. 136(10). 1205-1214.

Roy, S., Park, Y.C., Sause, R., Fisher, J.W., Kaufmann, E.J. (2011). “Cost-Effective Connection Details for Highway Sign, Luminaire, and Traffic Signal Structures.” NCHRP Report 176, Transportation Research Board, Washington, D.C.

Senior, H. (2018). “Analyzing the Effects of Walkway Attachments on Highway Cantilevered Overhead Sign Structures.” MS thesis, University of Kansas, Lawrence, KS.

Wang, P. (1999). “Acoustic Emission Testing and FEA of Cantilevered Traffic Signal Structures.” MS thesis, University of Wyoming, Laramie, WY.

Appendix A. Construction Drawings

FHWA REGION NO.	STATE	PROJECT NUMBER	SHEET NO.	TOTAL SHEETS
7	KANSAS	435-105-I-435-3(246)	81	70	82

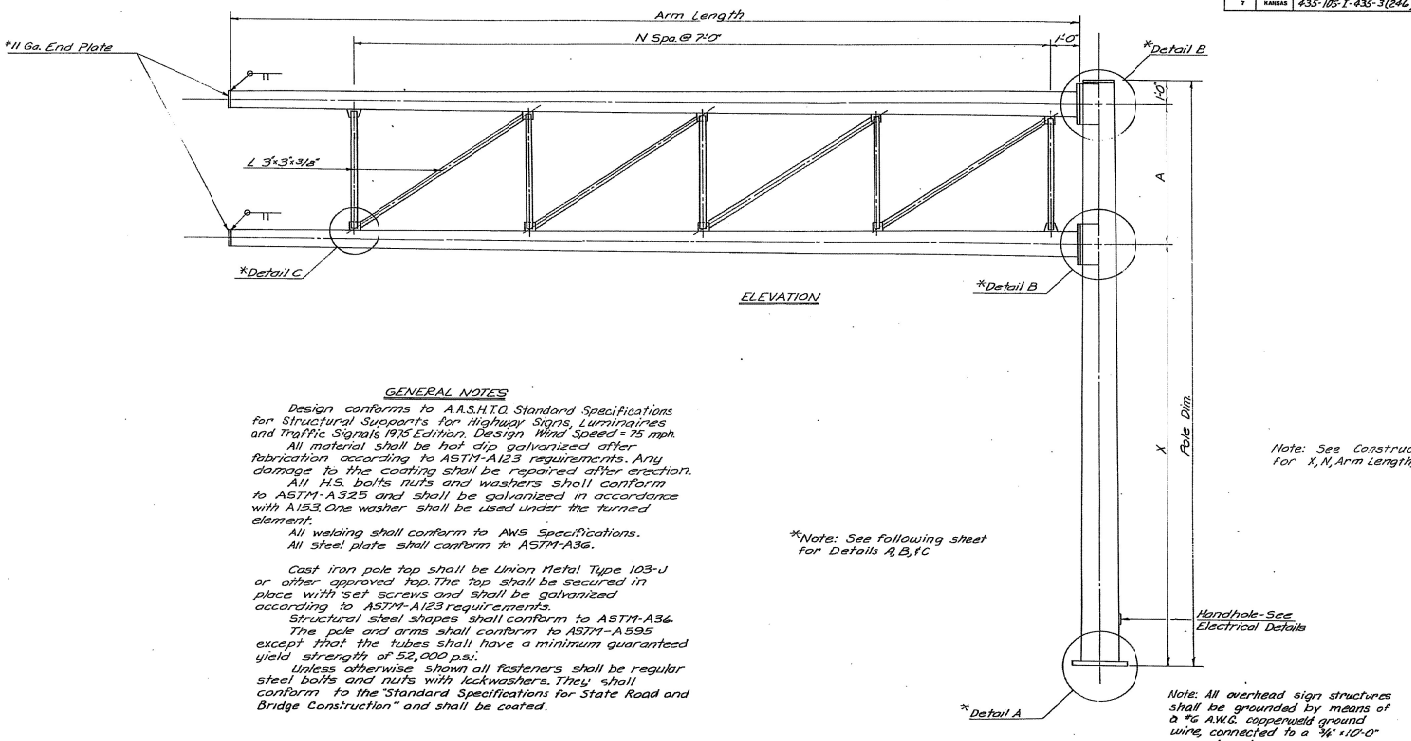

ELEVATION

GENERAL NOTES

Design conforms to A.A.S.H.T.O. Standard Specifications for Structural Supports for Highway Signs, Luminaires and Traffic Signals, 1975 Edition. Design Wind Speed = 75 mph.

All material shall be hot dip galvanized after fabrication according to ASTM-A123 requirements. Any damage to the coating shall be repaired after erection.

All H.S. bolts nuts and washers shall conform to ASTM-A325 and shall be galvanized in accordance with A153. One washer shall be used under the turned element.

All welding shall conform to AWS Specifications.

All steel plate shall conform to ASTM-A36.

Cast iron pole top shall be Union Metal Type 103-J or other approved top. The top shall be secured in place with set screws and shall be galvanized according to ASTM-A123 requirements.

Structural steel shapes shall conform to ASTM-A36.

The pole and arms shall conform to ASTM-A595 except that the tubes shall have a minimum guaranteed yield strength of 52,000 p.s.i.

Unless otherwise shown all fasteners shall be regular steel bolts and nuts with lockwashers. They shall conform to the "Standard Specifications for State Road and Bridge Construction" and shall be coated.

*Note: See following sheet for Details A, B, & C

Note: See Construction Layouts for X, M, Arm Length, and Design No.

Note: All overhead sign structures shall be grounded by means of a #6 A.W.G. copperweld ground wire, connected to a 5/8" x 10'-0" ground rod.

Dimension Design	Pole Dimension	Arm Dimension	A		T1	S	F	BC.	W1	W2	P	Anchor Bolt Size	T2	G	E	W3	W4	H	J	Bolt Size	W5
1	3 Spa. 15" x	3 Spa. 9.5" x (30'-0")	4'-0"		2"	1'-11"	1'-3 1/8"	1'-10"	3/4"	1 1/8"	7 3/8"	3"	1 1/8"	8 1/4"	1'-7 1/8"	3 1/8"	1/4"	1'-5 1/8"	7 1/4"	1 1/8" x 4"	1 1/4"
2	3 Spa. 13" x	3 Spa. 9.5" x (45'-0")	4'-0"		2"	1'-11"	1'-3 1/8"	1'-10"	3/4"	1 1/8"	7 3/8"	3"	1 1/8"	8 1/4"	1'-7 1/8"	3 1/8"	1/4"	1'-5 1/8"	7 1/4"	1 1/8" x 4"	1 1/4"
3	3 Spa. 12" x	2 Spa. 11" x (22'-0")	4'-0"		2"	2'-0 1/2"	1'-6"	2'-1 1/8"	7/8"	1"	7 7/8"	2"	1 1/8"	9 1/8"	1'-9 7/8"	3 1/16"	3/16"	1'-8 3/4"	7 1/8"	1 1/8" x 3 3/4"	1 1/8"
4	3 Spa. 18" x	2 Spa. 12.5" x (24'-0")	4'-0"		2"	2'-2 1/8"	1'-6"	2'-1 1/8"	1 1/16"	1 1/4"	7 3/8"	2"	1 1/8"	9 5/8"	1'-10 1/4"	3 1/16"	1'-0 1/4"	1'-9 1/4"	8 5/8"	1 1/8" x 4"	1 1/8"
5	0 Spa. 18" x	2 Spa. 12.5" x (28'-0")	2'-0"		2 1/16"	2'-3 3/8"	1'-6"	2'-1 1/8"	1 1/16"	1 1/2"	9 3/16"	2 1/16"	1 1/8"	9 5/8"	1'-10 1/4"	3 1/16"	1'-0 1/4"	1'-9 1/4"	8 5/8"	1 1/8" x 4"	1 1/4"
6	0 Spa. 18" x	3 Spa. 12.5" x (28'-0")	6'-0"		2 1/16"	2'-3 3/8"	1'-6"	2'-1 1/8"	1 1/16"	1 1/2"	9 3/16"	2 1/16"	1 1/8"	9 7/8"	1'-10 1/2"	3 1/2"	1'-2"	1'-9 1/2"	8 3/4"	1" x 4"	1 1/4"
7	0 Spa. 18" x	0 Spa. 13" x (31'-0")	6'-0"		2 1/16"	2'-2 1/8"	1'-6"	2'-1 1/8"	1 1/16"	1 1/16"	11 1/16"	2 1/4"	1 1/16"	10"	2'-0"	3 1/16"	5 1/16"	1'-9 1/2"	8 3/4"	1 1/8" x 4 1/2"	1 3/8"

*Note: All tubes have a decreasing taper of .14"/ft.

Note: Dimension in parentheses in the "Arm Dimension" column is the maximum for that design.

DEPARTMENT OF TRANSPORTATION - KANSAS
STANDARD STRUCTURAL SIGN SUPPORTS
CANTILEVER TYPE OVERHEAD
STEEL SUPPORT DETAILS

2-78

DESIGNED 70 82	DRAWN Various	SPEC.	TRACED KBA
RECOMMD BPH	CHECKED BPH	CHECKED	TRACE CK BPH
RECOMMD NLW	DETAIL CK NLW	QUAN. CK	

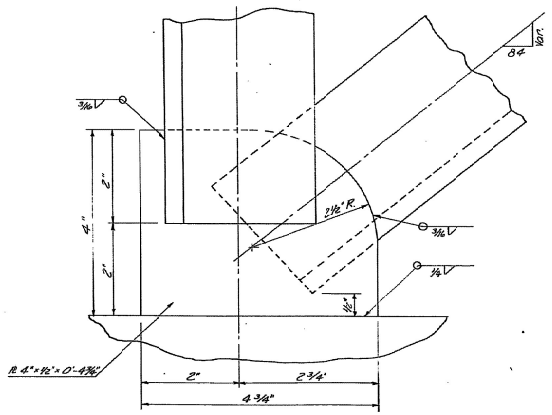

DETAIL C

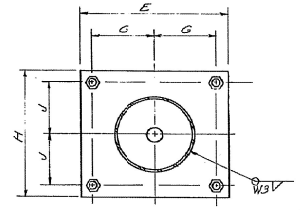

SECTION B-B

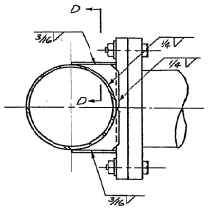

SECTION C-C

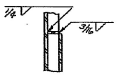

SECTION D-D

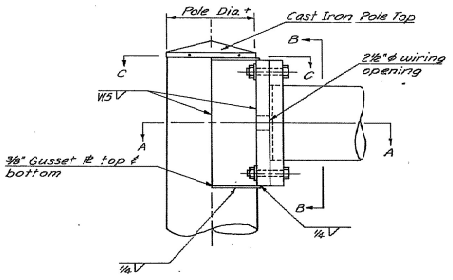

ELEVATION

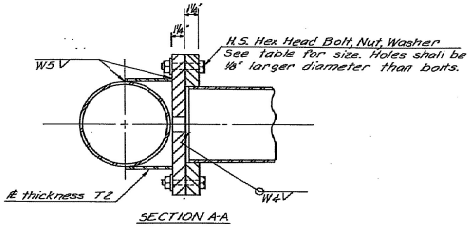

SECTION A-A

DETAIL B

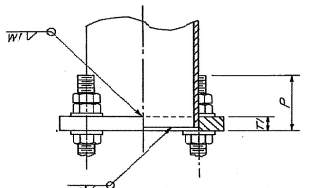

ELEVATION† SECTION

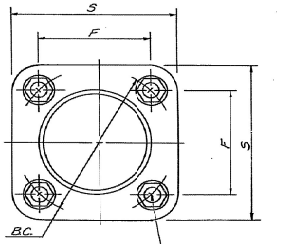

PLAN

Anchor bolts Type II. See table for size. Holes shall be 1/8" larger diameter than the bolts.

DETAIL A

STATE	PROJECT NO.	YEAR	SHEET NO.	TOTAL SHEETS
KANSAS	435-105-I-435-3(246)	1981	71	82

NO.	DATE	REVISIONS	BY	APP'D
3				
2				
1				

DEPARTMENT OF TRANSPORTATION-KANSAS

STANDARD STRUCTURAL SIGN SUPPORTS
CANTILEVER TYPE OVERHEAD
STEEL SUPPORT DETAILS

8-75

SHEET NO. 71 CHKD.	SCALE	APP'D	
DESIGNED DP/WLS	DETAILED LES	QUANTITIES	TRACED
DESIGN CK. NLW	DETAIL CK. DPE	QUAN. CK.	TRACE CK.

STATE	PROJECT NO.	YEAR	SHEET NO.	TOTAL SHEETS
KANSAS	235-87 KA-0161-04	2015	1522	2119

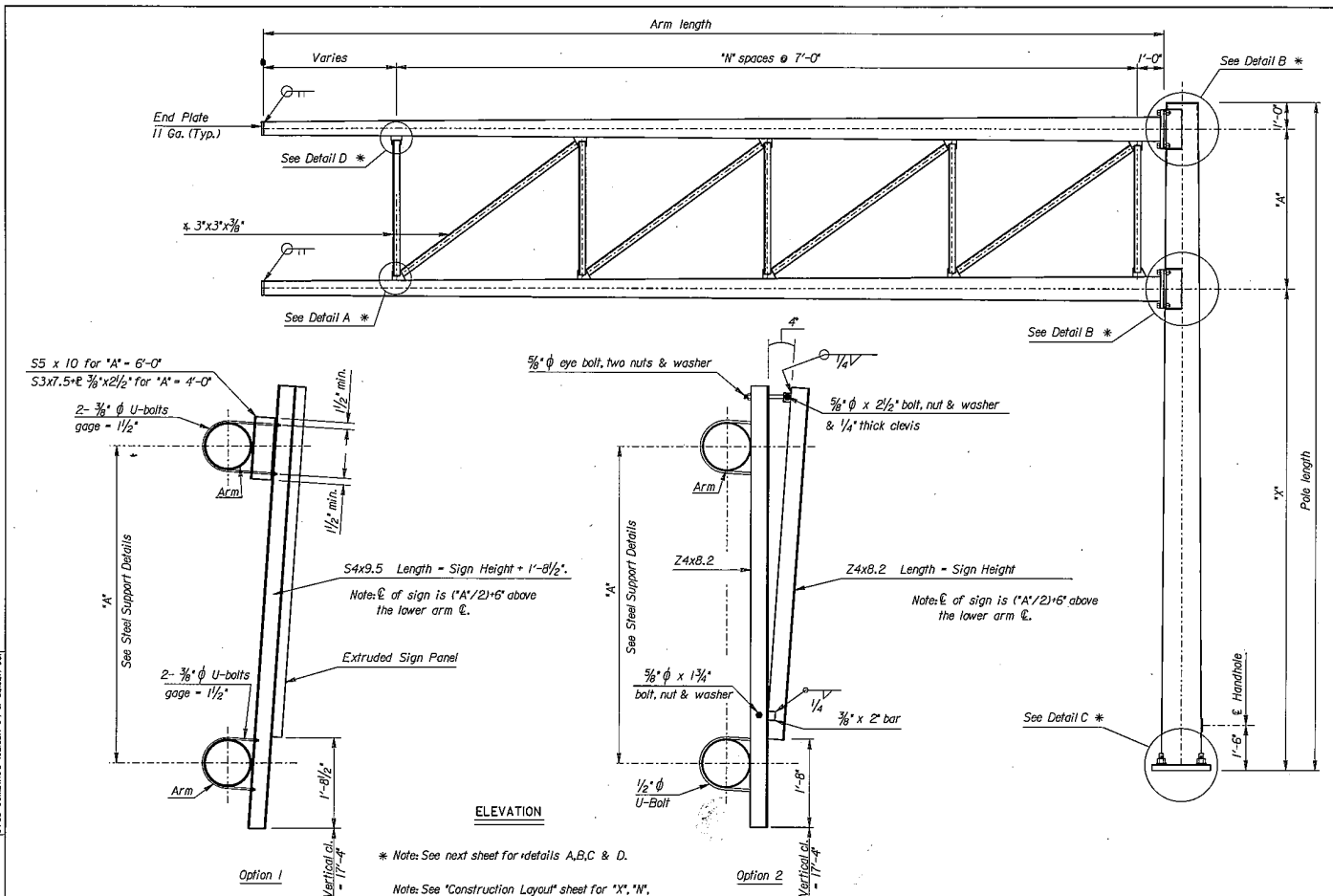

Note: The net area of the handhole frame bar shall not be less than 60 per cent of pole section removed. The pole section properties shall be maintained at the handhole.

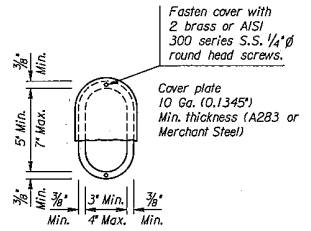

Elevation

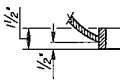

Partial Plan

HANDHOLE DETAIL

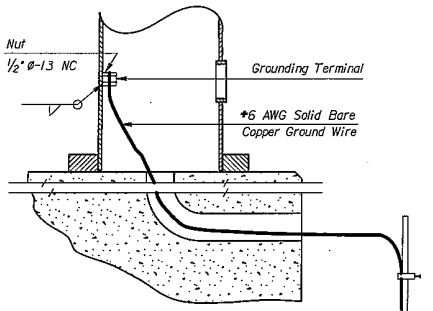

GROUNDING DETAILS

Dimension Design	Pole Dimension	Arm Dimension	A	T1	S	F	B.C.	W1	W2	P	T2	T3	G	E	H	J	Bolt Size	W3	W4
1	15" O.D. x 3 Ga. Wall	9.2" O.D. x 3 Ga. Wall	4'-0"	2"	1'-11"	1'-3 1/2"	1'-10"	3/8"	3/16"	7 3/8"	1 1/2"	1 1/4"	8 1/4"	1'-7 1/2"	1'-5 1/2"	7 1/4"	7/8" ϕ x 4 1/4"	3/8"	1/4"
2	18" O.D. x 3 Ga. Wall	11.0" O.D. x 7 Ga. Wall	6'-0"	2 1/2"	2'-2 1/2"	1'-6"	2'-1 1/2"	3/8"	3/16"	9 3/16"	1 1/2"	1 1/8"	9 1/2"	1'-9 1/2"	1'-5 1/2"	7 1/2"	3/4" ϕ x 4"	3/8"	3/16"
3	18" O.D. x 3 Ga. Wall	12.5" O.D. x 7 Ga. Wall	6'-0"	2 1/2"	2'-2 1/2"	1'-6"	2'-1 1/2"	3/8"	3/16"	9 3/16"	1 1/2"	1 1/8"	9 5/8"	1'-10 1/4"	1'-8 1/4"	8 5/8"	7/8" ϕ x 4 1/4"	3/8"	3/16"
4	18" O.D. x 0 Ga. Wall	12.5" O.D. x 7 Ga. Wall	6'-0"	2 1/2"	2'-2 1/2"	1'-6"	2'-1 1/2"	7/16"	1/4"	9 3/16"	1 1/2"	1 1/8"	9 5/8"	1'-10 1/4"	1'-8 1/4"	8 5/8"	7/8" ϕ x 4 1/4"	3/8"	3/16"
5	18" O.D. x 0 Ga. Wall	12.5" O.D. x 3 Ga. Wall	6'-0"	2 1/2"	2'-2 1/2"	1'-6"	2'-1 1/2"	7/16"	1/4"	9 3/16"	1 3/4"	1 3/8"	9 7/8"	1'-11 1/4"	1'-8 1/4"	8 3/8"	1" ϕ x 4 3/4"	3/8"	1/4"
6	18" O.D. x 0 Ga. Wall	13.0" O.D. x 0 Ga. Wall	6'-0"	2 1/2"	2'-2 1/2"	1'-6"	2'-1 1/2"	7/16"	1/4"	9 3/16"	1 7/8"	1 1/2"	10"	2'-0"	1'-9 1/2"	8 3/4"	1 1/8" ϕ x 5 1/4"	7/16"	5/16"

NO.	DATE	REVISIONS	BY	APP'D
2	2/14/15	Added DTI and Washer	KMP	TLF
1	5/2/11	Combined sheets SL152A-04 and SL152A-05	KMP	TLF

KANSAS DEPARTMENT OF TRANSPORTATION

STANDARD STRUCTURAL SIGN SUPPORTS
CANTILEVER TYPE OVERHEAD
STEEL SUPPORT DETAILS
TAPERED TUBE ALTERNATE

SL152B-01

FHWA APPROVAL		6-9-2014	APP'D	Terry L. Fleck	
DESIGNED	LES	DETAILED	LES	QUANTITIES	CADD DJE
DESIGN CK.	MAG	DETAIL CK.	MAG	QUAN. CK.	CADD CK. LES

KDOT Graphics Certified

KDOT Graphics Certified 08-04-2015

Sheet No. 1522

Std. Base Files:
Plotted By: lgood | Plot Locations
File: K:\01\61\04\pic-52.dgn
Plot Date: 8/7/2015 | Stds Combined (SL152A-04 & SL152A-05)

STATE	PROJECT NO.	YEAR	SHEET NO.	TOTAL SHEETS
KANSAS	235-87 KA-0161-04	2015	1523	2119

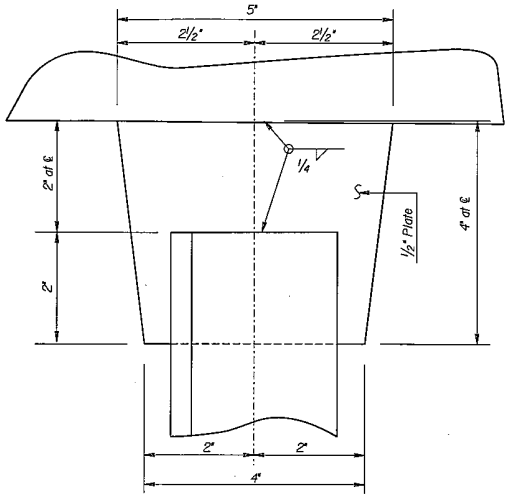

DETAIL D

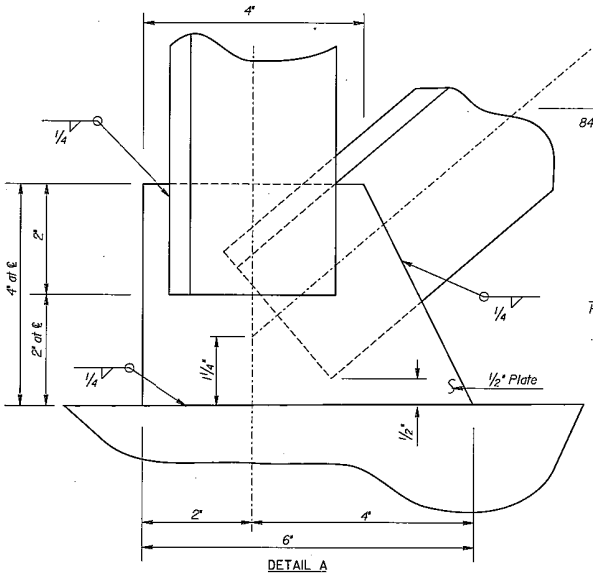

DETAIL A

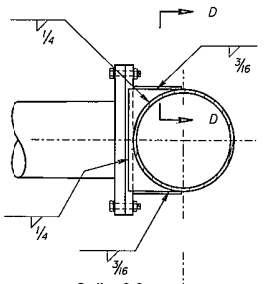

Section C-C

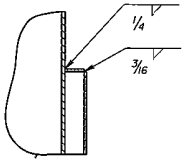

Section D-D

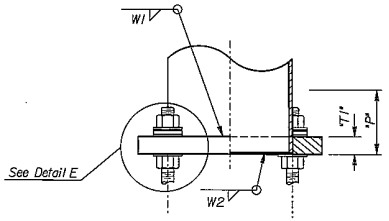

Elevation & Section

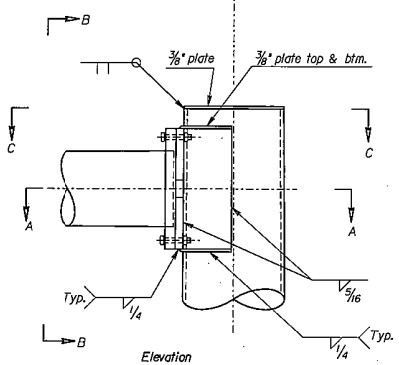

Elevation

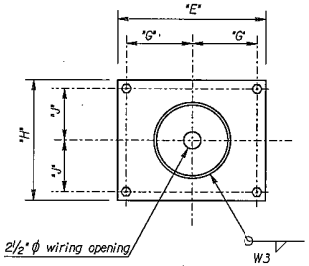

Section B-B

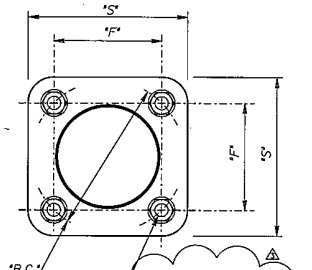

Plan

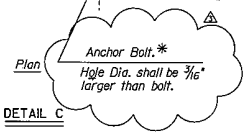

DETAIL C

* Adhere to KDOT standard specifications 1600 (grade 55).

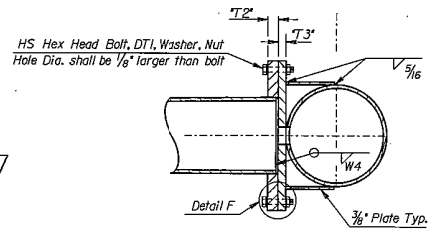

Section A-A

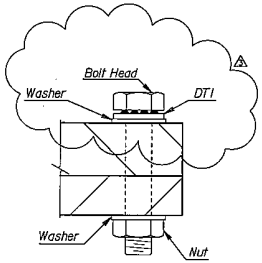

DETAIL F

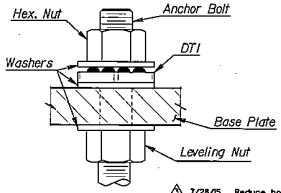

DETAIL E

NO.	DATE	REVISIONS	BY	APP'D
	7/28/15	Reduce hole size in base ℄ & Add washer to Detail F	KMP	CER
2	2/14/13	Added DTI and Washer	KMP	TLF
1	5/1/12	Update anchor bolt callout	KMP	TLF

KANSAS DEPARTMENT OF TRANSPORTATION

STANDARD STRUCTURAL SIGN SUPPORTS
CANTILEVER TYPE OVERHEAD
STEEL SUPPORT DETAILS
TAPERED TUBE ALTERNATE

~~SLI52B-02~~

FHWA APPROVAL			5-8-2008	APP'D	Terry L. Fleck
DESIGNED	LES	DETAILED	LES	QUANTITIES	TRACED DJC
DESIGN CK.	MAG	DETAIL CK.	MAG	QUAN.CK.	TRACE CK. LES

KDOT Graphics Certified 08-04-2015

Sheet No. 1523

KDOT Graphics Certified

Std. Base File: SLI52B-02.dgn
Plotted By: jgood
Plot Location:
Files: KA0161O4pss-63.dgn
Plot Date: 8/7/2015

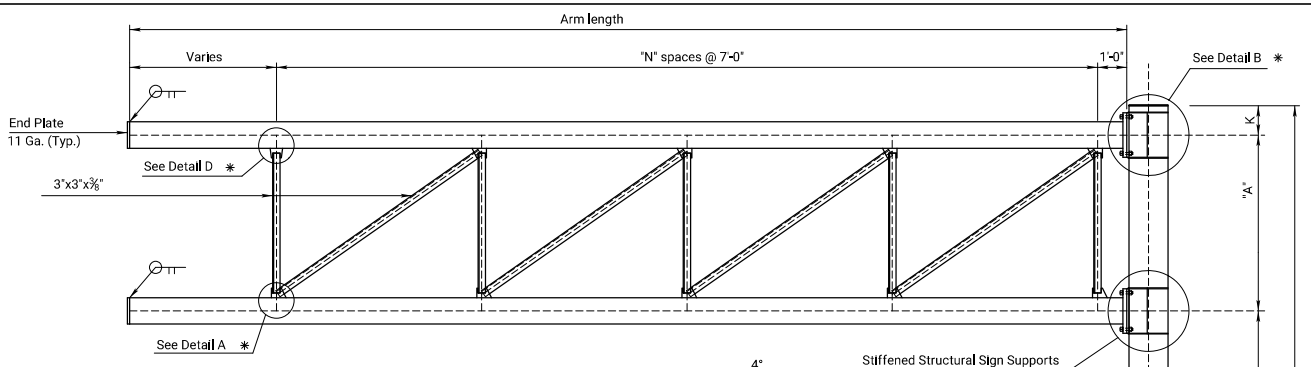

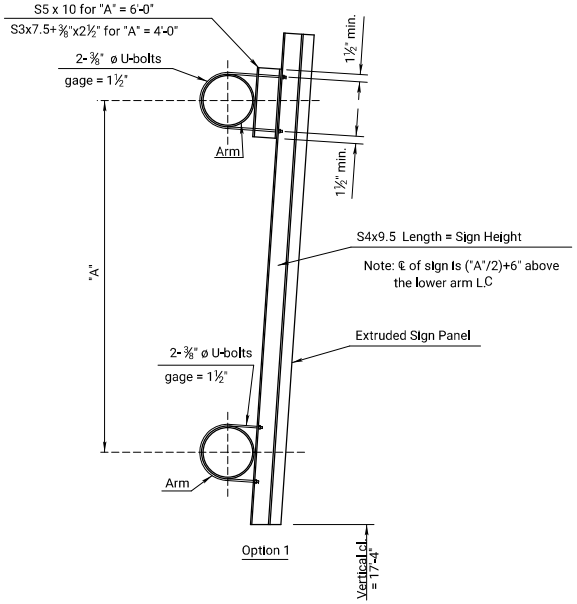

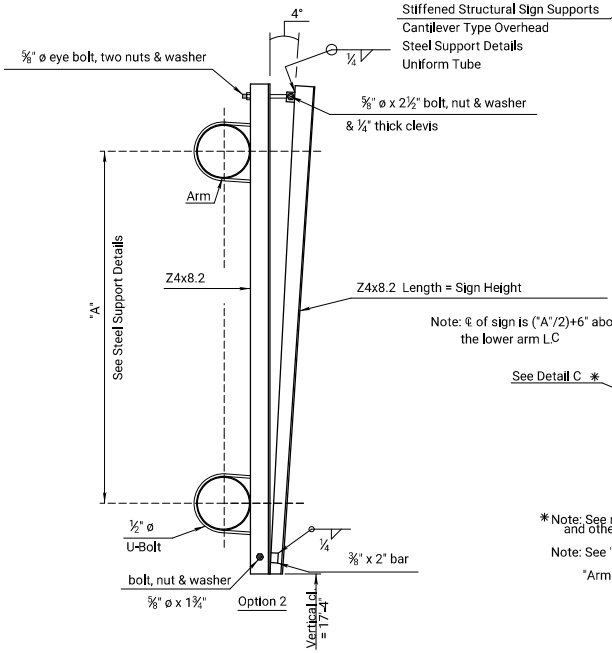

ELEVATION

✳ Note: See next sheet SL152C-04 for details A,B,C & D. and other dimension references.

Note: See "Construction Layout" sheet for "X", "N", "C", "Arm Length" and "Design No."

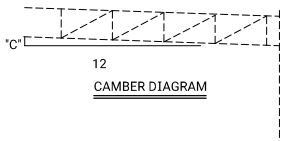

CAMBER DIAGRAM

Dimension / Design	Pole Dimension	Arm Dimension	A	T1	S	T2	T3	G	E	H	J	K	P	Bolt Size	W3	W4
7	18.0" O.D.x Schedule 60	14.0" O.D.x 5/8"	6'-0"	3"	2'-9"	2"	1 1/8"	1'-1 1/8"	2'-7 1/2"	2'-8"	1'-2"	1'-6"	6"	1 1/8" ø 5"	7/16"	5/16"
8	20.0" O.D.x Schedule 60	14.0" O.D.x 3/4"	6'-0"	3"	2'-9"	2"	1 1/8"	1'-2 1/8"	2'-9 1/2"	2'-8"	1'-2"	1'-6"	6"	1 1/8" ø 5"	7/16"	5/16"

STATE	PROJECT NO.	YEAR	SHEET NO.	TOTAL SHEETS
KANSAS				

NO.	DATE	REVISIONS	BY	APP'D
1	11/12/19	Current Version	KMP	MAH

KANSAS DEPARTMENT OF TRANSPORTATION
STIFFENED STRUCTURAL SIGN SUPPORTS
CANTILEVER TYPE OVERHEAD
STEEL SUPPORT DETAILS
UNIFORM TUBE

SL152C-03

FHWA APPROVAL	1-25-19	APP'D	Mark A. Hurt
DESIGNED KMP	DETAILED	QUANTITIES	CADD RAA
DESIGN CK. EMA	DETAIL CK.	QUAN.CK.	CADD CK. ECM

CADconform Certify This File

Sheet No.

Std. Base File:
Plotted By: Erik.Meyer
File: sl152c-03.dgn
Plot Date: 05-DEC-2019 15:53
Plot Location: Signing-Lighting
Stds Combined (SL152c-xx & SL152xx-06)

CADconform Certify This File

STATE	PROJECT NO.	YEAR	SHEET NO.	TOTAL SHEETS
KANSAS		0		

† Terminate weld ¼" ± ⅛" from edge of plate.

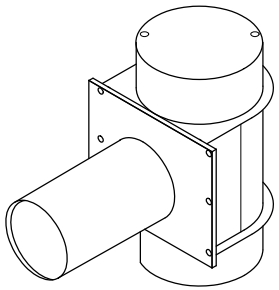

STIFFENED ARM CONNECTION

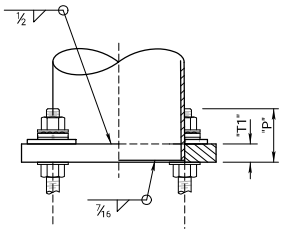

Elevation & Section

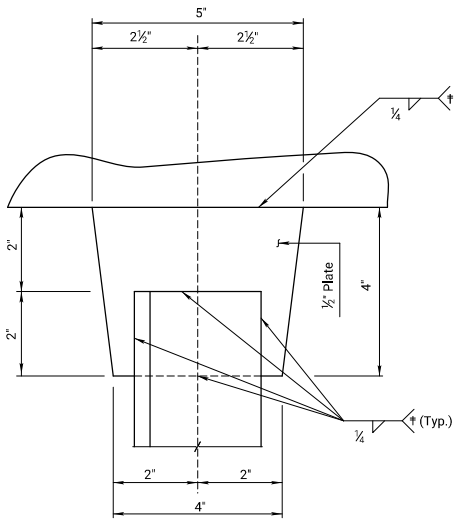

DETAIL D

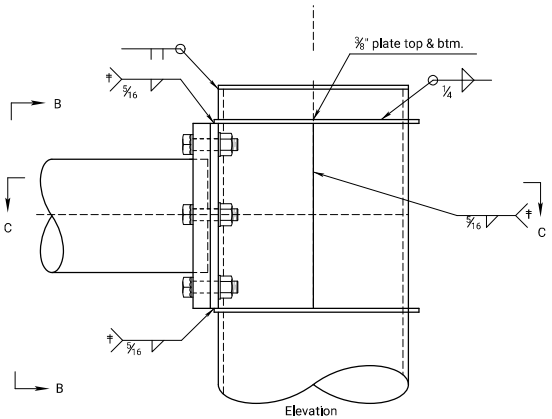

Elevation

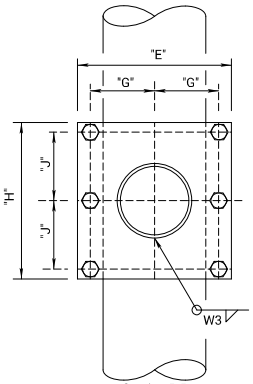

Section B-B

* Adhere to KDOT Standard Specification 1600 (Grade 55)

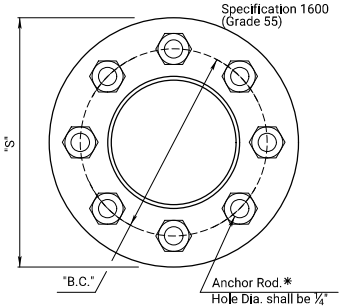

DETAIL C
Plan

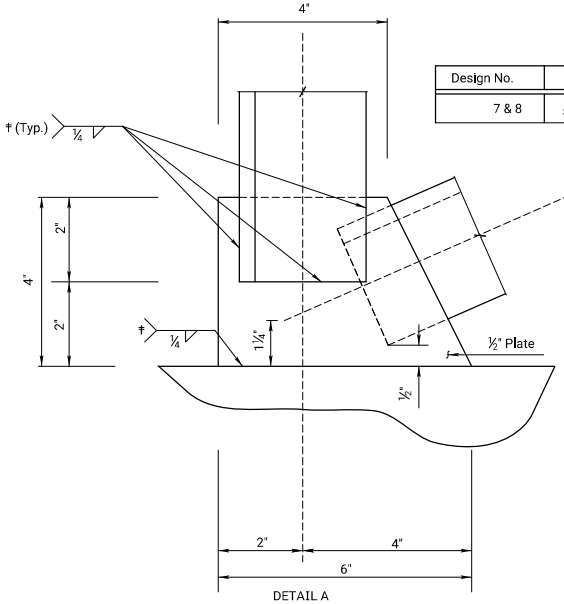

DETAIL A

Design No.	R
7 & 8	55.125

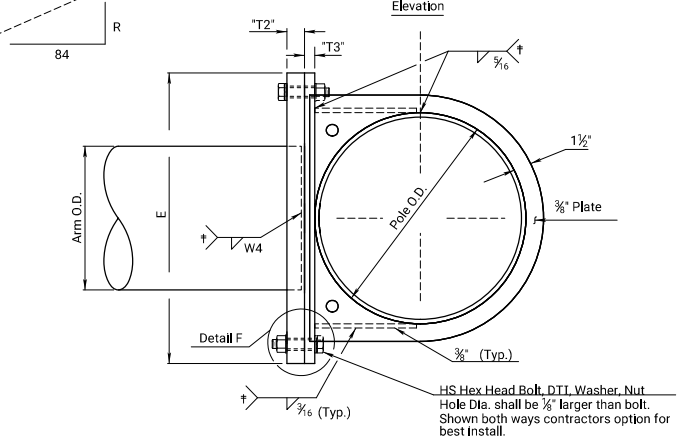

Section C-C

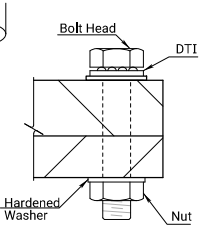

DTI INSTALLATION

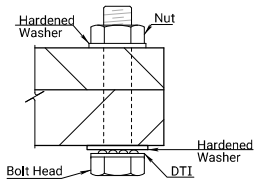

ALT. DTI INSTALLATION

NO.	DATE	REVISIONS	BY	APP'D
1	11/12/19	Current Version	KMP	MAH

KANSAS DEPARTMENT OF TRANSPORTATION
STIFFENED STRUCTURAL SIGN SUPPORTS
CANTILEVER TYPE OVERHEAD
STEEL SUPPORT DETAILS
UNIFORM TUBE

SL152C-04

FHWA APPROVAL		1-25-19	APP'D		Mark A. Hur
DESIGNED	KMP	DETAILED	QUANTITIES	CADD	RAA
DESIGN CK.	EMA	DETAIL CK.	QUAN.CK.	CADD CK.	ECM

CADconform Certify This File

Sheet No.

Std. Base File:
Plotted By: Erik.Meyer
File: sl152c04.dgn
Plot Date: 05-DEC-2019 15:53
Plot Location: Signing-Lighting

CADconform Certify This File

Structure 165 (KDOT Design #3, 1981 tapered)

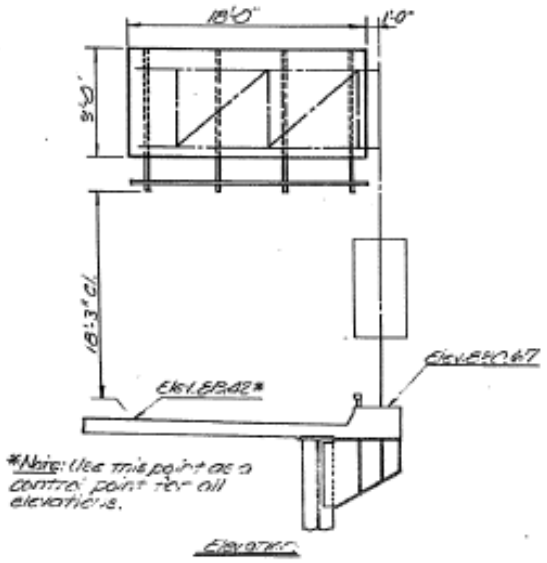

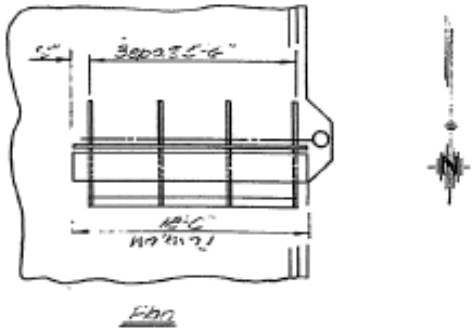

Structure No.	Y	Approx. Length	N
3	20'0"	18'-6"	2

Structure 309 (KDOT Design #7, 1981 tapered)

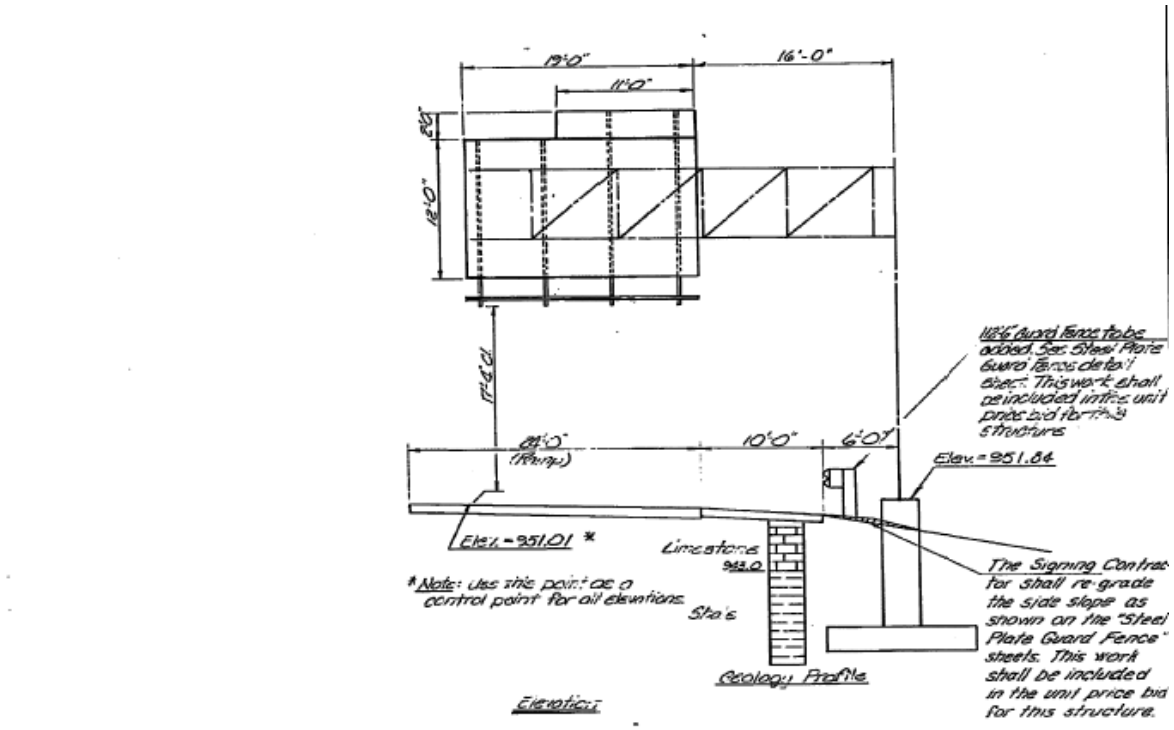

Note: Any pavement, paved shoulders, guard fence, etc. removed during construction of this portion, shall be restored to their original condition, at the Contractor's expense. Use saw cut joints to remove any concrete.

Note: The geology shown is the best information available to the Kansas Dept. of Transportation.

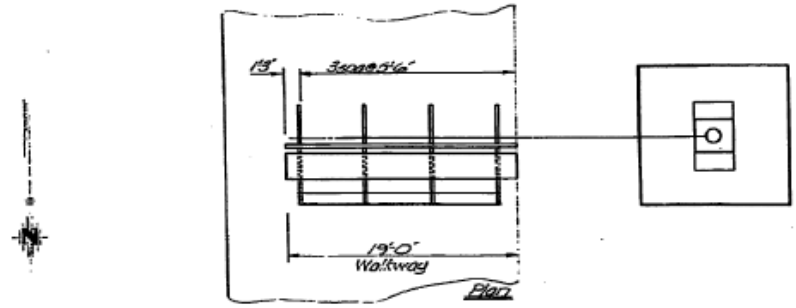

Station 358+02 (± C.L. I-435)

Cantilever Sign Supports Details			
Design No.	X	Arm Length	N
7	22'-0"	34'-0"	4

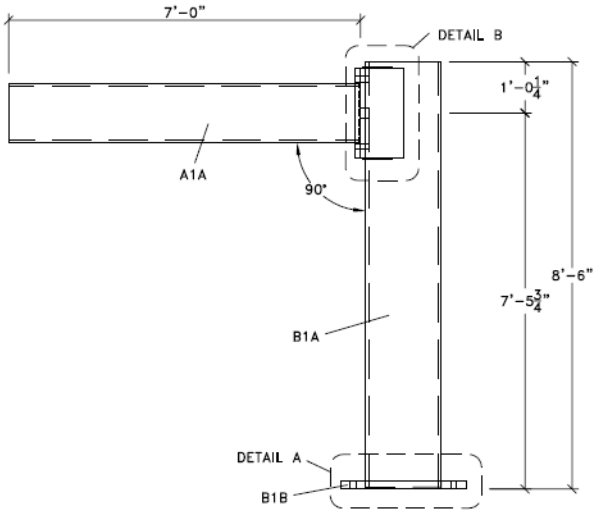

6 EA. MAST ARM ASSEMBLY A1
6 EA. COLUMN ASSEMBLY B1

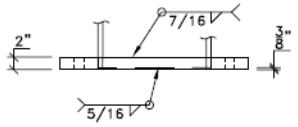

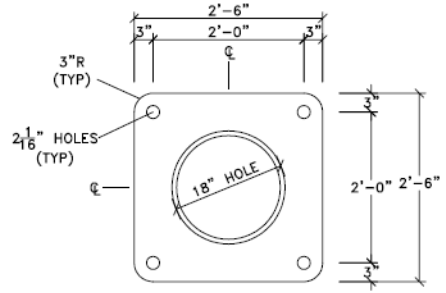

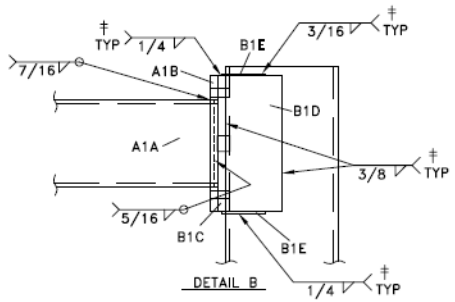

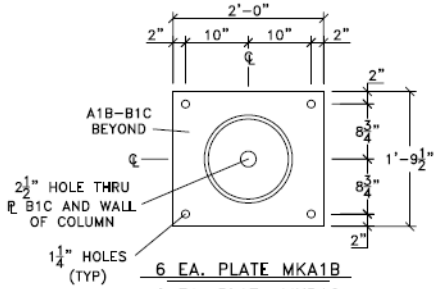

6 EA. PLATE MKA1B
6 EA. PLATE MKB1C

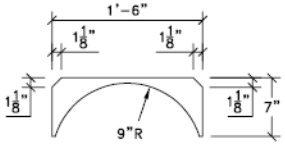

12 EA. PLATE MKB1E

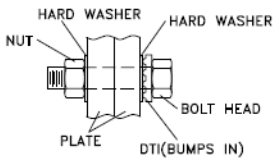

TYPICAL BOLT INSTALLATION

⚠ REVISED ENTIRE SHEET 4-23-21

MATERIAL LIST

QTY.	MK.	DESCRIPTION	SIZE FEET	SIZE INCHES	SPECIFICATION
6	A1A	14"O.D.x1/2"w TUBE	6	11 5/8	ASTM A500 GrB (GALV TO A123)
6	B1A	18" STD. PIPE (.375w)	8	5 5/8	↓↓
6	B1B	2"x2'-6" PLATE	2	6	A36
6	A1B	1 1/4"x1'-9 1/2" PLATE	2	0	
6	B1C	↓↓ ↓↓ ↓↓	2	0	
12	B1D	7/16"x9" PLATE	1	9 1/2	
12	B1E	3/8"x7" PLATE	1	6	↓↓ ↓↓
24		1 1/8" HHMB	0	4 1/2	A325 (GALV TO A153)
24		1 1/8" HEX NUT			A563DH
48		1 1/8" HARD WASHER			F436 ↓↓
24		1 1/8" DTI			↓↓ F959 B695

‡ TERMINATE WELD ¼" (±)⅛" FROM END OF PLATE

JOB #21074

STEVE JOHNSON COMPANIES
1555 S TYLER ROAD
WICHITA, KANSAS 67209
PHONE: (316) 722-2660
FAX: (316) 729-6356
sjohnson@stevejohnsoncompanies.com

PROJECT: TEST STRUCTURES

CUSTOMER: UNIVERSITY OF KANSAS

DATE: APRIL 12, 2021 | DRAWING NUMBER: 1 OF 1

Appendix B. Hand Calculation Examples

B.1. Full-Sized Model Loading Example

*Uses tD7L Structure

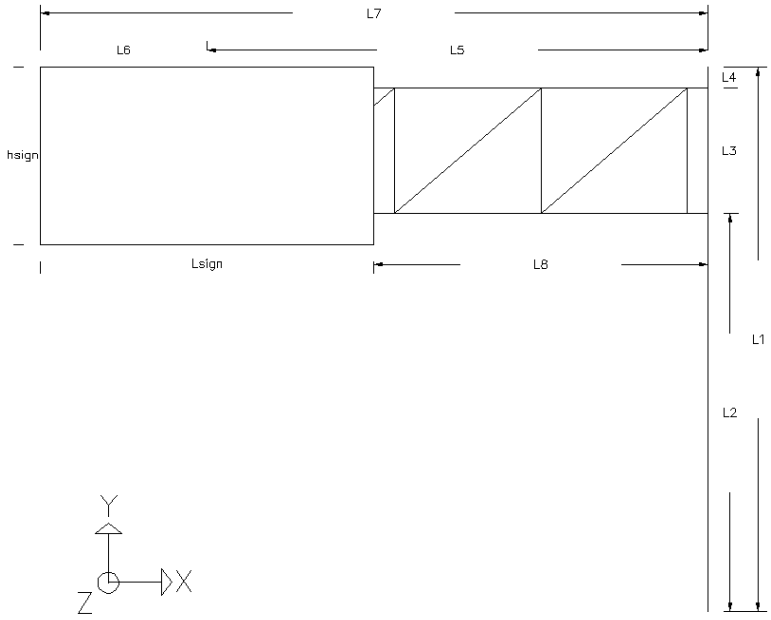

Dimensions

L_1= 29 ft.	L_2= 22 ft.	$L_{3=}$ 6 ft.
L_4= 1 ft.	L_8= 15 ft.	L_7= 34 ft.
L_5= 24.5 ft.	L_{sign}= 19 ft.	h_{sign}= 12 ft.
d_{pole}= 18 in.	d_{pole_tip}= 13.94 in.	
d_{arm}= 13 in.	$d_{arm\text{-}tip}$= 8.24 in.	taper= 0.14”/ft.

Pressures

I_F =1 $C_{d(sign)}$= 1.12 $C_{d(pole/arm)}$= 1.1

Galloping

$P_G = 21*I_F = 21$ psf

Natural Wind

$P_{NW} = 5.2*Cd*I_F$

$P_{NW(Sign)} = 5.82$ psf $P_{NW(Arm/Pole)} = 5.72$ psf

Truck-Induced Wind Gusts

$P_{TG} = 18.8*Cd*I_F$

$P_{TG(Sign)} = 21.06$ psf $P_{TG(Arm)} = 20.68$ psf

Forces for Abaqus Models

Galloping

Applied as a line load- $P_G*(h_{sign}*12)= 21*(12*12)= 3{,}024$ lb/ft= 21 lb/in

Natural Wind

Sign: applied as pressure- $P_{NW(Sign)}= 5.82$ psf= 0.0404 psi

$d_{pole\_avg}= \frac{d_{pole}+d_{pole\_tip}}{2} = 15.97$ in.

$d_{arm\_avg}= \frac{d_{arm}+d_{arm\_tip}}{2} = 10.62$ in.

Arm: applied as line load- $(P_{NW(Arm)} *(\frac{d_{arm\_avg}}{12})= 5.06$ lb/ft= 0.42 lb/in

Pole: applied as line load- $P_{NW(Pole)}* (\frac{d_{pole\_avg}}{12})= 7.61$ lb/ft= 0.63 lb/in

Pole and Arm loads were multiplied by mesh size for that area of application.

Example: 0.63 lb/in*0.01 mesh= 0.0063 lb/in

Truck-Induced Wind Gusts

$P_{TG(Sign)}$ = 21.06 psf= 0.146 psi $P_{TG(Arm)}$ = 20.68 psf= 0.144 psi

*These values were inputted into Excel at P_{TG} at 20 ft to 0 at 30 ft so that linear equations could be obtained and the TIWG values for each sign and arm height would be correct. If H_{Sign_Edge} or H_{Arm} is below 20 ft (240 in.) than P_{TG} is as shown above.

$P_{TG(Sign)}$ = -0.0009*H_{Sign_edge}+0.3712 $P_{TG(Arm)}$ = -0.0009H_{Arm}+0.3646

Sign

H_{Sign_edge}= L_2-($\frac{h_{sign}-L_3}{2}$)= 19 ft.= 228 in.

$P_{TG(Sign)}$= 0.146 psi

Arm (applied as line loads)

Top Arm (H_{Arm_T})= L_1-1-$\frac{d_{arm}/_2}{12}$= 27.46 ft.= 329.5 in.

$P_{TG(Arm\_T)}$= 0.0611 psi

$F_{TG(Arm\_T)}$= $P_{TG(Arm\_T)}$*d_{arm}= 0.795 lb/in

Bottom Arm (H_{Arm_B})= L_2+$\frac{d_{arm}/_2}{12}$= 22.54 ft.= 270.5 in.

$P_{TG(Arm\_T)}$= 0.1155 psi

$F_{TG(Arm\_T)}$= $P_{TG(Arm\_T)}$*d_{arm}= 1.501 lb/in

*F_{TG} is than multiplied by the mesh size for the area of application

Example: Top Arm- 0.795 lb/in*0.5= 0.397 lb/in

B.2. Stress Analysis Example

***Based on AASHTO SLT (2015) Connection Detail Categories and Examples in NCHRP 469**

***Example uses tD7L Structure**

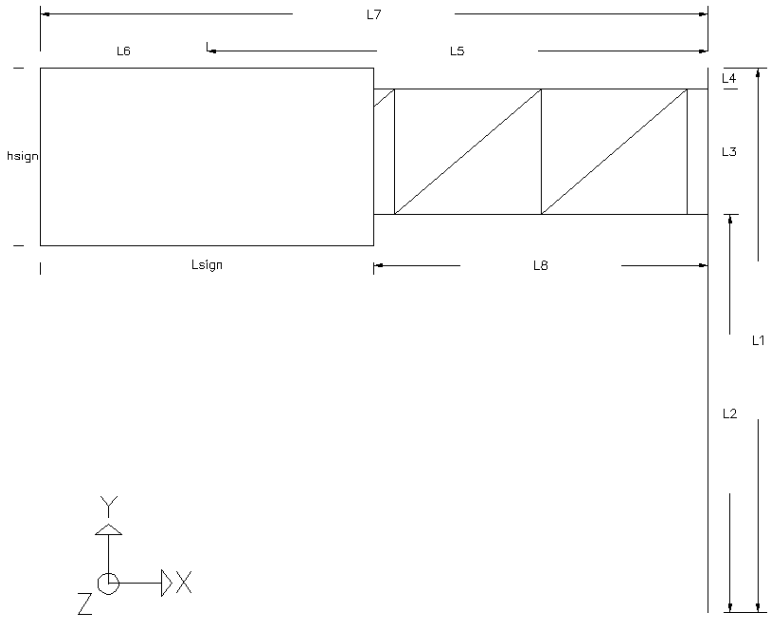

Dimensions

Pole

Pole Height (L_1)= 29 ft.

Pole Height to Bottom Box CL (L_2)= 22 ft.

Bottom Box CL to Top Box CL (L_3)= 6 ft.

Top Box CL to Top of Pole (L_4)= 1 ft.

Diameter (d_{pole})= 18 in.

Thickness (t_{pole})= 0.3125 in.

Dia. @ Pole Tip (d_{pole_tip})= 13.94 in.

Arm

Mast-Arm Length (L_7)= 34 ft.

Length to Sign (L_8)= 15 ft.

Length to CL of Sign (L_5)= 24.5 ft.

Diameter (d_{arm})= 13 in.

Thickness (t_{arm})= 0.3125 in.

Pole and Arm taper= 0.14”/ft.

Dia. @ Arm Tip (d_{arm_tip})= 8.24 in.

Sign

Sign Height (h_{sign})= 12 ft.

Sign Length (L_{sign})= 19 ft.

t_{sign}= 0.03125 in.

Sign mid-length (L_6)= 9.5 ft.

Forces

I_F =1 $C_{d(sign)}$= 1.12 $C_{d(pole/arm)}$= 1.1

Galloping

$P_G = 21*I_F = 21$ psf

$F_G = P_G*(A_{sign})_V = 21*(h_{sign})*(L_{sign})$= 4,788 lb= 4.79 kip

Natural Wind

$P_{NW} = 5.2*Cd*I_F$

$P_{NW(Sign)} = 5.82$ psf $P_{NW(Arm/Pole)} = 5.72$ psf

$F_{NW(Sign)} = P_{NW(Sign)}*(A_{sign})_V = 5.82*(h_{sign})*(L_{sign})$= 1,329.96 lb= 1.33 kip

$d_{pole\_avg}= \frac{d_{pole}+d_{pole\_tip}}{2}$ = 15.97 in.

$d_{arm\_avg}= \frac{d_{arm}+d_{arm\_tip}}{2}$ = 10.62 in.

$F_{NW(Pole)} = P_{NW(Pole)}*(A_{pole})_V = 5.72*L_1*(\frac{d_{pole\_avg}}{12})$= 220.76 lb= 0.22 kip

$F_{NW(Arm)} = P_{NW(Arm)}*(A_{arm})_V = 5.72*L_8*(\frac{d_{arm\_avg}}{12})$= 59.42 lb= 0.06 kip

Truck-Induced Wind Gusts

*As per the requirements of Section 11.7.4, the equivalent static pressure is to be applied along the outer 12 ft length of the mast-arm. (NCHRP 469 Appendix B and AASHTO SLT 2015)

$P_{TG} = 18.8*Cd*I_F$

$P_{TG(Sign)} = 21.06$ psf $\quad P_{TG(Arm)} = 20.68$ psf

$F_{TG(Sign)} = P_{TG(Sign)}*(A_{sign})_V = 21.06*(\frac{t_{sign}}{12})*(12') = 400.06$ lb= 0.40 kip

$d_{12\_arm}= d_{arm\_tip}+.14*1' = 8.38$ in.

$d_{arm\_12\_avg}= \frac{d_{12\_arm}+d_{arm\_tip}}{2} = 8.31$ in.

$F_{TG(Arm)} = P_{TG(Arm)}*(A_{arm})_V = 20.68*12'*(\frac{d_{arm\_12\_avg}}{12}) = 171.85$ lb= 0.17 kip

Moments

The bending moment at the centerline of the column:

$M_{z\_G} = F_G*L_5 = 117.31$ k*ft= 1,407.67 k*in

The bending moment at the base of the column:

$M_{x\_NW} = F_{NW(Pole)}*(\frac{L_1}{2}) + F_{NW(Arm)}*(L_2 + L_3) + F_{NW(Arm)}*L_2 + F_{NW(Sign)}*(L_2 + \frac{L_3}{2}) = 39.37$ k*ft= 472.42 k*in

The bending moment at the mast-arm connection:

$M_{y\_NW} = 2* F_{NW(Arm)}*(\frac{L_8}{2}) + F_{NW(Sign)}*L_5 = 33.66$ k*ft= 403.94 k*in

The bending moment at the centerline of the column:

$M_{z\_TG} = (F_{TG(Arm)} + F_{TG(Sign)})*(L_7 - L_3) = 192.16$ k*ft= 16.01 k*in

Stress Ranges

Pole-to-Baseplate Socket Connection (Detail 5.4: Cat E', CAFT=2.6 ksi)

$I_{pole}=(\frac{\pi}{64}) * [{d_{pole}}^4 - (d_{pole} - 2t_{pole})^4]$= 679.27 in^4

$(S_R)_{G\_pole}= \frac{M_G \frac{d_{pole}}{2}}{I_{pole}}$= 16.55 ksi

$(S_R)_{NW\_pole}= \frac{M_{x\_NW} \frac{d_{pole}}{2}}{I_{pole}}$= 5.55 ksi

Inadequately designed

Mast-Arm-to-Endplate Socket Connection (Detail 5.4: Cat E', CAFT=2.6 ksi)

$I_{arm}=(\frac{\pi}{64}) * [{d_{arm}}^4 - (d_{arm} - 2t_{arm})^4]$= 250.78 in^4

$(S_R)_{G\_arm}= \frac{M_G \frac{d_{arm}}{2}}{I_{arm}}$= 29.81 ksi

$(S_R)_{NW\_arm}= \frac{M_{z\_NW} \frac{d_{arm}}{2}}{I_{arm}}$= 12.24 ksi

Inadequately designed

KDOT's Alternative $(S_R)_{NW\_arm}$ Equation

$(S_R)_{NW\_arm}= \frac{\frac{M_{z\_NW} d_{arm}}{2}}{I_{arm}}$= 6.12 ksi

Inadequately designed

Built-up Box Connection

Dimensions

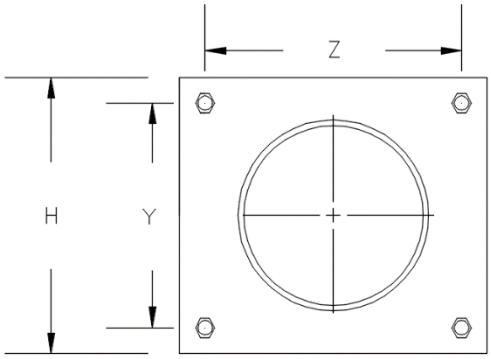

Y= 17.5 in. Z= 20 in. H= 21.5 in.

$t_{side\text{-}plate}$= 0.4375 in. $d_{pole\_BB\_CL}$= 14.92 in. $d_{pole\_TB\_CL}$= 14.08 in.

$I_{x\_box}=\frac{2*t_{side-plate}*H^3}{12}+2*t_{side\text{-}plate}*d_{pole}*(\frac{H}{2}+\frac{t_{side-plate}}{2})^2$

Bottom Box: 1,140.88 in^4

Top Box: 1,098.65 in^4

$I_{y\_box}=\frac{2*t_{side-plate}*d_{pole}{}^3}{12}+2*t_{side\text{-}plate}*H*(\frac{d_{pole}}{2}+\frac{t_{side-plate}}{2})^2$

Bottom Box: 1,061.22 in^4

Top Box: 938.5 in^4

Built-up-Box-to-side-plate Connection (Detail 5.3: Cat. E', CAFT=2.6 ksi) and Box-to-Pole (Detail 5.5 note b: Branching Member: box) (Cat ET, CAFT=1.2 ksi)

$(SR)_G=\frac{M_G*\frac{H}{2}}{I_{x\_box}}$

Bottom Box: 13.26 ksi

Top Box: 13.77 ksi

$(SR)_{y\_NW}=\frac{M_{y\_NW}*\frac{d_{pole}}{2}}{I_{y\_box}}$

Bottom Box: 2.84 ksi

Top Box: 3.03 ksi

***Inadequately designed**

Box-to-Pole (Detail 5.5 note b: main member: pole) (Cat. K_2, CAFT=1 ksi)

$(S_R)_{main\_in\text{-}plane} = (S_R)_{box,G} * \frac{t_{side-plate}}{t_{pole}} * 0.67$

Bottom Box: 12.44 ksi

Top Box: 12.92 ksi

$(S_R)_{main\_out\text{-}of\text{-}plane} = (S_R)_{box,NW} * \frac{t_{side-plate}}{t_{pole}} * 1.5$

Bottom Box: 5.96 ksi

Top Box: 6.36 ksi

If r/t ratio of pole at location of mast-arm is less than 24, limit is 1 ksi.

If r/t ratio of pole is greater than 24, limit is: $(F)_n = (\Delta F)_n^{K_2} * (\frac{24}{r/t})^2$ (ksi)

r/t ratio= 23.87 at bottom box and 22.53 top box- limit is 1 ksi

****Inadequately designed***

Pole below Box (Detail 5.5 note b: Cat. E, CAFT=4.5 ksi)

$I_{pole} = (\frac{\pi}{64}) * [{d_{pole}}^4 - (d_{pole} - 2t_{pole})^4]$

Bottom Box: 382.68 in^4

Top Box: 320.41 in^4

$(S_R)_G = \frac{M_G \frac{d_{pole}}{2}}{I_{pole}}$

Bottom Box: 27.44 ksi

Top Box: 30.93 ksi

$(S_R)_{y\_NW} = \frac{M_{y\_NW} \frac{d_{pole}}{2}}{I_{pole}}$

Bottom Box: 7.87 ksi

Top Box: 8.88 ksi

****Inadequately designed***

Appendix C. Data from Past Research

Table C.1. Baseplate Cracking

Source	Specimen	N	σ_R, ksi (MPa)	Socket Connection Type	Box Type
In-Plane (IP) Loading					
Roy	2.1	2.39E+06	6.90 (47.57)	Full Penetration Socket Weld	Gusseted
	4A.1	4.56E+07	7.82 (53.88)		
	4A.2	4.56E+07	7.53 (51.89)		
	1.5	2.36E+07	4.36 (30.03)		Ring-Stiffened
	1.7	2.83E+07	3.15 (21.71)		

Table C.2. Handhole Cracking

Source	Specimen	N	σ_R, ksi (MPa)	Socket Connection Type	Box Type
In-Plane (IP) Loading					
Roy	2.1	2.39E+06	7.00 (48.26)	Full Penetration Socket Weld	Gusseted
	2.2	2.03E+06	7.00 (48.26)		
	2.3	2.97E+06	7.00 (48.26)		
	1.1	2.72E+06	7.00 (48.26)	Fillet-Welded Socket	Ring-Stiffened
	1.2	3.77E+06	7.00 (48.26)		
	1.3	3.27E+06	7.00 (48.26)		
	1.4	2.74E+07	4.69 (32.32)		
	1.6	4.10E+07	3.61 (24.90)		
	3.1	1.04E+07	7.34 (50.60)	Full Penetration Socket Weld	
	3.2	1.82E+07	9.07 (62.56)		
	3.3	9.79E+06	7.02 (48.42)		
	3.4	5.75E+07	8.60 (59.31)		
	3.5	4.48E+07	8.17 (56.30)		
	3.6	2.70E+07	6.39 (44.06)		
	3.7	3.62E+07	8.52 (58.72)		
	3.8	1.06E+07	9.22 (63.56)		
	3.10	1.03E+07	9.17 (63.22)		
Diagonal (Dia.) Loading					
Roy	4B.1	1.52E+07	7.25 (49.97)	Full Penetration Socket Weld	Gusseted
	4B.2	4.18E+06	5.80 (39.99)		

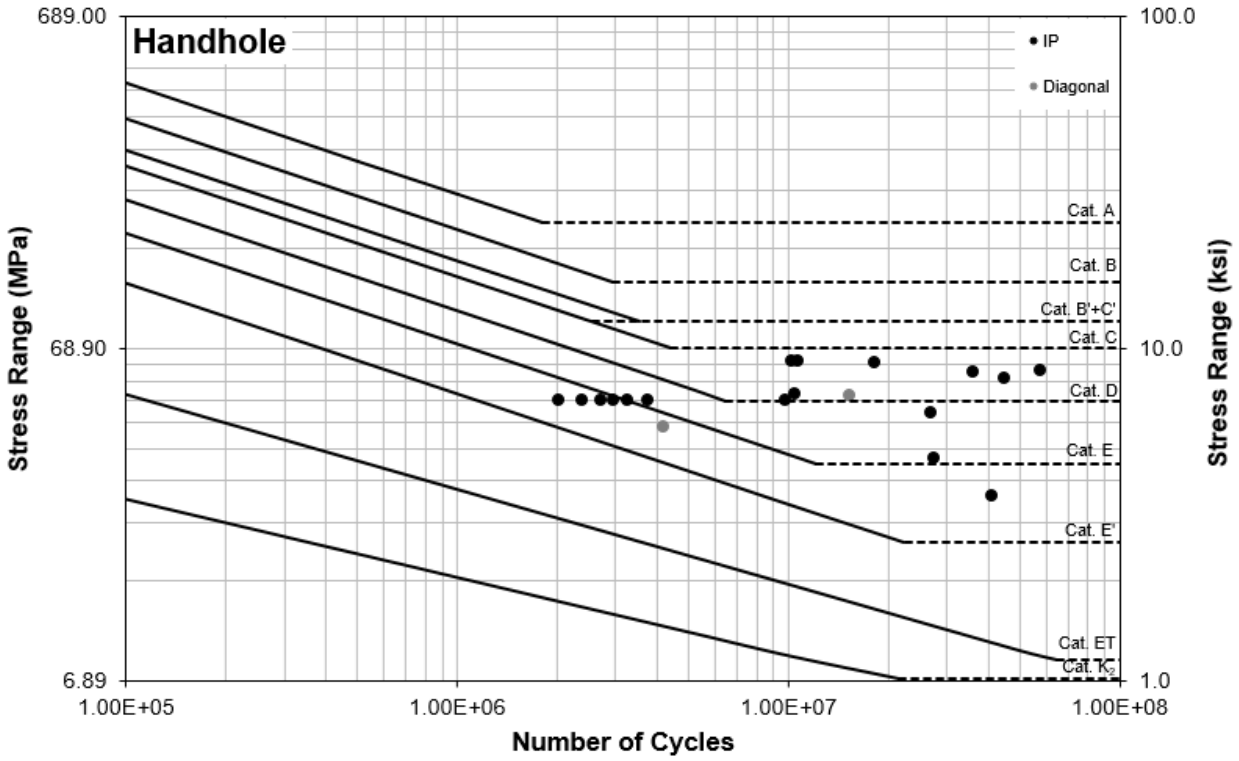

Figure C.1. S-N Curve for Handhole

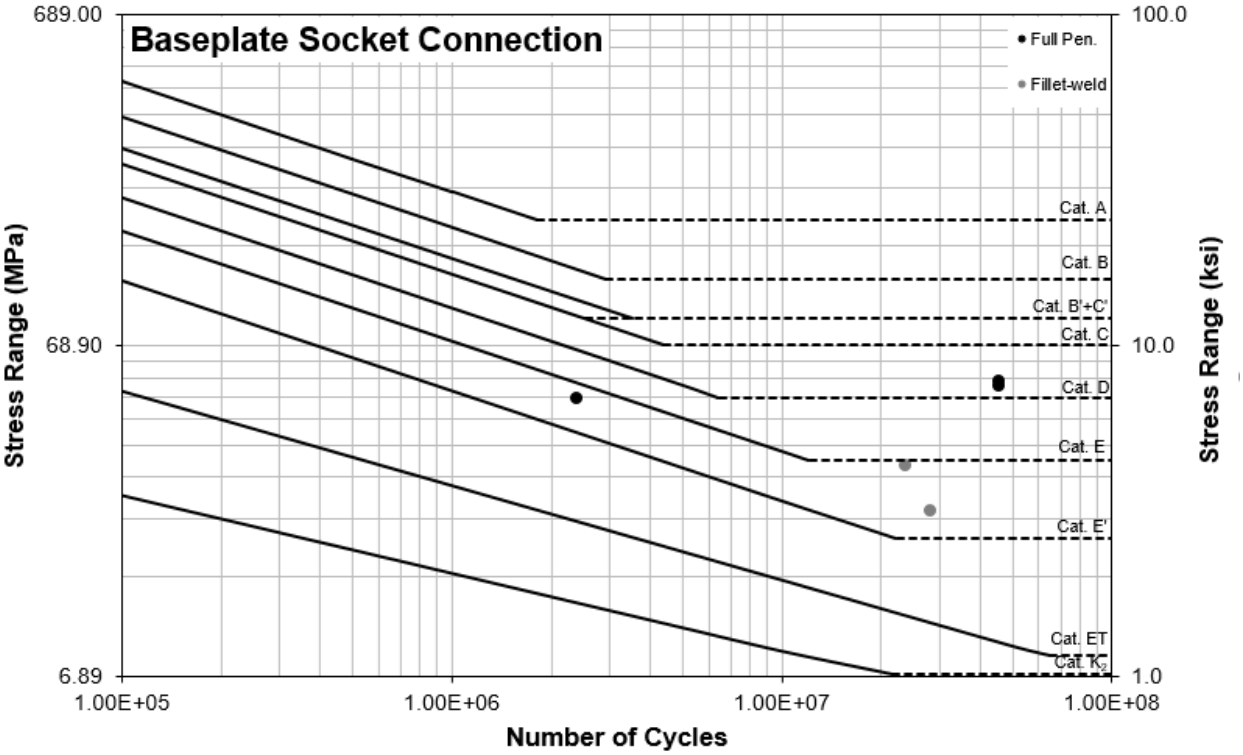

Figure C.2. S-N Curve for Baseplate Socket Connection

Appendix D. Finite Element Modeling Results

D.1. Tapered Tube Models

D.1.1. Matrix

Table D.1. Tapered Tube Model Matrix

	Sign Height, ft. (m)	Sign Length, ft. (m)	Arm Length, ft. (m)	Arm Dia., in. (cm)	Arm Thickness, in. (cm)	Pole Height, ft. (m)	Pole Dia. @ base, in. (cm)	Pole Dia. @ bottom box, in. (cm)	Pole Thickness, in. (cm)
Tapered Tube: Design #1/2									
Small	4 (1.22)	12 (3.66)	29 (8.84)	9.2 (23.37)	0.25 (0.64)	25 (7.62)	15 (38.1)	12.30 (31.24)	0.25 (0.64)
Medium	7.5 (2.29)	14.5 (4.42)	29 (8.84)			26 (7.92)		12.16 (30.89)	
Large	9 (2.74)	17.5 (5.33)	31 (9.45)			26 (7.92)		12.16 (30.89)	
Tapered Tube: Design #3									
Small	8 (2.44)	18 (5.49)	18 (5.49)	11 (27.94)	0.1875 (0.48)	27 (8.23)	18 (45.72)	15.30 (38.86)	0.25 (0.64)
Medium	8.5 (2.59)	19.5 (5.94)	31 (9.45)			27 (8.23)		15.30 (38.86)	
Large	9.5 (2.90)	18.5 (5.64)	30 (9.14)			30 (9.14)		14.88 (37.80)	
Tapered Tube: Design #7									
Small	6 (1.83)	11.5 (3.51)	30 (9.14)	13 (33.02)	0.3125 (0.79)	27 (8.23)	18 (45.72)	15.33 (38.94)	0.3125 (0.79)
Medium	10 (3.05)	15 (4.57)	31 (9.45)			32 (9.75)		14.63 (37.16)	
Large	12 (3.66)	19 (5.79)	34 (10.36)			29 (8.84)		15.05 (38.23)	

D.1.2. Hot Spot Analysis

Table D.2. Tapered Tube Model NW Hot Spot Stresses

	Hot Spot Stress, ksi (MPa)		
Model	Box	Arm	Baseplate
tD1S	10.44 (71.96)	9.19 (63.34)	3.64 (25.10)
tD1M	24.53 (169.12)	18.86 (130.07)	10.33 (71.22)
tD1L	36.17 (249.39)	28.38 (195.66)	14.86 (102.43)
tD3S	12.50 (86.17)	12.21 (84.22)	10.64 (73.35)
tD3M	27.65 (190.65)	25.40 (175.16)	12.68 (87.46)
tD3L	28.37 (195.64)	27.33 (188.44)	15.45 (106.53)
tD7S	8.11 (55.89)	8.55 (58.93)	4.64 (31.97)
tD7M	17.19 (118.51)	18.37 (126.64)	11.29 (77.83)
tD7L	17.85 (123.09)	18.80 (129.60)	13.39 (92.34)

Table D.3. Tapered Tube Model T+G Hot Spot Stresses

	Hot Spot Stress, ksi (MPa)		
Model	Box	Arm	Baseplate
tD1S	28.25 (194.77)	16.06 (110.74)	14.84 (102.32)
tD1M	51.49 (355.01)	32.03 (220.84)	33.97 (234.25)
tD1L	73.29 (505.31)	39.43 (271.86)	48.30 (333.02)
tD3S	20.88 (143.94)	13.29 (91.61)	18.50 (127.54)
tD3M	41.02 (282.86)	27.69 (190.92)	41.48 (285.98)
tD3L	50.52 (348.36)	29.90 (206.18)	40.94 (282.28)
tD7S	17.97 (123.90)	12.98 (89.50)	19.44 (134.01)
tD7M	35.98 (248.11)	24.26 (167.24)	33.80 (233.03)
tD7L	45.03 (310.51)	26.72 (184.22)	32.86 (226.54)

D.1.3. S-N Curves

Natural Wind (NW) S-N Curves

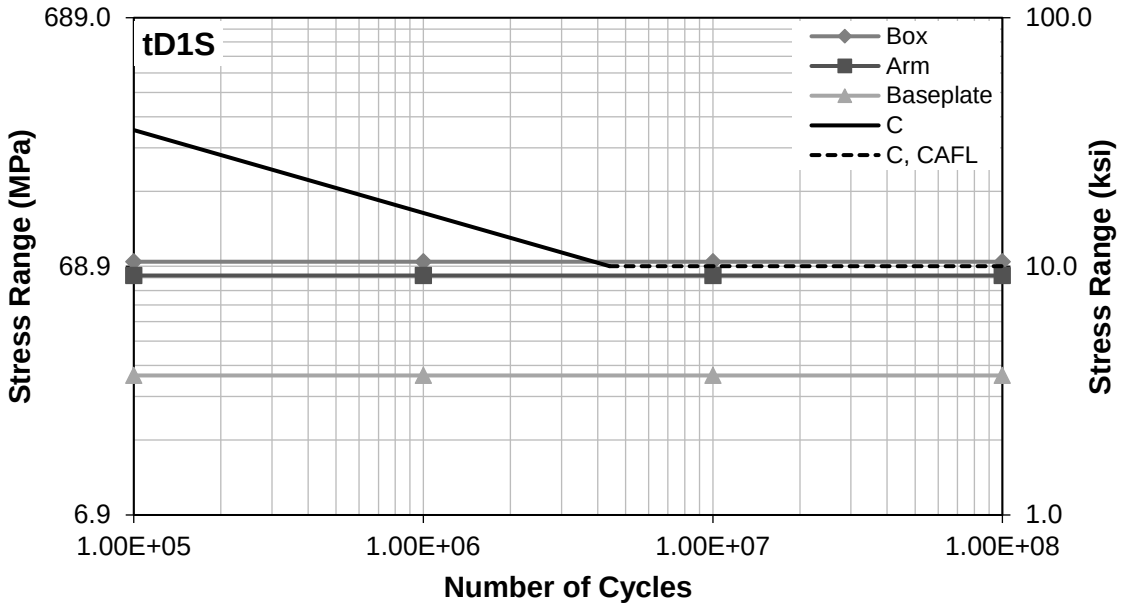

Figure D.1. S-N Curve for tD1S Hot Spot Stresses, NW

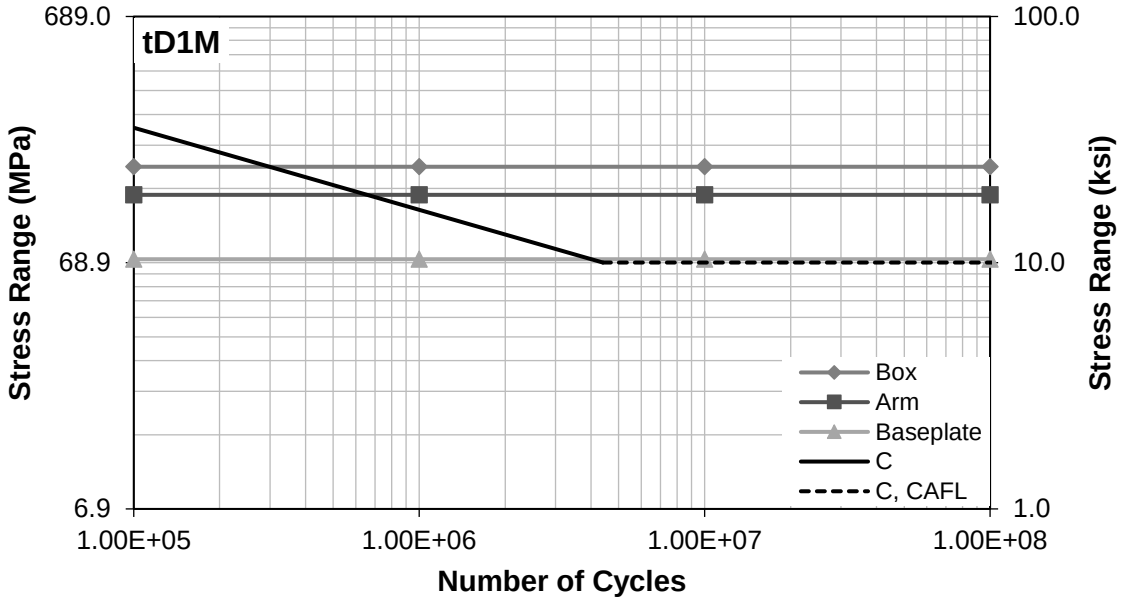

Figure D.2. S-N Curve for tD1M Hot Spot Stresses, NW

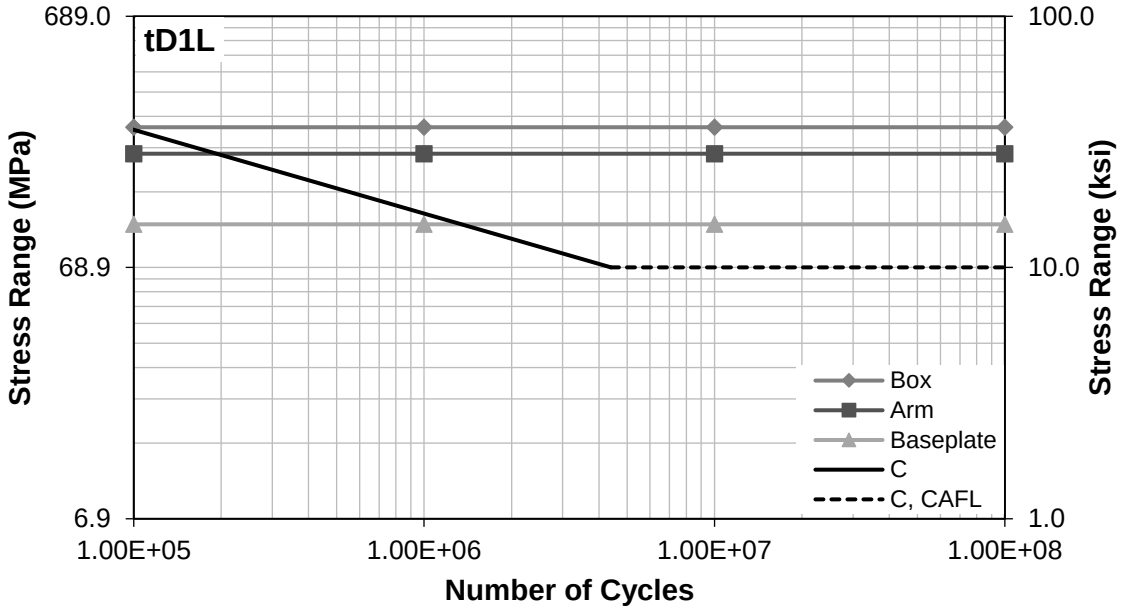

Figure D.3. S-N Curve for tD1L Hot Spot Stresses, NW

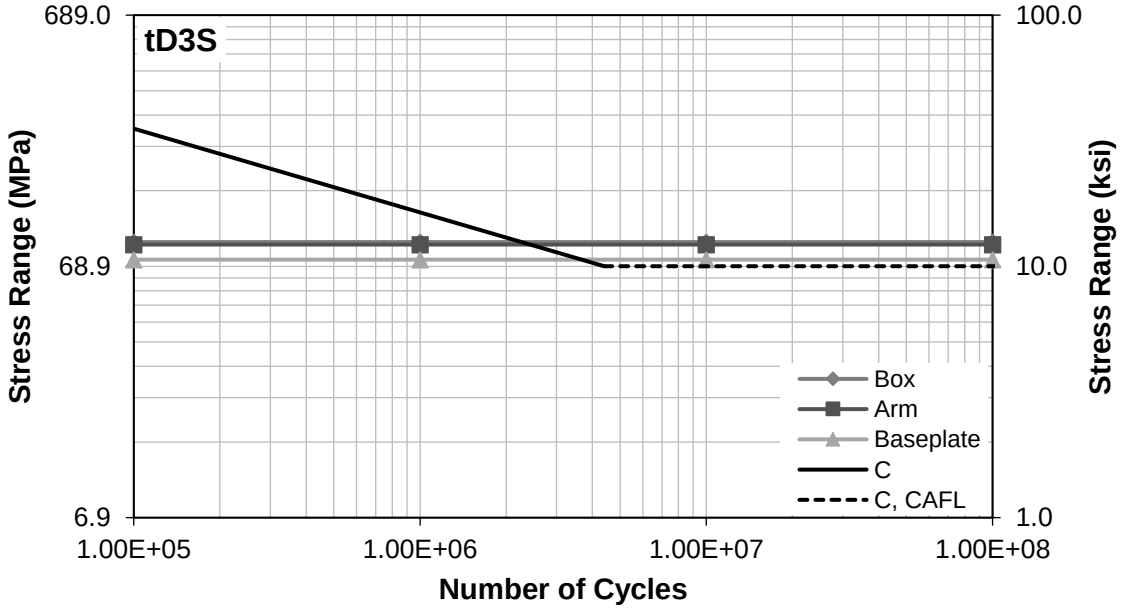

Figure D.4. S-N Curve for tD3S Hot Spot Stresses, NW

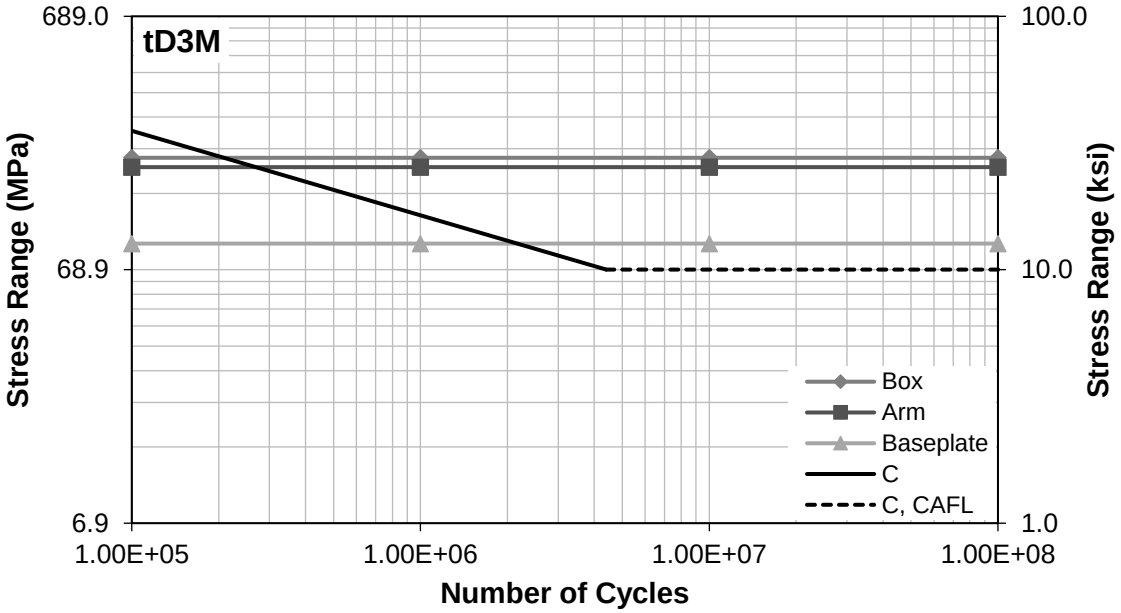

Figure D.5. S-N Curve for tD3M Hot Spot Stresses, NW

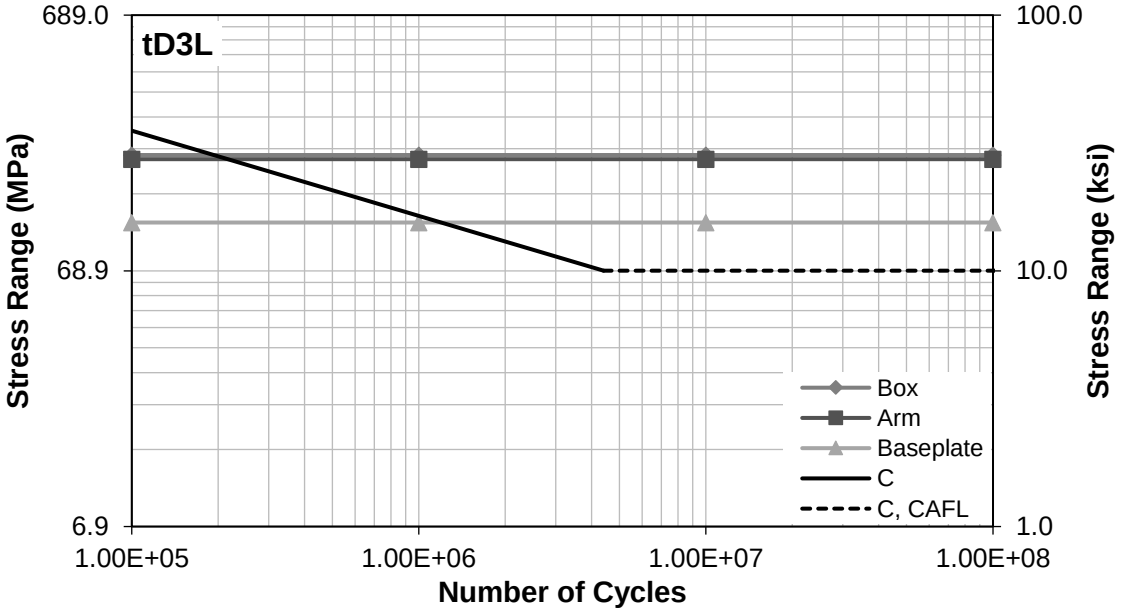

Figure D.6. S-N Curve for tD3L Hot Spot Stresses, NW

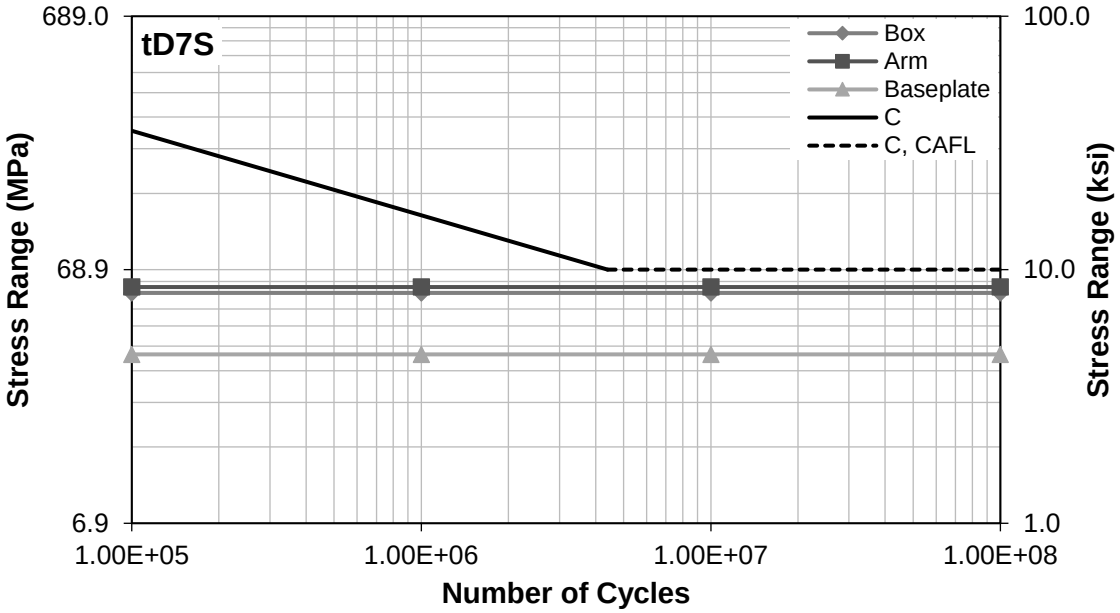

Figure D.7. S-N Curve for tD7S Hot Spot Stresses, NW

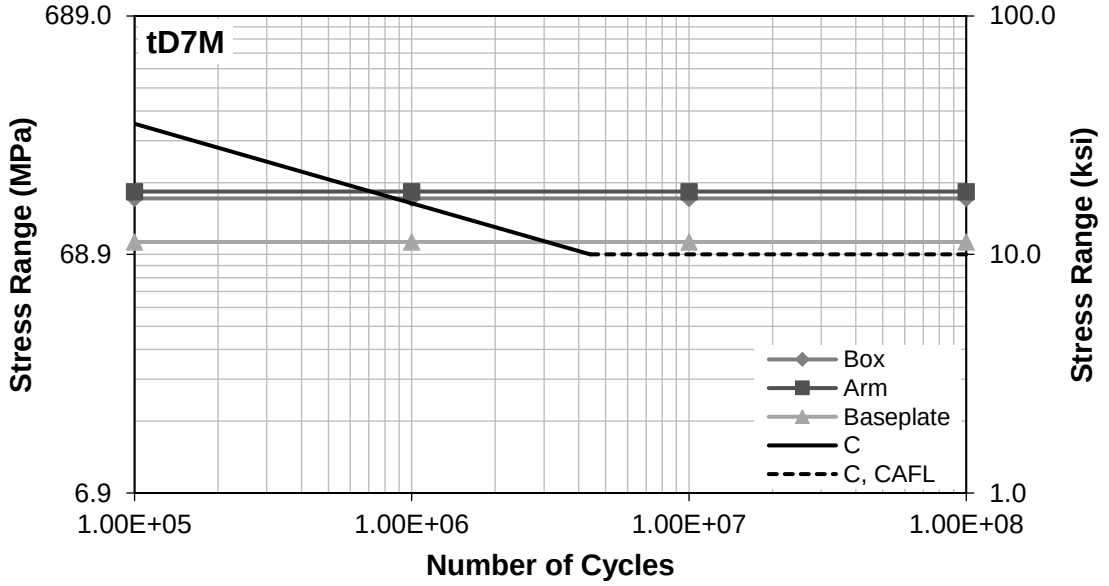

Figure D.8. S-N Curve for tD7M Hot Spot Stresses, NW

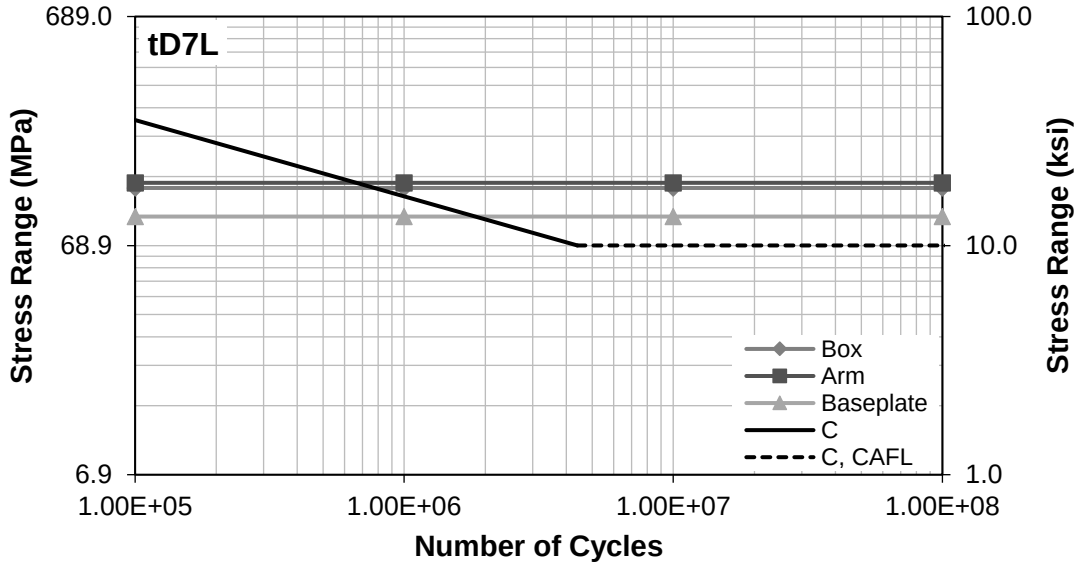

Figure D.9. S-N Curve for tD7L Hot Spot Stresses, NW

Truck-induced Wind Gusts plus Galloping (T+G) S-N Curves

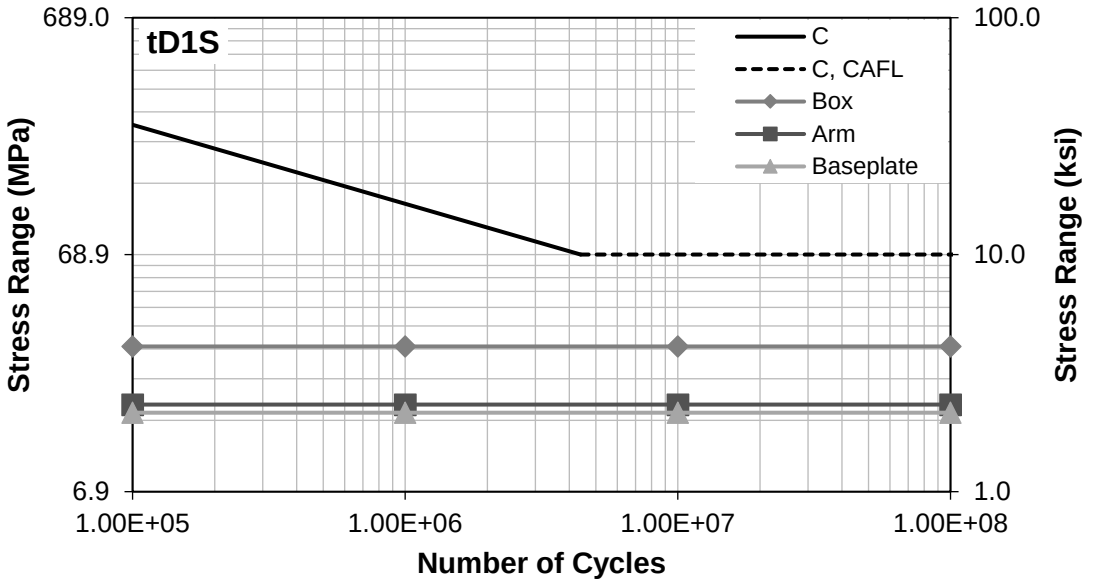

Figure D.10. S-N Curve for tD1S Hot Spot Stresses, T+G

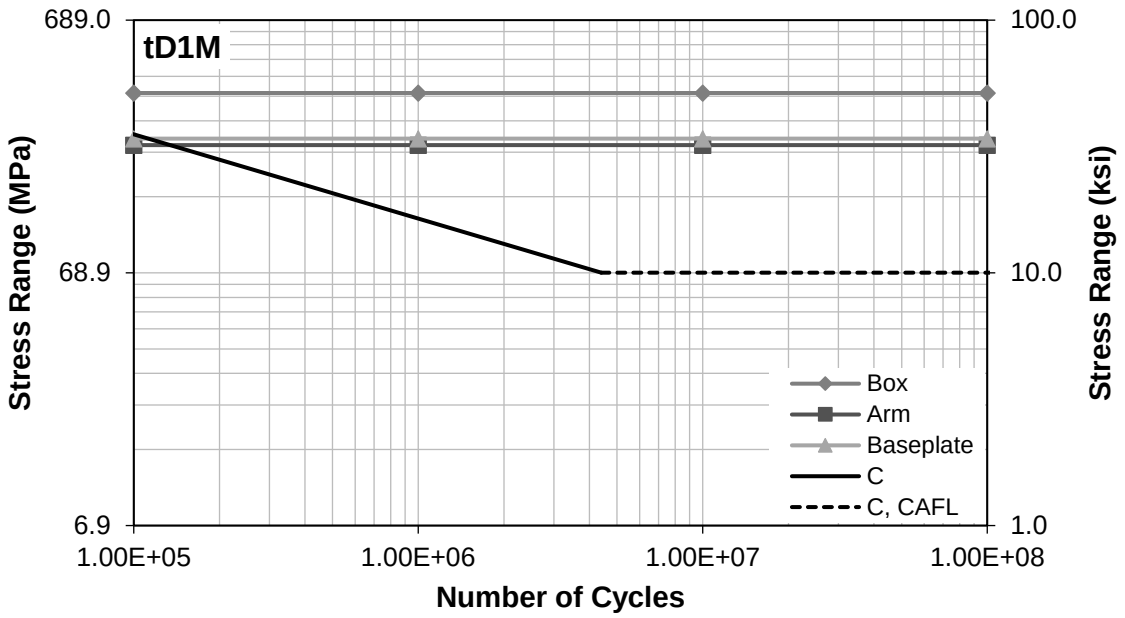

Figure D.11. S-N Curve for tD1M Hot Spot Stresses, T+G

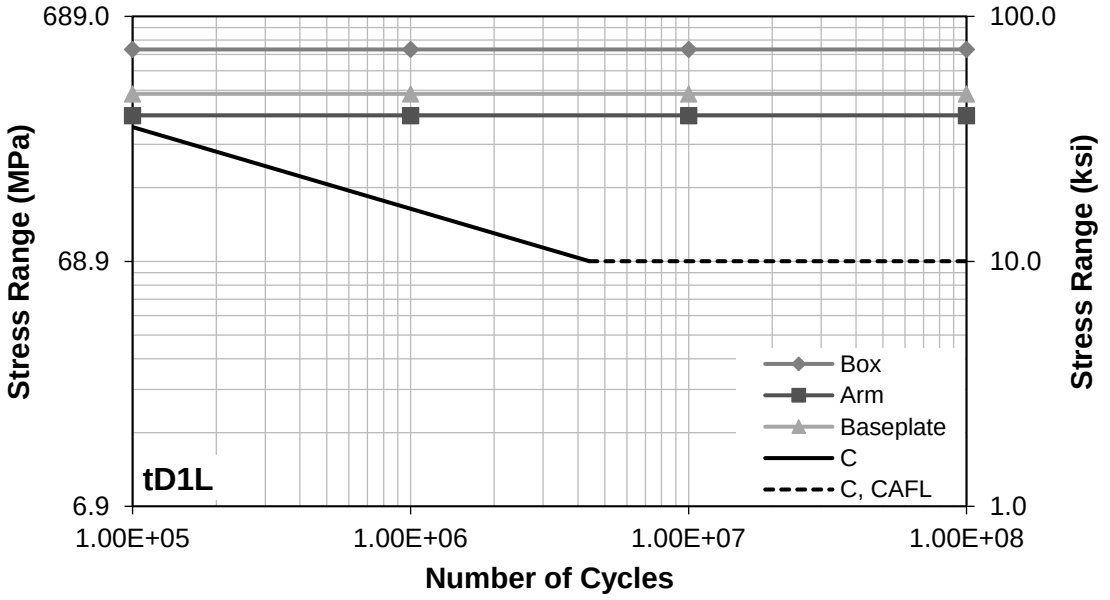

Figure D.12. S-N Curve for tD1L Hot Spot Stresses, T+G

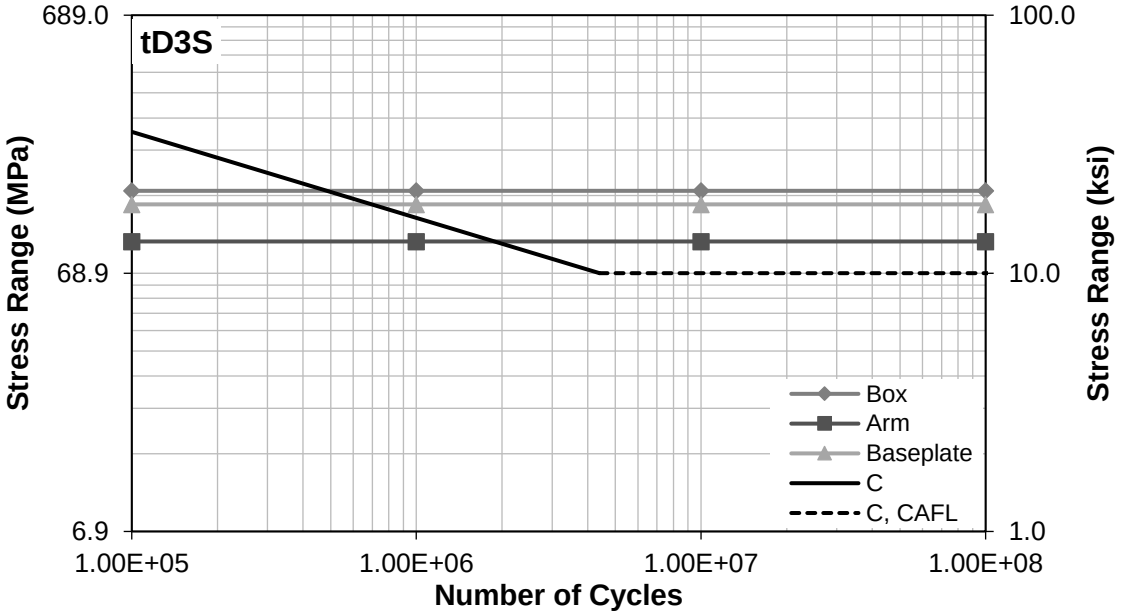

Figure D.13. S-N Curve for tD3S Hot Spot Stresses, T+G

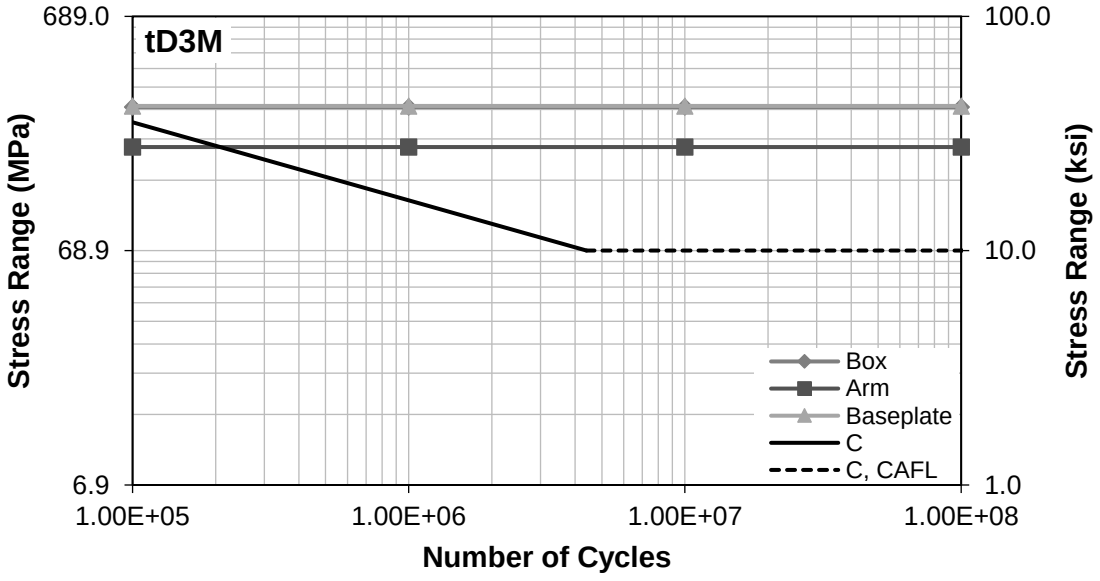

Figure D.14. S-N Curve for tD3M Hot Spot Stresses, T+G

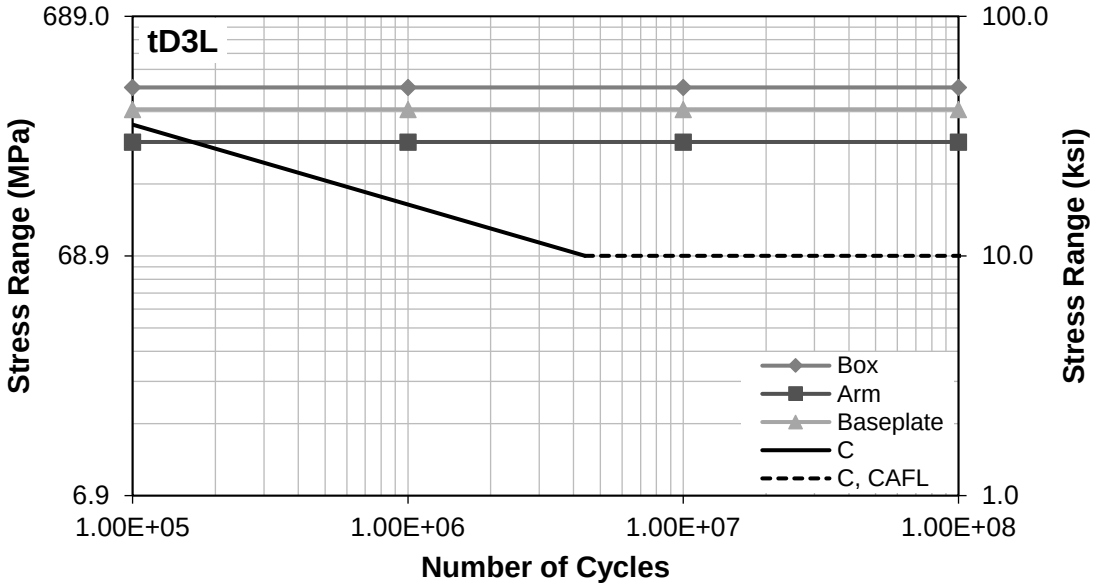

Figure D.15. S-N Curve for tD3L Hot Spot Stresses, T+G

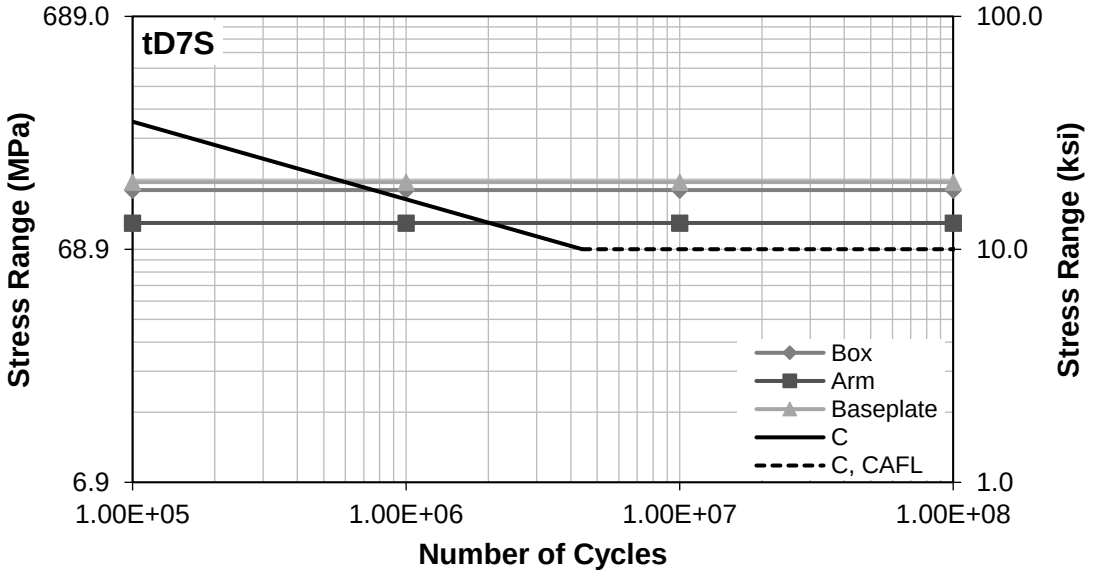

Figure D.16. S-N Curve for tD7S Hot Spot Stresses, T+G

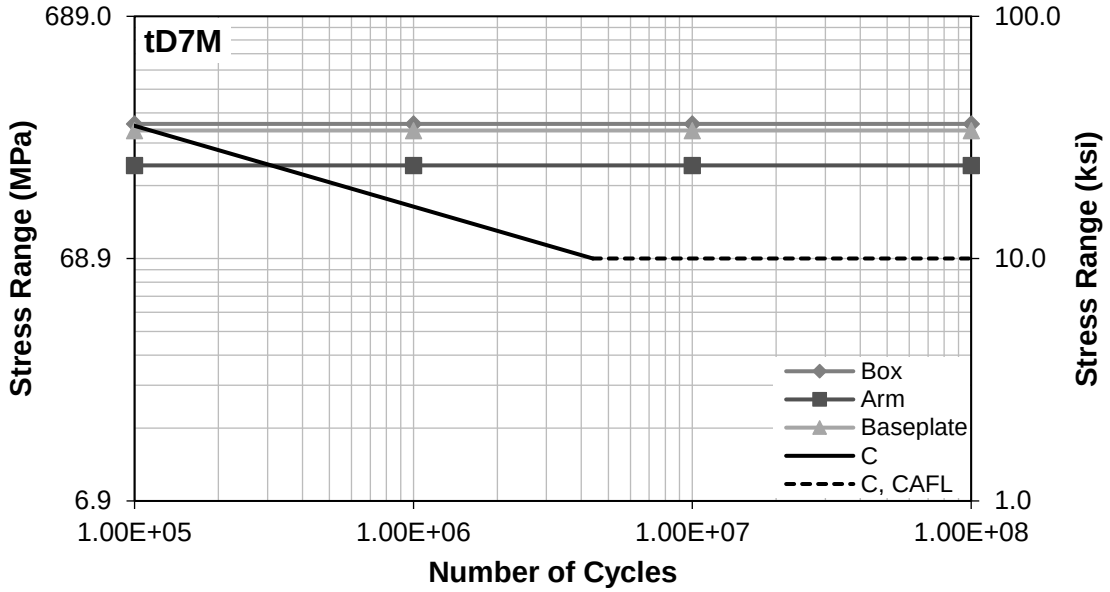

Figure D.17. S-N Curve for tD7M Hot Spot Stresses, T+G

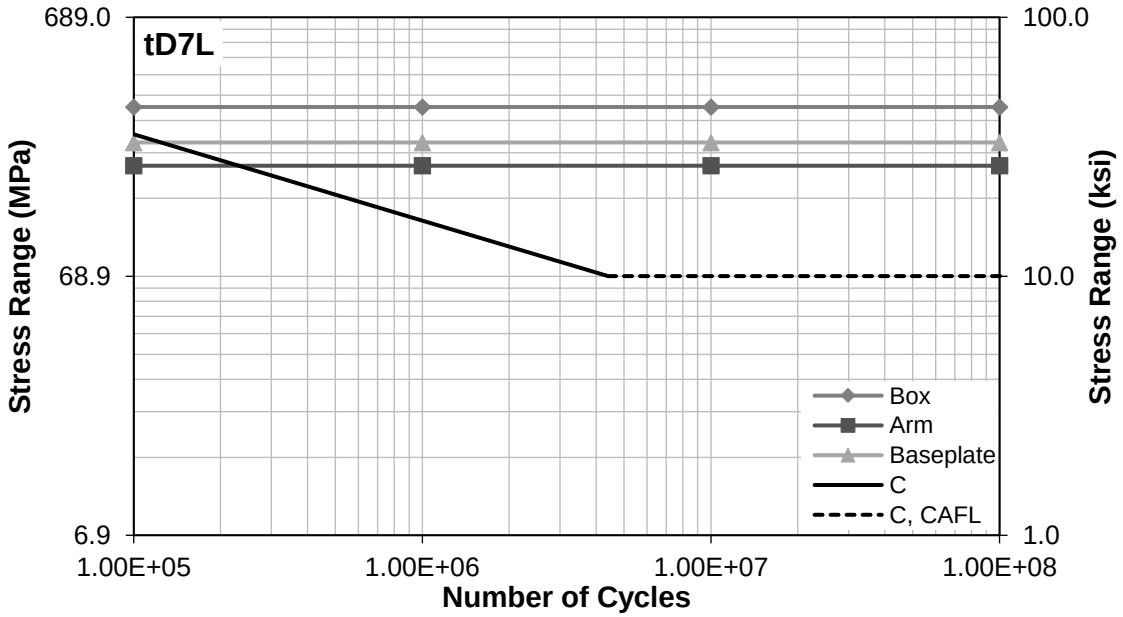

Figure D.18. S-N Curve for tD7L Hot Spot Stresses, T+G

D.1.4. Mises Stress Distributions

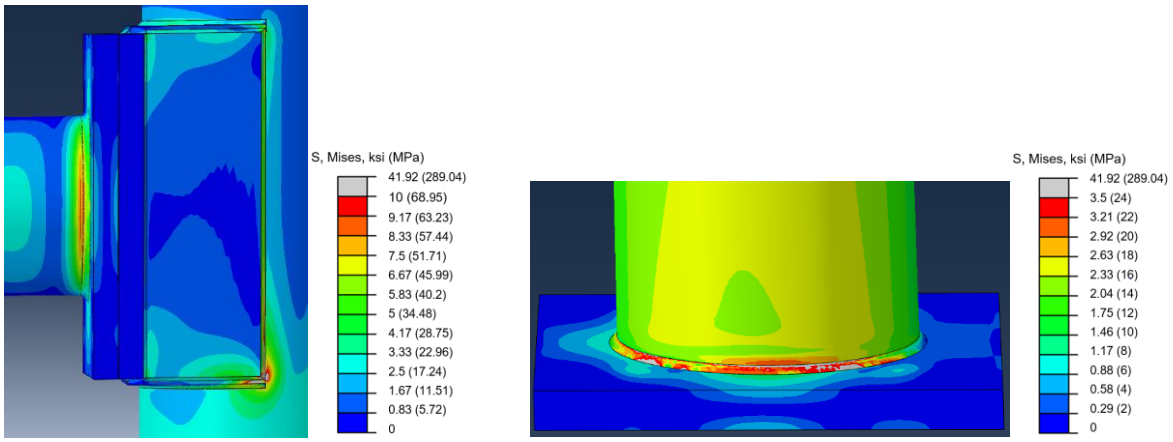

Box and Mast-Arm Connection

Baseplate Connection

Figure D.19. Mises Stresses, tD1S, NW

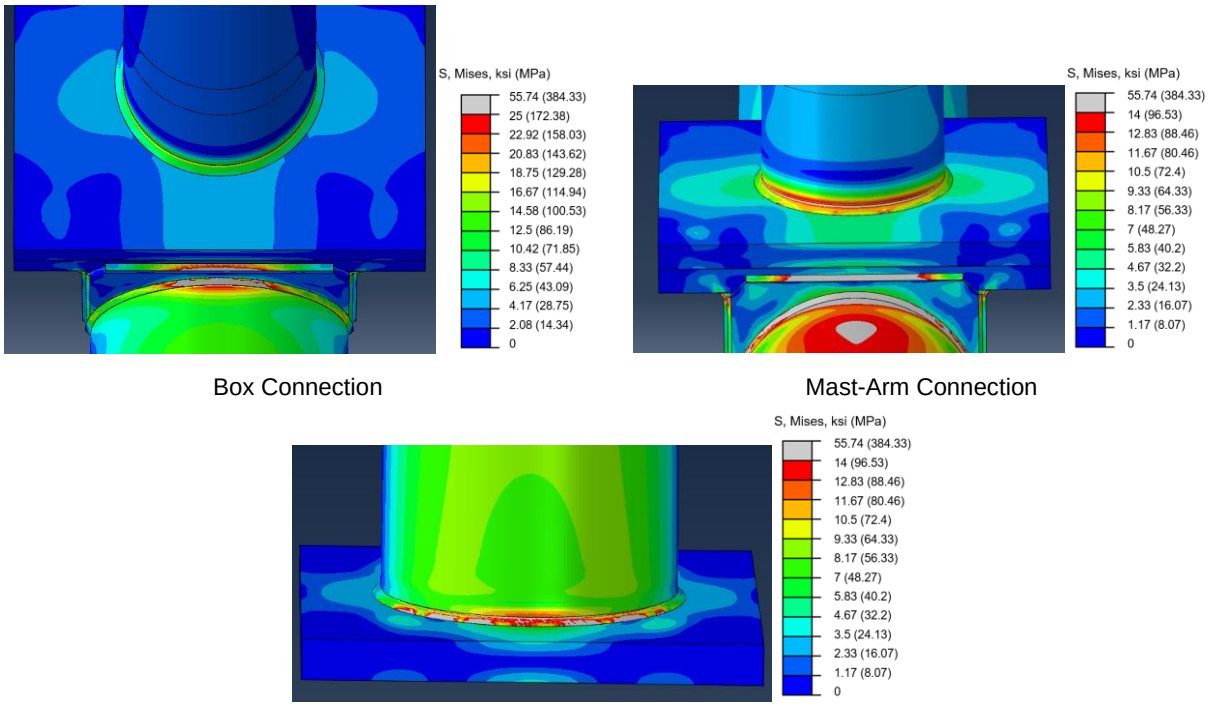

Box Connection

Mast-Arm Connection

Baseplate Connection

Figure D.20. Mises Stresses, tD1S, T+G

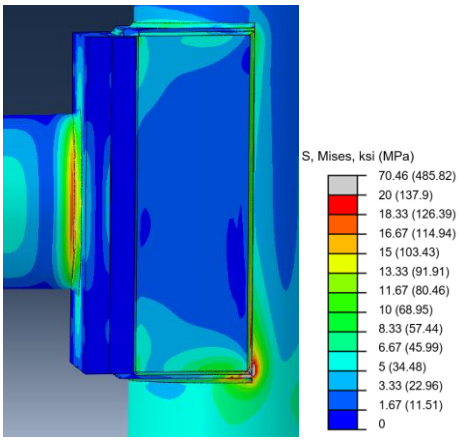

Box and Mast-Arm Connection

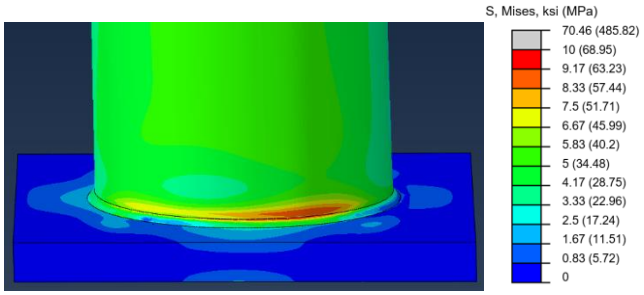

Baseplate Connection

Figure D.21. Mises Stresses, tD1M, NW

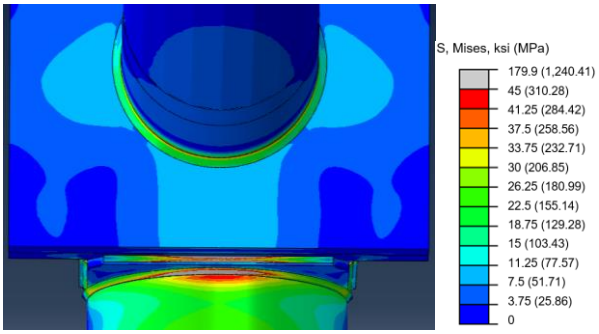

Box Connection

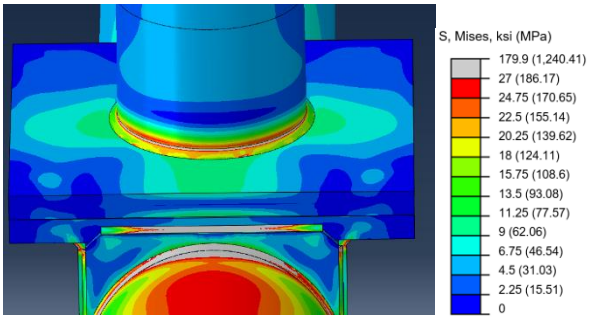

Mast-Arm Connection

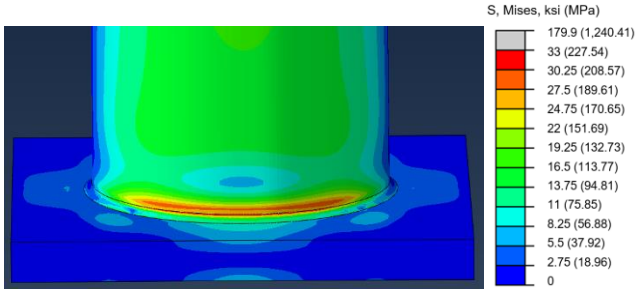

Baseplate Connection

Figure D.22. Mises Stresses, tD1M, T+G

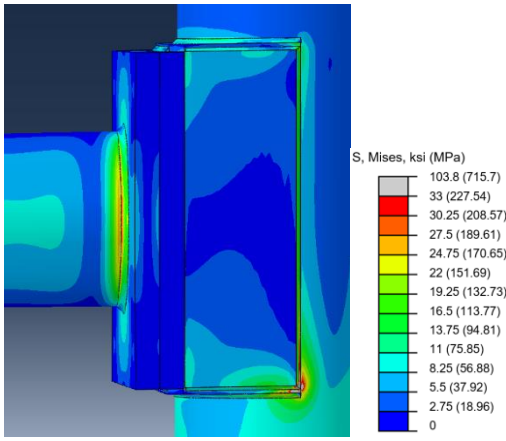

Box and Mast-Arm Connection

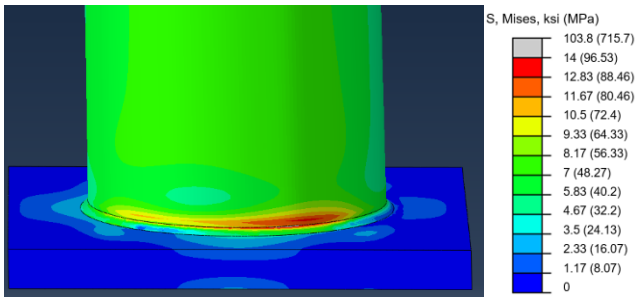

Baseplate Connection

Figure D.23. Mises Stresses, tD1L, NW

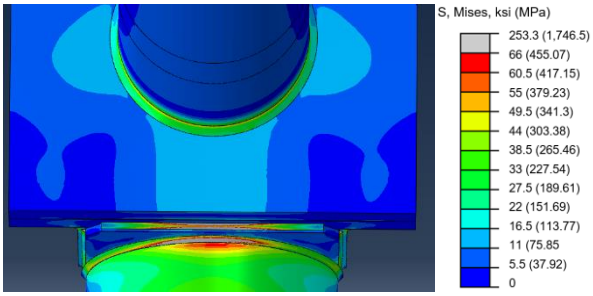

Box Connection

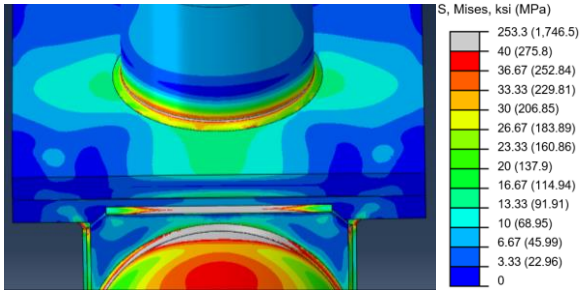

Mast-Arm Connection

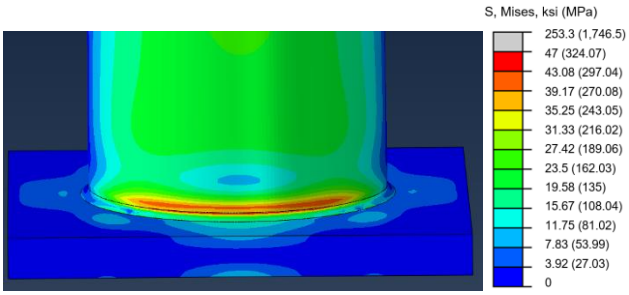

Baseplate Connection

Figure D.24. Mises Stresses, tD1L, T+G

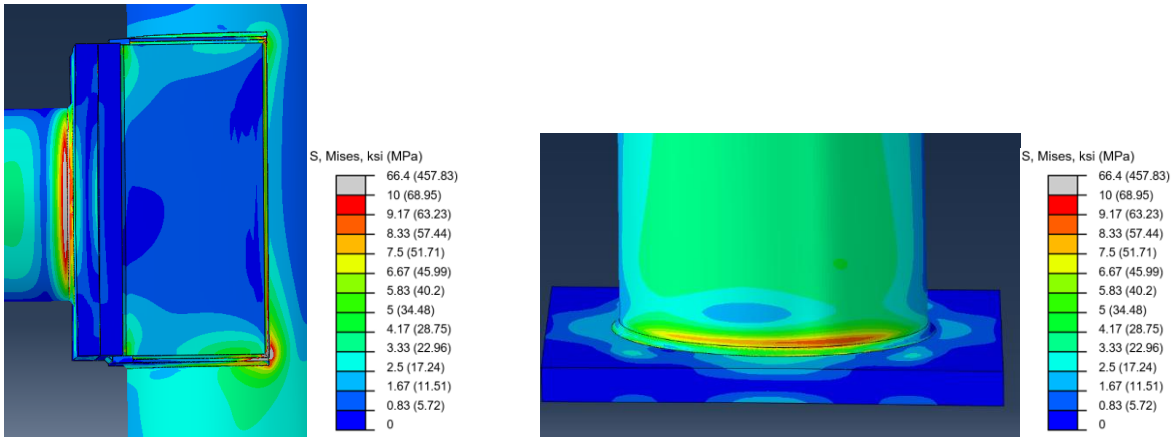

Box Connection Mast-Arm Connection

Figure D.25. Mises Stresses, tD3S, NW

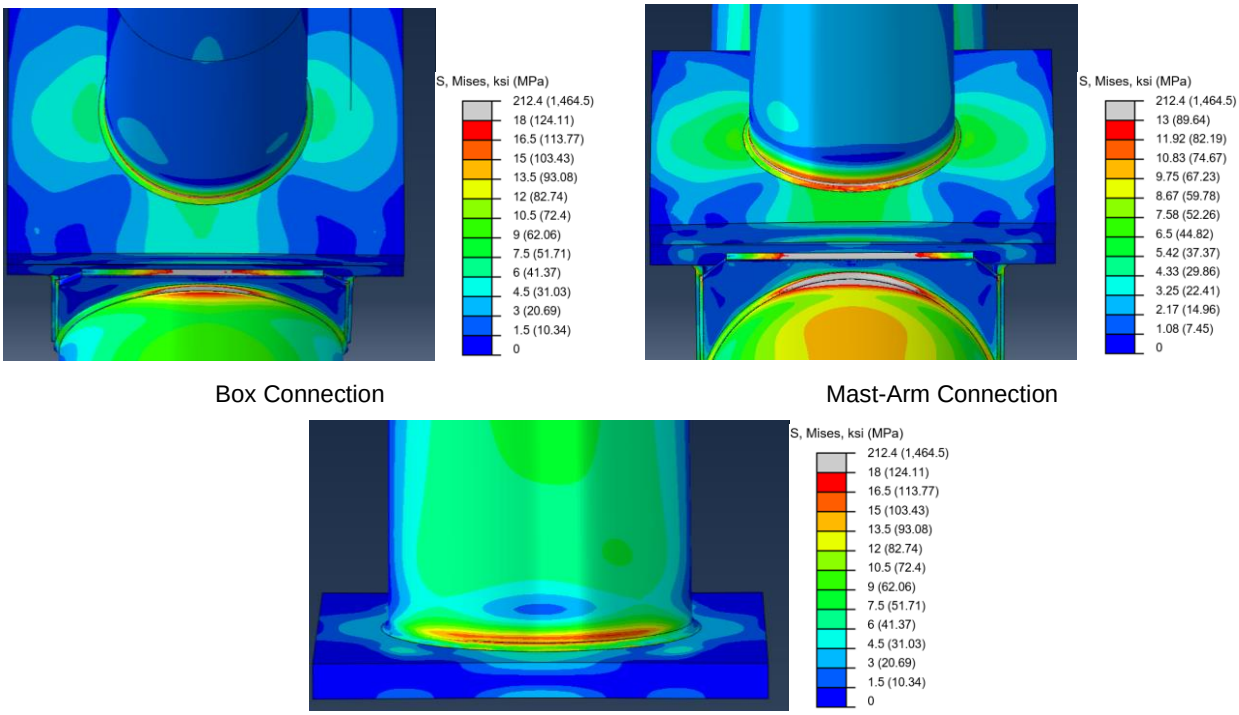

Box Connection Mast-Arm Connection

Baseplate Connection

Figure D.26. Mises Stresses, tD3S, T+G

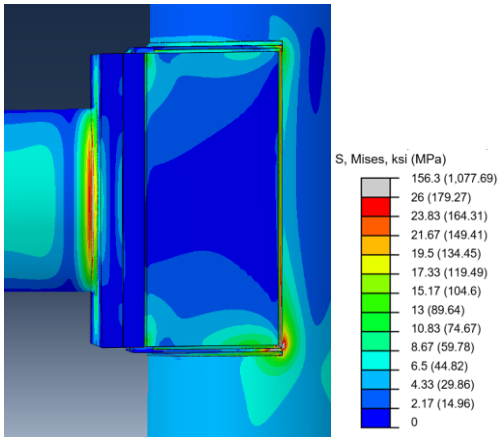

Box and Mast-Arm Connection

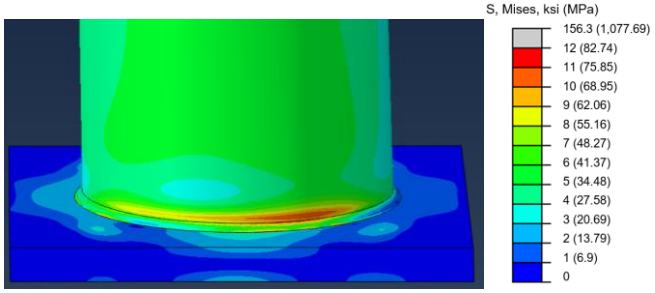

Baseplate Connection

Figure D.27. Mises Stresses, tD3M, NW

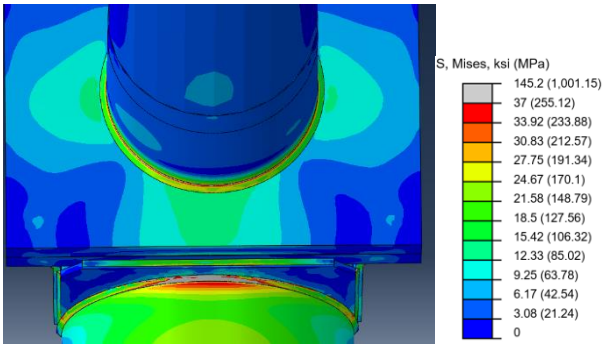

Box Connection

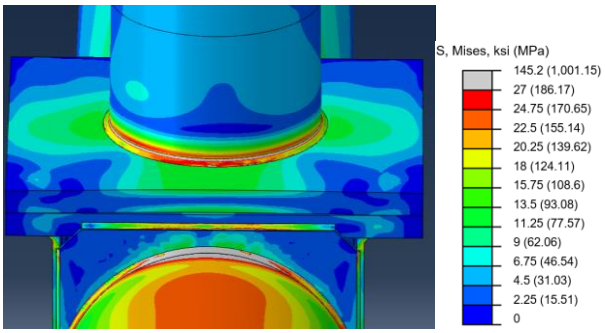

Mast-Arm Connection

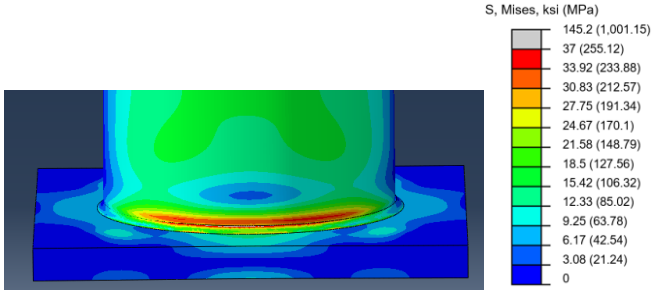

Baseplate Connection

Figure D.28. Mises Stresses, tD3M, T+G

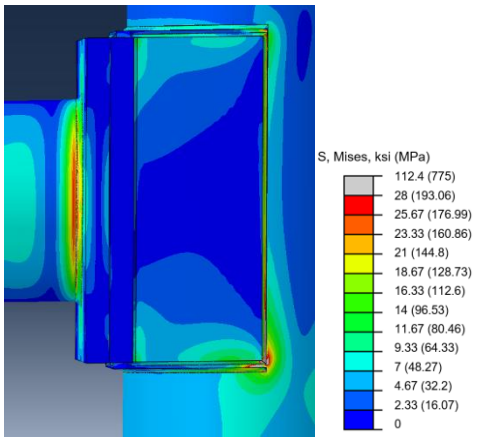

Box and Mast-Arm Connection

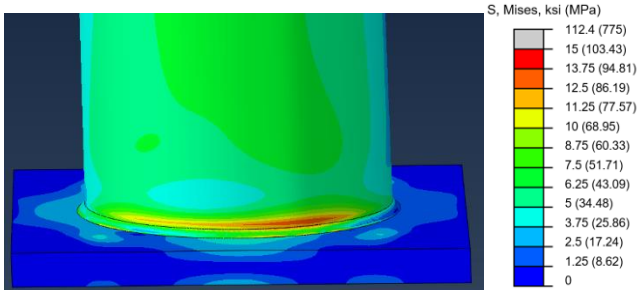

Baseplate Connection

Figure D.29. Mises Stresses, tD3L, NW

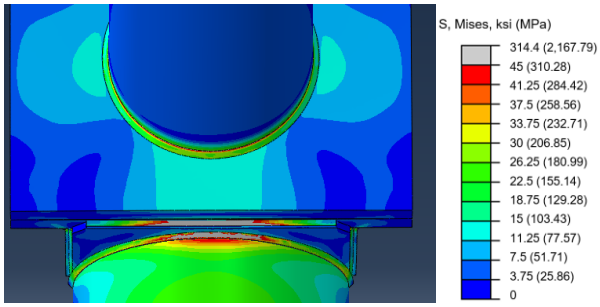

Box Connection

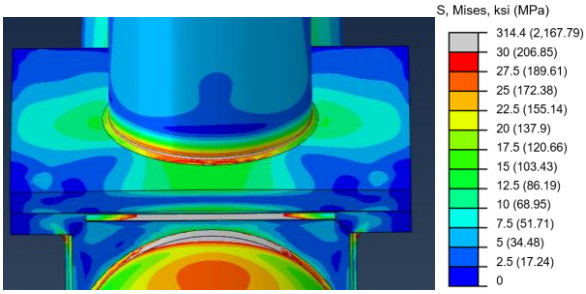

Mast-Arm Connection

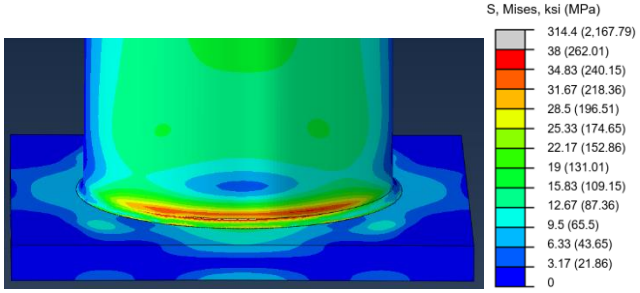

Baseplate Connection

Figure D.30. Mises Stresses, tD3L, T+G

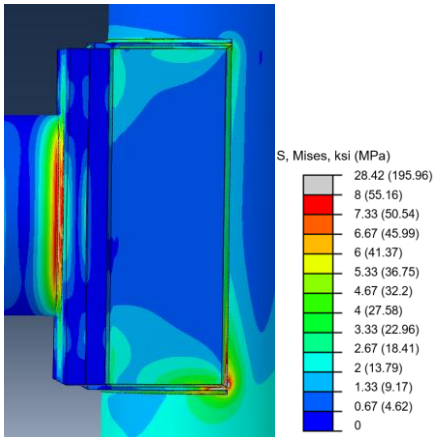

Box and Mast-Arm Connection

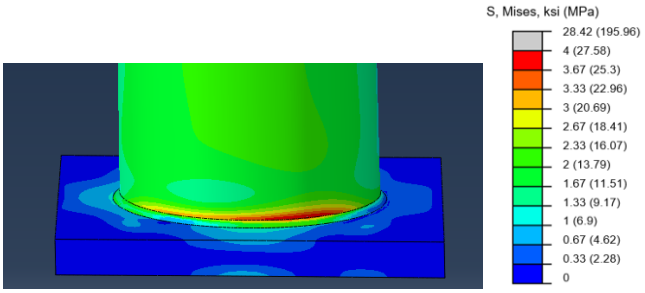

Baseplate Connection

Figure D.31. Mises Stresses, tD7S, NW

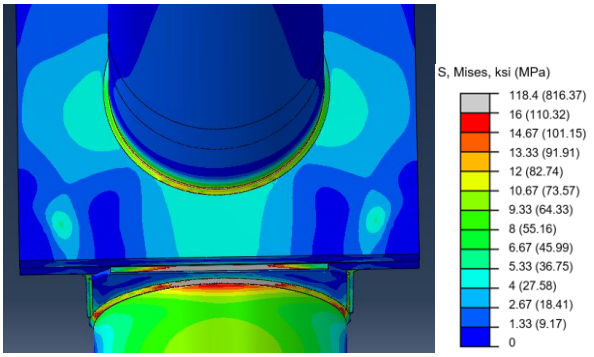

Box Connection

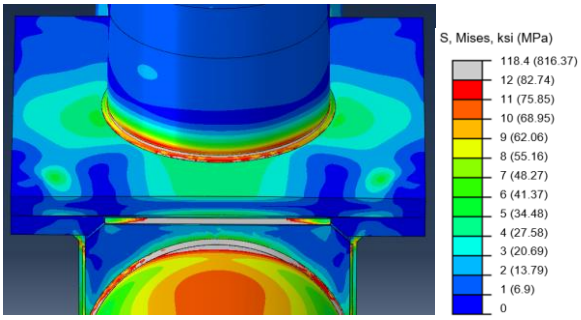

Mast-Arm Connection

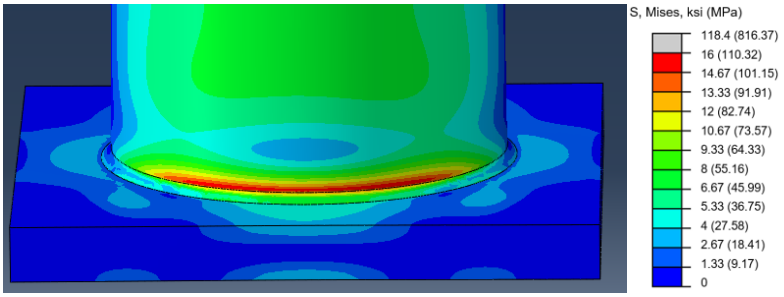

Baseplate Connection

Figure D.32. Mises Stresses, tD7S, T+G

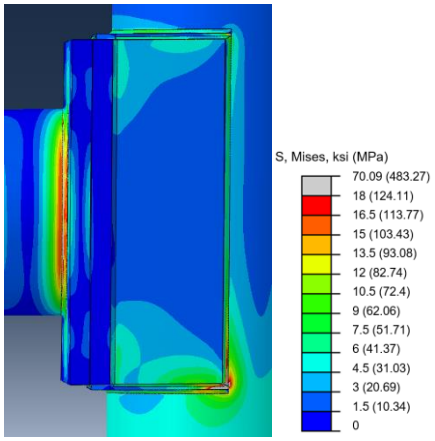

Box and Mast-Arm Connection

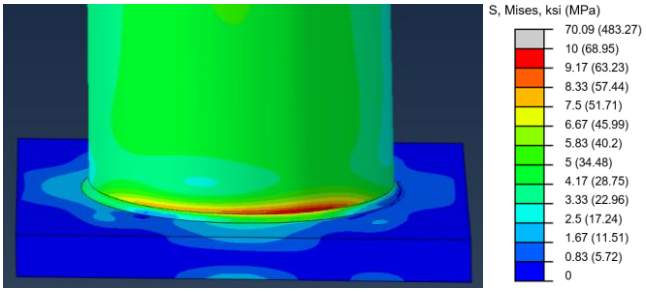

Baseplate Connection

Figure D.33. Mises Stresses, tD7M, NW

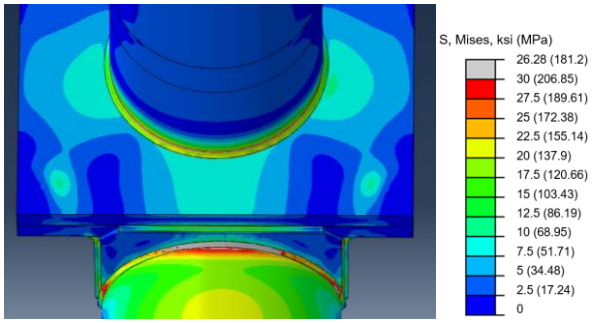

Box Connection

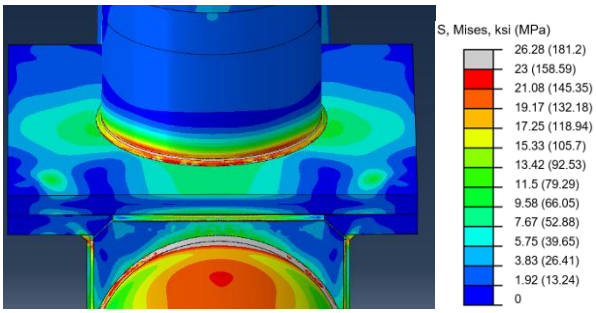

Mast-Arm Connection

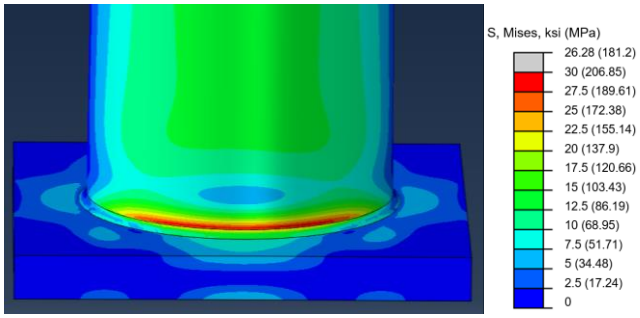

Baseplate Connection

Figure D.34. Mises Stresses, tD7M, T+G

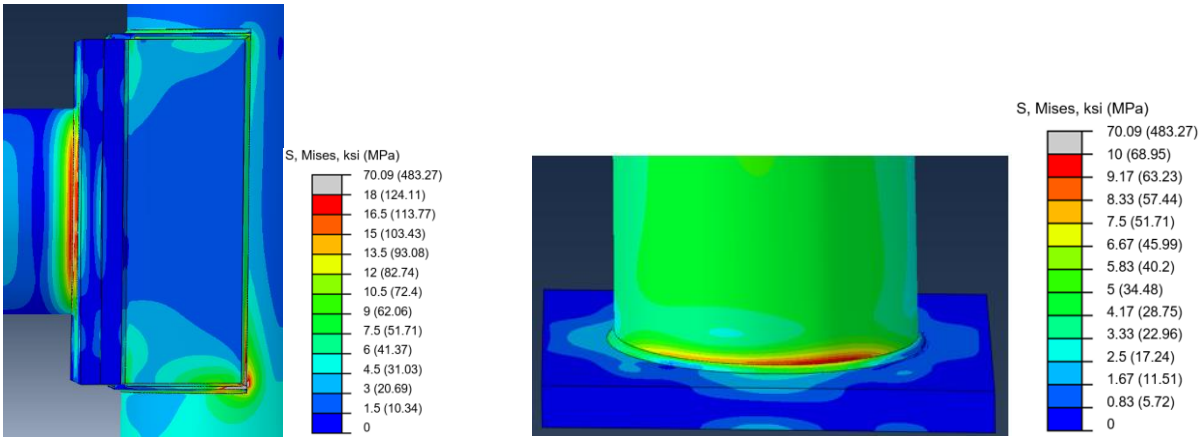

Box and Mast-Arm Connection

Baseplate Connection

Figure D.35. Mises Stresses, tD7L, NW

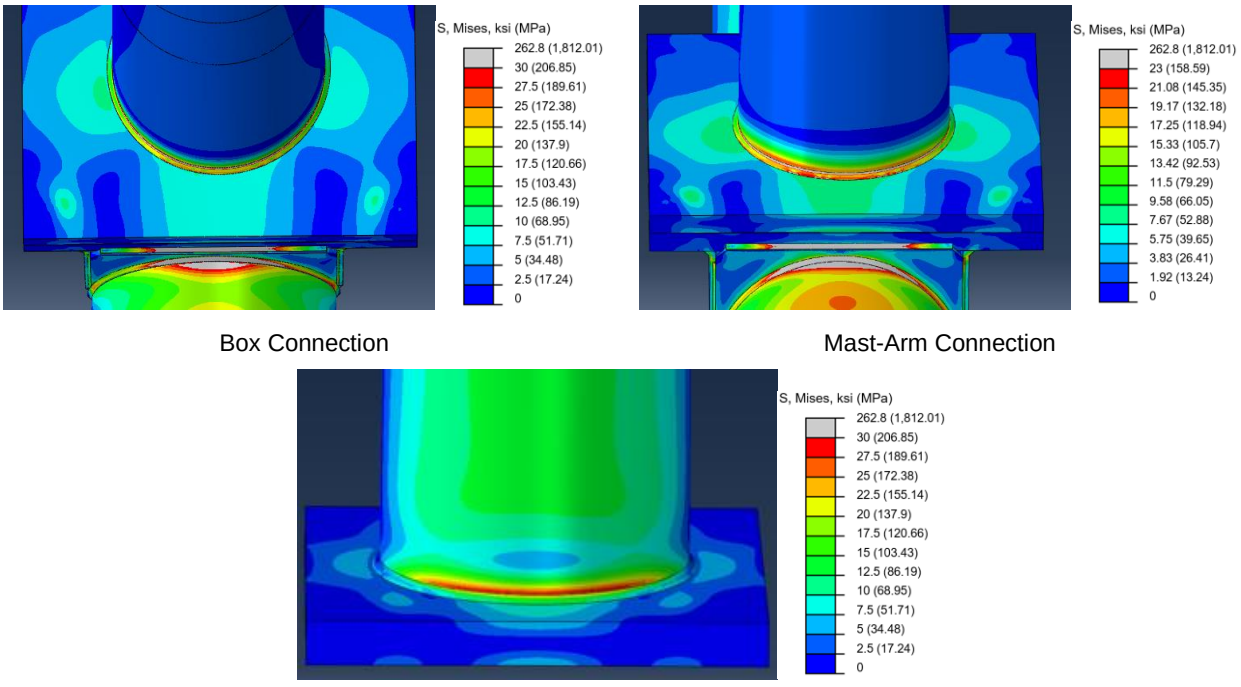

Box Connection

Mast-Arm Connection

Baseplate Connection

Figure D.36. Mises Stresses, tD7L, T+G

D.1.5. Max Principal Stress Paths

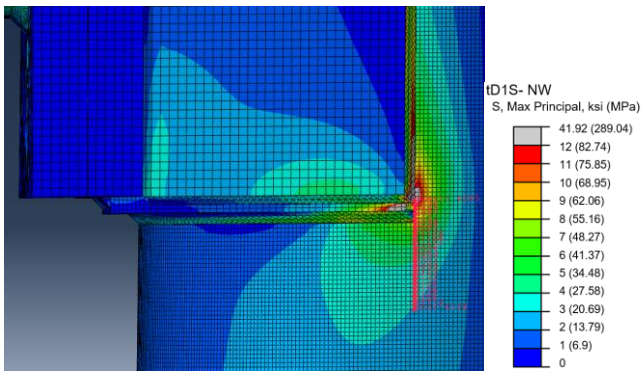

Box Connection

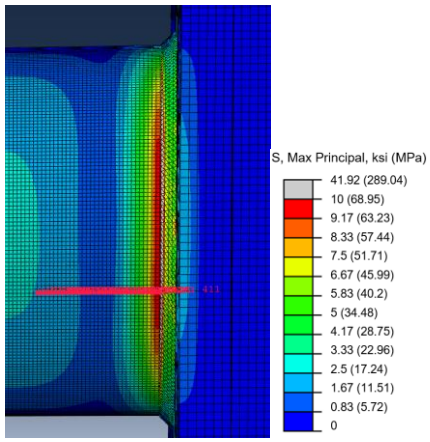

Mast-Arm Connection

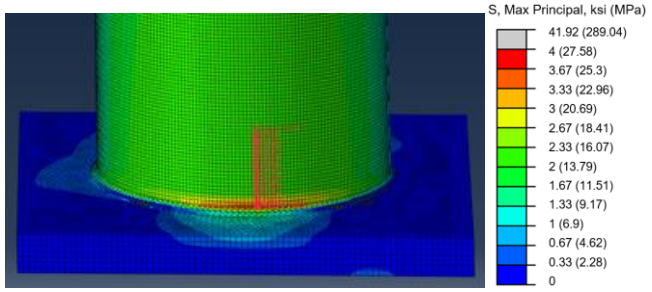

Baseplate Connection

Figure D.37. Paths, tD1S, NW

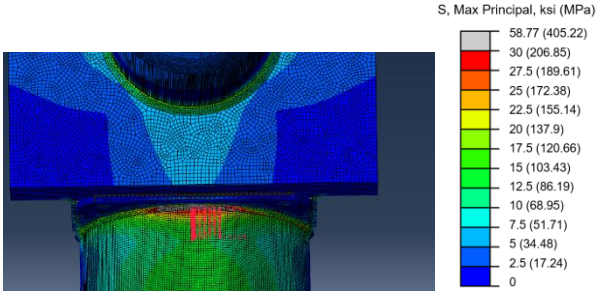

Box Connection

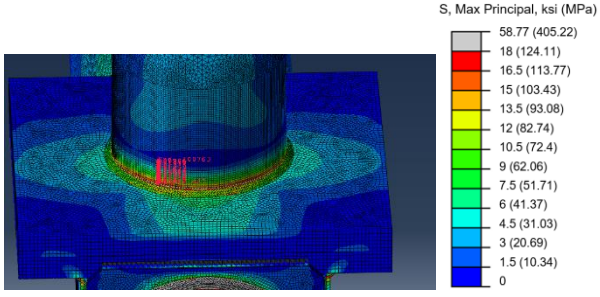

Mast-Arm Connection

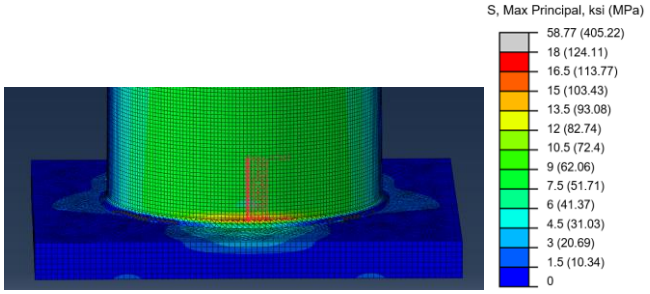

Baseplate Connection

Figure D.38. Paths, tD1S, T+G

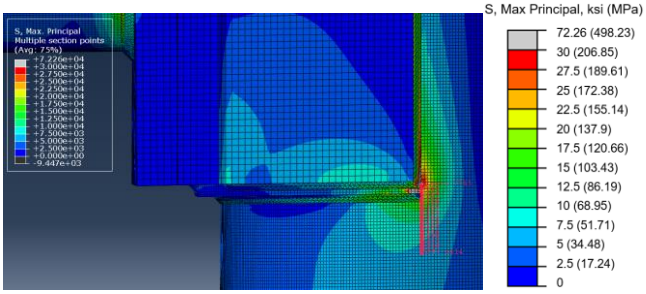

Box Connection

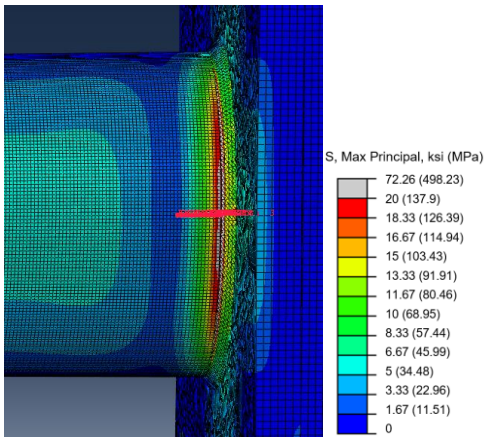

Mast-Arm Connection

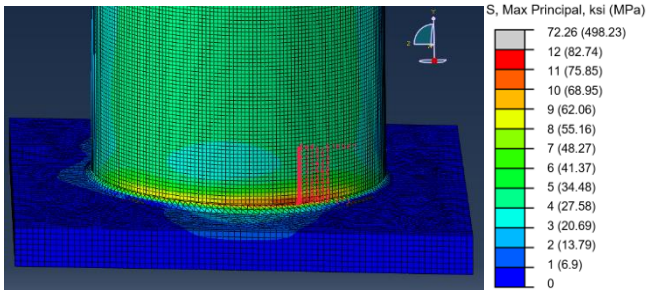

Baseplate Connection

Figure D.39. Paths, tD1M, NW

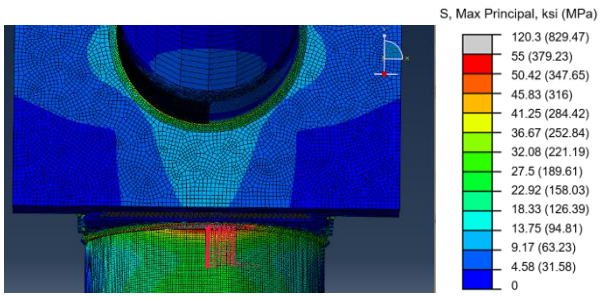

Box Connection

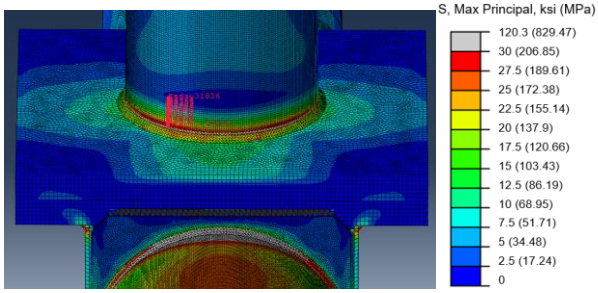

Mast-Arm Connection

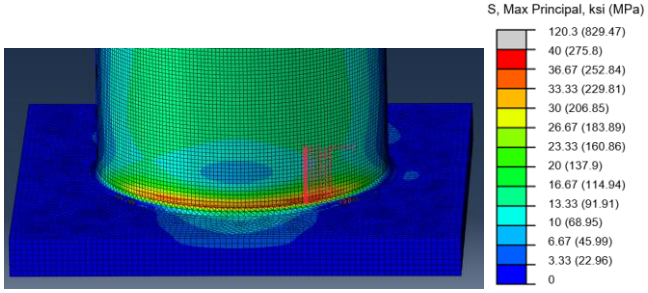

Baseplate Connection

Figure D.40. Paths, tD1M, T+G

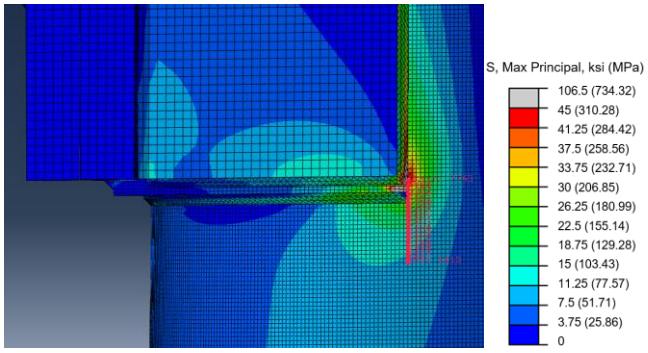

Box Connection

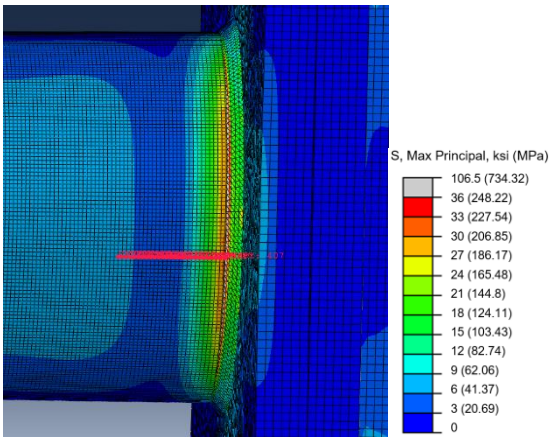

Mast-Arm Connection

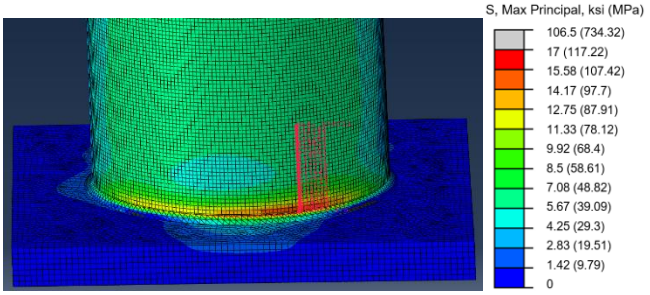

Baseplate Connection

Figure D.41. Paths, tD1L, NW

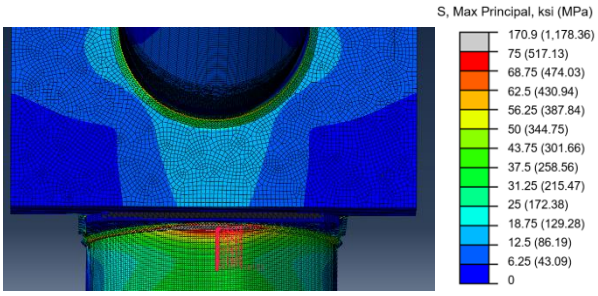

Box Connection

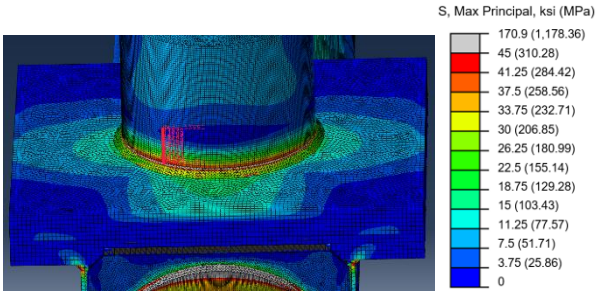

Mast-Arm Connection

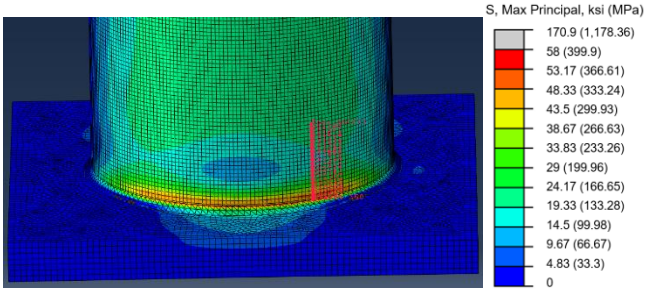

Baseplate Connection

Figure D.42. Paths, tD1L, T+G

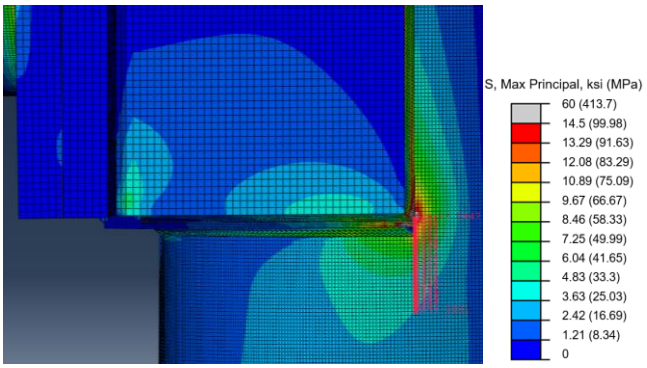

Box Connection

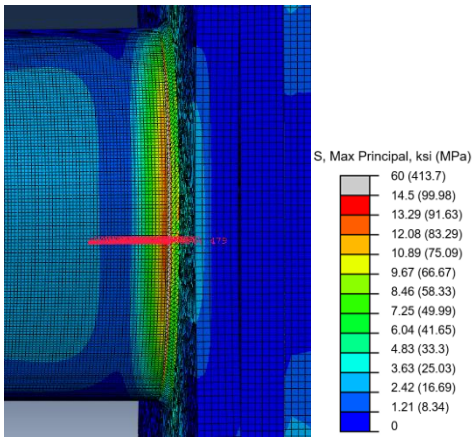

Mast-Arm Connection

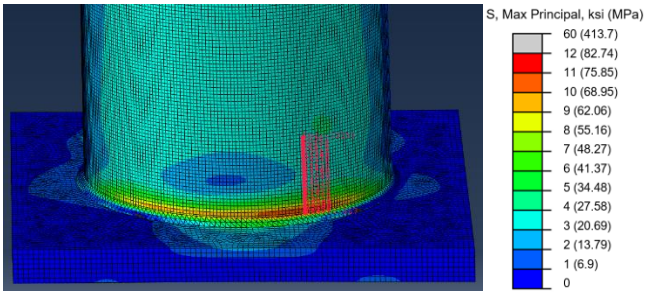

Baseplate Connection

Figure D.43. Paths, tD3S, NW

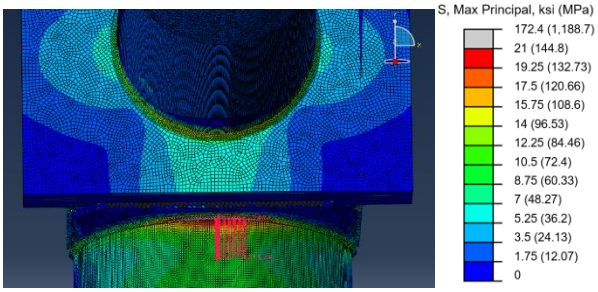

Box Connection

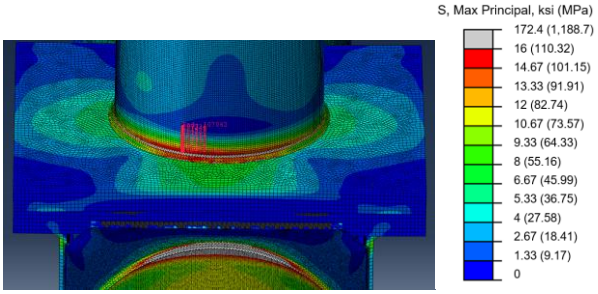

Mast-Arm Connection

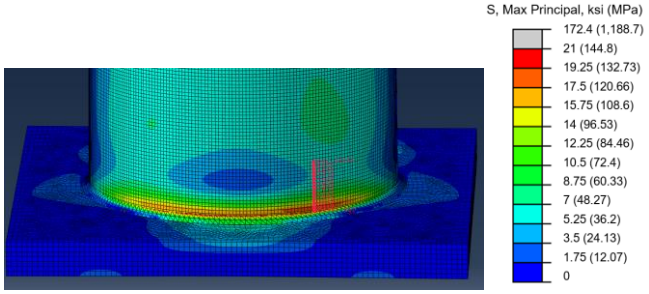

Baseplate Connection

Figure D.44. Paths, tD3S, T+G

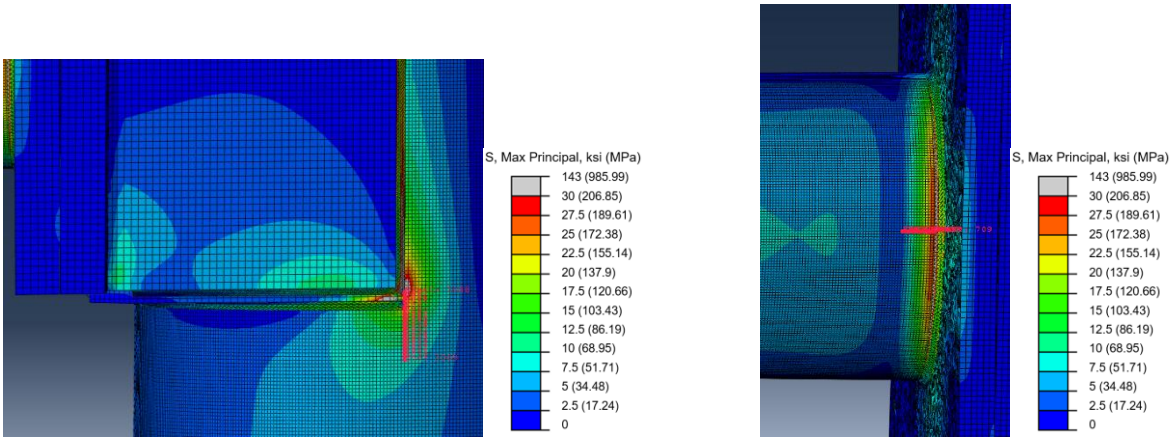

Box Connection

Mast-Arm Connection

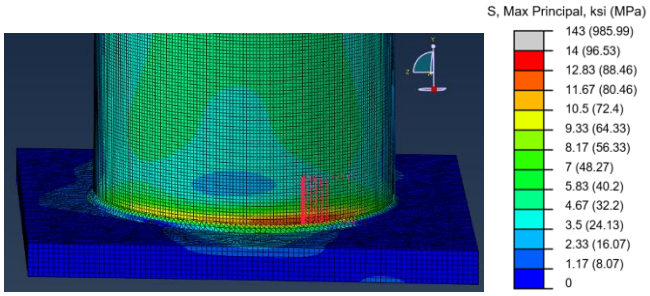

Baseplate Connection

Figure D.45. Paths, tD3M, NW

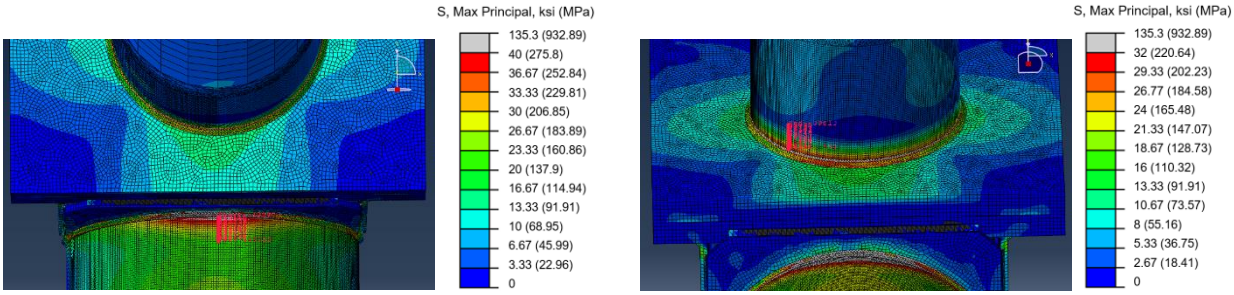

Box Connection

Mast-Arm Connection

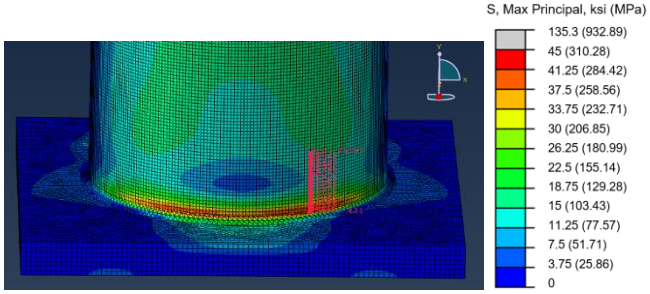

Baseplate Connection

Figure D.46. Paths, tD3M, T+G

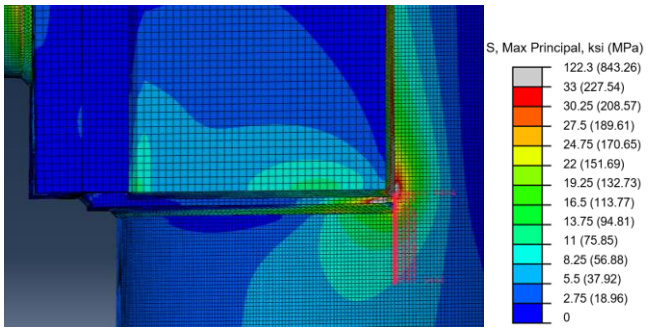

Box Connection

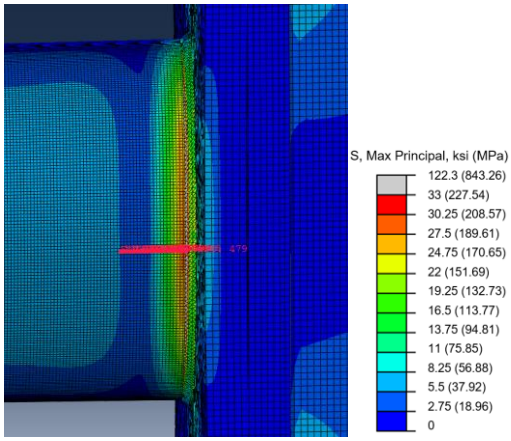

Mast-Arm Connection

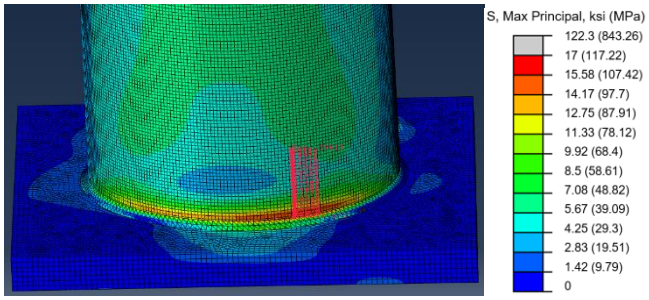

Baseplate Connection

Figure D.47. Paths, tD3L, NW

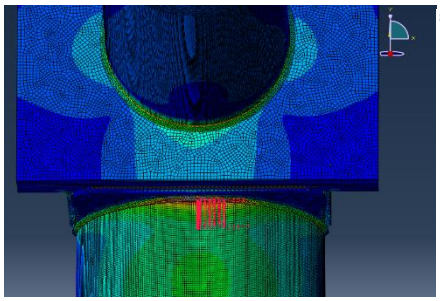

Box Connection

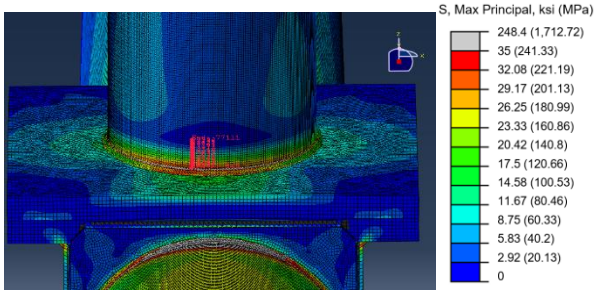

Mast-Arm Connection

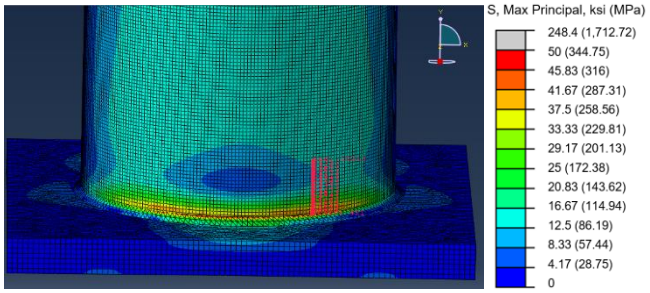

Baseplate Connection

Figure D.48. Paths, tD3L, T+G

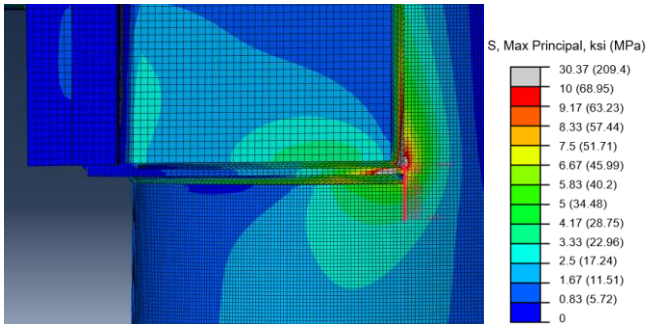

Box Connection

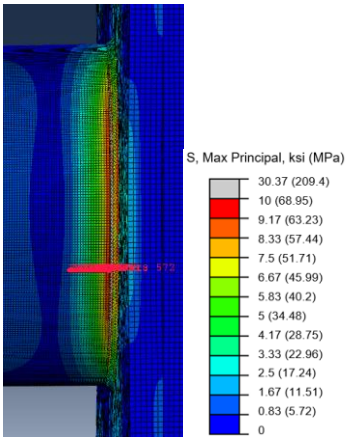

Mast-Arm Connection

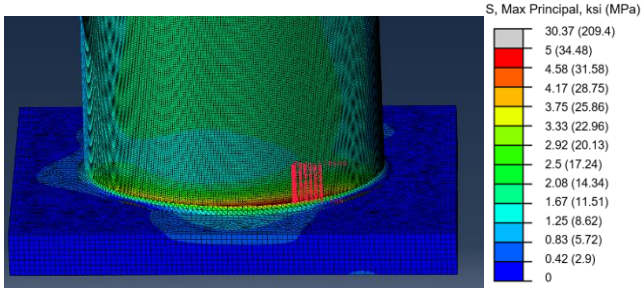

Baseplate Connection

Figure D.49. Paths, tD7S, NW

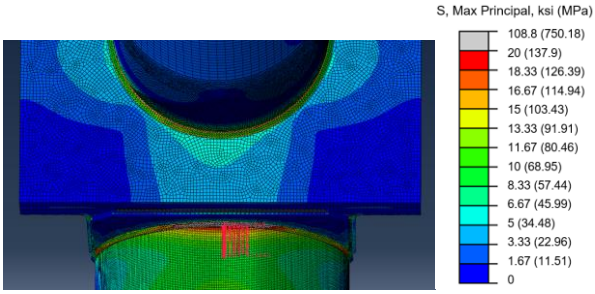

Box Connection

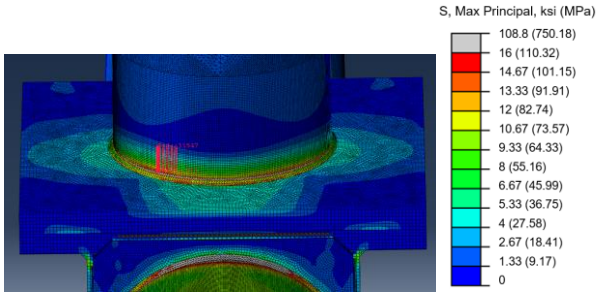

Arm Connection

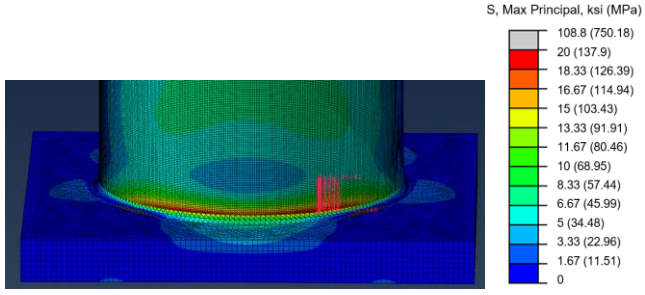

Baseplate Connection

Figure D.50. Paths, tD7S, T+G

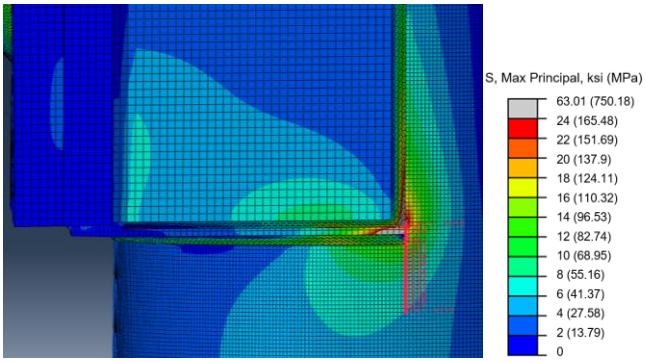

Box Connection

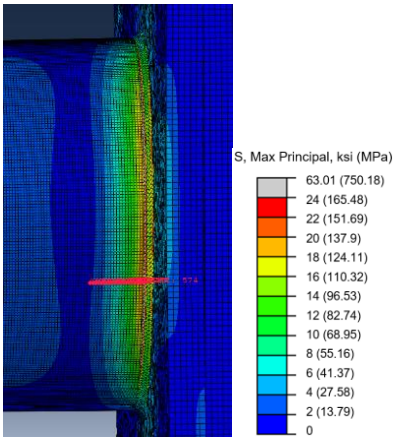

Mast-Arm Connection

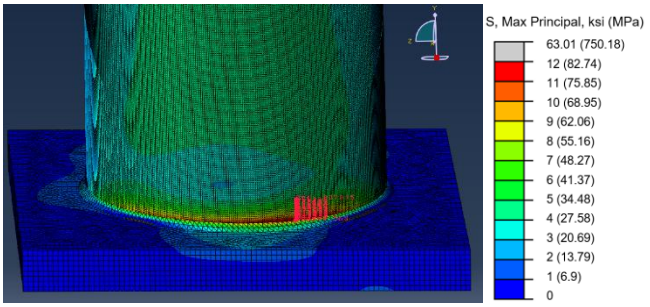

Baseplate Connection

Figure D.51. Paths, tD7M, NW

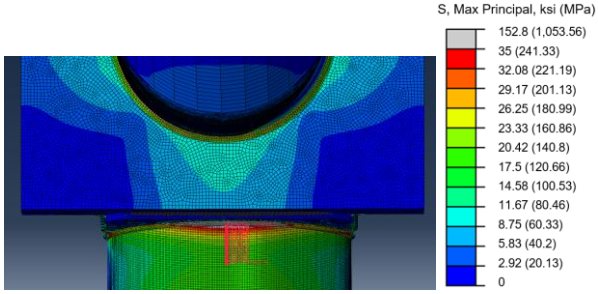

Box Connection

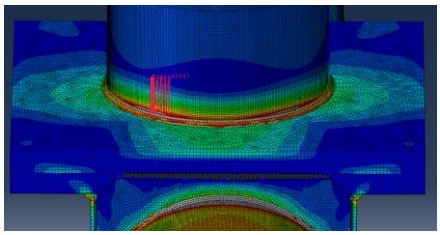

Mast-Arm Connection (25)

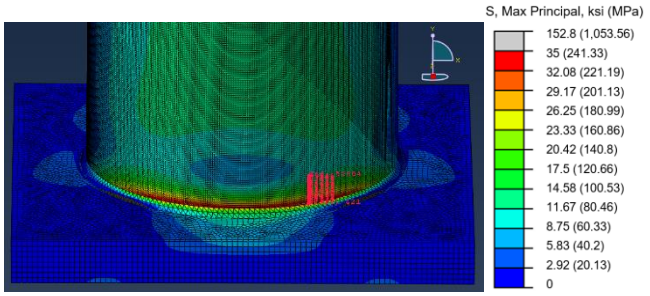

Baseplate Connection

Figure D.52. Paths, tD7M, T+G

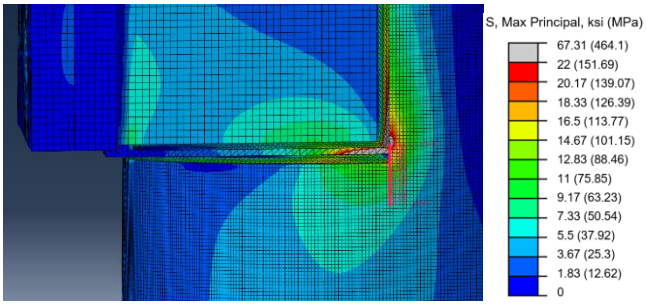

Box Connection

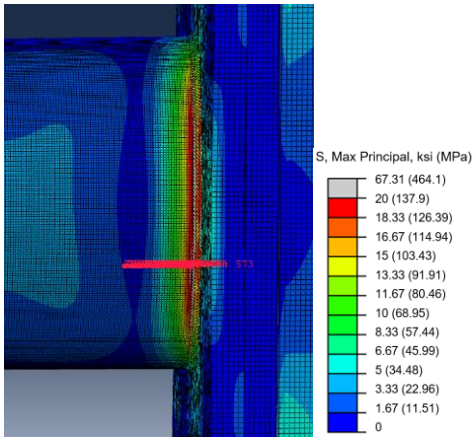

Mast-Arm Connection

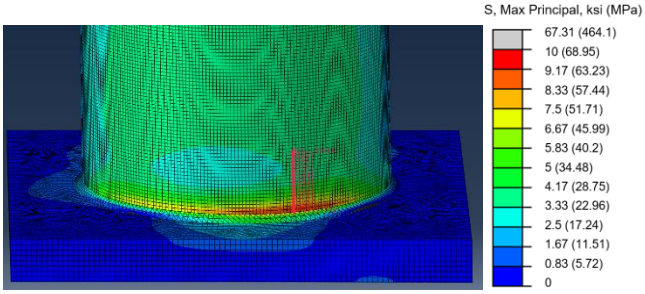

Baseplate Connection

Figure D.53. Paths, tD7L, NW

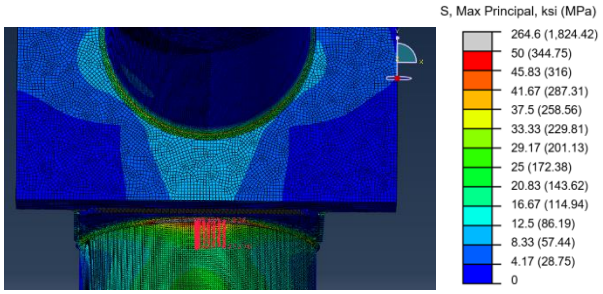

Box Connection

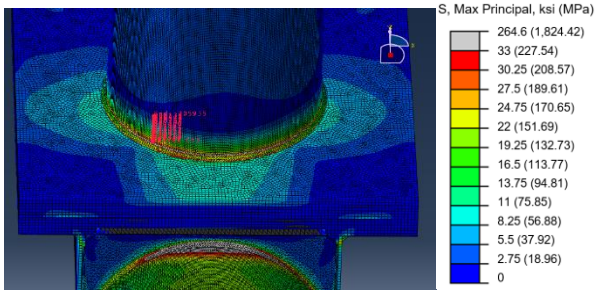

Mast-Arm Connection

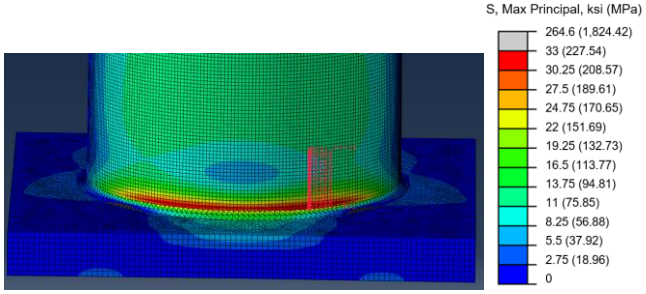

Baseplate Connection

Figure D.54. Paths, tD7L, T+G

D.2. Straight Tube Models

D.2.1. Matrix

Table D.4. Straight Tube Model Matrix

	Sign Height, ft. (m)	Sign Length, ft. (m)	Arm Length, ft. (m)	Arm Dia., in. (cm)	Arm Thickness, in. (cm)	Pole Height, ft. (m)	Pole Dia., in. (cm)	Pole Thickness, in. (cm)
Straight Tube: Design #1								
Small	4 (1.22)	12 (3.66)	29 (8.84)	8.625 (21.91)	0.5 (1.27)	25 (7.62)	16 (40.64)	0.375 (0.95)
Medium	7.5 (2.29)	14.5 (4.42)	29 (8.84)			26 (7.92)		
Large	9 (2.74)	17.5 (5.33)	31 (9.45)			26 (7.92)		
Straight Tube: Design #3								
Small	8 (2.44)	18 (5.49)	18 (5.49)	12.75 (32.39)	0.25 (0.635)	27 (8.23)	18 (45.72)	0.375 (0.95)
Medium	8.5 (2.59)	19.5 (5.94)	31 (9.45)			27 (8.23)		
Large	9.5 (2.90)	18.5 (5.64)	30 (9.14)			30 (9.14)		
Straight Tube: Design #6								
Small	6 (1.83)	11.5 (3.51)	30 (9.14)	12.75 (32.39)	0.5 (1.27)	27 (8.23)	18 (45.72)	0.5 (1.27)
Medium	10 (3.05)	15 (4.57)	31 (9.45)			32 (9.75)		
Large	12 (3.66)	19 (5.79)	34 (10.36)			29 (8.84)		

D.2.2. Hot Spot Analysis

Table D.5. Straight Tube Model NW Hot Spot Stresses

	Hot Spot Stress, ksi (MPa)		
Model	Box	Arm	Baseplate
sD1S	3.26 (22.48)	5.55 (38.26)	3.39 (23.39)
sD1M	8.17 (56.31)	11.71 (80.74)	7.56 (52.13)
sD1L	12.00 (82.71)	17.14 (118.17)	9.30 (64.15)
sD3S	4.29 (29.61)	6.93 (47.79)	8.38 (57.80)
sD3M	9.73 (67.09)	17.64 (121.60)	9.97 (68.73)
sD3L	10.69 (73.68)	18.10 (124.80)	12.19 (84.07)
sD6S	2.91 (20.07)	4.21 (29.00)	2.84 (19.57)
sD6M	5.53 (38.13)	8.69 (59.95)	9.23 (63.66)
sD6L	9.61 (66.23)	13.79 (95.05)	10.21 (70.43)

Table D.6. Straight Tube Model T+G Hot Spot Stresses

	Hot Spot Stress, ksi (MPa)		
Model	Box	Arm	Baseplate
sD1S	13.53 (93.29)	8.09 (55.78)	13.48 (92.95)
sD1M	25.01 (172.42)	11.94 (82.33)	25.39 (175.06)
sD1L	35.34 (243.64)	21.65 (149.29)	30.56 (210.68)
sD3S	13.71 (94.53)	10.93 (75.39)	16.03 (110.50)
sD3M	29.42 (202.88)	20.46 (141.09)	34.96 (241.08)
sD3L	29.34 (202.33)	20.49 (141.28)	35.39 (244.03)
sD6S	12.02 (82.88)	6.60 (45.47)	11.37 (78.43)
sD6M	20.97 (144.58)	11.52 (79.45)	22.12 (152.52)
sD6L	32.95 (227.19)	18.99 (130.92)	35.12 (242.17)

D.2.3. S-N Curves

NW S-N Curves

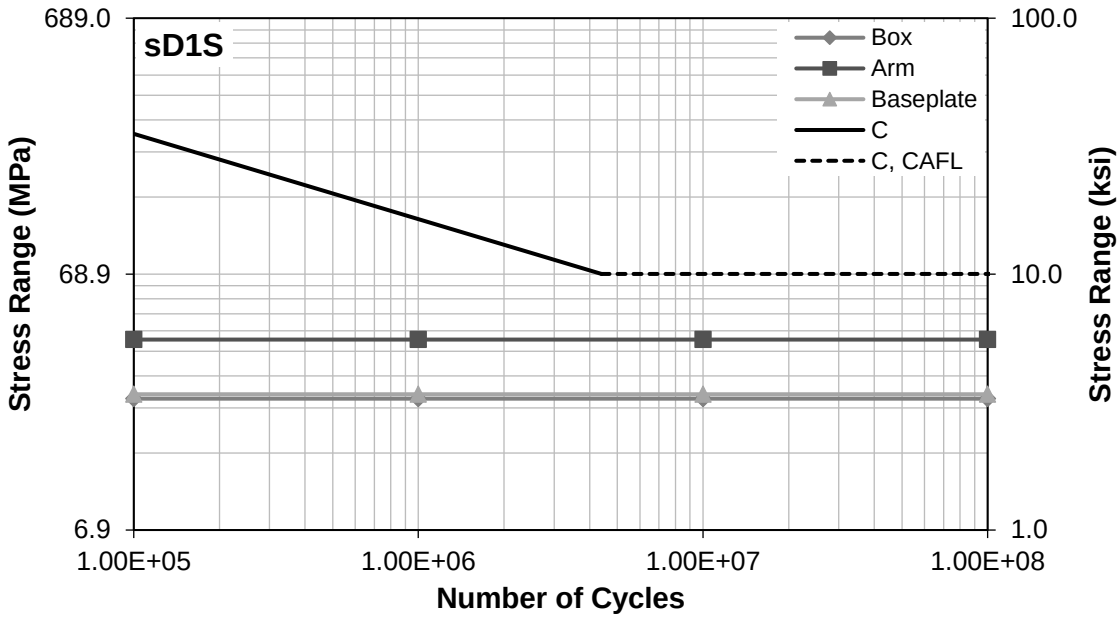

Figure D.55. S-N Curve for sD1S Hot Spot Stresses, NW

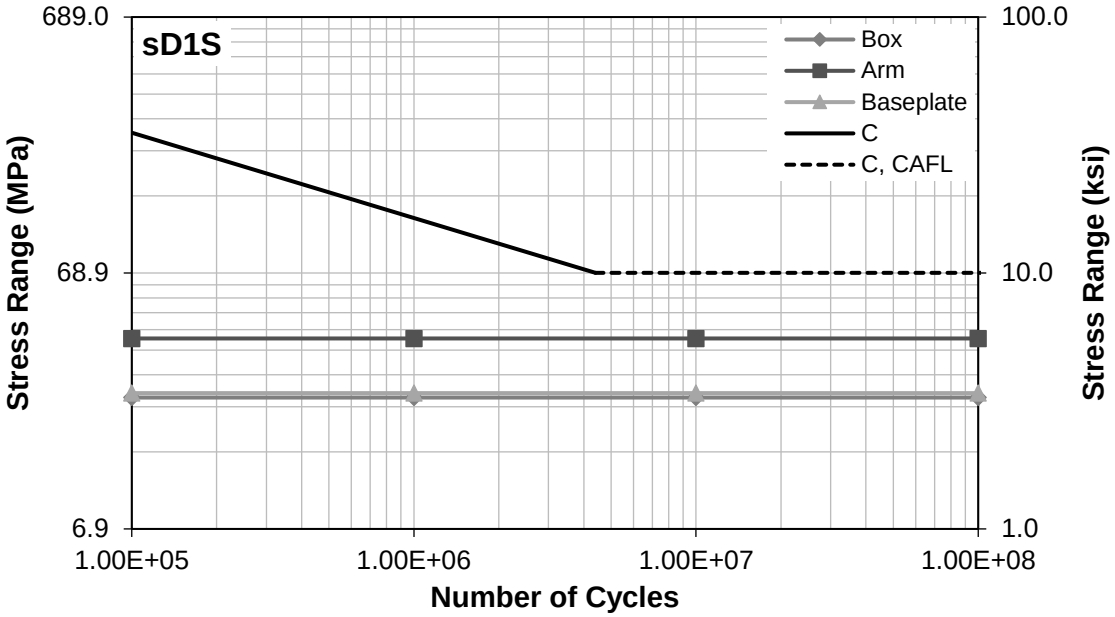

Figure D.56. S-N Curve for sD1M Hot Spot Stresses, NW

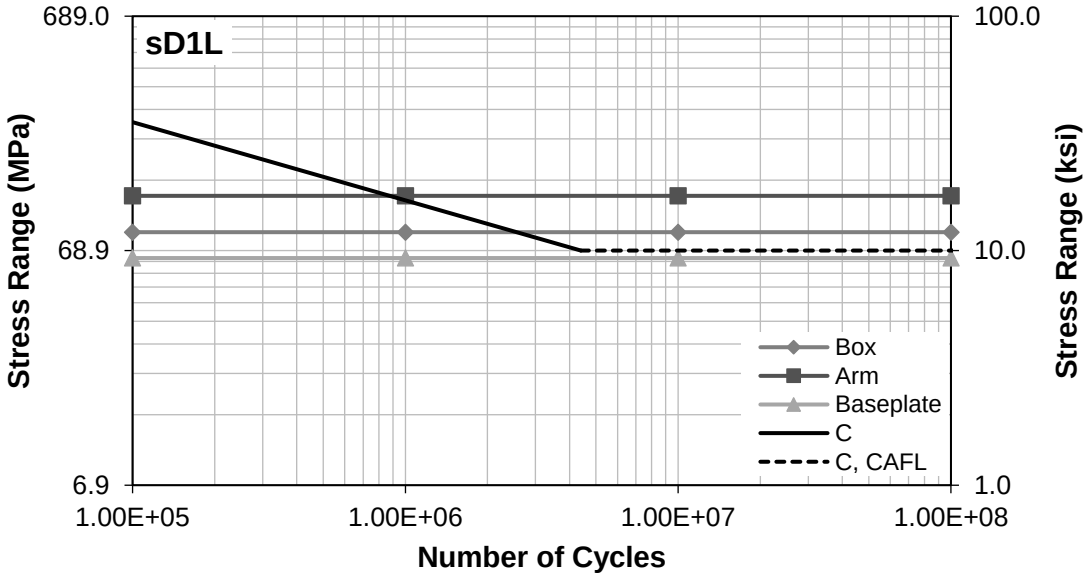

Figure D.57. S-N Curve for sD1L Hot Spot Stresses, NW

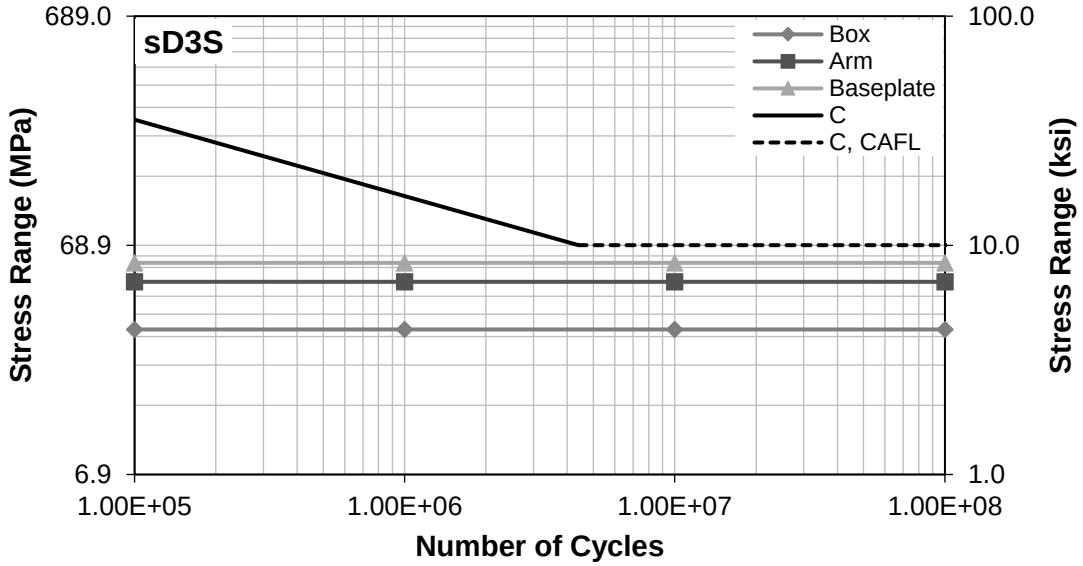

Figure D.58. S-N Curve for sD3S Hot Spot Stresses, NW

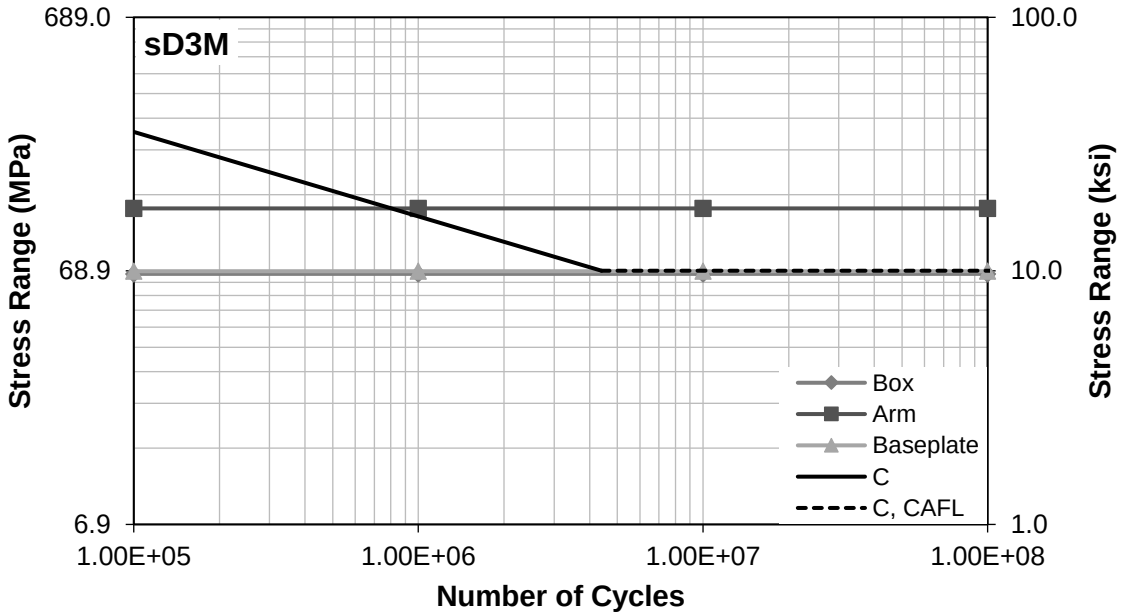

Figure D.59. S-N Curve for sD3M Hot Spot Stresses, NW

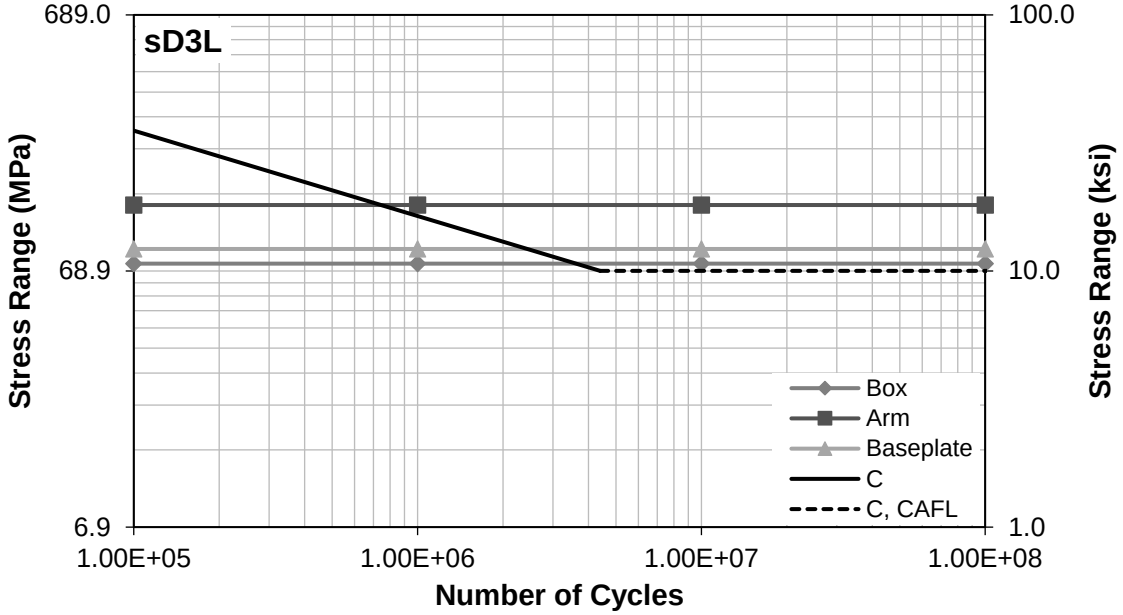

Figure D.60. S-N Curve for sD3L Hot Spot Stresses, NW

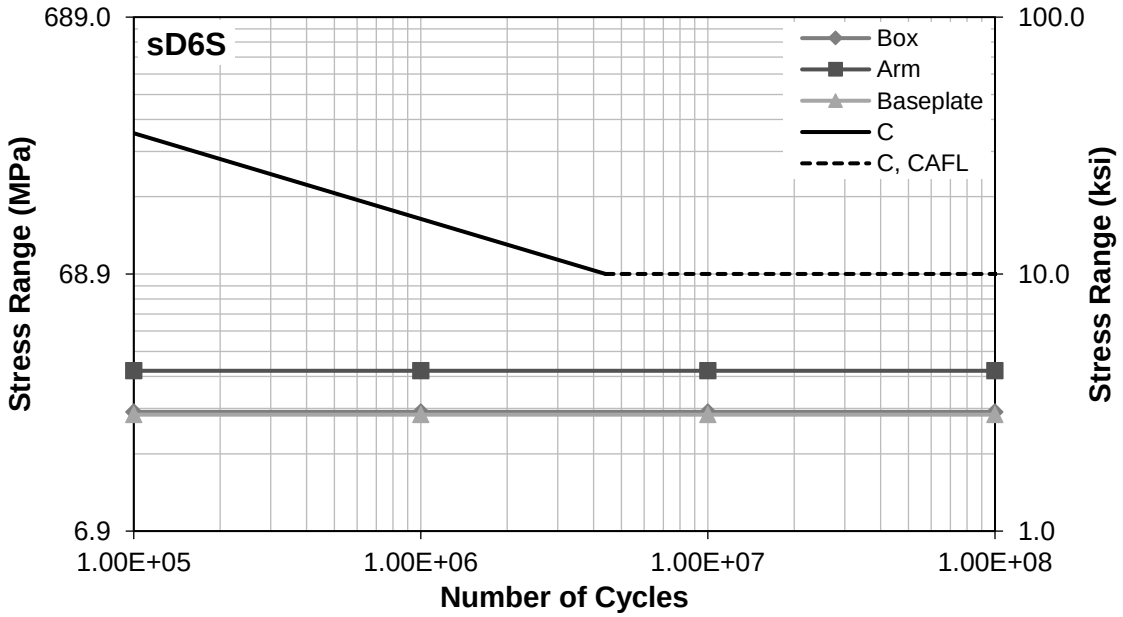

Figure D.61. S-N Curve for sD6S Hot Spot Stresses, NW

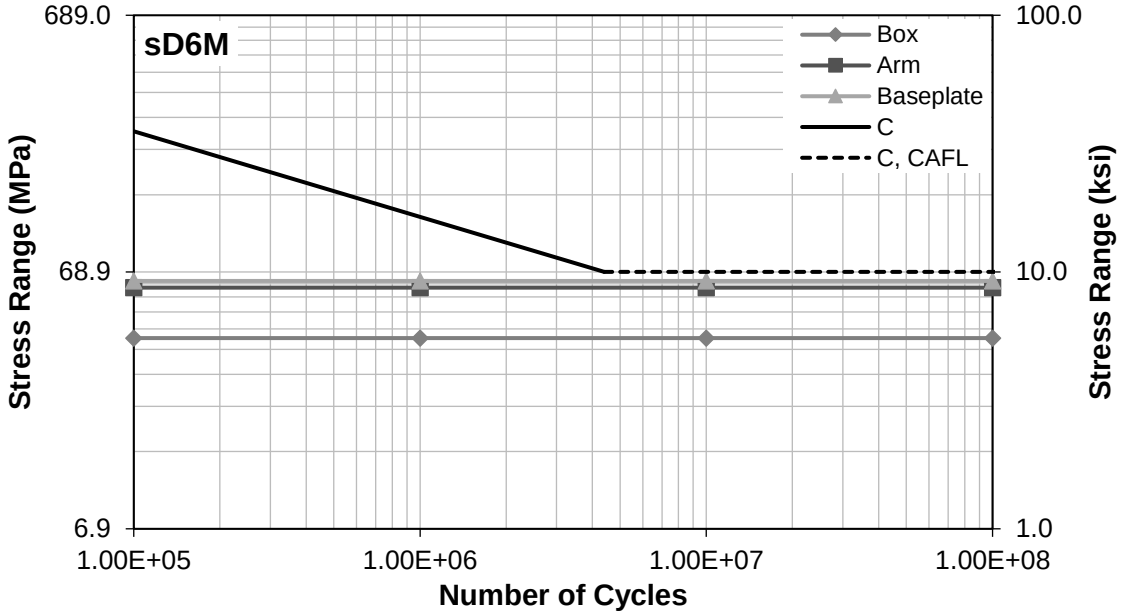

Figure D.62. S-N Curve for sD6M Hot Spot Stresses, NW

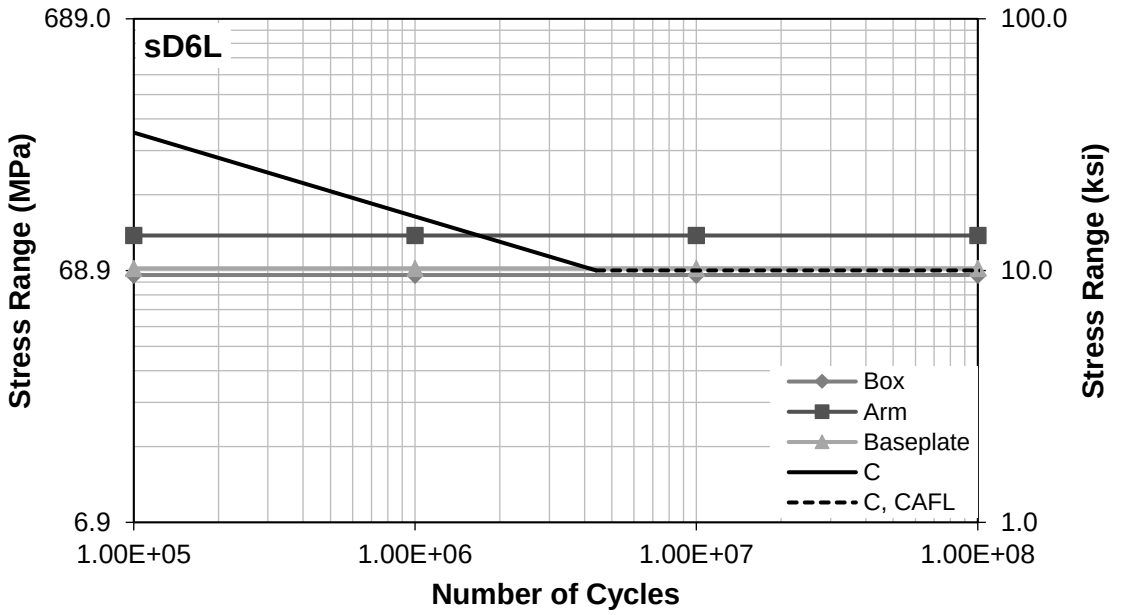

Figure D.63. S-N Curve for sD6L Hot Spot Stresses, NW

T+G S-N Curves

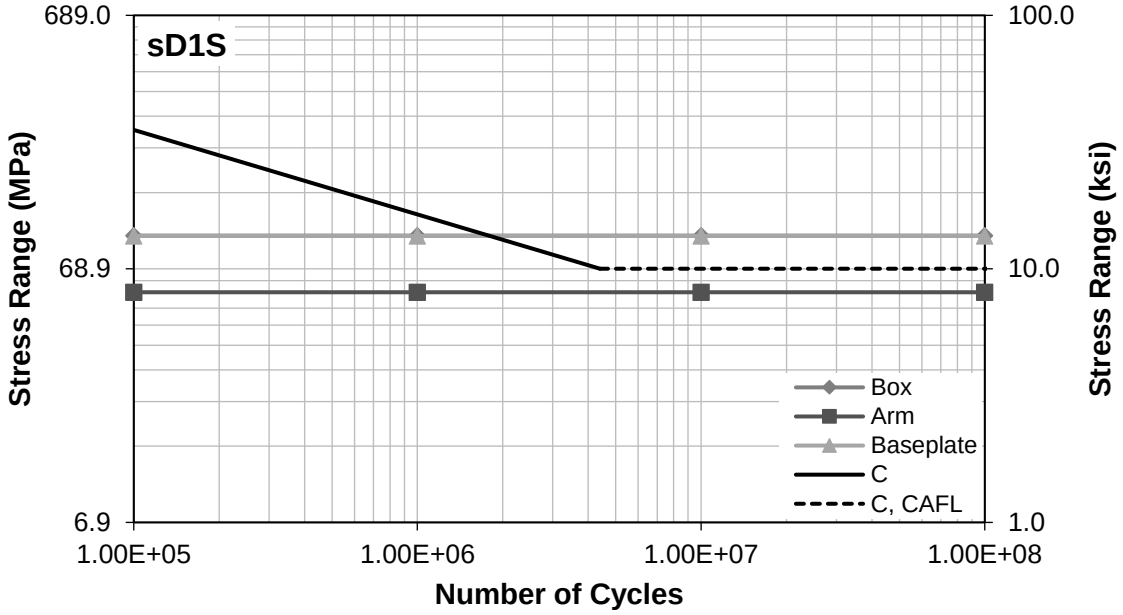

Figure D.64. S-N Curve for sD1S Hot Spot Stresses, T+G

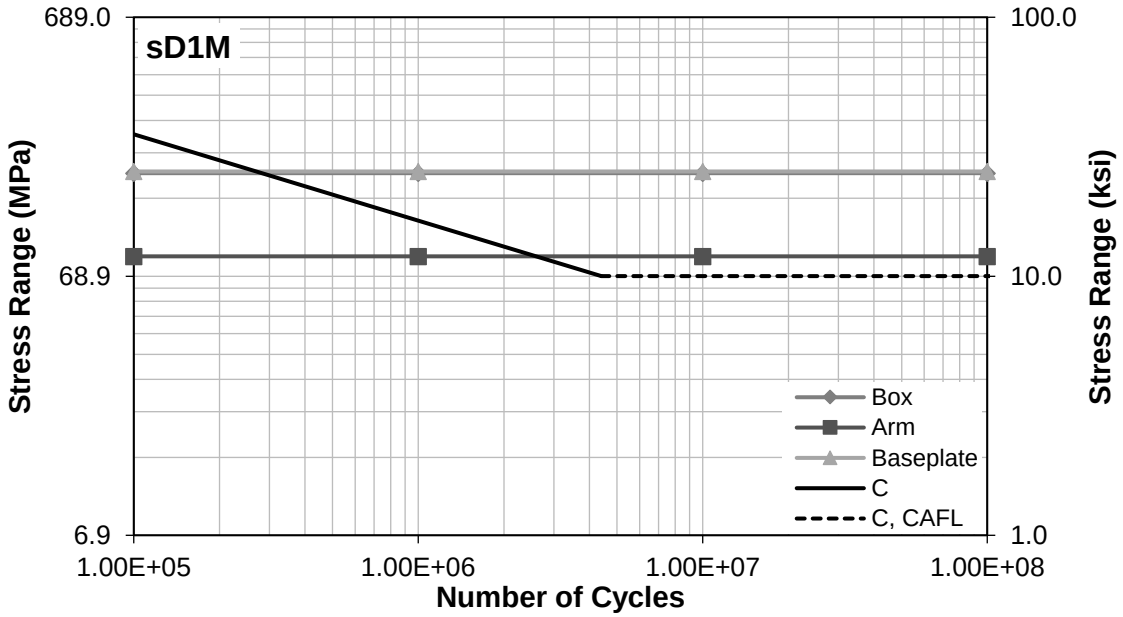

Figure D.65. S-N Curve for sD1M Hot Spot Stresses, T+G

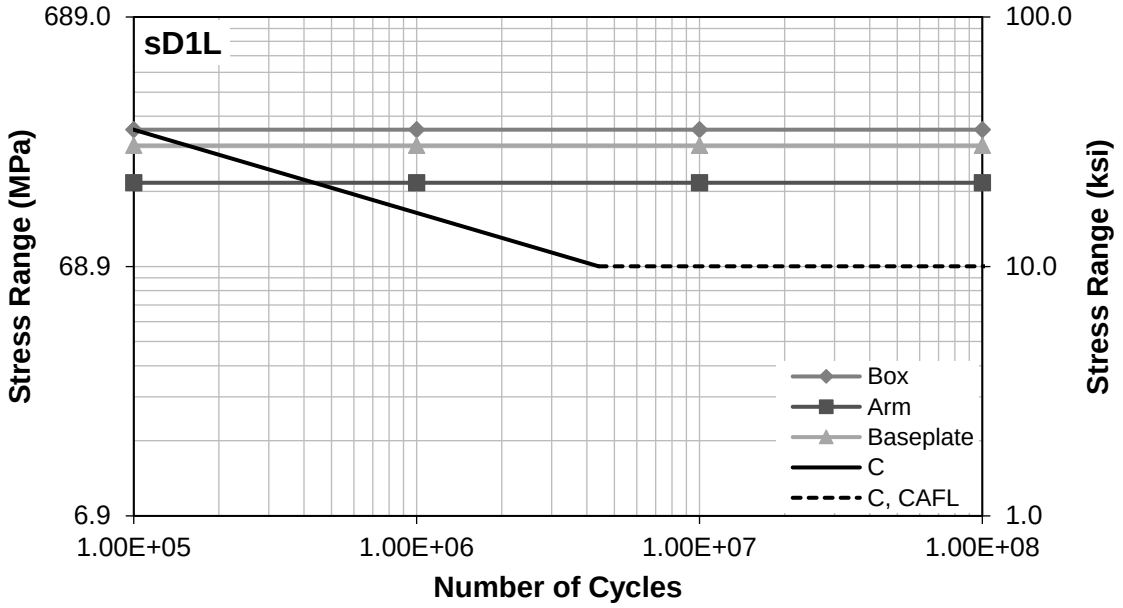

Figure D.66. S-N Curve for sD1L Hot Spot Stresses, T+G

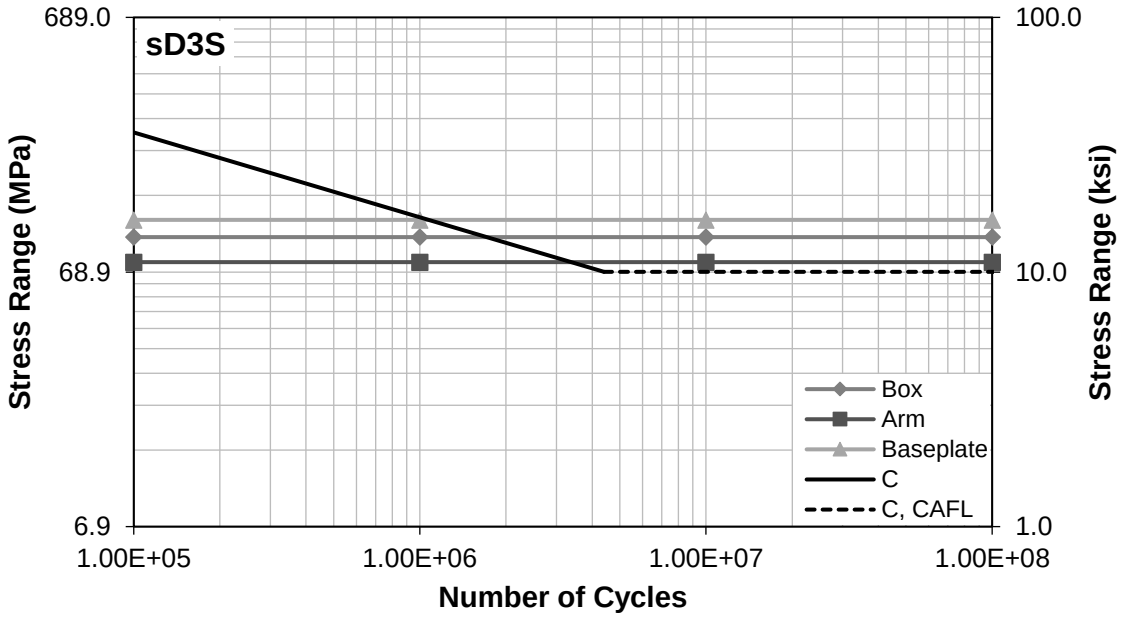

Figure D.67. S-N Curve for sD3S Hot Spot Stresses, T+G

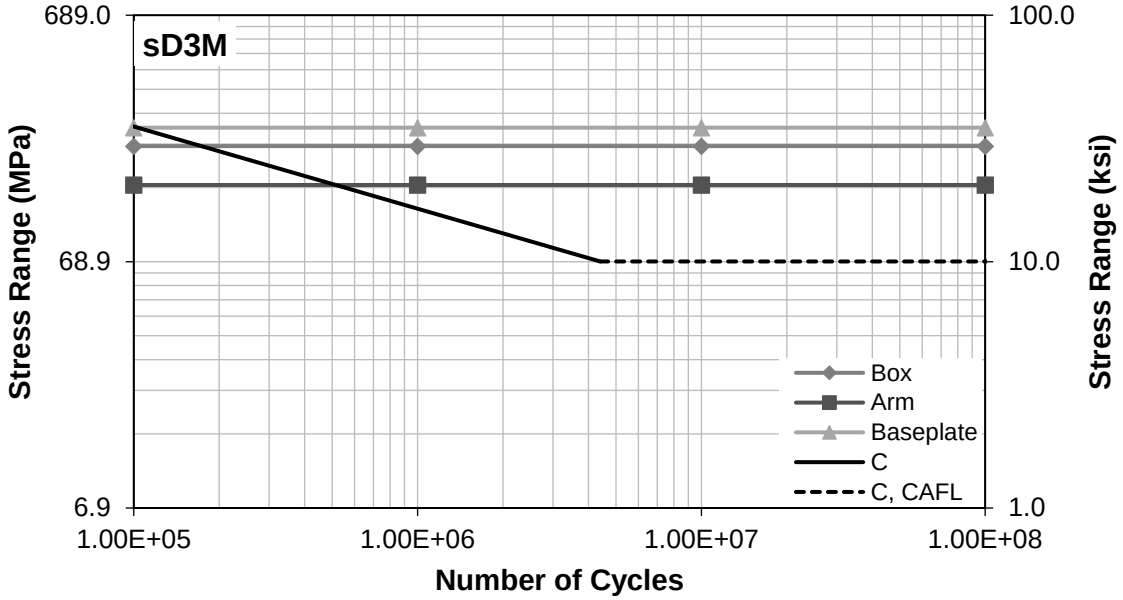

Figure D.68. S-N Curve for sD3M Hot Spot Stresses, T+G

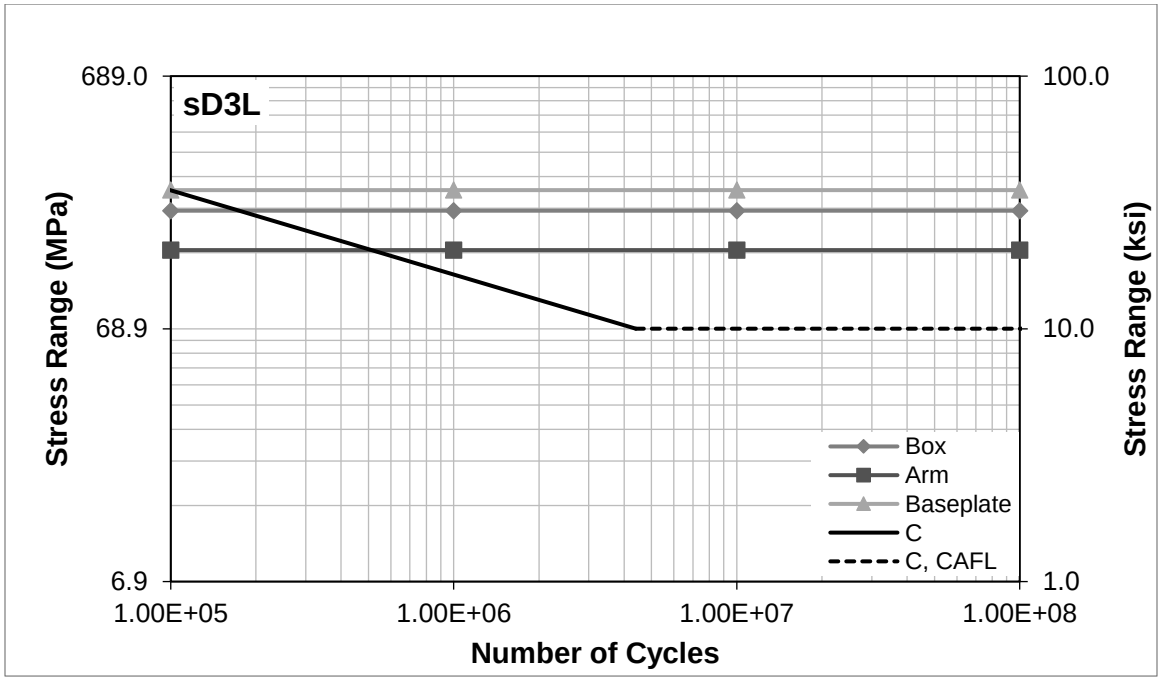

Figure D.69. S-N Curve for sD3L Hot Spot Stresses, T+G

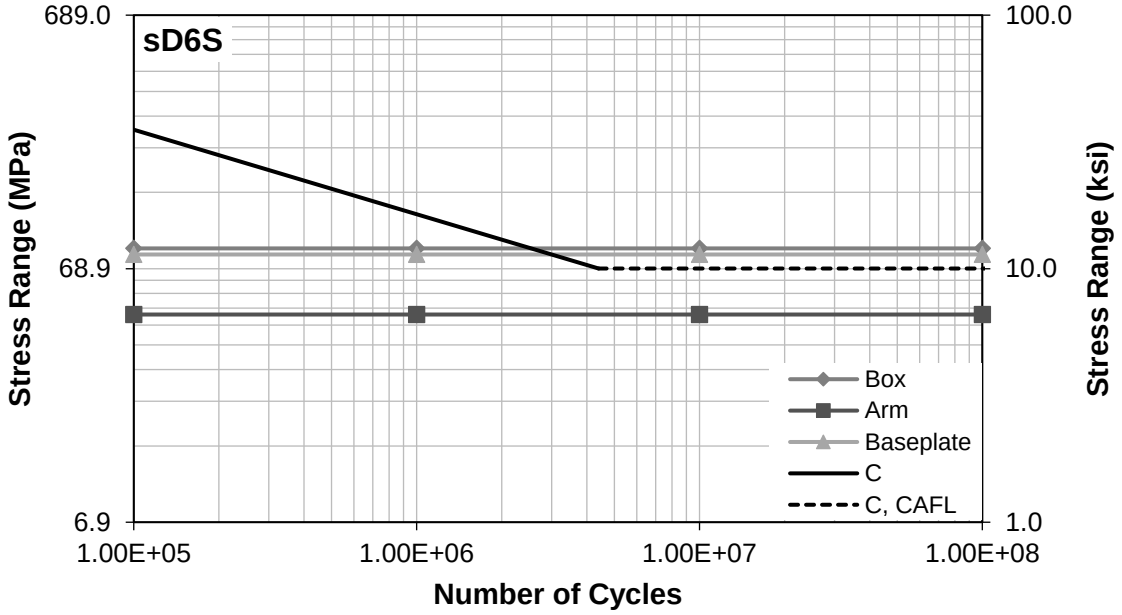

Figure D.70. S-N Curve for sD6S Hot Spot Stresses, T+G

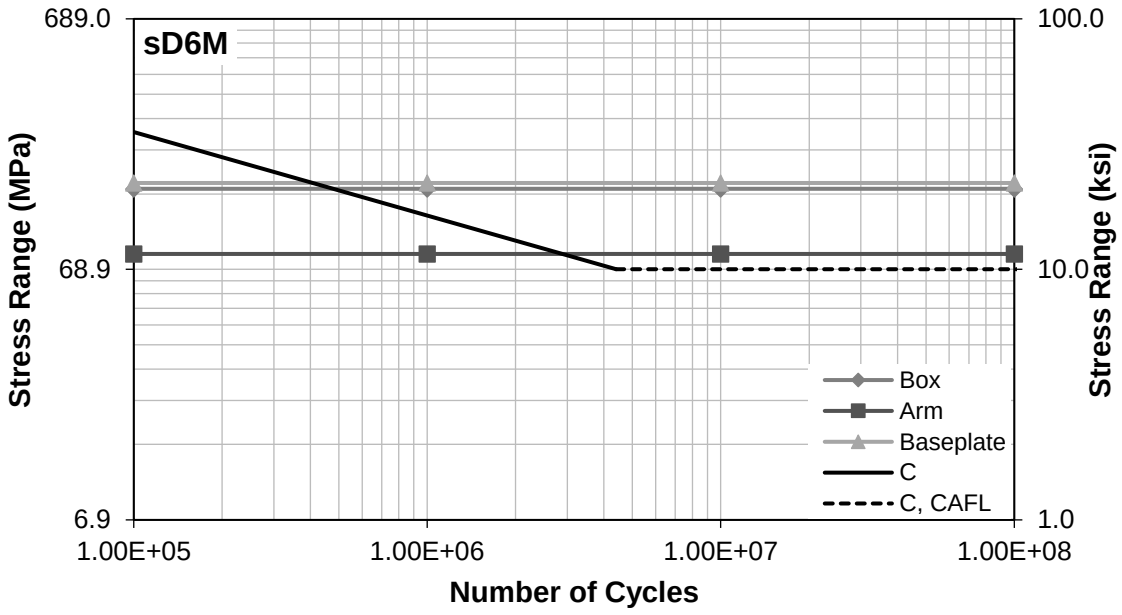

Figure D.71. S-N Curve for sD6M Hot Spot Stresses, T+G

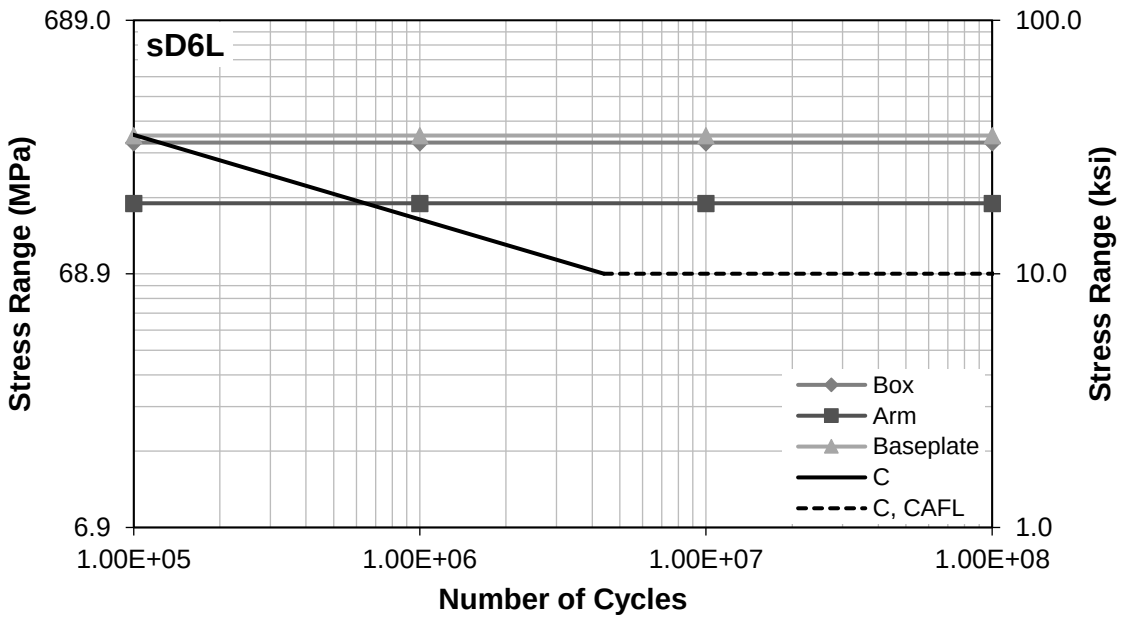

Figure D.72. S-N Curve for sD6L Hot Spot Stresses, T+G

D.2.4. Mises Stress Distributions

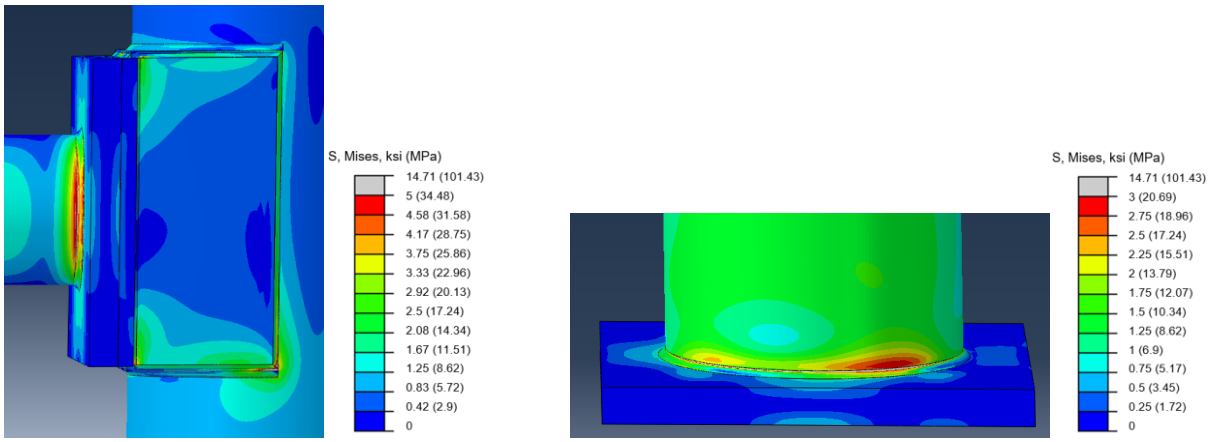

Box and Mast-Arm Connection

Baseplate Connection

Figure D.73. Mises Stresses, sD1S, NW

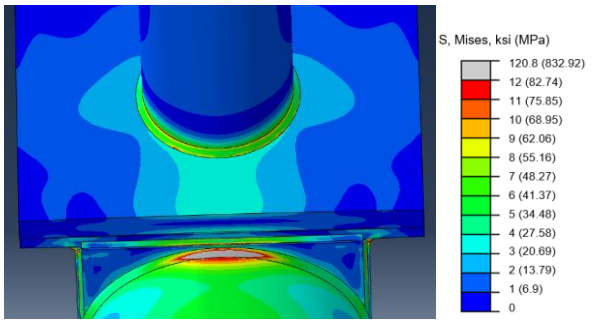

Box Connection

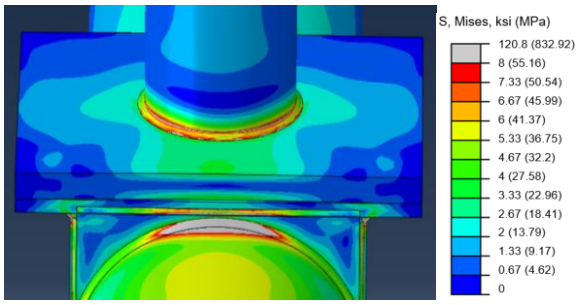

Mast-Arm Connection

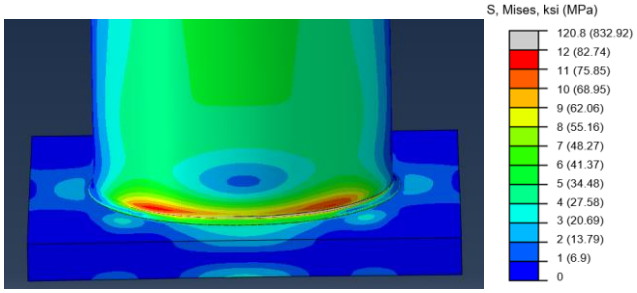

Baseplate Connection

Figure D.74. Mises Stresses, sD1S, T+G

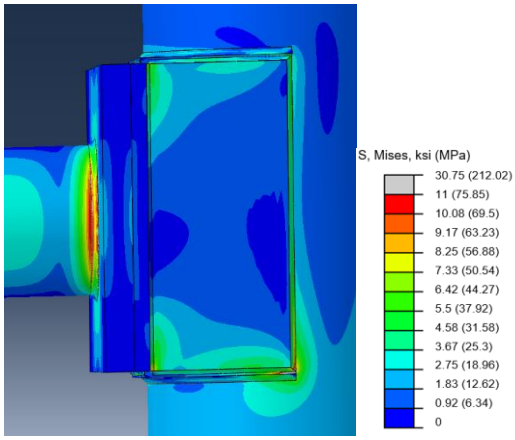

Box and Mast-Arm Connection

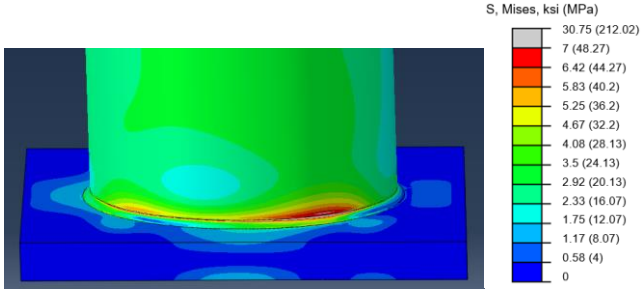

Baseplate Connection

Figure D.75. Mises Stresses, sD1M, NW

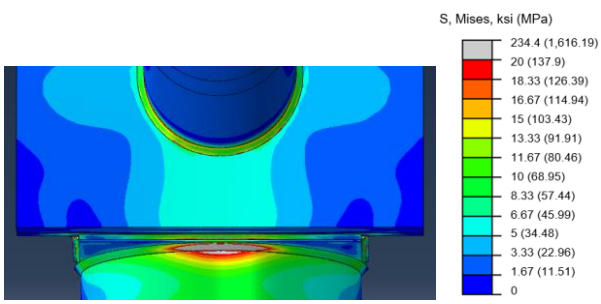

Box Connection

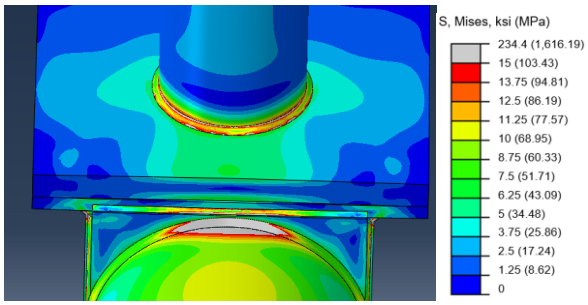

Mast-Arm Connection

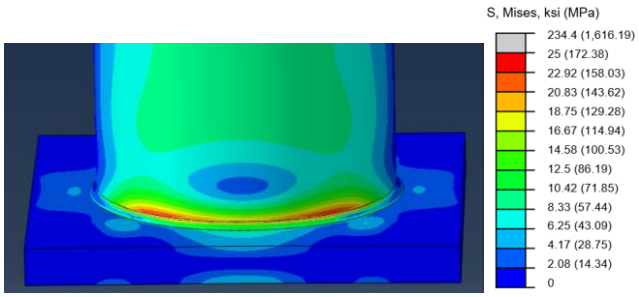

Baseplate Connection

Figure D.76. Mises Stresses, sD1M, T+G

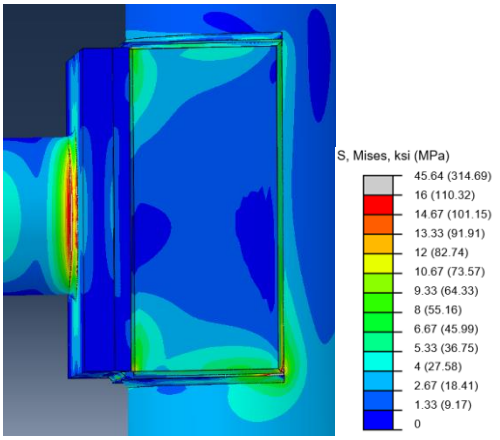

Box and Mast-Arm Connection

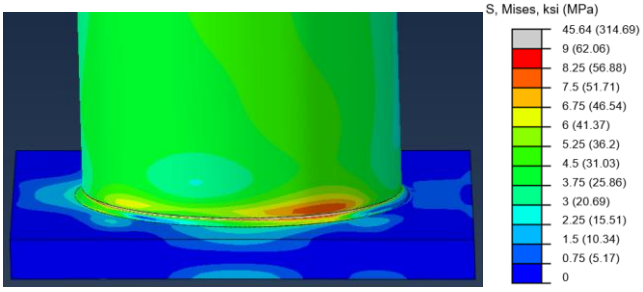

Baseplate Connection

Figure D.77. Mises Stresses, sD1L, NW

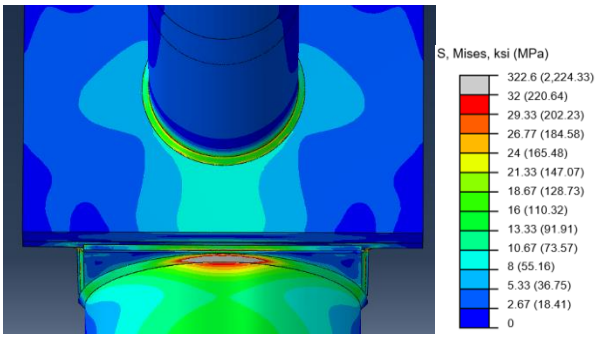

Box Connection

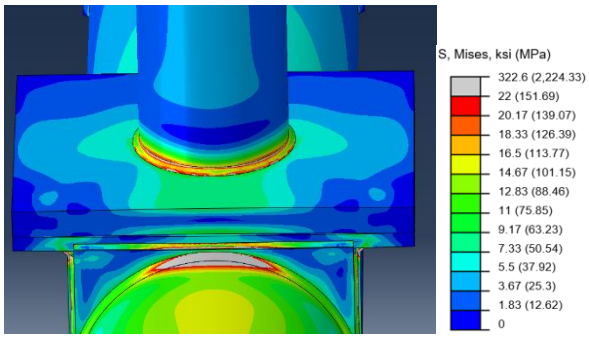

Mast-Arm Connection

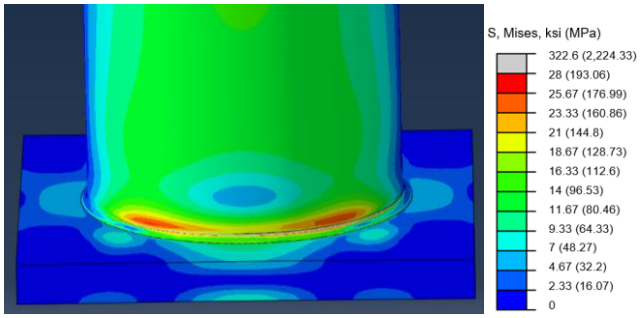

Baseplate Connection

Figure D.78. Mises Stresses, sD1L, T+G

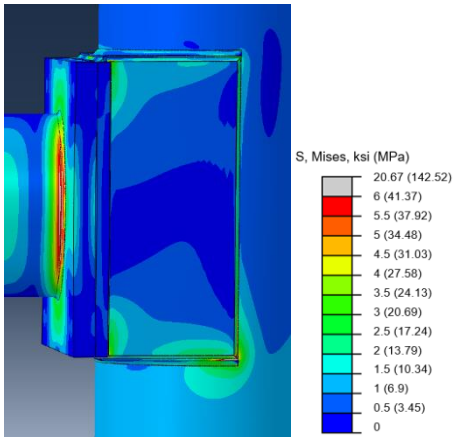

Box and Mast-Arm Connection

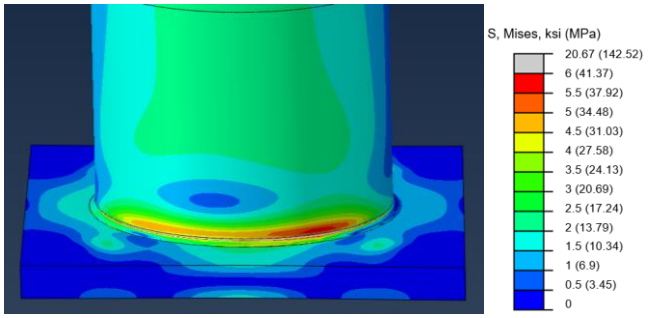

Baseplate Connection

Figure D.79. Mises Stresses, sD3S, NW

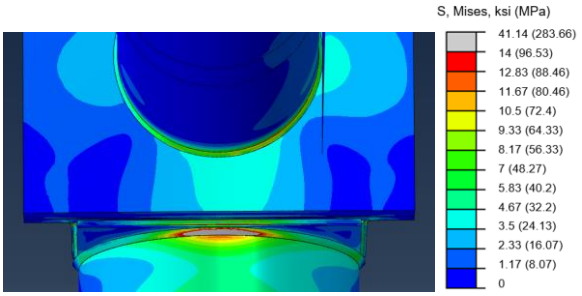

Box Connection

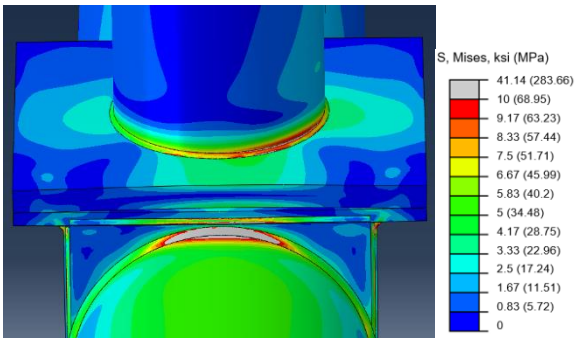

Mast-Arm Connection

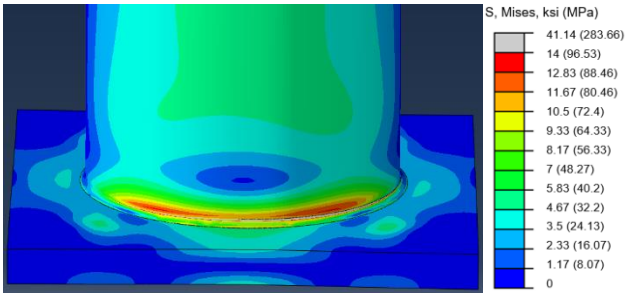

Baseplate Connection

Figure D.80. Mises Stresses, sD3S, T+G

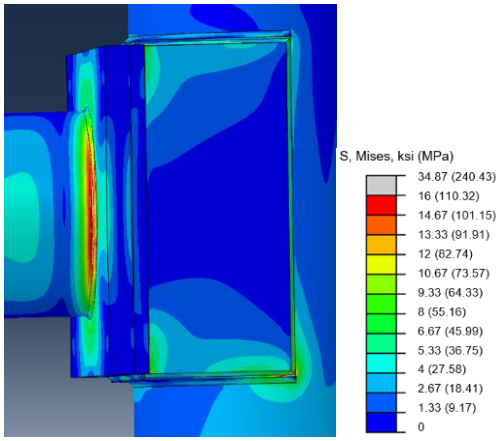

Box and Mast-Arm Connection

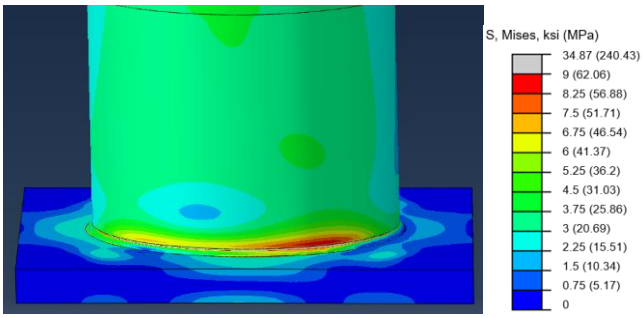

Baseplate Connection

Figure D.81. Mises Stresses, sD3M, NW

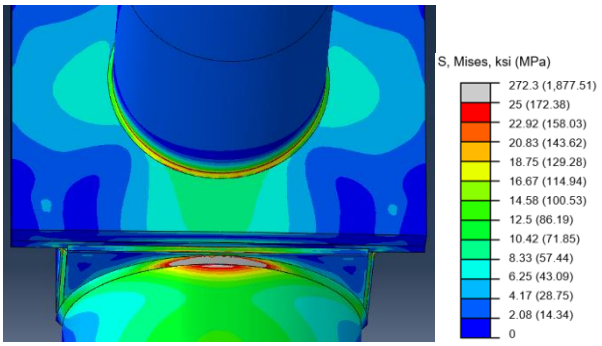

Box Connection

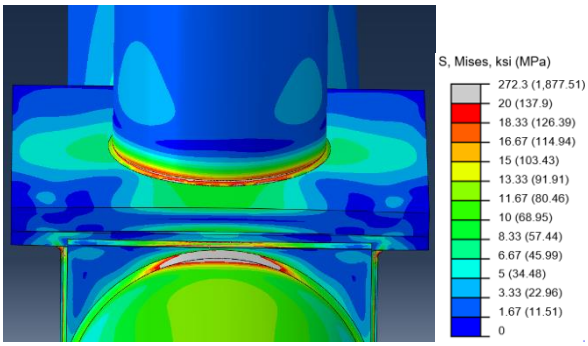

Mast-Arm Connection

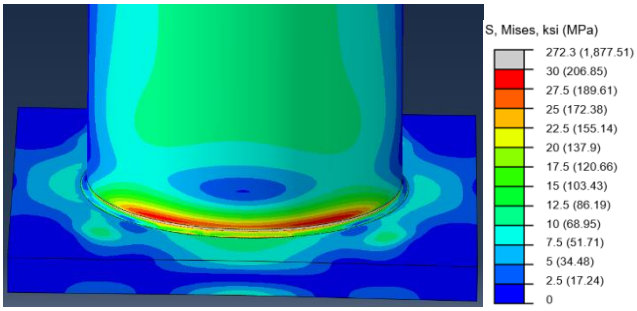

Baseplate Connection

Figure D.82. Mises Stresses, sD3M, T+G

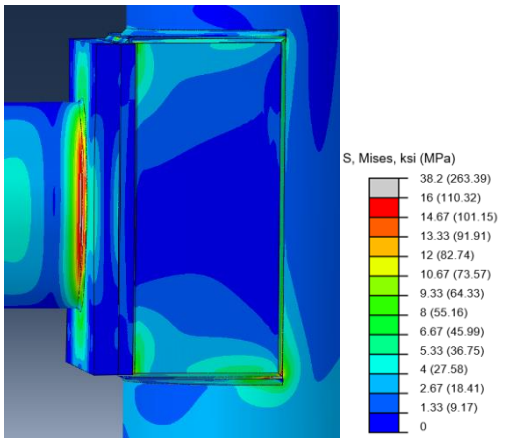

Box and Mast-Arm Connection

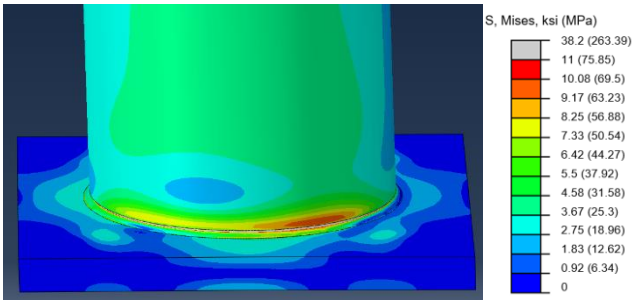

Baseplate Connection

Figure D.83. Mises Stresses, sD3L, NW

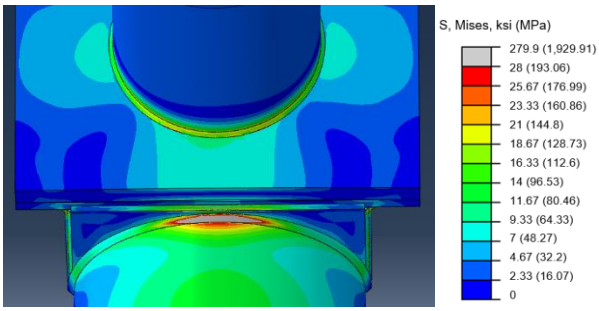

Box Connection

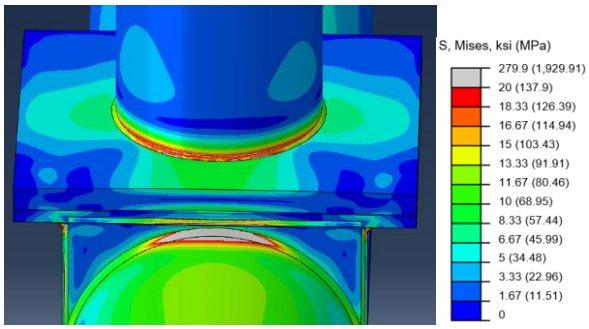

Mast-Arm Connection

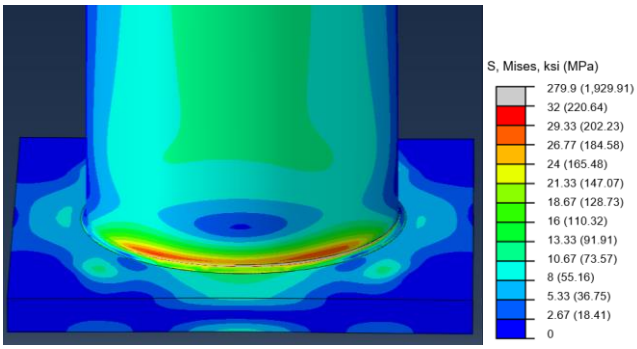

Baseplate Connection

Figure D.84. Mises Stresses, sD3L, T+G

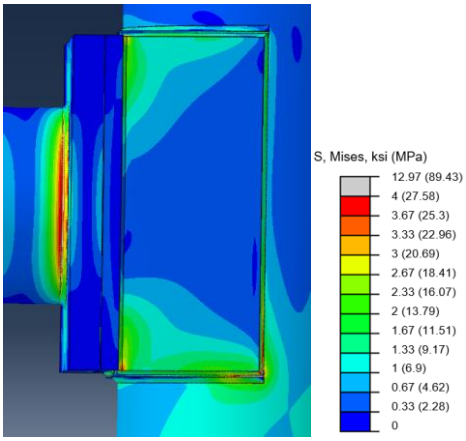

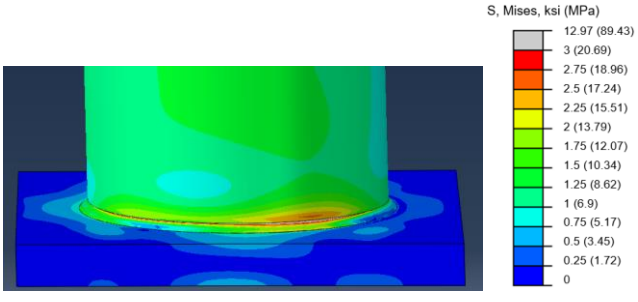

Baseplate Connection

Box and Mast-Arm Connection

Figure D.85. Mises Stresses, sD6S, NW

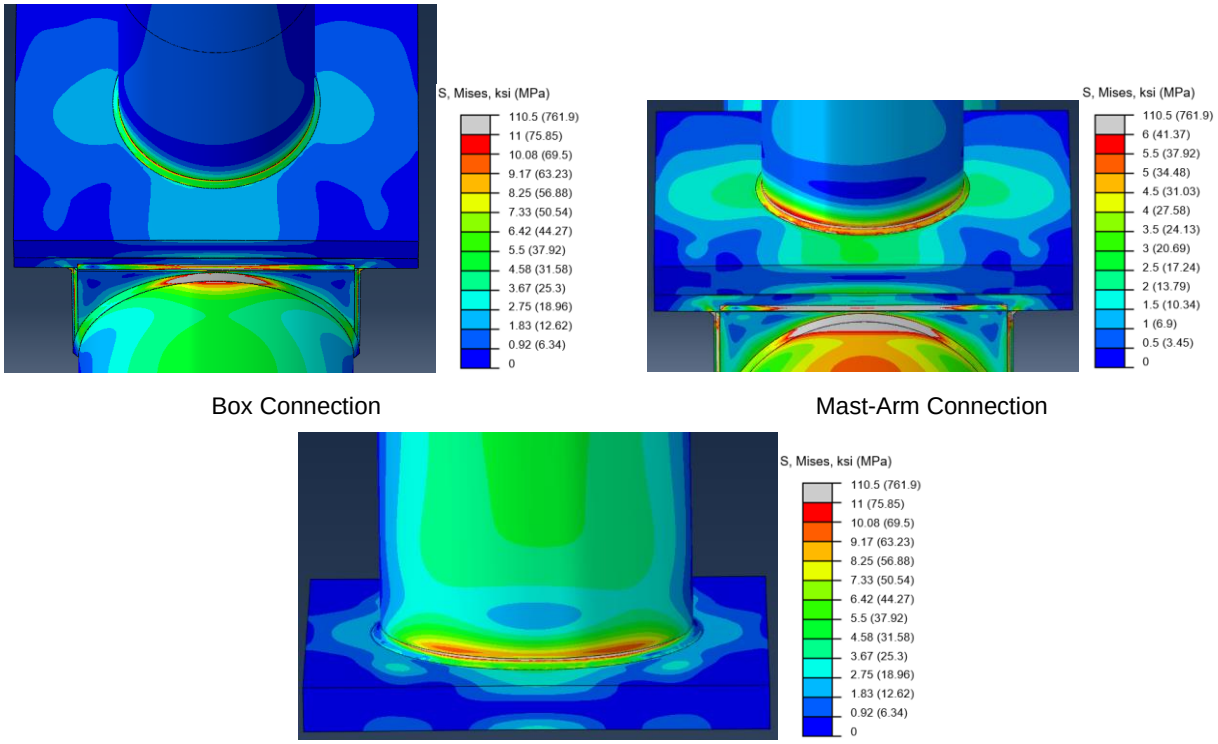

Box Connection

Mast-Arm Connection

Baseplate Connection

Figure D.86. Mises Stresses, sD6S, T+G

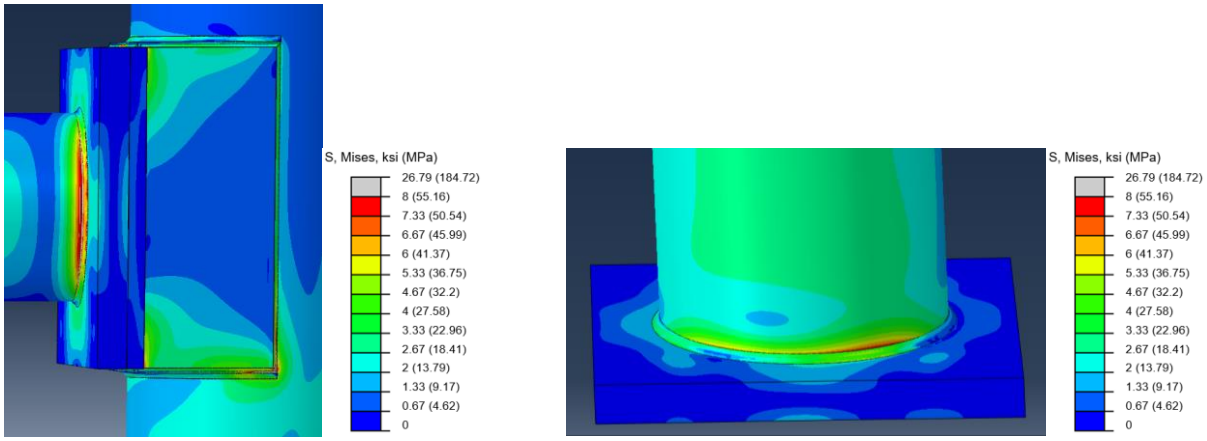

Box and Mast-Arm Connection

Baseplate Connection

Figure D.87. Mises Stresses, sD6M, NW

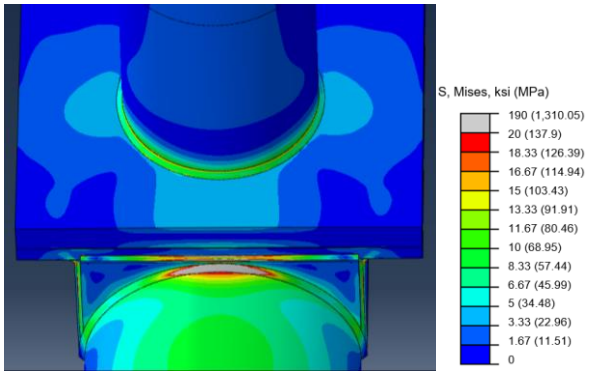

Box Connection

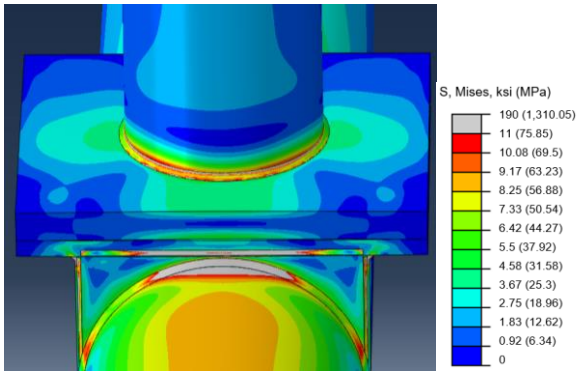

Mast-Arm Connection

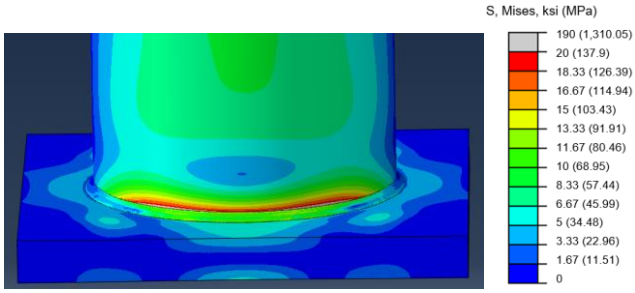

Baseplate Connection

Figure D.88. Mises Stresses, sD6M, T+G

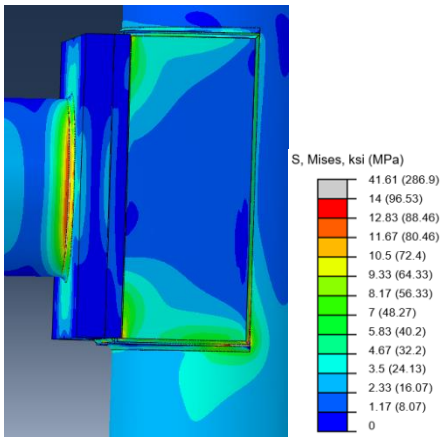

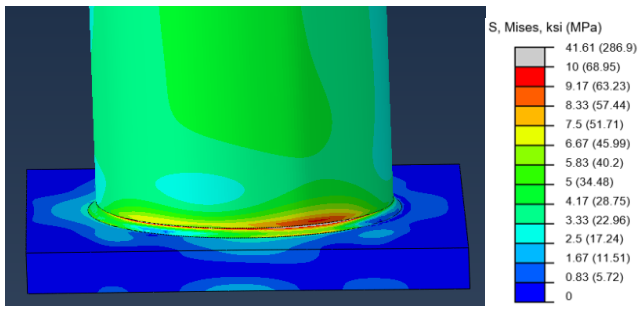

Baseplate Connection

Box and Mast-Arm Connection

Figure D.89. Mises Stresses, sD6L, NW

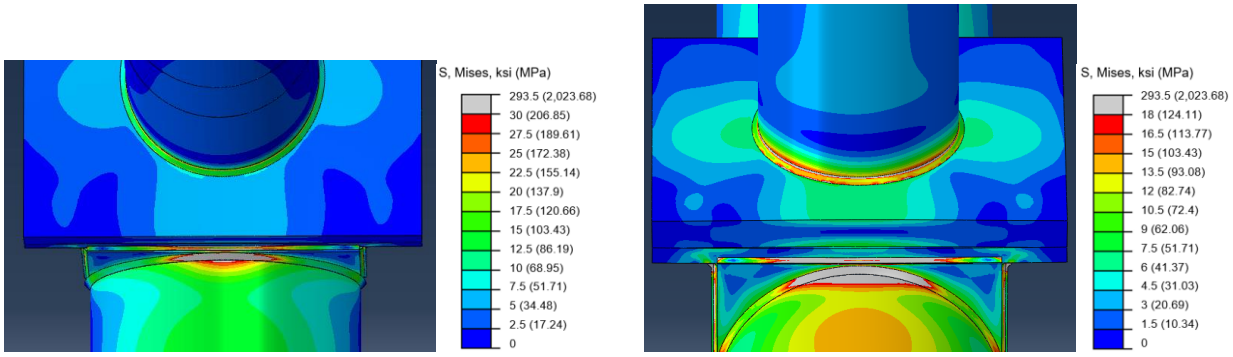

Box Connection Mast-Arm Connection

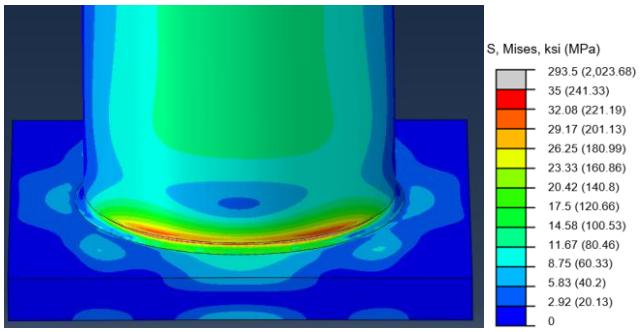

Baseplate Connection

Figure D.90. Mises Stresses, sD6L, T+G

D.2.5. Paths- Max Principal Stress

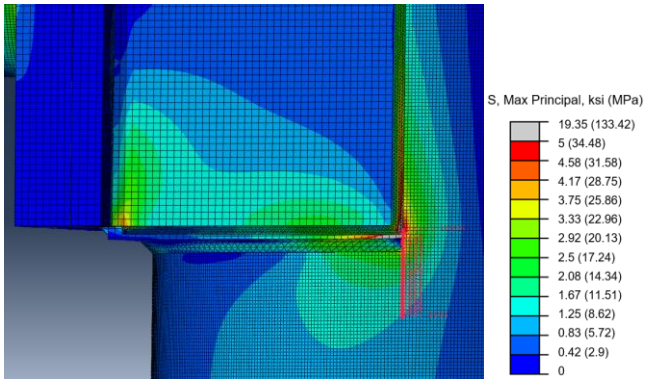

Box Connection

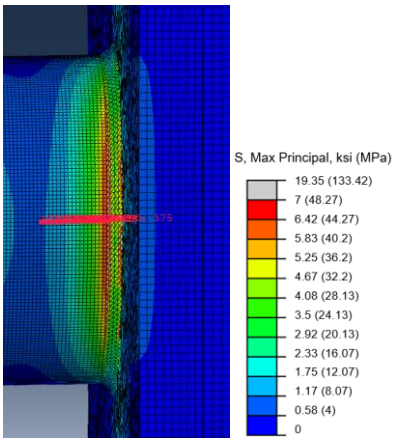

Mast-Arm Connection

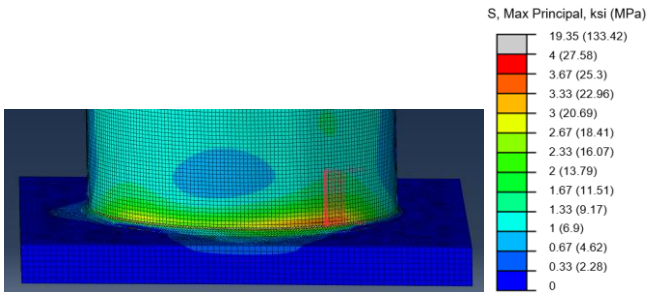

Baseplate Connection

Figure D.91. Paths, sD1S, NW

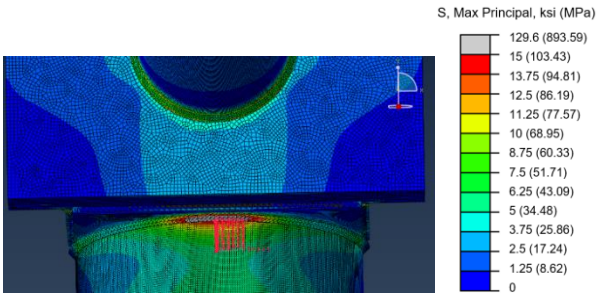

Box Connection

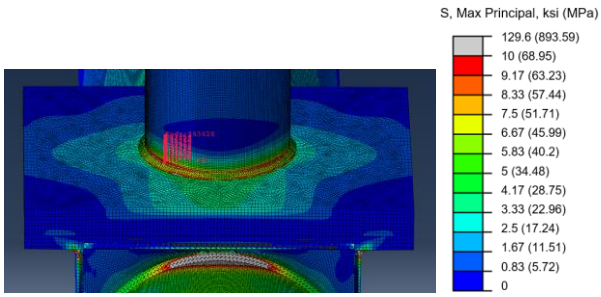

Mast-Arm Connection

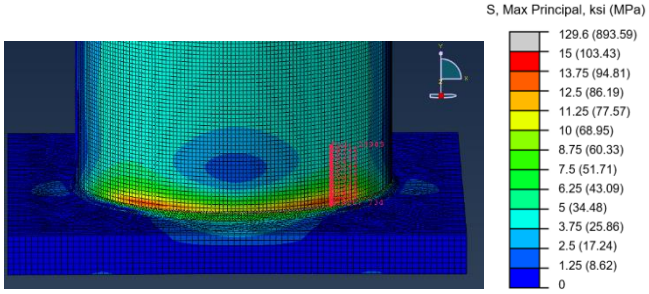

Baseplate Connection

Figure D.92. Paths, sD1S, T+G

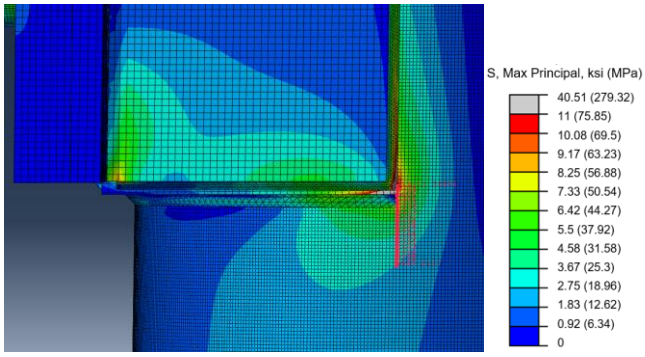

Box Connection

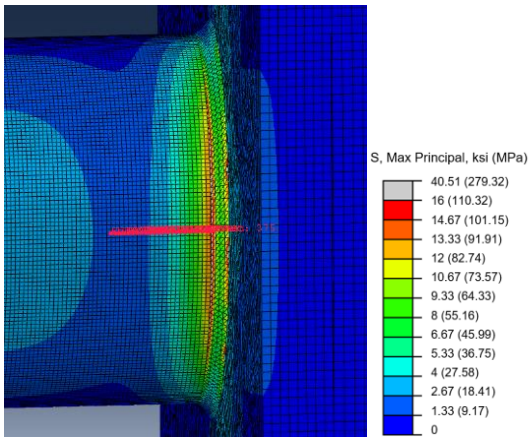

Mast-Arm Connection

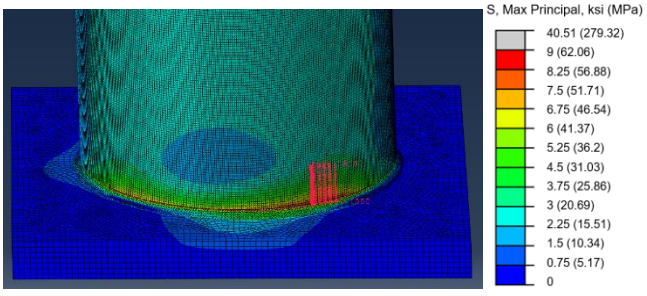

Baseplate Connection

Figure D.93. Paths, sD1M, NW

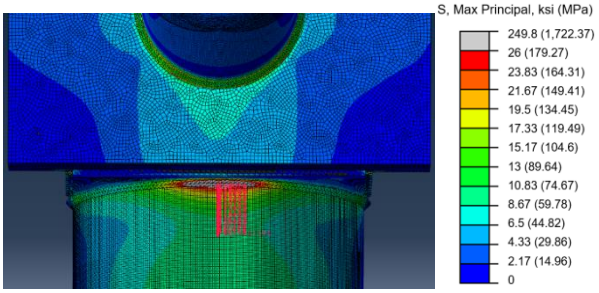

Box Connection

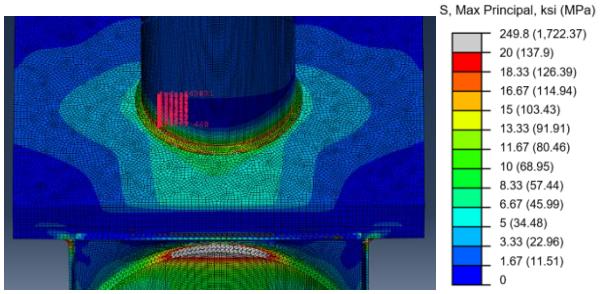

Mast-Arm Connection

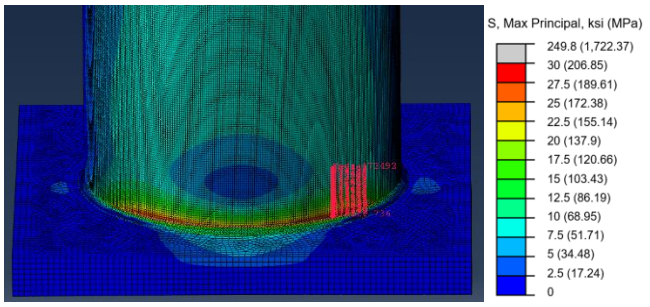

Baseplate Connection

Figure D.94. Paths, sD1M, T+G

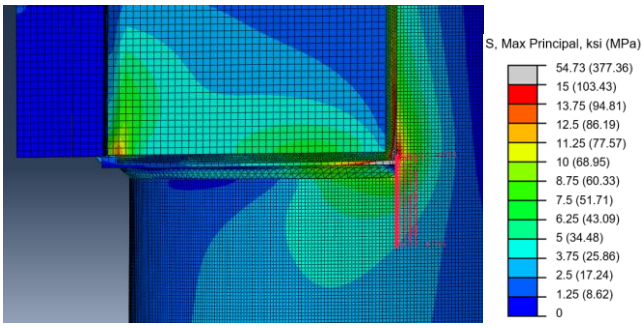

Box Connection

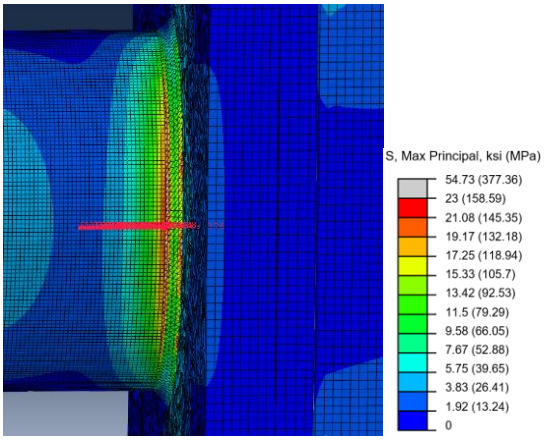

Mast-Arm Connection

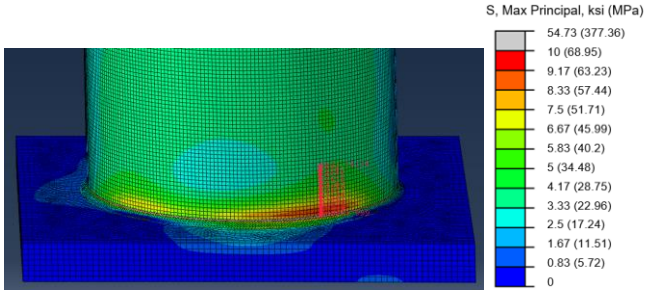

Baseplate Connection

Figure D.95. Paths, sD1L, NW

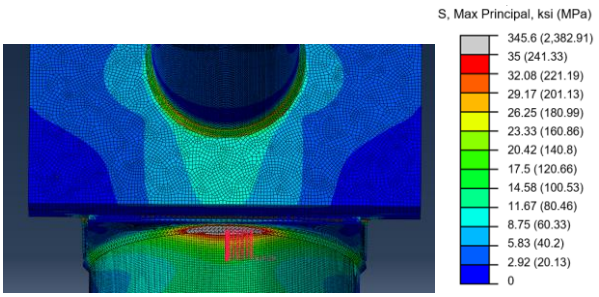

Box Connection

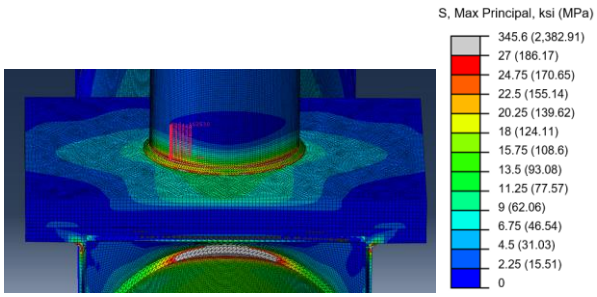

Mast-Arm Connection

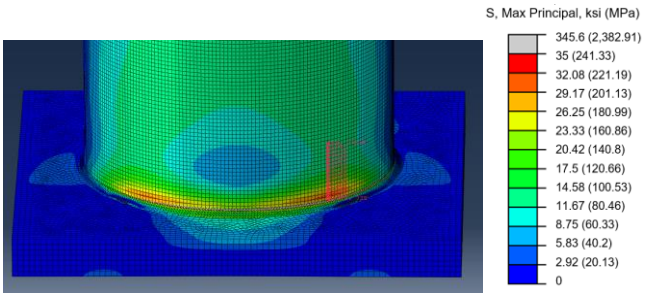

Baseplate Connection

Figure D.96. Paths, sD1L, T+G

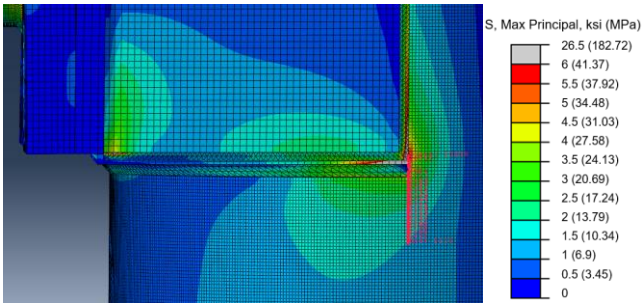

Box Connection

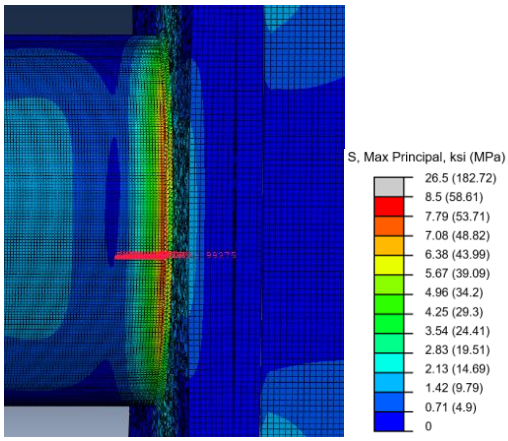

Mast-Arm Connection

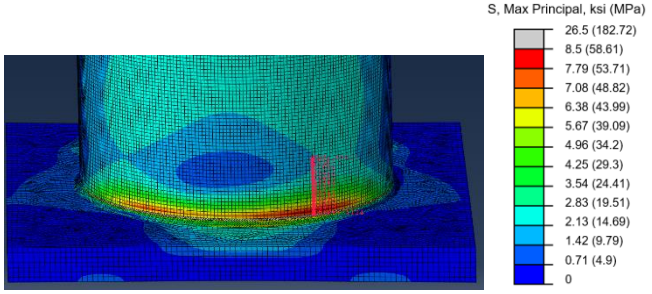

Baseplate Connection

Figure D.97. Paths, sD3S, NW

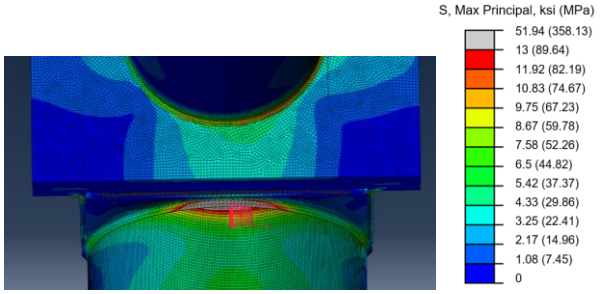

Box Connection

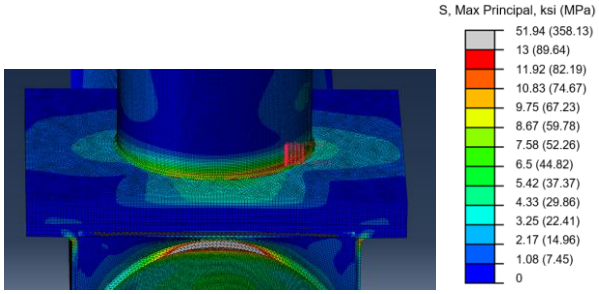

Mast-Arm Connection

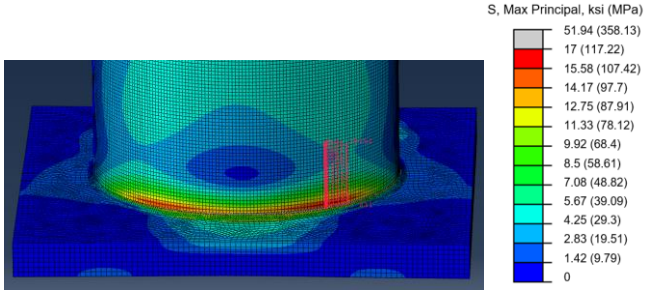

Baseplate Connection

Figure D.98. Paths, sD3S, T+G

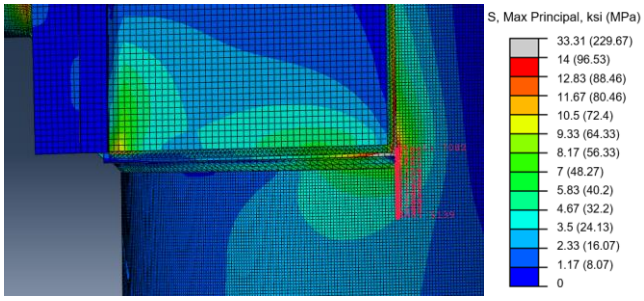

Box Connection

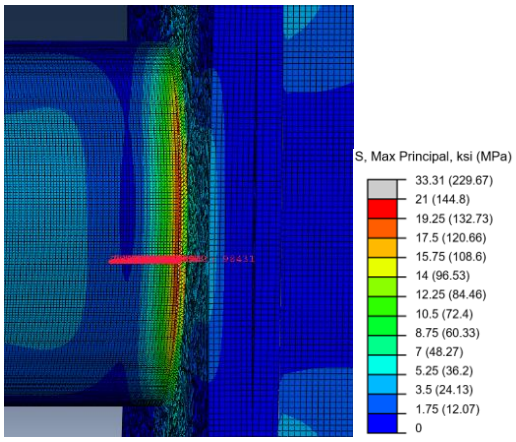

Mast-Arm Connection

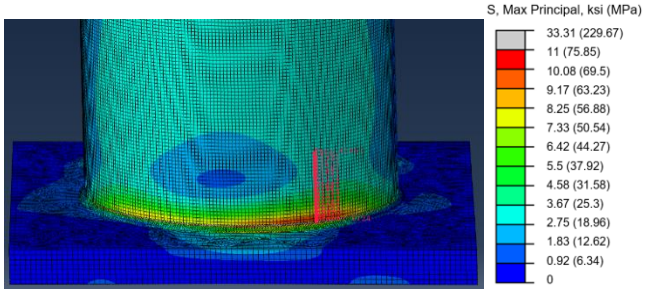

Baseplate Connection

Figure D.99. Paths, sD3M, NW

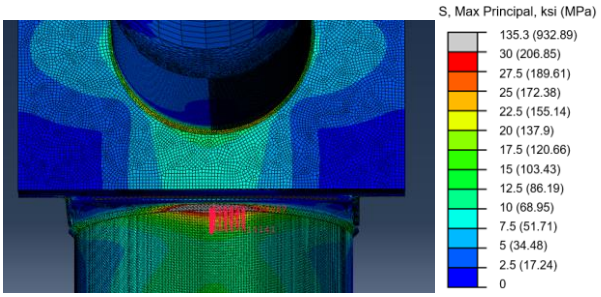

Box Connection

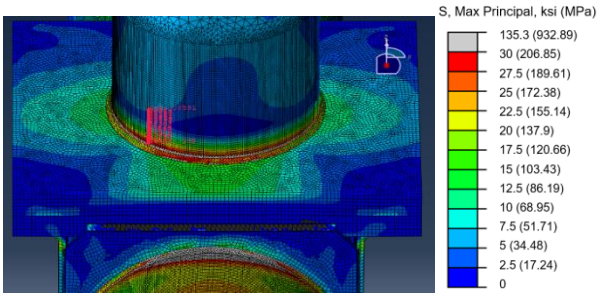

Mast-Arm Connection

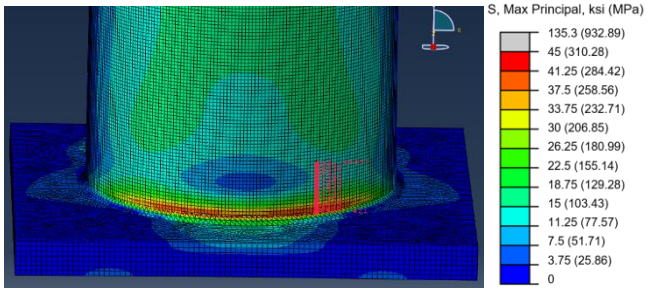

Baseplate Connection

Figure D.100. Paths, sD3M, T+G

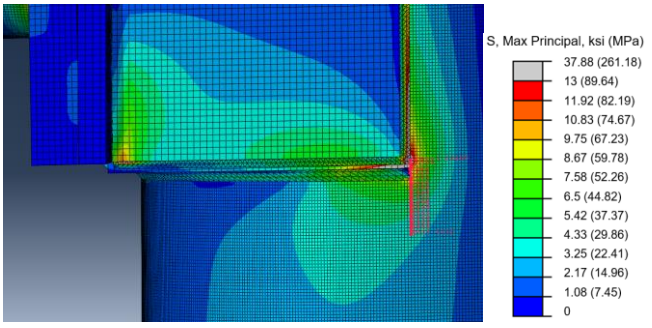

Box Connection

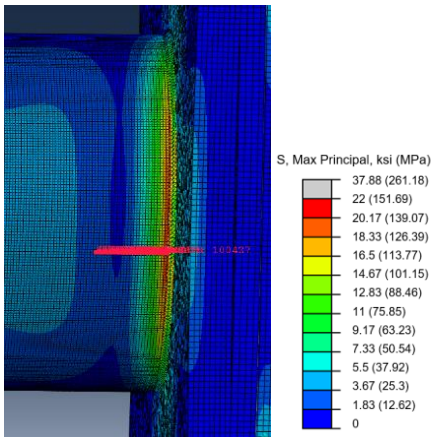

Mast-Arm Connection

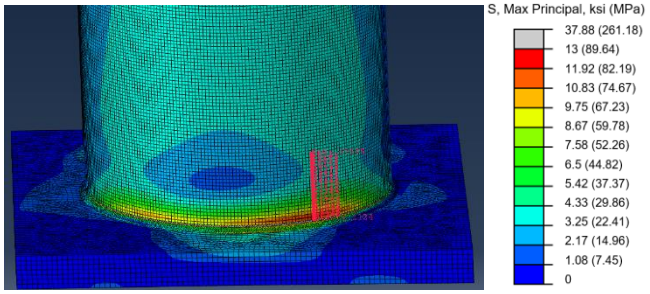

Baseplate Connection

Figure D.101. Paths, sD3L, NW

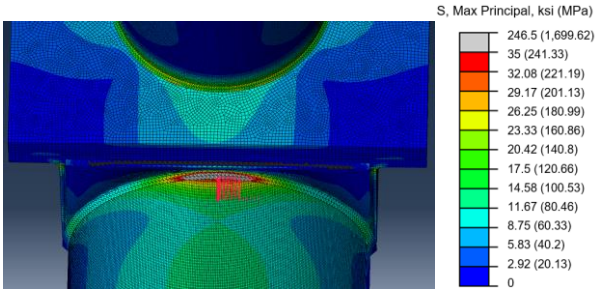

Box Connection

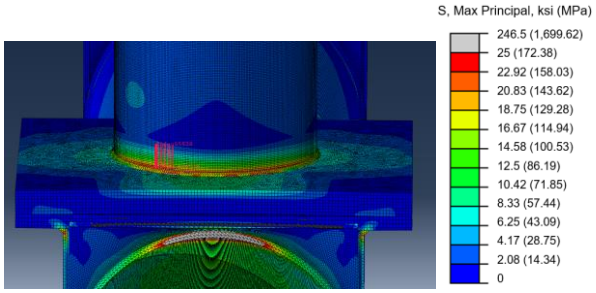

Mast-Arm Connection

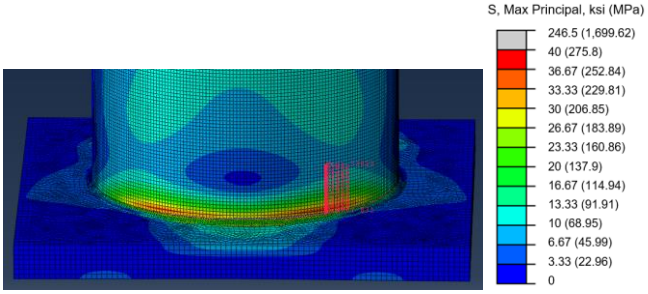

Baseplate Connection

Figure D.102. Paths, sD3L, T+G

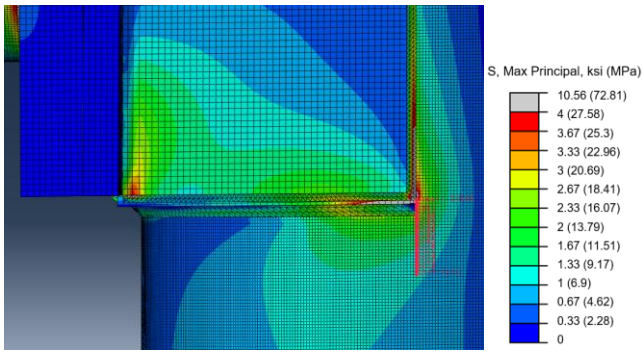

Box Connection

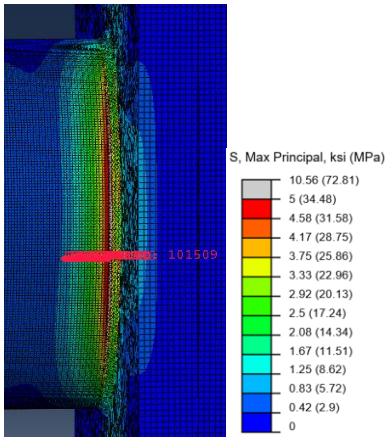

Mast-Arm Connection

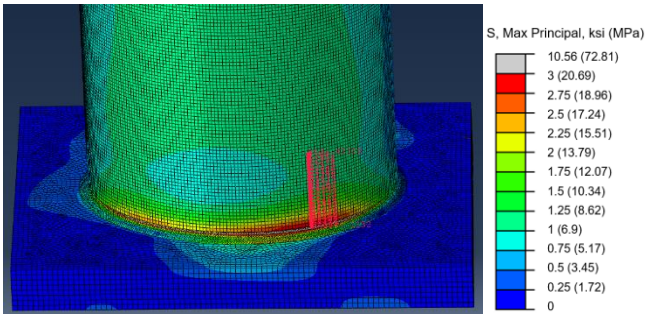

Baseplate Connection

Figure D.103. Paths, sD6S, NW

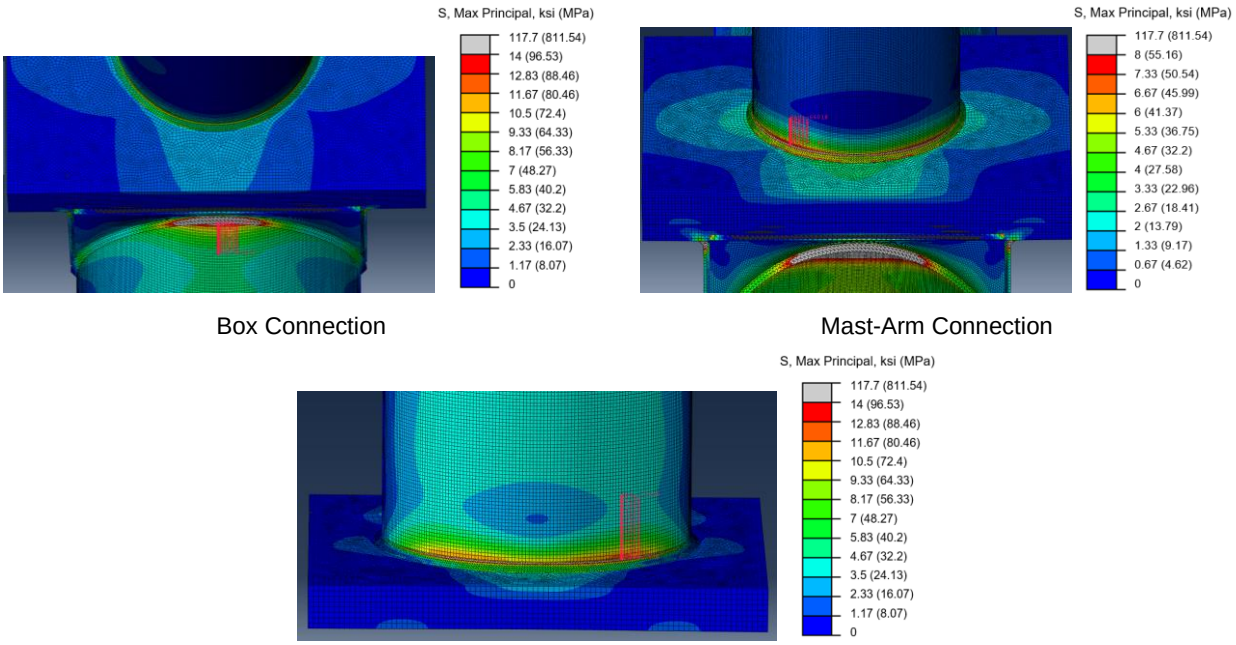

Box Connection

Mast-Arm Connection

Baseplate Connection

Figure D.104. Paths, sD6S, T+G

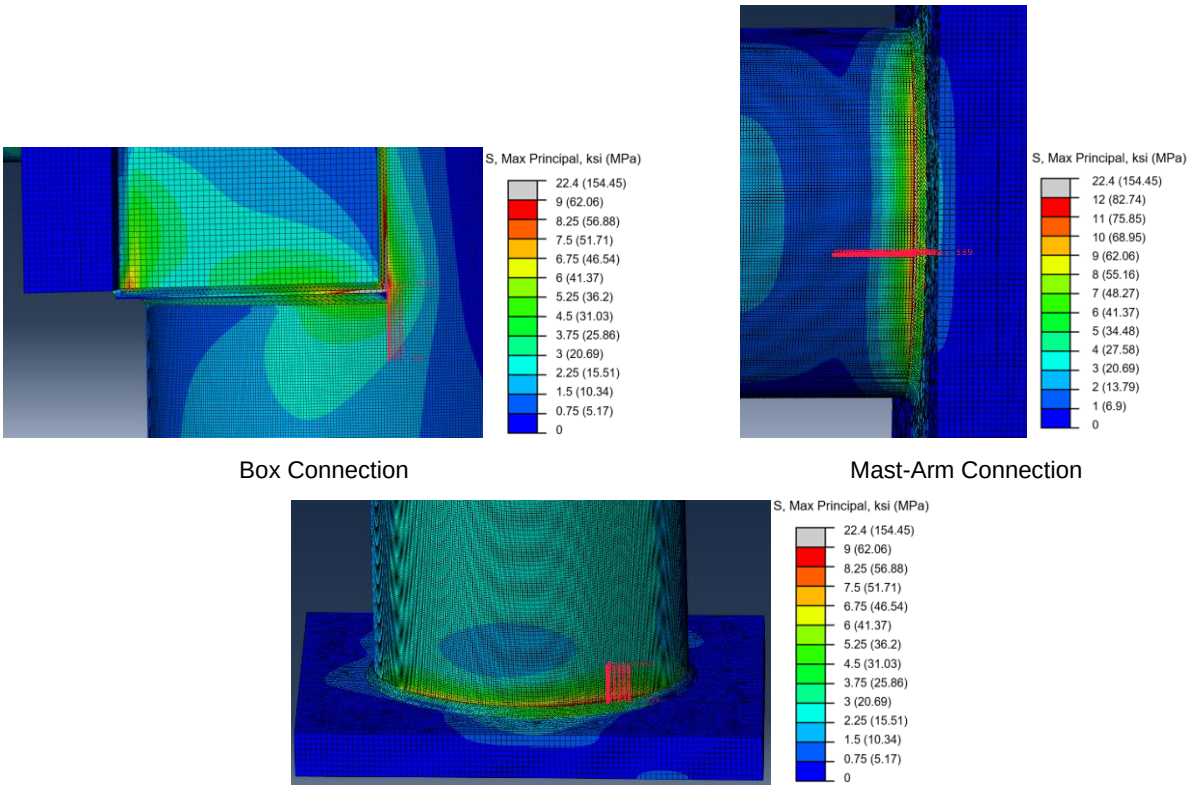

Box Connection

Mast-Arm Connection

Baseplate Connection

Figure D.105. Paths, sD6M, NW

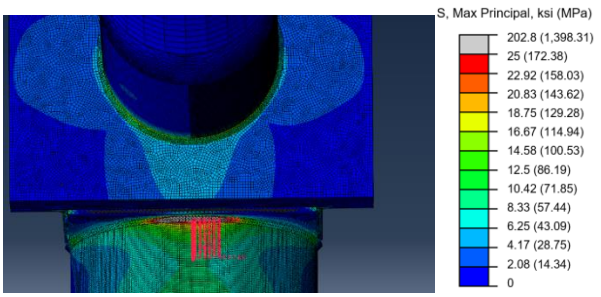

Box Connection

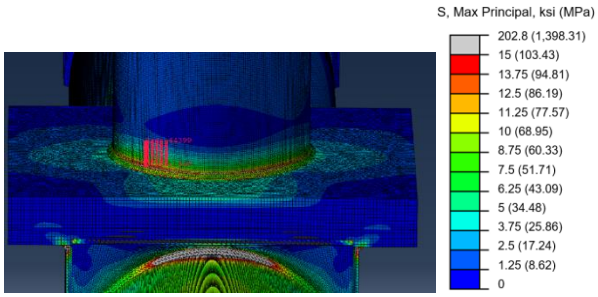

Mast-Arm Connection

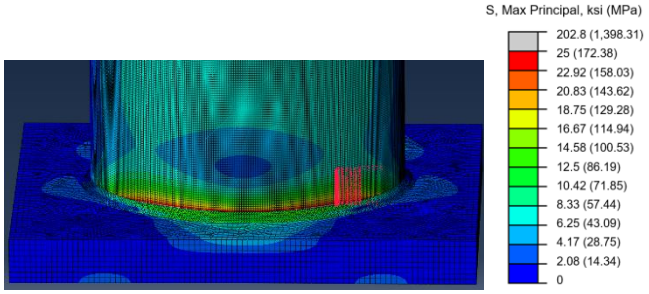

Baseplate Connection

Figure D.106. Paths, sD6M, T+G

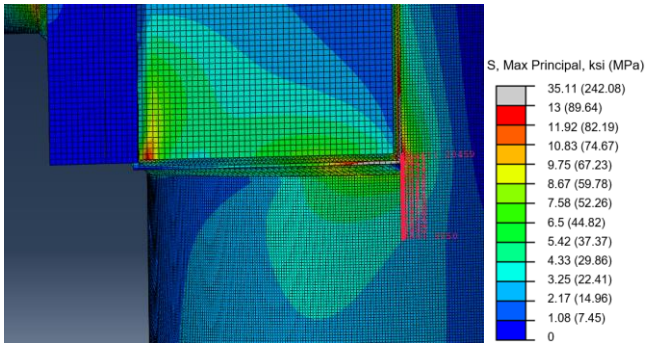

Box Connection

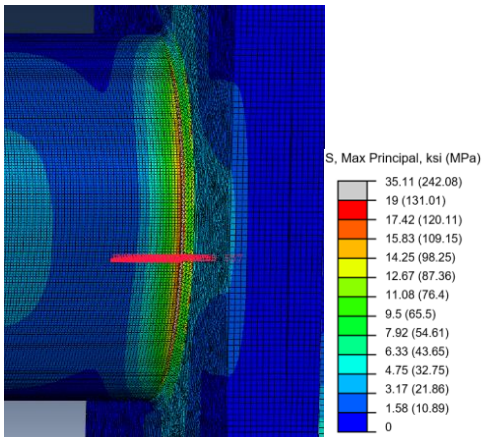

Mast-Arm Connection

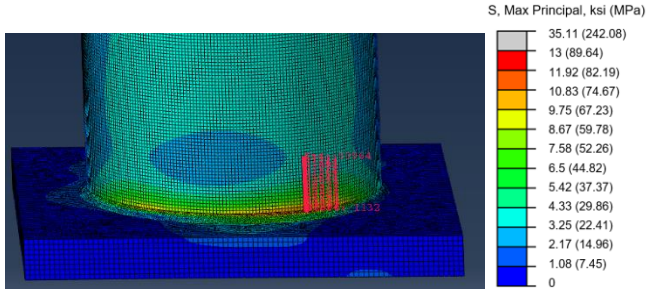

Baseplate Connection

Figure D.107. Paths, sD6L, NW

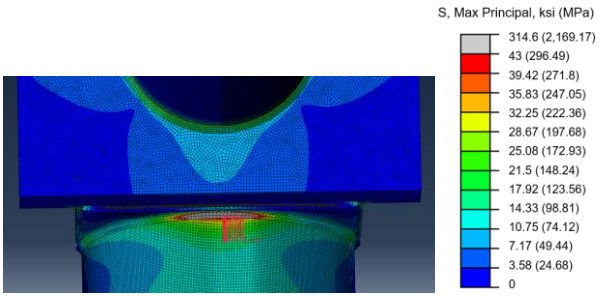

Box Connection (43)

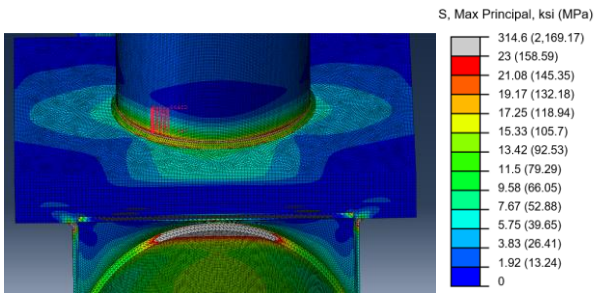

Mast-Arm Connection (23)

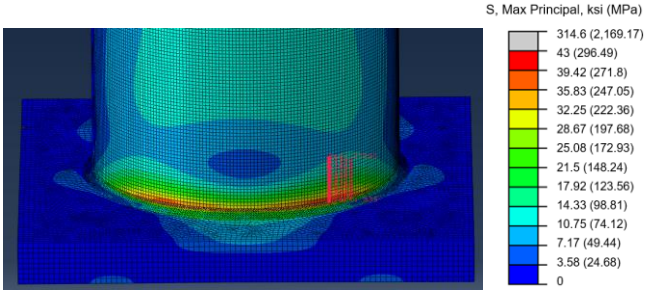

Baseplate Connection (43)

Figure D.108. Paths, sD6L, T+G

D.3. Ring-Stiffened Box Connection Models

D.3.1. Matrix

Table D.7. Ring-Stiffened Box Connection Model Matrix

	Sign Height, ft. (m)	Sign Length, ft. (m)	Arm Length, ft. (m)	Arm Dia., in. (cm)	Arm Thickness, in. (cm)	Pole Height, ft. (m)	Pole Dia., in. (cm)	Pole Thickness, in. (cm)
Ring-Stiffened Box Connection: Design #7								
Small	6 (1.83)	11.5 (3.51)	30 (9.14)	14 (35.56)	0.625 (1.59)	36 (10.97)	18 (45.72)	0.75 (1.91)
Medium	10 (3.05)	15 (4.57)	31 (9.45)			32 (9.75)		
Large	12 (3.66)	19 (5.79)	34 (10.36)			29 (8.84)		

D.3.2. Hot Spot Analysis

Table D.8. Ring-Stiffened Box Connection NW Hot Spot Stresses

	Hot Spot Stress, ksi (MPa)		
Model	Box	Arm	Baseplate
rD7S	1.73 (11.93)	3.16 (21.78)	2.09 (14.43)
rD7M	4.06 (28.01)	7.25 (50.01)	5.23 (36.04)
rD7L	6.06 (41.76)	11.15 (76.87)	7.00 (48.26)

Table D.9. Ring-Stiffened Box Connection T+G Hot Spot Stresses

	Hot Spot Stress, ksi (MPa)		
Model	Box	Arm	Baseplate
rD7S	8.83 (60.88)	5.06 (34.87)	9.42 (64.97)
rD7M	7.83 (54.01)	5.72 (39.40)	11.02 (75.99)
rD7L	13.21 (91.06)	7.29 (50.30)	14.25 (98.27)

D.3.3. S-N Curves

NW S-N Curves

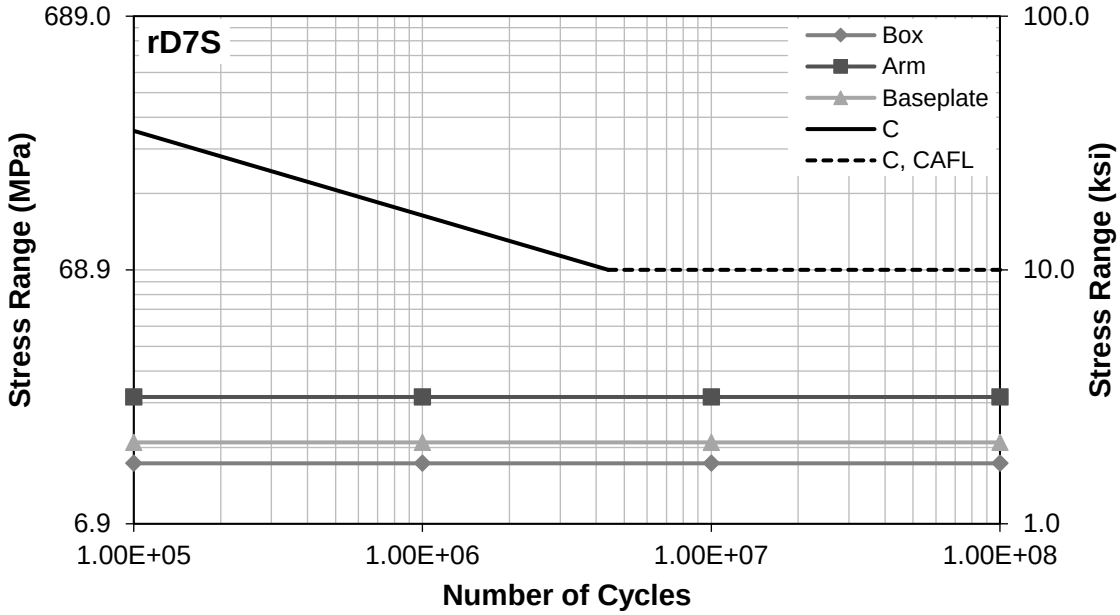

Figure D.109. S-N Curve for rD7S Hot Spot Stresses, NW

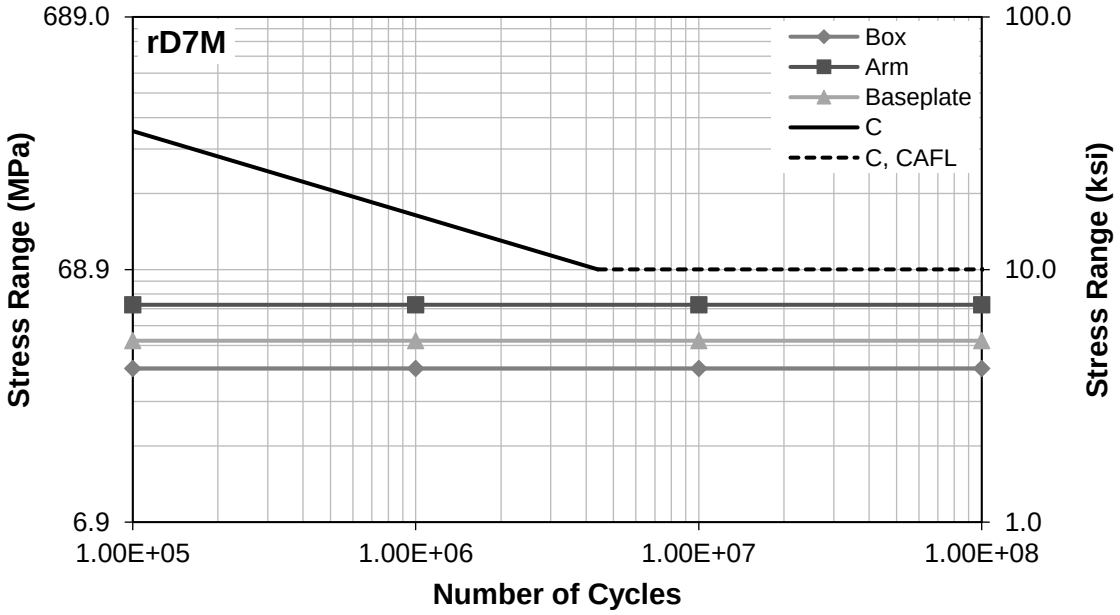

Figure D.110. S-N Curve for rD7M Hot Spot Stresses, NW

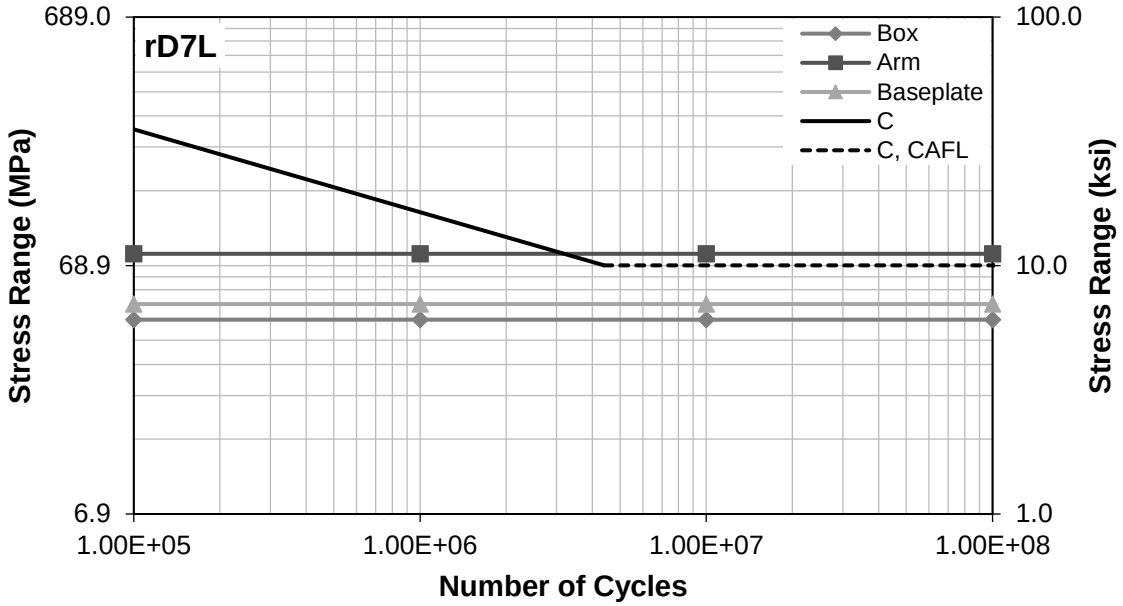

Figure D.111. S-N Curve for rD7L Hot Spot Stresses, NW

T+G S-N Curves

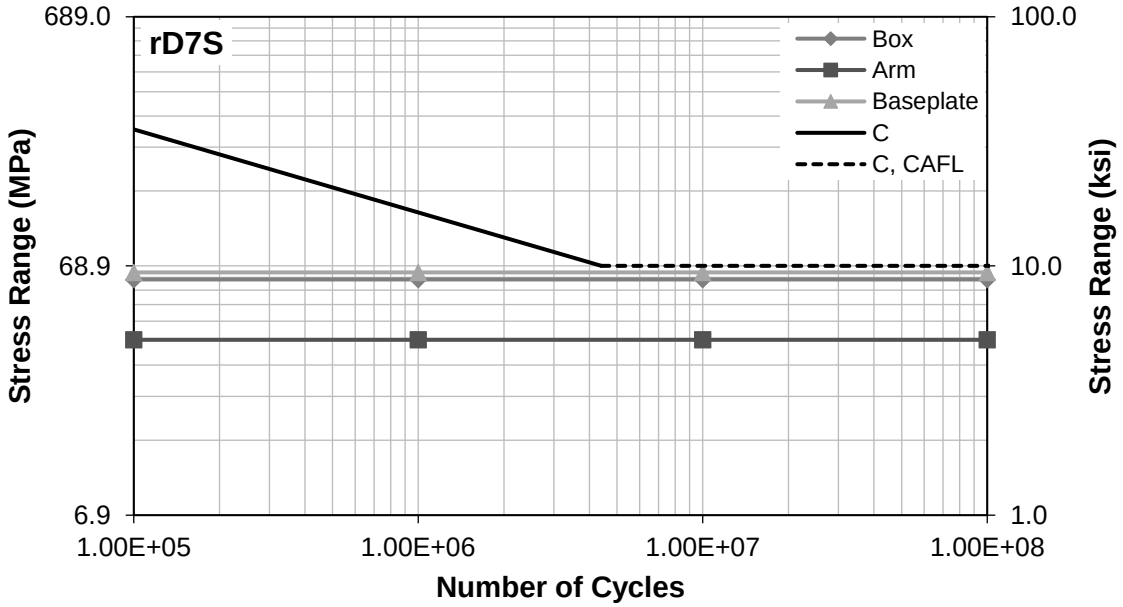

Figure D.112. S-N Curve for rD7S Hot Spot Stresses, T+G

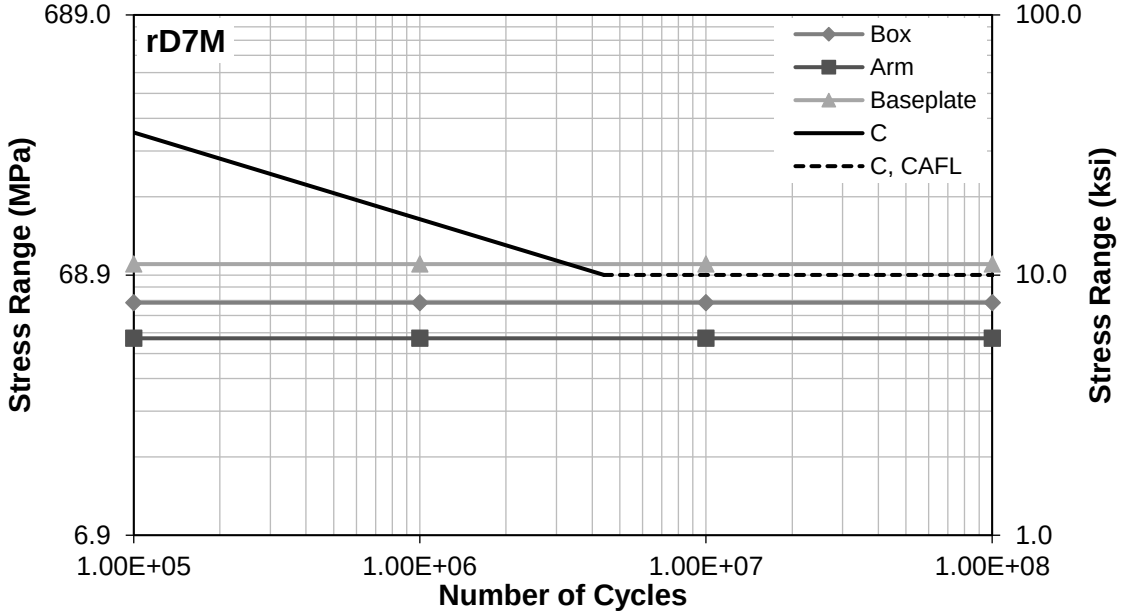

Figure D.113. S-N Curve for rD7M Hot Spot Stresses, T+G

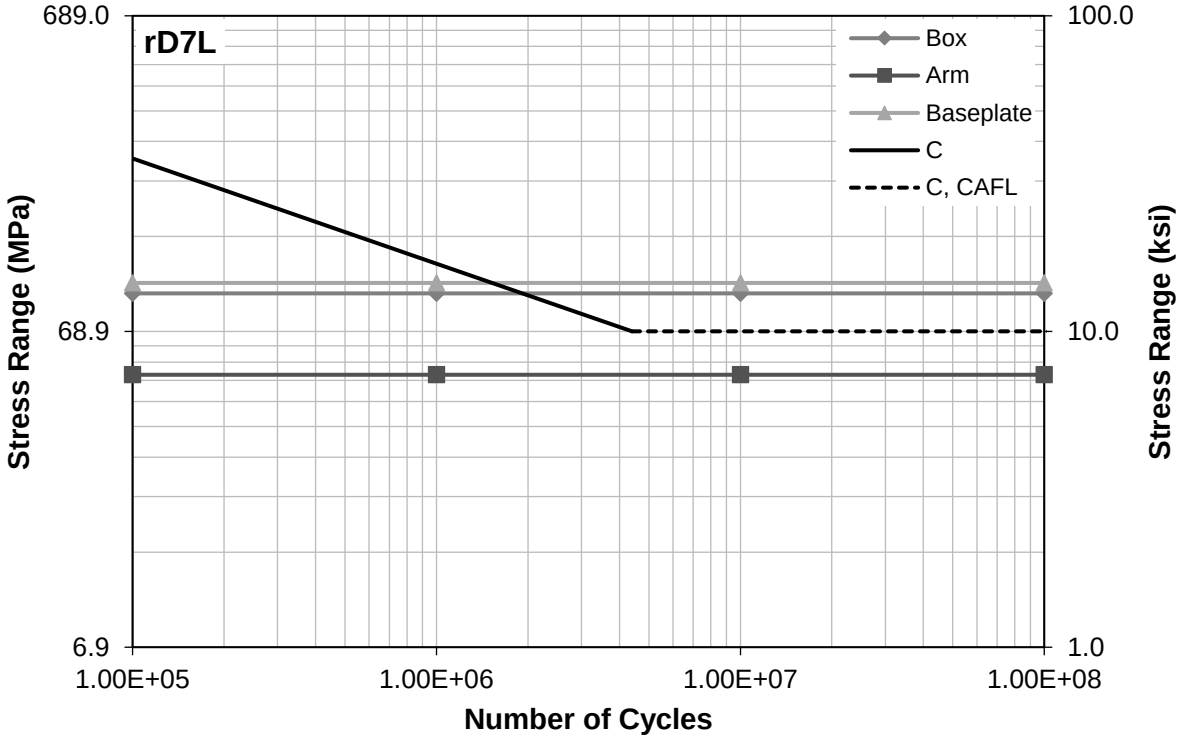

Figure D.114. S-N Curve for rD7L Hot Spot Stresses, T+G

D.3.4. Mises Stress Distributions

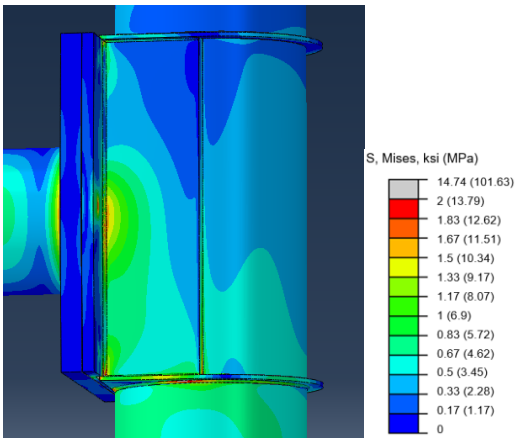

Box Connection

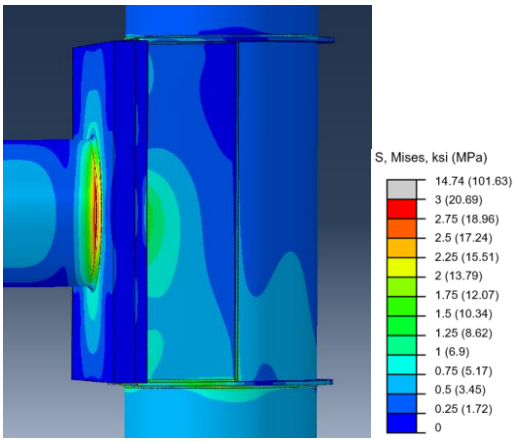

Mast-Arm Connection

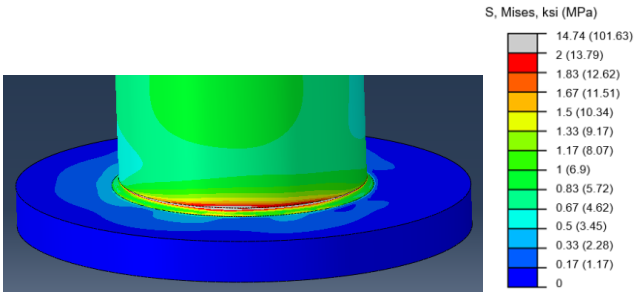

Baseplate Connection

Figure D.115. Mises Stresses, rD7S, NW

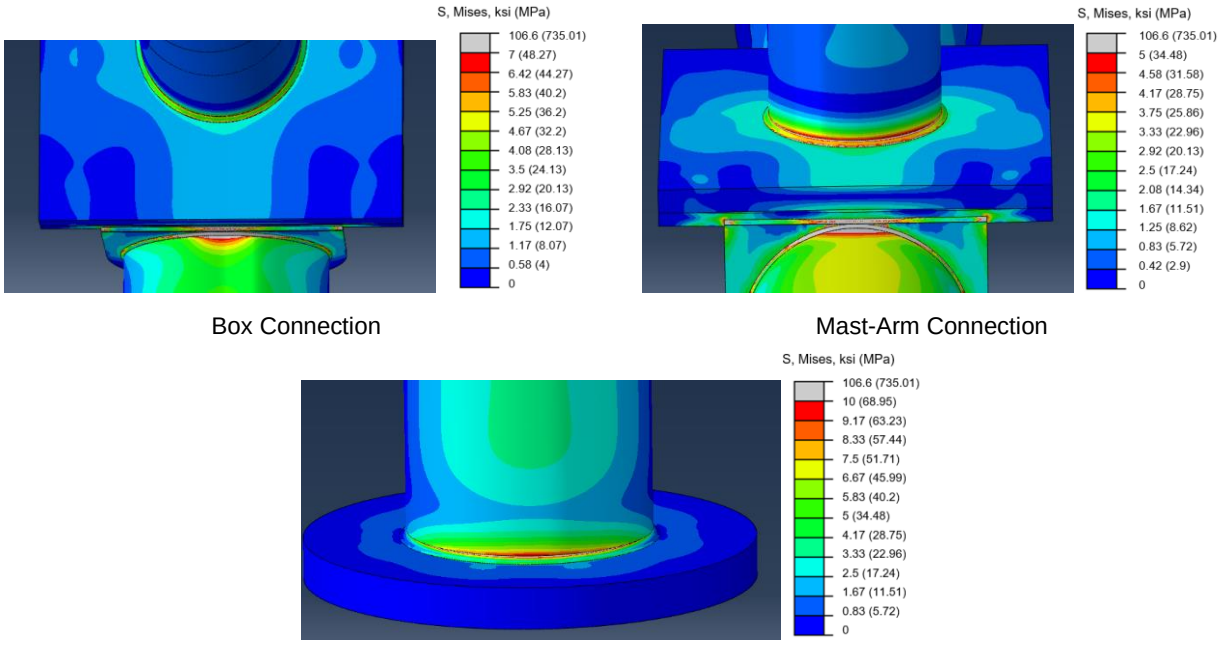

Box Connection

Mast-Arm Connection

Baseplate Connection

Figure D.116. Mises Stresses, rD7S, T+G

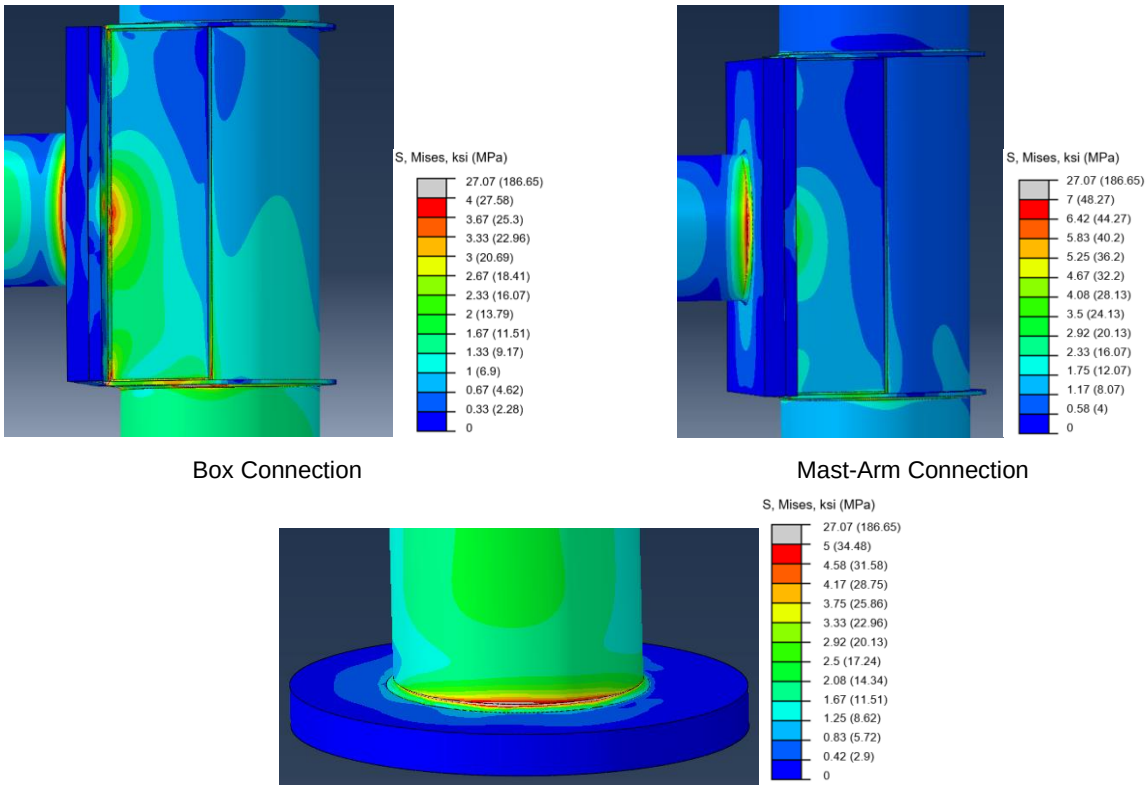

Box Connection

Mast-Arm Connection

Baseplate Connection

Figure D.117. Mises Stresses, rD7M, NW

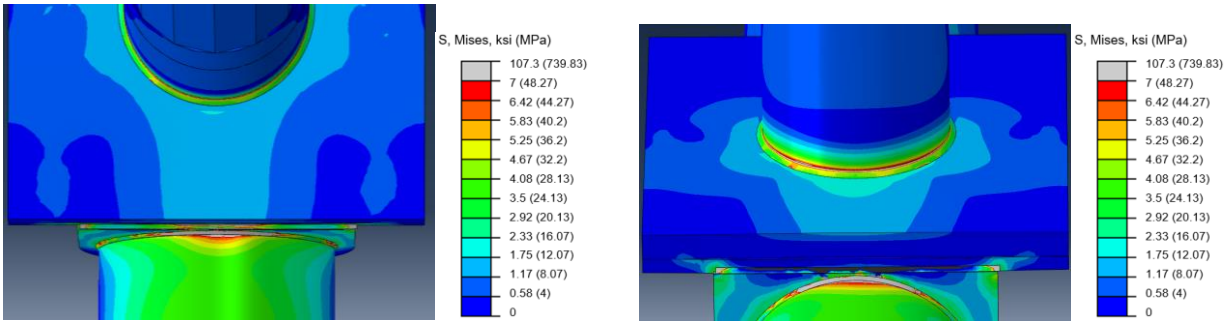

Box Connection

Mast-Arm Connection

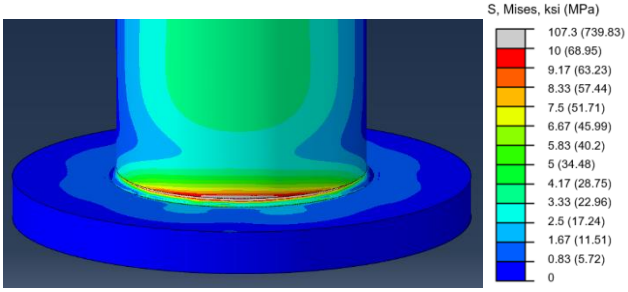

Baseplate Connection

Figure D.118. Mises Stresses, rD7M, T+G

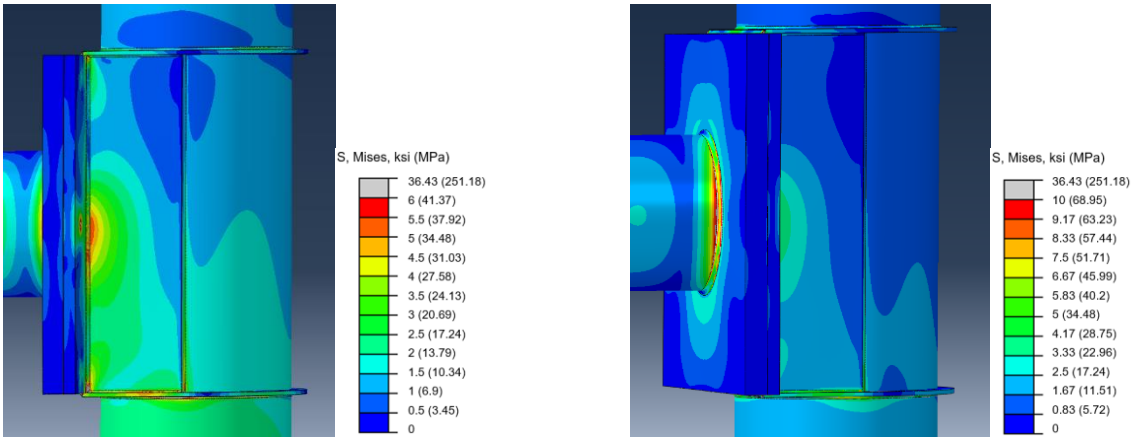

Box Connection

Mast-Arm Connection

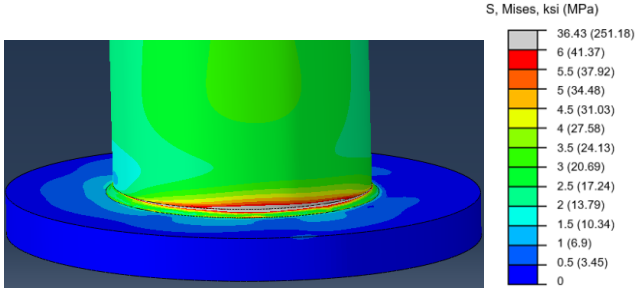

Baseplate Connection

Figure D.119. Mises Stresses, rD7L, NW

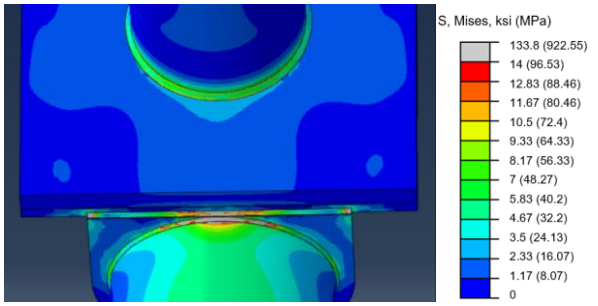

Box Connection

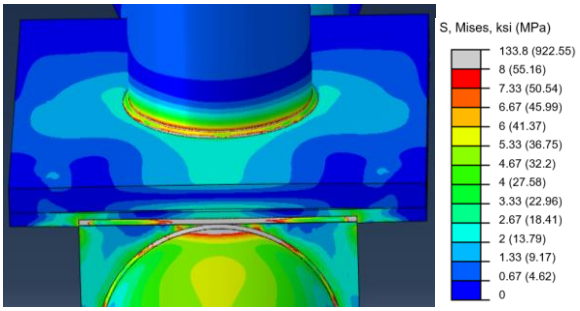

Mast-Arm Connection

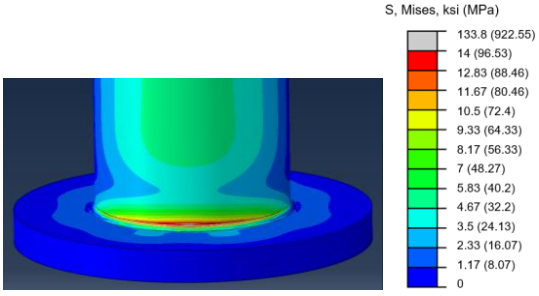

Baseplate Connection

Figure D.120. Mises Stresses, rD7L, T+G

D.3.5. Max Principal Stress Paths

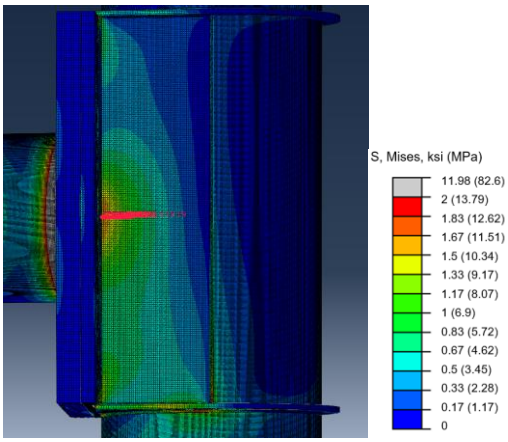

Box Connection

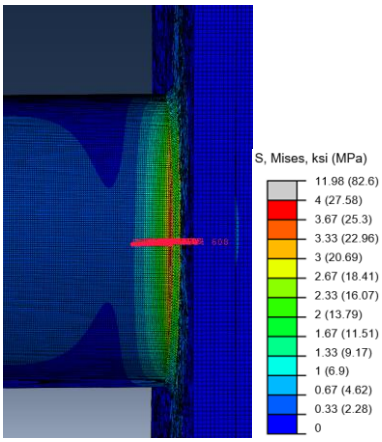

Mast-Arm Connection

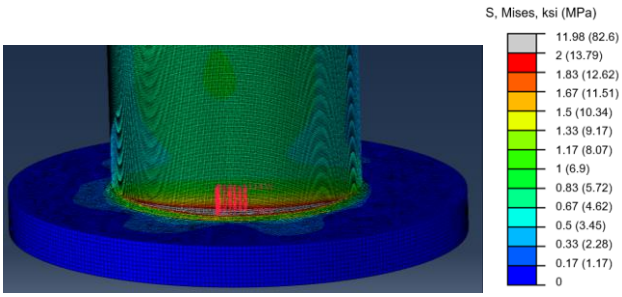

Baseplate Connection

Figure D.121. Paths, rD7S, NW

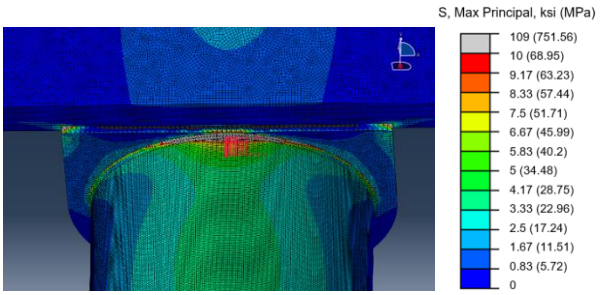

Box Connection (10)

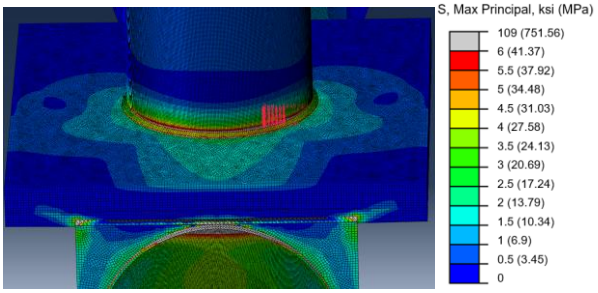

Mast-Arm Connection (6)

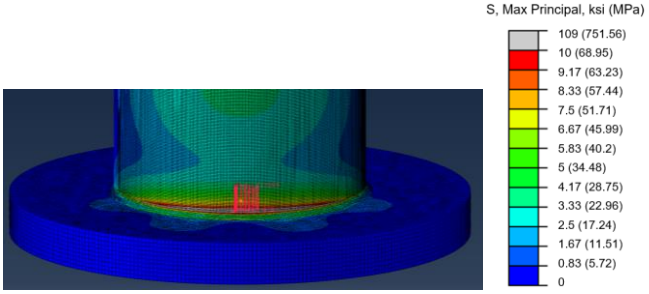

Baseplate Connection (10)

Figure D.122. Paths, rD7S, T+G

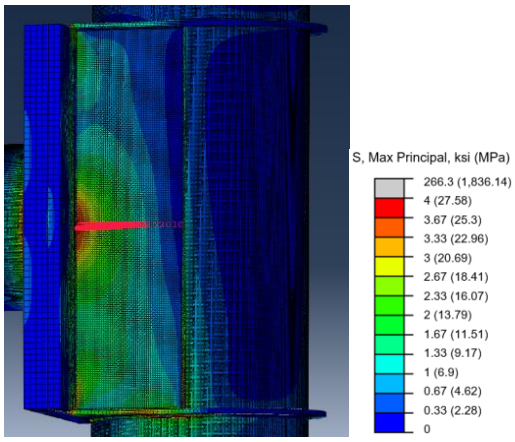

Box Connection

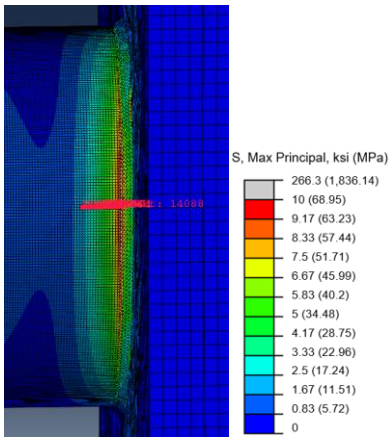

Mast-Arm Connection

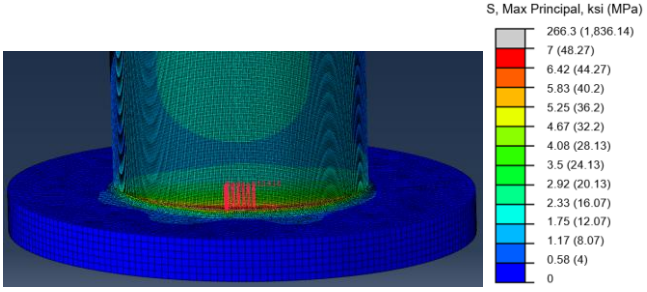

Baseplate Connection

Figure D.123. Paths, rD7M, NW

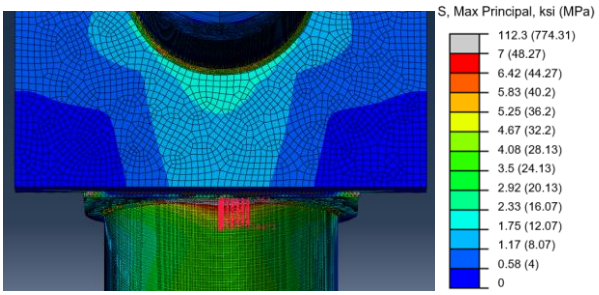

Box Connection

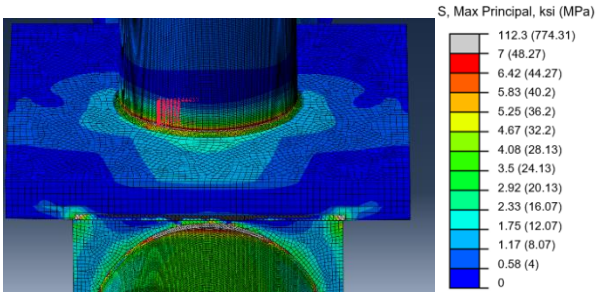

Mast-Arm Connection

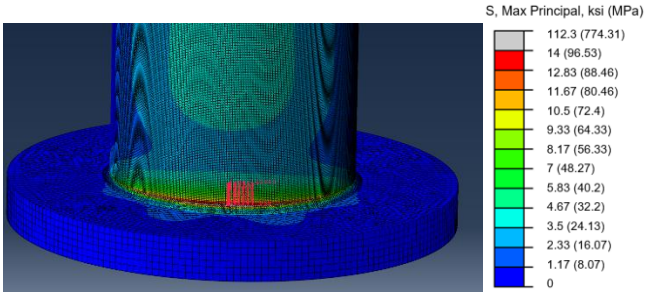

Baseplate Connection

Figure D.124. Paths, rD7M, T+G

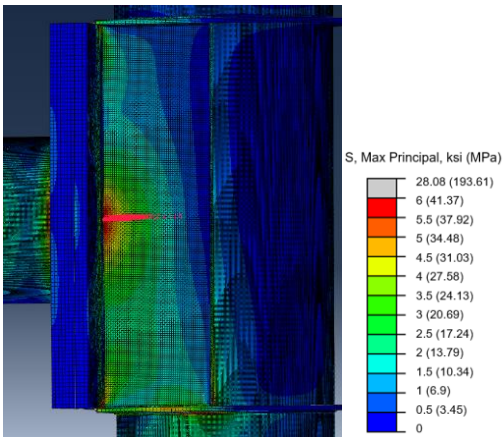

Box Connection

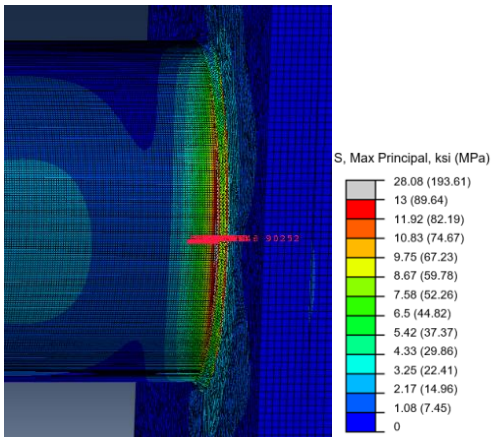

Mast-Arm Connection

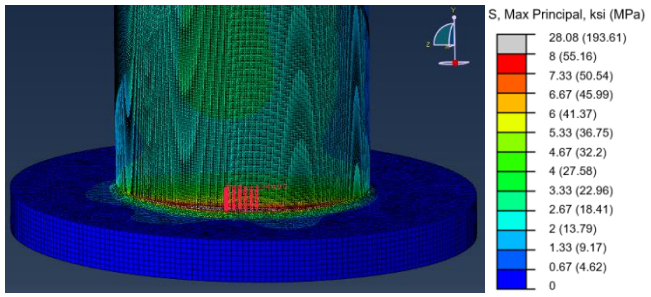

Baseplate Connection

Figure D.125. Paths, rD7L, NW

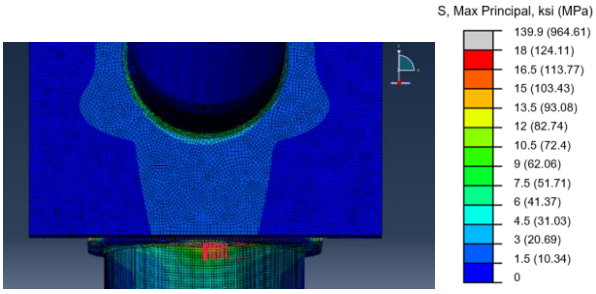

Box Connection

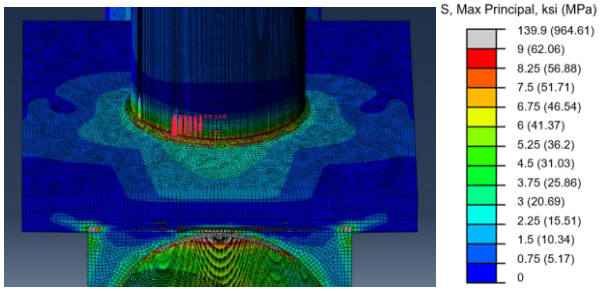

Mast-Arm Connection

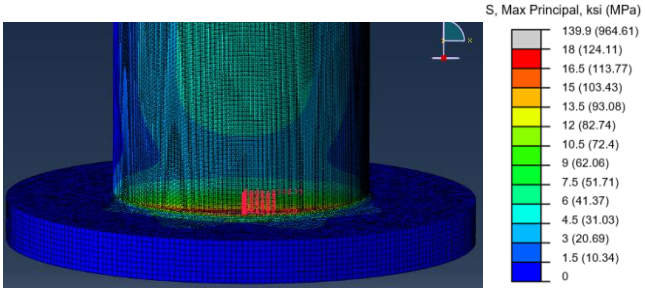

Baseplate Connection

Figure D.126. Paths, rD7L, T+G

D.4. Full-Sized Model Comparison

Table D.10. Percent Decrease of Stresses between Structure Types, NW

	% Stress Decrease		
Model Comparison	**Box**	**Arm**	**Baseplate**
Tapered to Ring-Stiffened			
tD7S to rD7S	78.67%	63.04%	54.96%
tD7M to rD7M	76.38%	60.53%	53.68%
tD7L to rD7L	66.05%	40.69%	47.72%
Average	73.70%	54.76%	52.12%
Straight to Ring-Stiffened			
sD6S to rD7S	40.55%	24.94%	26.41%
sD6M to rD7M	26.58%	16.57%	43.34%
sD6L to rD7L	36.94%	19.14%	31.44%
Average	34.69%	20.22%	33.73%
Tapered to Straight			
tD1S to sD1S	68.77%	39.61%	6.87%
tD1M to sD1M	66.69%	37.91%	26.82%
tD1L to sD1L	66.82%	39.61%	37.42%
tD3S to sD3S	65.68%	43.24%	21.24%
tD3M to sD3M	64.81%	30.55%	21.37%
tD3L to sD3L	62.32%	33.77%	21.10%
tD7S to sD6S	64.12%	50.76%	38.79%
tD7M to sD6M	67.83%	52.69%	18.25%
tD7L to sD6L	46.16%	26.65%	23.75%
Average	63.69%	39.42%	23.96%

Table D.11. Percent Decrease of Stresses between Structure Types, T+G

	% Stress Decrease		
Model Comparison	**Box**	**Arm**	**Baseplate**
Tapered to Ring-Stiffened			
tD7S to rD7S	50.86%	61.02%	51.54%
tD7M to rD7M	78.24%	76.42%	67.40%
tD7L to rD7M	70.66%	72.72%	56.63%
Average	66.59%	70.05%	58.52%
Straight to Ring-Stiffened			
sD6S to rD7S	26.54%	23.33%	17.15%
sD6M to rD7M	62.66%	50.35%	50.18%
sD6L to rD7L	59.91%	61.61%	59.42%
Average	49.70%	45.10%	42.25%
Tapered to Straight			
tD1S to sD1S	52.11%	49.63%	9.16%
tD1M to sD1M	51.43%	62.72%	25.26%
tD1L to sD1L	51.78%	45.09%	36.73%
tD3S to sD3S	34.34%	17.76%	13.35%
tD3M to sD3M	28.28%	26.11%	15.72%
tD3L to sD3L	41.92%	31.47%	13.56%
tD7S to sD6S	33.11%	49.15%	41.51%
tD7M to sD6M	41.72%	52.51%	34.56%
tD7L to sD6L	26.83%	28.93%	-6.88%*
Average	40.17%	40.38%	20.33%

*Stresses in the straight model were larger than the tapered model, leading to a slight increase

Table D.12. Percent Decrease of Stresses with Arm Thickness Increase

		% Stress Decrease, NW		% Stress Decrease, T+G	
Model Comparison	**Thickness Change (in.)**	**Box**	**Arm**	**Box**	**Arm**
Small Sign Models					
tD1S to sD1S	0.25 to 0.5	68.75%	39.59%	52.10%	49.63%
tD3S to sD3S	0.1875 to 0.25	65.64%	43.26%	34.33%	17.70%
tD7S to sD6S	0.3125 to 0.5	64.09%	50.79%	33.11%	49.19%
sD6S to rD7S	0.5 to 0.625	40.56%	24.88%	26.55%	23.32%
tD7S to rD7S	0.3125 to 0.625	78.65%	63.04%	50.87%	61.04%
Medium Sign Models					
tD1S to sD1S	0.25 to 0.5	66.71%	37.93%	51.43%	62.72%
tD3S to sD3S	0.1875 to 0.25	64.81%	30.58%	28.28%	26.10%
tD7S to sD6S	0.3125 to 0.5	67.82%	52.66%	41.73%	52.49%
sD6S to rD7S	0.5 to 0.625	26.53%	16.57%	62.64%	50.40%
tD7S to rD7S	0.3125 to 0.625	76.36%	60.51%	78.23%	76.44%
Large Sign Models					
tD1S to sD1S	0.25 to 0.5	66.83%	39.61%	51.78%	45.09%
tD3S to sD3S	0.1875 to 0.25	62.34%	33.77%	41.92%	31.48%
tD7S to sD6S	0.3125 to 0.5	46.19%	26.66%	26.83%	28.93%
sD6S to rD7S	0.5 to 0.625	36.94%	19.12%	59.92%	61.58%
tD7S to rD7S	0.3125 to 0.625	66.07%	40.69%	70.67%	72.7%
Average		59.89%	38.64%	47.36%	47.25%

Table D.13. Percent Decrease of Stresses with Pole Thickness Increase

		% Stress Decrease, NW		% Stress Decrease, T+G	
Model Comparison	**Thickness Change (in.)**	**Box**	**Arm**	**Box**	**Arm**
Small Sign Models					
tD1S to sD1S	0.25 to 0.375	68.77%	6.87%	52.11%	9.16%
tD3S to sD3S	0.25 to 0.375	65.68%	21.24%	34.34%	13.35%
tD7S to sD6S	0.3125 to 0.5	64.12%	38.79%	33.11%	41.51%
sD6S to rD7S	0.5 to 0.75	40.55%	26.41%	26.54%	17.15%
tD7S to rD7S	0.3125 to 0.75	78.67%	54.96%	50.86%	51.54%
Medium Sign Models					
tD1S to sD1S	0.25 to 0.375	66.69%	49.13%	51.43%	25.26%
tD3S to sD3S	0.25 to 0.375	64.81%	21.37%	28.28%	15.72%
tD7S to sD6S	0.3125 to 0.5	67.83%	18.25%	41.72%	34.56%
sD6S to rD7S	0.5 to 0.75	26.58%	43.34%	62.66%	50.18%
tD7S to rD7S	0.3125 to 0.75	76.38%	53.68%	78.24%	67.40%
Large Sign Models					
tD1S to sD1S	0.25 to 0.375	66.82%	37.42%	51.78%	10.04%
tD3S to sD3S	0.25 to 0.375	62.32%	21.10%	41.92%	13.56%
tD7S to sD6S	0.3125 to 0.5	46.16%	23.75%	26.83%	-6.88%*
sD6S to rD7S	0.5 to 0.75	36.94%	31.44%	59.91%	59.42%
tD7S to rD7S	0.3125 to 0.75	66.05%	47.72%	70.66%	56.63%
Average		59.89%	33.03%	47.36%	30.57%

*Stresses in the straight model were larger than the tapered model, leading to a slight increase

D.5. Test Specimen Models

D.5.1. Hot Spot Analysis

Table D.14. Hot Spot Stresses for Initial Test Specimen Design

Hot Spot Stress, ksi (MPa)		
Box	Arm	Baseplate
17.64 (121.62)	19.80 (136.52)	12.98 (89.49)

Table D.15. Hot Spot Stresses for Real Specimen Model

Hot Spot Stress, ksi (MPa)		
Box	Arm	Baseplate
18.02 (124.24)	20.61 (142.1)	12.99 (89.56)

D.5.2. S-N Curves

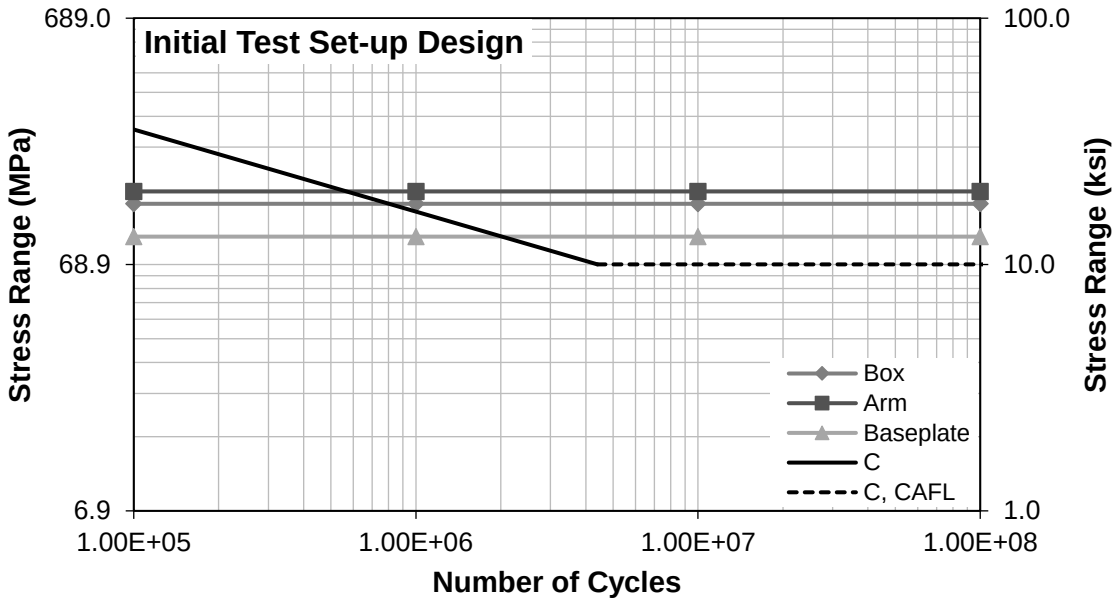

Figure D.127. S-N Curve for Initial Test Specimen Design Hot Spot Stresses

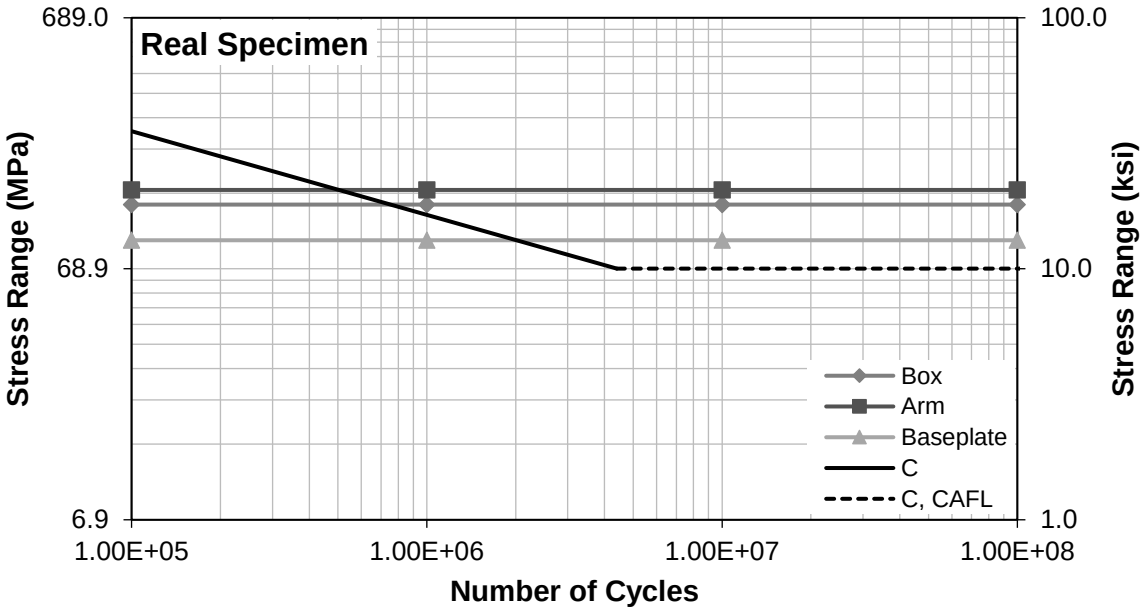

Figure D.128. S-N Curve for Real Specimen Model Hot Spot Stresses

D.5.3. Mises Stress Distributions

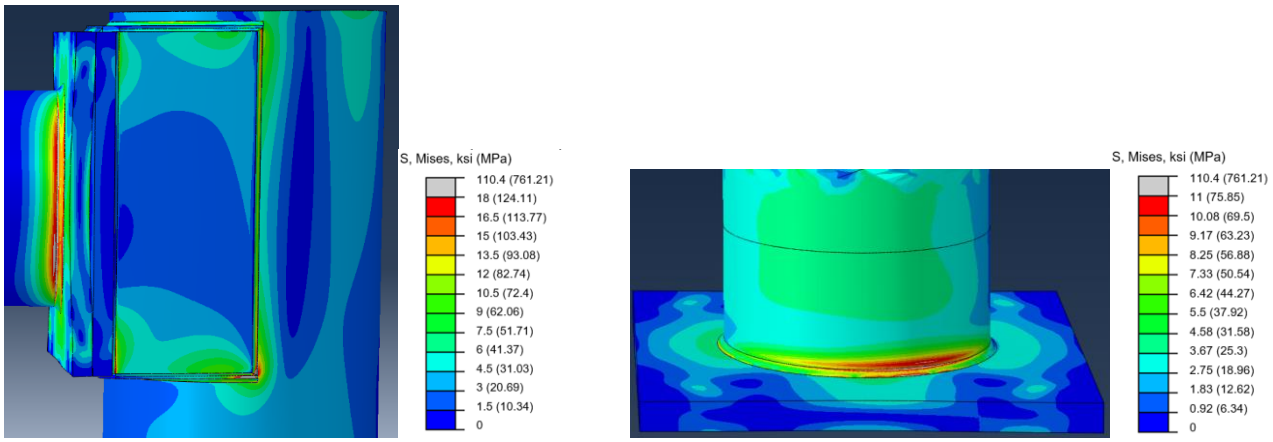

Box and Mast-Arm Connection Baseplate Connection

Figure D.129. Mises Stress, Initial Test Specimen Design

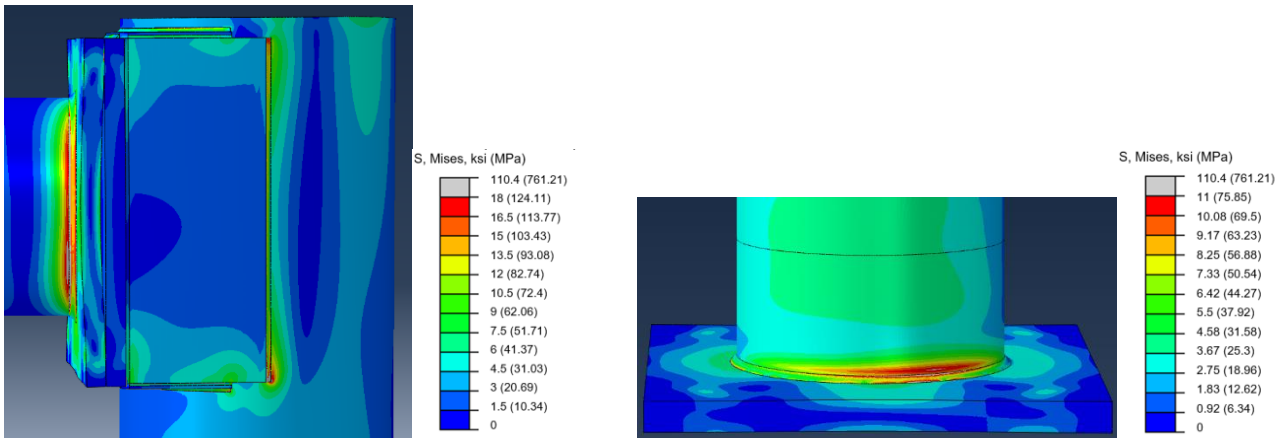

Box and Mast-Arm Connection Baseplate Connection

Figure D.130. Mises Stresses, Real Specimen

D.5.4. Max Principal Stress Paths

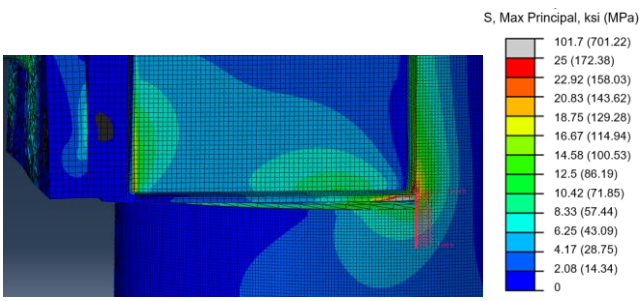

Box Connection

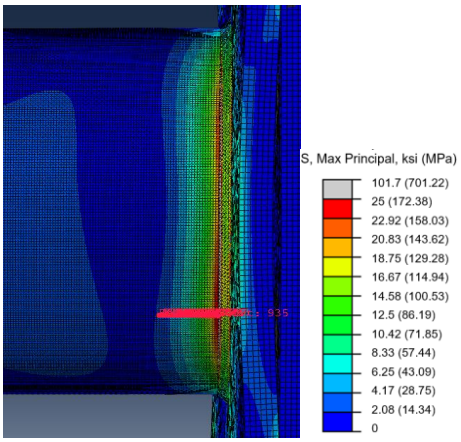

Mast-Arm Connection (25)

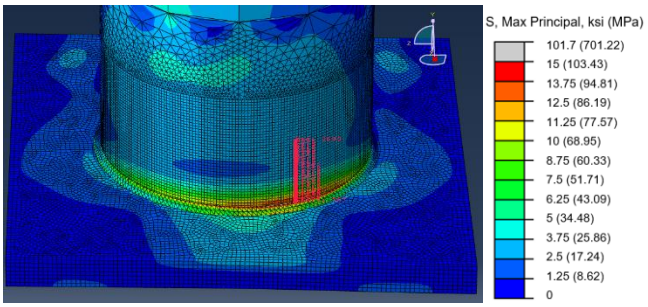

Baseplate Connection

Figure D.131. Paths, Initial Test Specimen Design

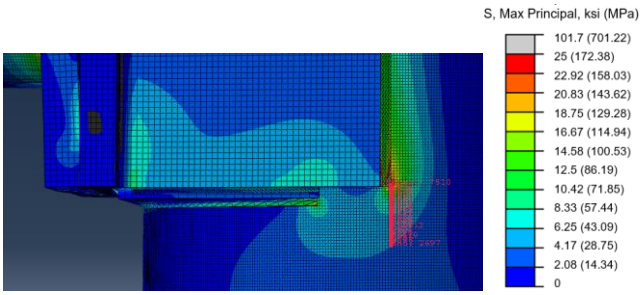

Box Connection

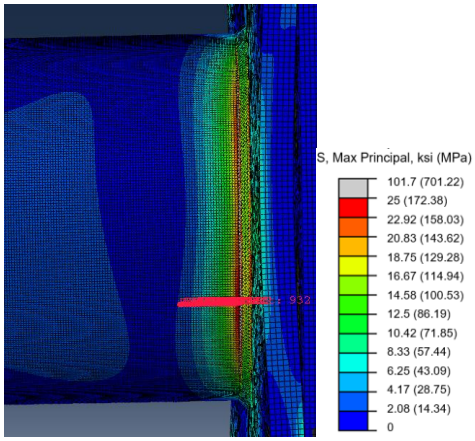

Mast-Arm Connection

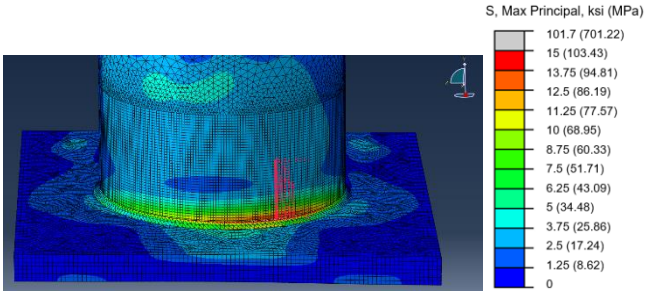

Baseplate Connection

Figure D.132. Paths, Real Specimen